Ph.D. Thesis

Theoretical study of signals from binary neutron star mergers

連星中性子星合体からの信号に関する理論研究

Kenta Hotokezaka

仏坂健太

Kyoto University

January 6, 2014

Abstract

Binary neutron stars (NS–NSs) are among the strong gravitational-wave emitters in the Universe. They are one of the main targets of the second generation ground based gravitational-wave observatories such as Advanced LIGO, Advanced Vigro, and KAGRA. In this thesis, we systematically study NS–NS mergers based on numerical-relativity simulations. In particular, we focus on the dependence of the merger dynamics, gravitational waveforms, and mass ejection on equations of state (EOSs) of neutron-star matter. Then we make theoretical predictions for expected gravitational-wave and electromagnetic signals from NS–NS mergers within the uncertainties of the EOS of neutron-star matter. This research covers following topics:

(1) Tidal effects during a late inspiral stage of an NS–NS. We perform long-term numerical simulations of NS–NS inspirals ($\lesssim 10$ orbits) in order to explore tidal effects in a coalescing NS–NS, which reflect finite size of a neutron star in gravitational waves. We show that the numerical errors due to finite differencing dominate in our current numerical simulations. In order to obtain the physical waveforms, we perform the resolution-extrapolation of waveforms by analyzing numerical data with different grid resolutions. Comparing the extrapolated numerical and analytical waveforms, we find the strong tidal effects in our numerical simulations in a last few orbits. Here the analytical waveforms are computed by a post-3.5 Newtonian formalism or effective one body formalism. Both the formalisms include tidal effects as a perturbation. We also find that the extrapolated-numerical waveforms obtained by our current simulations can not be used as template waveforms due to numerical errors. Therefore we need higher-accuracy simulations in order to construct end-to-end waveforms of NS–NS mergers.

(2) Post-merger dynamics and resulting gravitational waveforms. Recent discoveries of heavy pulsars indicate that the EOS of neutron-star matter is sufficiently stiff. Based on such a stiff EOS, a massive neutron star is likely to be formed after an NS–NS merger. We study the first outcome of NS–NS mergers for several masses and EOSs. We find that a massive neutron star mostly survives for an NS–NS merger with the total mass range from $2.6M_{\odot}$ to $2.8M_{\odot}$, irrespective of the EOS. On the other hand, their final fates depend on the EOS and the total mass. These results encourage us to take into account the existence of a remnant massive neutron star, when we study the central engine of gamma-ray bursts (GRBs) based on the compact binary merger hypothesis.

These remnant massive neutron stars can be strong gravitational-wave emitters. Gravitational waveforms from massive neutron stars are analyzed. As a result, we find the

correlation between the characteristic frequency of the gravitational waves and neutron star radii. Furthermore, we attempt to construct a phenomenological-waveform model of the post-merger waveforms, which can describe numerical waveforms with the mismatch of $\lesssim 10\%$. Such a phenomenological modeling of numerical waveforms will be useful for gravitational-wave data analysis.

(3) Mass ejection from an NS–NS merger. A fraction of material is expected to be dynamically ejected at the merger. We study dynamical mass ejection from an NS–NS merger based on numerical relativity-simulations. In order to compute dynamics of unbound material, a relatively wide computational domain is employed. As a result, we find that ejecta mass is in the range of 10^{-4}–$10^{-2} M_{\odot}$ and the ejecta velocity is in the range of 0.1–$0.5c$, for the various total masses, mass ratios, and EOSs. Remarkably, we find that the amount of ejecta is large for the case of hypermassive neutron star (HMNS) formation. As long as a long-lived HMNS is formed, the following properties can be found: (i) For a given EOS, the ejecta mass increases with total mass of an NS–NS. (ii) For a given mass, an NS–NS merger with a softer EOS produces a larger amount of ejecta. (iii) Ejecta have a spheroidal shape rather than a disk-like shape. These features of mass ejection of NS–NS mergers will be helpful to investigate electromagnetic signals from the NS–NS merger ejecta. Furthermore, a spheroidal shape of ejecta indicates that a relativistic jet which may produce a GRB is inevitable to interact with ejecta. This will be an important subject in a context of production of short GRBs.

(4) A kilonova candidate associated with the short GRB 130603B. A near-infrared excess was observed at 9 days after the *Swift* short GRB 130603B by *Hubble Space Telescope*. This excess can be explained as an r-process kilonova/macronova emission produced either by an NS–NS merger or a black hole–neutron star merger. We explore the possible progenitor model based on numerical-relativity and radiative transfer simulations. As a result, we show that NS–NS merger models with soft EOSs and black hole–neutron star merger models with stiff EOSs are the possible progenitor model of the short GRB 130603B. This result support the fact that a kilonova/macronova will be an observable electromagnetic counterpart to a gravitational-wave signal from a compact binary merger.

Contents

The physical constants adopted in this thesis.

$$
\begin{array}{ll}
G & 6.67384 \times 10^{-8}\ \mathrm{cm}^3\ \mathrm{g}^{-1}\mathrm{s}^{-2} \\
c & 2.99792458 \times 10^{10}\ \mathrm{cm\ s}^{-1} \\
\hbar & 1.054571628 \times 10^{-27}\ \mathrm{erg\ s} \\
m_p & 1.6726217 \times 10^{-24}\ \mathrm{g} \\
m_e & 9.10938291 \times 10^{-28}\ \mathrm{g} \\
e & 4.80320425 \times 10^{-10}\ \mathrm{erg}^{1/2}\mathrm{cm}^{1/2} \\
\sigma_{\mathrm{T}} & 6.6524574 \times 10^{-25}\ \mathrm{cm}^2 \\
k_{\mathrm{B}} & 1.3806488 \times 10^{-16}\ \mathrm{erg\ K}^{-1} \\
\sigma_{\mathrm{SB}} & 5.6704 \times 10^{-5}\ \mathrm{erg\ cm}^{-2}\mathrm{s}^{-1}\mathrm{K}^{-4} \\
M_\odot & 1.9884 \times 10^{33}\ \mathrm{g} \\
GM_\odot & 1.32712440018 \times 10^{26}\ \mathrm{cm}^3\mathrm{s}^{-2} \\
R_\odot & 6.955 \times 10^{10}\ \mathrm{cm} \\
\mathrm{Jy} & 10^{-23}\ \mathrm{erg\ s}^{-1}\mathrm{cm}^{-2}\mathrm{Hz}^{-1} \\
\mathrm{pc} & 3.08568 \times 10^{18}\ \mathrm{cm}
\end{array}
\tag{1}
$$

Throughout this thesis, we adopt the geomtetrical units in which $G = c = M_\odot = 1$, unless otherwise stated. We use the spacetime metric signature $(-, +, +, +)$.

Chapter 1

Introduction

1.1 Binary neutron star

Hulse and Taylor discovered a pulsar PSR B 1913+16 with a pulsation period that modulates systematically with a period about 8 hours (Hulse and Taylor 1975). This was the first discovery of the radio pulsar contained in a binary system. This system was turned out to be a binary neutron star (NS–NS) because the component mass of the binary system was measured $M_A \approx M_B \approx 1.4 M_\odot$ through general relativistic effects (Taylor et al. 1979). The continuous efforts of the pulsar surveys increase the number of known NS–NS systems. Until now, nine NS–NS systems* have been discovered (Lorimer 2008). In Table 1.1, NS–NS systems of which at least two post-Keplerian parameters are measured are listed.

These systems provide us the unique laboratory to test the physics of strong gravity. For instance, the value of post-Keplerian parameters agrees with the expected value from general relativity within uncertainties of 1% by the observations of PSR J 0737-3039A/B (Kramer et al. 2006). A remarkable fact is that the orbital periods of the observed NS–NS decrease with time. The rate of change of orbital periods agrees with the expected value from general relativity with high accuracy. Moreover, some of the observed NS–NS systems will coalesce within 10 Gyr (see Table 1.1). From these observational facts, we obtain two important evidences: (i) gravitational waves are generated by compact binary systems, (ii) NS–NS systems which coalesce within the age of the universe exist. At the coalescence of a compact binary, gravitational waves are strongly emitted. Therefore the merger of an NS–NS system can provide us the opportunity to directly detect gravitational waves on the Earth.

The merger rate of NS–NS binaries can be estimated from these observed NS–NS systems (Phinney 1991; Narayan et al. 1991; Kim et al. 2003). Of course, the estimation depends on the assumptions of the lifetime of pulsars, observable probability of a pulsar

*PSR B1820-11 is a candidate of an NS–NS system (Lorimer 2008). But it is likely to be a neutron star–white dwarf system (Portegies Zwart and Yungelson 1999).

Table 1.1: Parameters of Binary Neutron Stars of which at least two post-Keplarian parameters are measured.

Name	Mass($M_\odot$)	$P_{\rm orb}$(day)	e	$t_{\rm c}$(Gyr)	References
PSR J 0737-3039A	1.3381(7)	0.10225156248	0.0877775	0.085	Burgay et al. (2003); Kramer et al. (2006)
PSR J 0737-3039B	1.2489(7)	—	—	—	
PSR B 1534+12	1.3332(10)	0.42073729912	0.273677	3	Stairs et al. (2002)
Companion	1.3452(10)	—	—	—	
PSR J 1756-2251	1.312(17)	0.31963389	0.18056	2	Faulkner et al. (2005)
Companion	1.258(18)	—	—	—	
PSR J 1906+0746	1.323(11)	0.165993045(8)	0.085303(2)	0.3	Lorimer et al. (2006); Kasian (2012)
Companion‡	1.290(11)	—	—	—	
PSR B 1913+16	1.4398(2)	0.322997448911(14)	0.6171334(5)	0.3	Weisberg et al. (2010)
Companion	1.3886(2)	—	—	—	
PSR B 2127+11C	1.358(10)	0.33528204828(5)	0.681395(2)	0.2	Jacoby et al. (2006)
Companion	1.354(11)	—	—	—	
PSR J 1807-2500B	1.3655(21)	9.9566681588(27)	0.747033198(40)	10^3	Lynch et al. (2012)
Companion	1.2064(20)	—	—	—	

beam, and so on. The ultra-conservative estimation for the NS–NS merger rate gives a lower limit 6×10^{-4} Mpc^{-3}Myr^{-1}. An upper limit of the NS–NS merger rate can be estimated from the event rate of type Ibc supernovae as 50 Mpc^{-3}Myr^{-1} †. More recently, a plausible range of the expected merger rate is estimated as 0.01–10 Mpc^{-3}Myr^{-1} (Abadie et al. 2010). These estimations allow us to design gravitational-wave detectors and to study phenomena related to compact binary mergers. In this thesis, we focus on NS–NS mergers with the total mass of in the range from $2.6M_\odot$ to $2.9M_\odot$.

1.2 Gravitational-wave astronomy of binary neutron star merger

Ground-based gravitational-wave interferometers, such as LIGO§, Virgo¶, GEO600‖, and TAMA300** have tried to detect gravitational waves. These detectors have a good sensitivity in the frequency range of the gravitational waves from stellar mass compact binary mergers. Until 2013, however, any gravitational waves have not been detected yet. LIGO and Virgo observations between Jul. 7, 2009 and Oct. 20, 2010 give an upper limit of the compact binary merger rates (Abadie et al. 2012): 130 Mpc^{-3}Myr^{-1} for NS–NS mergers, 31 Mpc^{-3}Myr^{-1}. This value is still larger than the expected event rate as mentioned previous section.

†NS–NS binaries are thought to be formed through type Ibc supernovae.
§http://www.ligo.caltech.edu/
¶http://www.ego-gw.it/
‖http://www.geo600.org/
**http://tamago.mtk.nao.ac.jp/spacetime/index.html

Now the second generation ground-based interferometers, advanced LIGO, advanced Virgo, and KAGRA[††] are under construction and will start observation from 2016–2018. The sensitivity of these interferometers will be 10 times better than that of the previous ones. Because the amplitude of gravitational waves is proportional to the inverse of the distance to the source, the observable volume of these advanced detectors as well as the event rate will be 1000 times larger than that of the previous observations. The observable distance of gravitational waves from NS–NS mergers will reach beyond 200 Mpc and their expected event rate is 0.4–400 yr^{-1} (Abadie et al. 2010). Even for the ultra-conservative estimation gives a lower limit of the expected detection rate as 0.2 yr^{-1}. Therefore we expect that the first detection of gravitational waves will be achieved by these second generation detectors.

After the first detection of gravitational waves, gravitational-wave astronomy will open. For instance, gravitational waves from compact binary mergers will provide us valuable information, such as component masses, coalescence time, luminosity distance to the source, the finite size of neutron stars, compact binary merger rate, and so on. Using such information, we will be able to develop our understanding of gravity, astrophysics, cosmology, and nuclear physics. In order to achieve the gravitational-wave astronomy, we need to prepare template waveforms of the compact binary coalescence.

1.3 Electromagnetic-wave astronomy of binary neutron star merger

Electromagnetic counterparts to gravitational-wave signals must be very helpful for maximizing scientific outcomes (Kochanek and Piran 1993). Because most gravitational-wave events will be detected close to the detection threshold of the detectors, the detection of electromagnetic counterparts will support the discovery of gravitational waves. Moreover, electromagnetic counterparts will provide us the abundant information of gravitational-wave sources. In particular, the second generation gravitational-wave detectors will not be able to determine the positions gravitational-wave sources within their host galaxies. Therefore the detection of the electromagnetic counterparts to gravitational waves will be needed to identify them. Such an identification of the host galaxy in which an NS–NS merger happen allows us to estimate the distance to the source and to develop astronomy.

The coalescence of a compact binary with at least one neutron star is likely to emit bright electromagnetic signals. In particular, short gamma-ray bursts (GRBs) are speculated to be originated from compact binary coalescence (Paczynski 1986; Goodman 1986; Eichler et al. 1989). However, the detection probability of a short GRB associated with gravitational waves may be small, because a short GRB may be produced by a collimated relativistic jet, which emits photons only in the direction of the jet propagation due to the

[††]http://gwcenter.icrr.u-tokyo.ac.jp/en/

relativistic beaming effect (Fong et al. 2013) Many efforts have been made to theoretically investigate possible electromagnetic counterparts of gravitational-wave sources which can be observable from any direction (see e.g. Metzger and Berger 2012). Many of these theoretical studies is motivated by possible existence of mass ejection at an NS–NS merger, which is a similar situation to supernova explosion. Therefore understanding of mass ejection from a compact binary merger is playing a key role to estimate electromagnetic counterparts to gravitational-wave signals.

The first studies of this field have been done by Ruffert et al. (1997); Rosswog et al. (1999, 2000) in Newtonian hydrodynamics. They found that the some material in the tidal tail of a less massive neutron star is ejected, and thus, the ejecta concentrates on the equatorial plane of the binary orbit. Subsequently, Oechslin et al. (2007) have taken into account strong gravity due to the general relativistic effect by employing the conformal flat approximation. They have shown that the some material at the interface of the coalescing neutron stars is also ejected by the strong shock heating at the merger. Therefore it is important to compute mass ejection based on full general relativistic computation.

1.4 Numerical-relativity simulation of binary neutron star merger

Numerical relativity is a powerful tool to compute the dynamical and non-linear evolution of a spacetime, such as a compact binary merger and gravitational collapse of a star. Because these systems can be gravitational-wave sources, numerical relativity has been rapidly developed by many authors from the first work.

The first numerical relativity simulation of an NS–NS merger has been performed by (Shibata and Uryū 2000) with the formalism (Shibata 1999). After that, several groups develop binary neutron star merger simulations. One direction of the aim of these simulations is in the computation of gravitational waveforms which are precise enough to be used as template waveforms like binary black hole cases. Provided such template waveforms, to detect the gravitational waveforms from NS–NS mergers will provide us a unique laboratory of the extreme-dense matter. Although several groups have succeeded to perform long-term orbital evolution of NS–NS mergers (about 10 orbits; Baiotti et al. 2011; Thierfelder et al. 2011; Hotokezaka et al. 2013c), the accuracy of these simulations is not high enough to construct template waveforms. In order to obtain a waveform with a high accuracy, it is important to study the convergence of numerical relativity simulations with matter fields and to develop formalisms of which the convergence is better than that of the previous simulations (see e.g. Radice and Rezzolla 2012; Hilditch et al. 2013).

Another direction of the numerical relativity simulations of NS–NS mergers is in to study the mechanism of supernova explosions and central engine of GRBs by including electromagnetic and weak interactions (Sekiguchi et al. 2011a,b; Deaton et al. 2013; Rezzolla et al. 2011; Giacomazzo and Perna 2013). These studies are helpful to understand high-energy astrophysics.

1.5 Neutron-star equation of state

The equation of state (EOS) of neutron-star matter is one of the most important ingredients to understand phenomena related to neutron stars. However, it is difficult to explore the EOS of neutron-star matter because any experiment on the Earth has not reached the central density of neutron stars $\sim 10^{15}$ g/cm^3. Therefore the understanding of the phenomena related neutron stars can be developed only within the uncertainties from the EOS of neutron-star matter. Recently, the two solar-mass neutron stars with white dwarf companions, PSR J1614-2230 with mass $1.97 \pm 0.04 M_\odot$ (Demorest et al. 2010) and PSR J0348+0432 with $2.01 \pm 0.04 M_\odot$ (Antoniadis et al. 2013), were discovered. The existence of these heavy neutron stars constrain the EOS of neutron-star matter (Lattimer and Prakash 2010).

In this thesis, we employ several neutron star models, which can support more than two solar mass, in order to systematically study NS–NS mergers. Furthermore, we explore possible ways to constrain the EOS of neutron-star matter by using observations of signals from NS–NS mergers.

1.6 Organization of this thesis

In Chap. 2, we briefly review the motion of a compact binary inspiral with tidal effects. The resulting gravitational waveforms will be compared with numerical waveforms in Chap. 5. In Chap. 3, we summarize current understanding expected electromagnetic counterparts of compact binary mergers. In Chap. 4, the formulations adopted in numerical relativity code `SACRA` are summarized. Here we also mention the set up of numerical simulations in this thesis. In Chap. 5, we analyze numerical waveforms in the late stage of NS–NS inspirals. Here, comparing numerical waveforms and analytical waveforms, we discuss tidal effects in this stage. In Chap. 6, in particular, we focus on the formation and evolution of a remnant massive neutron star of an NS–NS merger and gravitational waveforms emitted by them. In Chap. 7, dynamical mass ejection from NS–NS mergers are discussed. Based on these ejecta, in Chap. 8, we discuss possible progenitor models of kilonova candidate which was discovered as a near infrared counterpart of the short GRB 130603B. In Chap. 9, we summarize the main results of this thesis and discuss future directions of this research field.

Chapter 2

Orbital motion of binary neutron stars

The general relativistic problem of motion of two-body systems has been studied from the early days after the establishment of general relativity. This kind of calculation allows us to test general relativity with the binary pulsar systems. In addition, we can predict gravitational waveforms of compact binary coalescence, which will play a crucial role to detect gravitational waves. In this chapter, we briefly summarize the orbital motion of a compact binary, tidal effects of an NS–NS inspiral, and measurability of finite size of a neutron star by gravitational-wave observations.

2.1 Orbital motion of point-mass systems

2.1.1 Quadrupole formula

Gravitational waves are generated by two stars orbiting around each other. The gravitational-wave radiation can be calculated by the quadrupole formula in the leading order as

$$h_{ij}^{\mathrm{TT}}(t,r) = \frac{2G}{c^4 D}\ddot{I}^{\mathrm{TF}}, \tag{2.1}$$

where I^{TF} is the trace free part of the quadrupole moment and D is the distance to the source. The power of the gravitational-wave radiation is written as

$$L_{\mathrm{GW}} = \frac{G}{5c^5}\langle \dddot{I}_{ij}^{\mathrm{TF}} \dddot{I}_{ij}^{\mathrm{TF}} \rangle, \tag{2.2}$$

where $\langle \quad \rangle$ means an average over several wavelengths. Supposing that a binary with a circular orbit losses its energy through gravitational-wave radiation. For such a system, the orbital energy and the rate of energy loss are given by

$$E = -\frac{GM_A M_B}{2a}, \quad L_{\mathrm{GW}} = \frac{32G^4}{5c^5}\frac{M_A M_B M}{a^5}, \tag{2.3}$$

where M_A and M_B are the component gravitational mass of star A and B at inifinite separation, $M = M_A + M_B$, and a is the semi-major axis of the binary orbit. Due to a radiation reaction, the semi-major axis decreases with time. The evolution equation describing the semi-major axis is obtained from Eqs. (2.3) as

$$\frac{da}{dt} = -\frac{64}{5}\frac{G^3 M_A M_B M}{c^5 a^3}. \tag{2.4}$$

The coalescence time of the binary with an initial semi-axis a_0 can be written as

$$\begin{aligned} t_c(a_0) &= \frac{5}{256}\frac{c^2 a_0}{GM_A}\frac{c^2 a_0}{GM_B}\frac{c^2 a_0}{GM}\frac{a_0}{c}, \\ &\simeq 0.15 \text{ Gyr} \left(\frac{a_0}{1R_\odot}\right)^4 \left(\frac{M_A}{1M_\odot}\right)^{-1} \left(\frac{M_B}{1M_\odot}\right)^{-1} \left(\frac{M}{1M_\odot}\right)^{-1}. \end{aligned} \tag{2.5}$$

It is worthy to note that there are NS–NS systems of which the expected coalescence time is shorter than 0.15 Gyr (see Table 1.1). This fact implies that these binaries have semi-major axis of order $\sim 1R_\odot$. However, the progenitor star of a neutron star should have experienced red-giant phase, in which the stellar radius becomes large at least $10^2 R_\odot$. Therefore there must exist some mechanism, which makes a wide binary to a close binary. For instance, a common envelope phase is suggested as a candidate of such a mechanism (Paczynski 1976). This problem is still an open question of binary stellar evolution (Ivanova et al. 2013).

2.1.2 Post-Newtonian formalism

A very useful method to solve the general relativistic two-body problems is the post-Newtonian approximation, in which Einstein equation is expanded in powers of the following small quantities

$$\epsilon_{\rm PN} \sim \frac{GM}{c^2 R} \sim \left(\frac{v}{c}\right)^2 \sim \frac{p}{\rho} \tag{2.6}$$

The 1PN-accurate equation of motion, in which terms of order $\epsilon_{\rm PN}$ are taken into account, is the so-called Einstein-Infeld-Hoffmann equation of motion. The leading contribution of a radiation-reaction is at 2.5PN order (see Eq.2.4). This force drives a binary inspiral. Until now, 3.5PN-accurate evolution of equation of the orbital frequency is obtained as

$$\frac{dx}{dt} = F(x, M_A, M_B), \tag{2.7}$$

where $x = (M\omega)^{2/3}$ with ω being the angular velocity of the binary and

$$F^{\rm T4} = \frac{64\nu}{5M} x^5 \left[1 - \left(\frac{743}{336} + \frac{11}{4}\nu\right) x + 4\pi x^{3/2} \right. \tag{2.8}$$
$$+ \left(\frac{34103}{18144} + \frac{13661}{2061}\nu + \frac{59}{18}\nu^2\right) x^2 - \left(\frac{4159}{672} + \frac{189}{8}\nu\right) \pi x^{5/2}$$
$$+ \left\{ \frac{16447322263}{139708800} - \frac{1712}{105}\gamma - \frac{56198689}{217728}\nu \right.$$
$$\left. + \frac{541}{896}\nu^2 - \frac{5605}{2592}\nu^3 + \frac{\pi^2}{48}(256 + 451\nu) - \frac{856}{105}\ln(16x\ ) \right\} x^3$$
$$\left. + \left(-\frac{4415}{4032} + \frac{358675}{6048}\nu + \frac{91495}{1512}\nu^2\right) \pi x^{7/2} \right],$$

where $\nu = M_A M_B / M^2$ is the symmetric mass ratio, and $\gamma = 0.577126...$ is an Euler's constant. The form of Eq. (2.8) is called as the Taylor T4 approximant. As shown by Boyle et al. (2007), the evolution of the angular velocity of the Taylor T4 approximant agrees well with those of the numerical relativity simulations for the inspiral of equal-mass non-spinning binary black holes up to $M\omega \sim 0.1$. In fact, the accumulated difference in gravitational-wave phase is less than 0.05 radian over 30 cycles.

2.1.3 Effective-one body formalism

The effective-one body (EOB) formalism maps the dynamics of two point masses to the Hamiltonian dynamics of an effective particle moving in an effective external potential (Buonanno and Damour 1999, 2000; Damour 2001). Because the EOB formalism goes beyond the adiabatic approximation for binary inspirals, it is suitable for describing the late inspiral stage of a binary, for which the adiabatic approximation is not very accurate. In this work, we employ the resummed EOB description which is largely the same as that in Pan et al. (2011) for the point-mass part.

The EOB effective metric is defined by

$$ds^2_{\rm eff} = -A(r)dt^2 + \frac{D(r)}{A(r)}dr^2 + r^2\left(d\theta^2 + \sin^2\theta d\phi^2\right), \tag{2.9}$$

where (t, r, ϕ) are the dimensionless coordinates and their canonical momenta are (p_r, p_ϕ). We replace the radial canonical momentum p_r with the canonical momentum p_{r_*}, where the tortise-like radial coordinate r_* is defined by

$$\frac{dr_*}{dr} = \frac{\sqrt{D(r)}}{A(r)}. \tag{2.10}$$

Then the binary dynamics can be described by the EOB Hamiltonian

$$\hat{H}_{\rm real}(r, p_{r_*}, p_\phi) = \frac{1}{\nu}\sqrt{1 + 2\nu\left(\hat{H}_{\rm eff} - 1\right)} - \frac{1}{\nu}, \tag{2.11}$$

where the effective Hamiltonian is defined by,

$$\hat{H}_{\rm eff} = \sqrt{p_{r_*}^2 + A(r)\left(1 + \frac{p_\phi^2}{r^2} + 2\,(4-3\nu)\,\nu\frac{p_{r_*}^4}{r^2}\right)}. \tag{2.12}$$

The $A(r)$ up to the 5PN order is given by

$$A(r) = P_5^1\left[1 - 2u + 2\nu u^3 + a_4\nu u^4 + a_5\nu u^5 + a_6\nu u^6\right], \tag{2.13}$$

where $a_4 = 94/3 - 41\pi^2/32$, $u = 1/r$, and P_5^1 denotes a $(1,5)$ Pade approximant. In the definition of $A(r)$, there are two analytically undetermined parameters (a_5, a_6), which correspond to the 4PN and 5PN corrections. Here, we adopt the values $(a_5, a_6) = ((-5.828 - 143.5\nu + 477\nu^2)\nu, 184\nu)$ following Pan et al. (2011).

For the calculation of the binary orbit, we solve the EOB Hamilton equations (Buonanno and Damour 1999, 2000; Damour 2001)

$$\begin{aligned}
\frac{dr}{dt} &= \frac{A(r)}{\sqrt{D_3^0(r)}}\frac{\partial \hat{H}_{\rm real}}{\partial p_{r_*}}, & (2.14)\\
\frac{d\phi}{dt} &= \frac{\partial \hat{H}_{\rm real}}{\partial p_\phi}, & (2.15)\\
\frac{dp_{r_*}}{dt} &= -\frac{A(r)}{\sqrt{D_3^0(r)}}\frac{\partial \hat{H}_{\rm real}}{\partial r} + \hat{\mathcal{F}}_\phi\frac{p_{r_*}}{p_\phi}, & (2.16)\\
\frac{dp_\phi}{dt} &= \hat{\mathcal{F}}_\phi, & (2.17)
\end{aligned}$$

where $D_3^0(r)$ is a $(0,3)$ Pade approximant of $D(r)$ (Pan et al. 2011), and $\hat{\mathcal{F}}_\phi$ is the radiation-reaction force given by

$$\hat{\mathcal{F}}_\phi = -\frac{1}{8\pi\nu\hat{\omega}}\sum_{l=2}^{8}\sum_{m=1}^{l}(m\hat{\omega})^2\,|\frac{R}{M}h_{lm}|^2. \tag{2.18}$$

where h_{lm} denotes the inspiral and plunge waveform for a binary black hole of mass M_A and M_B. Here, h_{lm} is given by Eqs. (13)–(22) of Pan et al. (2011).

2.2 Orbital motion of tidally interacting systems

The equation of motion of a binary with a point-mass approximation breaks down at 5PN order and higher due to tidal interactions. Therefore one has to extend a point-mass approximation scheme to a scheme which can describe bodies with mass and current multipole moments. In this section, we briefly introduce the motion of bodies with mass multipole moments and discuss the resulting gravitational waveforms.

2.2.1 Equation of motion for stars with multipole moments

The kinematics of stars in a multiple system can be described by the equations of fluid mechanics as

$$\partial_t \rho + \partial_i \rho v^i = 0, \tag{2.19}$$

$$\partial_t \rho v^i + \partial_j \left(\rho v^i v^j + t^{ij}\right) = -\rho \partial_i \phi, \tag{2.20}$$

$$\nabla^2 \phi = 4\pi\rho, \tag{2.21}$$

where t^{ij} is stress tensor. Now we consider an N-body system of which each star is labeled by $1 \leq A \leq N$. The gravitational potential at the point x^i produced by a star 'A' is at $z_A(t)$ given by

$$\phi_A^{\rm int}(t, x^i) = -\int_A d^3x' \frac{\rho(t, x'^i)}{|x^i - x'^i|}. \tag{2.22}$$

For $|z_A^i - x^i| \gg |z_A^i - x'^i|$,

$$\phi_A^{\rm int}(t, x^i) = -\sum_{l=0}^{\infty} \frac{(-1)^l}{l!} \left(\int_A d^3x' \rho(t, x')(x'^i - z_A^i(t))^L\right) \partial_L \frac{1}{|x^i - z_A^i|}, \tag{2.23}$$

where $V_L = V_{i1} V_{i2} \cdots V_{il}$. Mass multipole moment of the star A is defined as

$$M_A^L(t) = \int_A d^3x \rho(t, x^i) \left(x - z_A(t)\right)^{\langle L \rangle}, \tag{2.24}$$

where $\langle \cdots \rangle$ stands for symmetric trace free. For instance, the positon of the center of mass of the star A is

$$z_A^i(t) = \frac{1}{M_A} \int_A d^3x \rho(t, x) x^i. \tag{2.25}$$

The external potential around the star A is given by

$$\phi_A^{\rm ext}(t, x^i) = \sum_{B \neq A} \phi_B^{\rm int}. \tag{2.26}$$

For the vicinity of the star A $|z_A^i - x^i| \ll |z_B - x^i|$, The external potential can be expanded as

$$\phi^{\rm ext}(t, x^i) = \sum_{l=0}^{\infty} \frac{1}{l!} \partial_L \phi_A^{\rm ext}|_{x=z_A} \left(x - z_A(t)\right)^L. \tag{2.27}$$

We define tidal moments around the star A as

$$G_A^L(t) = -\partial_L \phi_A^{\rm ext}(t, x)|_{x=z_A}. \tag{2.28}$$

The equation of motion for the star A under the gravitational potential $\phi_A^{\rm ext}$ is given by

$$\begin{aligned} M_A \ddot{z}_A^i(t) &= \int_A d^3x \ddot{\rho}(t, x^i) x^i \\ &= -\int_A d^3x \rho(t, x^i) \partial_i \phi_A^{\rm ext} \\ &= -\int_A d^3x \sum_{l=0}^{\infty} \frac{1}{l!} G_A^L(t) \left(x - z_A\right)^{L-i} \rho(t, x^i) \\ &= \sum_{l=0}^{\infty} \frac{1}{l!} M_A(t)^L G_A^{Li}(t) \end{aligned}$$

where Eq. (2.19), Eq. (2.20), Eq. (2.24), and Eq. (2.28) are used. To solve the equation of motion Eq. (2.29) for a given initial condition, one has to know the mass multipole moments $M_A^L(t)$ at each time. As long as one considers stars which are slightly deformed from a spherical shape, the contribution of higher-order multipoles is expected to be small. For such a case, the closure is given by the linear response of the star to a tidal potential as

$$M_A^{ij} = \lambda_A G_A^{ij}, \tag{2.29}$$

where λ is the tidal defomability parameter of the star A. For a two-body system with the mass M and orbital separation r, Eq. (2.29) roughly evaluated as

$$M\ddot{z} \sim -\frac{M}{r^2}\left(M + \frac{\lambda}{r^5} + \mathcal{O}(r^{-6})\right). \tag{2.30}$$

The second term of Eq. (2.30) is attractive force due to the coupling between the tidal deformation of a star and the tidal field induced by its companion star. In terms of the post-Newtonian theory, the leading term of tidal effects appears in the equation of motion as the post 5 Newtonian order.

2.2.2 Post-Newtonian formalism for the motion of tidally interacting compact stars

The motion of tidally interacting NS–NS binaries in close orbits is affected by the stellar internal structure. As long as the degree of the tidal interaction is small, the correction of this effect can be described only through the tidal deformability λ (Vines et al. 2011). The evolution of the orbital angular velocity in the inspiral of a tidally interacting binary is described by

$$\frac{dx}{dt} = F(x, M_A, M_B, \lambda_A, \lambda_B). \tag{2.31}$$

The function F can be decomposed into the following two parts,

$$F = F_{\rm pm}(x, M_A, M_B) + F_{\rm tidal}(x, M_A, M_B, \lambda_A, \lambda_B), \tag{2.32}$$

where $F_{\rm pm}$ is the contribution of the point-mass part described by Eq. (2.8), and $F_{\rm tidal}$ is the contribution associated with the tidal interactions. We adopt the tidal part which is derived by Vines and his collaborators (Vines et al. 2011) as follows,

$$F_{\rm tidal} = \frac{32 M_A \lambda_B}{5 M^7} \left[12 \left(1 + 11 \frac{M_A}{M} \right) x^{10} \right. \tag{2.33}$$
$$+ \left(\frac{4421}{28} - \frac{12263}{28} \frac{M_B}{M} + \frac{1893}{2} \left(\frac{M_B}{M} \right)^2 \right.$$
$$\left. \left. -661 \left(\frac{M_B}{M} \right)^3 \right) x^{11} \right] + (A \leftrightarrow B).$$

In particular, for the case of equal-mass binaries, $F_{\rm tidal}$ is given by

$$F_{\rm tidal} = \frac{52}{5M} x^{10} k_2 C^{-5} \left(1 + \frac{5203}{4368} x \right), \tag{2.34}$$

where $C = M_{\rm A}/R_{\rm A}$ $(= M_{\rm B}/R_{\rm B})$ is the compactness of the neutron star. It can be shown that $\lambda_A \propto R_A^5$, where R_A. Although the tidal interaction affects NS-NS inspirals only at 5PN order, its coefficient is of order 10^4 for typical neutron stars of radius $10 - 15$ km, $k_2 \sim 0.1$, and $C \sim 0.14 - 0.20$, and thus, it plays an important role in the late inspiral stage.

2.2.3 Effective-one body formalism for the motion of tidally interacting compact stars

In order to describe the late inspiral stage of tidally interacting relativistic stars, EOB formalism may be better because it includes higher order PN contributions as mentioned Sec. 2.1.3.

For a tidally interacting binary, the metric component $A(r)$ is decomposed into two parts as

$$A(r) = A_{\rm pm}(r) + A_{\rm tidal}(r), \tag{2.35}$$

where $A_{\rm pm}(r)$ is the point-mass part and $A_{\rm tidal}(r)$ is associated with the tidal effects. The point-particle part up to the 5PN order is given by Eq. (2.13).

The tidal part of $A(r)$ is given by

$$A_{\rm tidal}(r) = \sum_{l \geq 2} -\kappa_l u^{2l+2} \hat{A}_l(u), \tag{2.36}$$

where $\hat{A}_l$ includes the PN tidal contributions for each multipole, and κ_l is its coefficient. This coefficient is related to the tidal Love number k_l and the compactness of two stars by

$$\kappa_l = 2 \frac{M_B M_A^{2l}}{M^{2l+1}} \frac{k_l^A}{C_A^{2l+1}} + (A \leftrightarrow B). \tag{2.37}$$

In this work, we include only the tidal-interaction part of the lowest multipole $l = 2$. Up to the next-to-leading order, $\hat{A}_{l=2}$ is given by Damour and Nagar (2010)

$$\hat{A}^{(\mathrm{A})}_{l=2}(u) = 1 + \alpha^{(\mathrm{A})}_1 u, \tag{2.38}$$

where $\alpha^{(\mathrm{A})}_1 = 5M_A/2M$. The tidal-interaction term up to the 2PN corrections is currently known, and the coefficient α_2 is larger than α_1 (Bini et al. 2012). In addition, an analysis in the test-mass limit ($M_\mathrm{A} \ll M_\mathrm{B}$) suggests that the tidal part $\hat{A}^{(\mathrm{A})}_{l=2}$ has the pole-like behavior near the last unstable orbit located at $3M_\mathrm{B}$ (the light ring orbit). Thus, it is reasonable to expect that the higher-PN corrections would amplify the tidal effects. In this work, we employ the resummed version of the tidal metric including up to the next-to-next-to-leading order given by Bini et al. (2012)

$$\hat{A}^{(\mathrm{A})}_{l=2}(u) = 1 + \alpha^{(\mathrm{A})}_1 u + \alpha^{(\mathrm{A})}_2 \frac{u^2}{1 - \hat{r}_\mathrm{LR} u}, \tag{2.39}$$

where

$$\alpha^{(\mathrm{A})}_2 = 337M_A^2/28M^2 + M_A/8M + 3, \tag{2.40}$$

and

$$\hat{r}_\mathrm{LR}(\nu, \kappa_2) = 3\left[1 - \frac{5\nu}{3^3} + \frac{4}{3^6}\kappa_2 + O(\nu^2, \kappa_2\nu, \kappa_2^2\ )\right], \tag{2.41}$$

is the dimensionless radius of the light ring orbit.

$$\hat{\mathcal{F}}_\phi = -\frac{1}{8\pi\nu\hat{\omega}} \sum_{l=2}^{8} \sum_{m=1}^{l} (m\hat{\omega})^2 \left|\frac{R}{M} h_{lm}\right|^2. \tag{2.42}$$

Here, $\hat{\omega} = d\phi/dt$, h_{lm} denote the multipolar waveforms, and R is the radius of extracting gravitational waves. The waveforms are described by

$$h_{lm} = h^0_{lm} + h^{\mathrm{tidal,A}}_{lm} + h^{\mathrm{tidal,B}}_{lm}, \tag{2.43}$$

where h^0_{lm} denotes the inspiral and plunge waveform for a binary black hole of mass M_A and M_B, and $h^{\mathrm{tidal,A}}_{lm}$ is the contribution due to the tidal deformation of star A. In this work, h^0_{lm} is given by Eqs. (13)–(22) of Pan et al. (2011) and $h^{\mathrm{tidal,A}}_{lm}$ is basically given by Eqs. (A14)–(A17) of Damour et al. (2012). Because the 2PN term associated with the tidal effect in the waveform is currently unknown, we include the contributions of the tidal effect to $h^{\mathrm{tidal,A}}_{lm}$ up to the 1PN term even for the case that the next-to-next-to-leading order term is taken into account in the radial potential.

2.2.4 Linear response of a compact star to tidal fields

In a close binary system for which the separation between two stars is a few times larger than the stellar radius, each star is deformed from its hypothetical equilibrium shape in isolation due to the tidal fields. Assuming that neutron stars are spherically symmetric in the zeroth order, such deformation can be described as the linear responses of neutron stars to external tidal fields Hinderer (2008); Damour and Nagar (2009); Binnington and Poisson (2009), as long as the degree of the tidal deformation is small. In this linear theory, one assumes that the mass quadrupole moment of a star, Q_{ij}, is proportional to the external quadrupolar tidal fields $\mathcal{E}_{ij}$ as,

$$Q_{ij} = -\lambda \mathcal{E}_{ij}, \tag{2.44}$$

where λ is the quadrupolar tidal deformability of the star. This relation is called the *adiabatic* approximation for the tidal deformation of a star, which is valid only when the time scale in the change of the weak tidal field is much longer than the dynamical time scale of the star. The tidal deformability is related to the quadrupolar tidal Love number k_2 by

$$\lambda = \frac{2}{3} R^5 k_2, \tag{2.45}$$

where R is the radius of the (spherical) star in isolation. For a given EOS and a central density, one can calculate the quantities mass, R, k_2, and λ of neutron stars by solving the Tolman-Oppenheimer-Volkoff equations and the metric perturbation equations Hinderer (2008); Damour and Nagar (2009).

2.2.5 Measurability of tidal deformability parameters and beyond

The measurability of tidal deformability parameters through gravitational-wave observation was first discussed by Flanagan and Hinderer (2008). They noted that the tidal deformability parameter can be constrained by the second generation gravitational-wave detectors for NS–NS merger events occurring within 50 Mpc by using a 3.5PN waveform with the leading terms of tidal corrections ($l = 2$), where the tidal deformability parameter is computed with the adiabatic approximation. Specifically, the tidal deformability can be constrained for a neutron star with $1.4 M_\odot$ and $R \geq 13.6$ km (≥ 15.3 km) for a n=0.5 (=1.0) polytrope EOS. They also pointed out that this simple waveform will break down due to the several types of higher-order corrections in the high frequency ($f_{\rm GW} \gtrsim 400$ Hz): (i) higher multipole corrections of the tidal deformation, (ii) corrections due to the breakdown of the adiabatic approximation, (iii) non-linear hydrodynamical corrections to the tidal effects, and (iv) post Newtonian corrections to the tidal effects. Recently, Favata (2013); Yagi and Yunes (2013) showed that the 4PN and higher order corrections to the point mass part of the waveform can prevent us to measure tidal deformability parameters.

Damour et al. (2012) evaluated the measurability of the tidal deformability parameter using the EOB waveforms, assuming the waveforms are valid up to the contact frequency of NS–NSs. They concluded that the second generation gravitational-wave detectors can constrain the tidal deformability parameters for the event with a signal-to-noise ratio 16. This result may hold even for the EOS of which the radius of a neutron star with $1.4M_\odot$ is about 11 km. However, the approximations adopted in their work may be break down due to the reasons as mentioned above. Therefore calculation of higher-order corrections and comparison between numerical-relativity simulations and analytical-relativity calculations are needed to prepare the high-accuracy waveforms.

Once the neutron-star EOS is known, one also can measure the relationship between the luminosity distance and the redshift of the binary using only the information of the gravitational waveform through the tidal deformation of the inspiralling neutron stars (Messenger and Read 2012) with more refined detectors such as Einstein telescope (Punturo et al. 2010). Therefore, modeling the gravitational waveform in NS-NS inspirals including tidal effects is important not only from astrophysical point of view but also from the viewpoint of nuclear physics and cosmology.

Chapter 3

Electromagnetic signals from binary neutron stars

NS–NS mergers and black hole-neutron star binary (BH–NS) mergers are among the most promising astrophysical gravitational-wave sources for the second generation ground-based laser interferometers. The discovery of the electromagnetic counterparts to gravitational-wave signals will provide us additional information of the sources (Kochanek and Piran 1993; Metzger and Berger 2012). In particular, the electromagnetic counterparts will allow us to locate the position of the gravitational-wave sources within their host galaxies, which is difficult to determine precisely with these interferometers.

For the discovery of the electromagnetic counterparts, it is important to address the question: *What is the promising electromagnetic counterpart of a compact binary merger?* A good electromagnetic counterpart should satisfy the following conditions. First, it should be bright enough to be detected by the present or upcoming telescopes. Second, it should be observable from any direction. Third, it should be distinguishable from other electromagnetic transients. The expected electromagnetic counterparts of NS–NS mergers are listed in Table 3.1 and the expected light curves of these electromagnetic emissions are plotted in Fig. 3.1. We divide the predicted emission models into the following subgroups. First, we classify the emission models by the origin of the emission: (i) a relativistic jet and (ii) sub-relativistic ejecta. Basically, the emission models associated with GRBs are originated from relativistic jets. Note that the emission from such a relativistic jet can be detected only from an observer who observes the jet within the viewing angle $1/\Gamma$. Second, the emission models are classified by the dependence on the density of circumstellar medium n. This is also an important property, because some compact binary merger will occur at outskirts of a galaxy or even at intergalactic region due to a large pulsar kick at their birth.

In this chapter, we will discuss short GRBs, kilonovae/macronovae, and merger remnants in more details.

transiet	brightness[erg/cm^2/s]	wavelength	origin	depends on n?	Refs
Short GRBs	10^{51}	X − γ	Jet	No	[1]
Orphan Afterglow	10^{45}	radio − X	Jet	Yes	[2]
Extended Emission	10^{45}	X	?	No	[3]
Kilonova	10^{41}	IR − optical	Ejecta	No	[4]
Merger remnant	10^{41}	radio–γ	Ejecta	Yes	[5]
Merger-shock breakout	10^{41}	radio − X	Ejecta	Yes	[6]
Magnetar-wind nebula	10^{41}	radio–X	Ejecta	Yes	[7]

Table 3.1: Expected electromagnetic counterparts of NS–NS mergers. References are as follows: [1] Nakar (2007), [2] Metzger and Berger (2012), [3] Nakamura et al. (2013), [4] Li and Paczyński (1998); Metzger et al. (2010); Piran et al. (2013); Barnes and Kasen (2013); Tanaka and Hotokezaka (2013); Grossman et al. (2013), [5] Nakar and Piran (2011); Piran et al. (2013); Takami et al. (2013), [6] Kyutoku et al. (2012), [7] Zhang (2013); Gao et al. (2013)

3.1 Short gamma-ray bursts

Gamma-ray bursts (GRB) are very intense flashes of gamma-rays. Traditionally, GRBs are classified into two groups according to their burst durations T_{90} (Kouveliotou et al. 1993). GRBs with $T_{90} \geq 2$ s and with $T_{90} \leq 2$ s are long GRBs and short GRBs, respectively. The discovery of the long GRB associated with the hypernova 1998bw (Galama et al. 1998; Iwamoto et al. 1998) indicates that collapse of a massive star could produce a long GRB.

The first discovery of afterglow of short GRBs was achieved by *Swift* satellite in 2005 (Gehrels et al. 2005). Shortly after that, HETE-2 discovered a short GRB and *Chandra X-ray Observatory* detected the X-ray afterglow (Villasenor et al. 2005; Fox et al. 2005). Until 2013, afterglows are found for nearly 50 short GRBs and 20 short GRB in optical (Berger 2013). Although the discovery of afterglows reveals short GRBs are cosmological events, the progenitors of short GRBs have not been known yet. NS–NS and BH–NS star mergers are thought to be one of the most probable candidates of progenitors of short GRBs (Paczynski 1986; Goodman 1986; Eichler et al. 1989). If one has succeeded to observe gravitational waves from compact binary mergers and a shot GRB simultaneously, it would be a smoking gun of the compact binary merger hypothesis of short GRBs and a very attractive electromagnetic counterpart to the GW source. There are clues which indicate the compact binary merger hypothesis as the followings.

Prompt emission: Duration and Energetics
The distribution of duration of observed GRBs seems to have a bimodal distribution (Kouveliotou et al. 1993), which may reflect the fact that there exist two different type of progenitors of GRBs. Although the duration which separates bimodal distribution depends

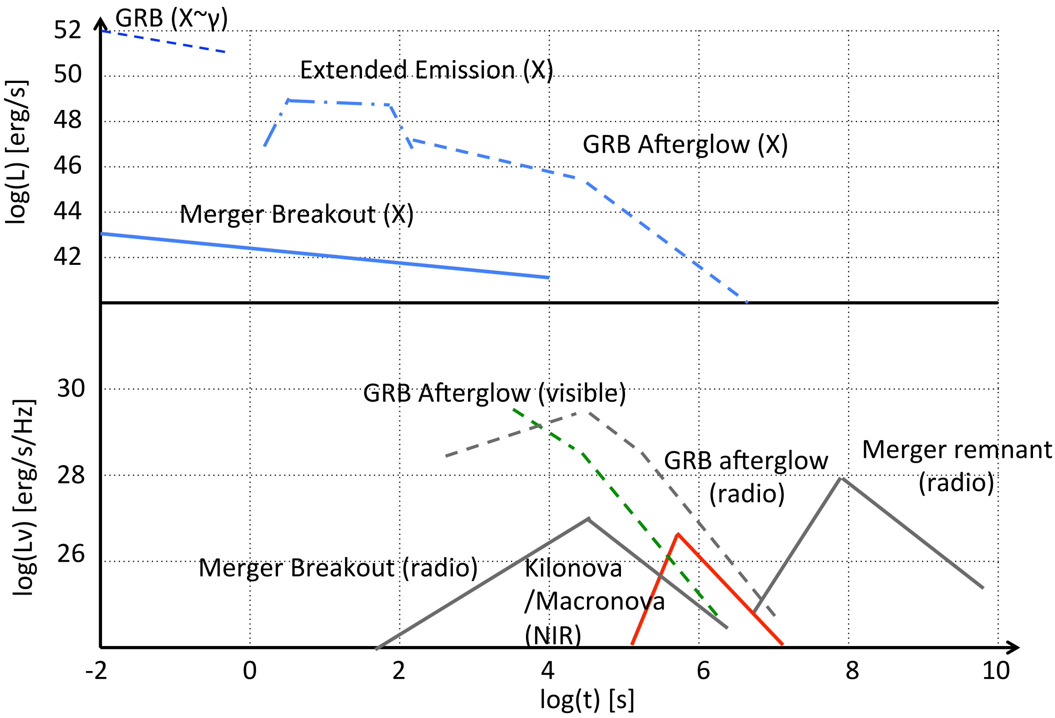

Figure 3.1: Expected light curves of electromagnetic counterparts of NS–NS mergers. The light curves in the X and γ-ray bands are plotted as νL_ν erg/cm^2/s. The light curves in the other bands are plotted as L_ν erg/cm^2/s/Hz. The emissions which likely to have a strong dependence on the viewing angle are denoted by a dashed line. The emissions which are expected to be observable from any direction are denoted by lines. The dash-dotted line denotes the emission which some model predicts the 4π emission.

on the detectors *BATSE*, *Swift*, and *Fermi* the bimodal distribution is indeed exist as shown by Bromberg et al. (2013).

Tsutsui et al. (2013) showed the E_p-L_p and E_p-E_{iso} correlations exist for short GRBs as well as long GRBs, where E_p is the rest frame spectral peak energy, L_p is the peak isotropic luminosity, and E_{iso} is the isotropic energy. Furthermore, the correlations are different from those of long GRBs. The correlations of short GRBs are 5–100 times dimmer than those of long GRBs. This result indicates that the difference of the progenitor between long and short GRBs.

Host galaxies

Until now, host galaxies are identified for nearly 40 short GRBs (see, for a review, Berger 2013). A half of the identified galaxies is classified into a late-type galaxy. About 20% of the host galaxies of short GRBs is an early-type galaxy, in which star formation is inactive. Furthermore, the detailed analysis of host galaxies of short GRBs showed that short GRBs in their hosts have relatively large off set (see, e.g., Fong and Berger 2013). These facts imply that the progenitors of short GRBs are old stellar systems and migrate from their birth site. These support for the compact binary merger scenario of short GRBs.

Event rate and opening angle

The opening angle of a relativistic jet can be estimated from the achromatic break in afterglow light curves. Fong et al. (2013) found that the average half opening angle of the short GRB jet θ_j is about 6° for the four samples of the GRBs with measured half opening angles and $\approx 10°$ for 13 samples including short GRBs with upper limits of the half opening angles. Using this value, the beaming factor $f_b = 1 - \cos\theta_j$ is ≈ 0.015. It is worthy to note that the beaming corrected event rate of short GRBs is 0.7 $\mathrm{Mpc}^{-3}\mathrm{Myr}^{-1}$. This rate is consistent with the expected NS–NS merger rate from pulsar observations.

A 'kilonova/macronova' associated with the short GRB 130603B

A kilonova/macronova candidate was discovered after the short GRB 130603B (Tanvir et al. 2013; Berger et al. 2013; de Ugarte Postigo et al. 2013). Such observation can be direct evidence of the compact binary merger scenario of short GRBs. We will focus on this topic in the next section and Chap. 8.

3.2 Kilonova/Macronova

A fraction of material of an NS–NS system is expected to be ejected at a merger. In turn, radioactive nuclei may be produced in the rapidly expanding ejecta. These nuclei radioactively decay and heat up NS–NS merger ejecta. Li and Paczyński (1998) proposed radioactively powered emission as one of the observable electromagnetic signatures at 1 to 10 days after an NS–NS merger. Such a radioactively powered transient is a so-called 'kilonova'* , because the luminosity of radioactively powered emission is expected to be 1000 times brighter than a nova and 1/10 to 1/100 as bright as supernova. If one could succeed in detecting the emission of kilonova after a short GRB, it can be strong evidence of the compact binary merger scenario of short GRBs.

3.2.1 Light curve of kilonova

In this subsection, we briefly summarize the basic concept of kilonova (Li and Paczyński 1998). We consider the expanding material ejected at an NS–NS or BH–NS merger. We want to evaluate the thermal emission from the expanding ejecta of the merger.

*The name of this type of electromagnetic transient has not been fixed. For instance, there is a lot names such as kilonova, macronova, r-process nova, and so on. In this thesis, we use "kilonova" hereafter.

For this purpose, the thermal history of the expanding ejecta has to be computed. Here, we assume the spherically expanding matter, its mass $M_{\rm ej}$, the velocity $v_{\rm ej}$, the surface radius $R_{\rm ej}$, and the uniform density ρ for simplicity. Therefore the density is given by

$$\rho = \frac{3M_{\rm ej}}{4\pi v_{\rm ej}^3} t^{-3}, \tag{3.1}$$

where we use $R_{\rm ej} = v_{\rm ej} t$, t is the time from the merger. The thermal history of an expanding ejecta can be described by the first law of thermodynamics

$$\frac{1}{\rho} dU = T ds - \frac{4}{3} U d\frac{1}{\rho}, \tag{3.2}$$

where U is the internal energy density and s is the specific entropy. Here we adopt the EOS $U = aT^4$ because the density of the ejecta becomes very low while the heating due to the decay of radioactive nuclei keep them hot. The second term in the right hand side of Eq. (3.2) corresponds to the adiabatic cooling. Total heat balance of the system is given by

$$M_{\rm ej} T ds = M_{\rm ej} \epsilon(t) - L, \tag{3.3}$$

where $\epsilon(t)$ is the nuclear heating rate per unit mass and L is the luminosity of the radiative cooling from the ejecta surface. Taking into account the heat balance, the evolution equation for the internal energy density becomes

$$t^3 \frac{dU}{dt} + 4t^2 U = \frac{3M_{\rm ej}}{4\pi v_{\rm ej}^3} \epsilon(t) - \frac{\pi v_{\rm ej} c}{\kappa M_{\rm ej}} t^4 U, \tag{3.4}$$

where we assume

$$L = 4\pi R_{\rm ej}^2 F \simeq 4\pi R_{\rm ej}^2 \frac{\sigma_{\rm SB} T^4}{\kappa \rho R_{\rm ej}}. \tag{3.5}$$

Here κ is the opacity and $\sigma_{\rm SB}$ is the Stefan-Boltzmann constant. In Eq. (3.5), we use the diffusion approximation for the radiative transfer in the ejecta. Therefore Eq. (3.4) is valid only for the case of $\kappa \rho R_{\rm ej} \gg 1$.

For the NS–NS and BH–NS merger, the ejected material is composed by various nuclear species. Based on the Fermi theory, such a statistical ensemble of β-decays results in the decay rate proportional to $t^{-1.2} - t^{-1.4}$ as we will discuss this property in the next subsection. Here, we adopt the rate of β-decay as

$$\epsilon(t) = \frac{fc^2}{t}, \tag{3.6}$$

for simplicity. Here f is the conversion efficiency of the mass energy to the thermal energy of decays. Using this heating rate, Eq. (3.4) can be rewritten in the dimension less form as

$$\frac{d\tilde{U}}{d\tau} + \left(\frac{4}{\tau} + \frac{3\tau}{4\beta} \right) \tilde{U} = \frac{1}{\tau^4}, \tag{3.7}$$

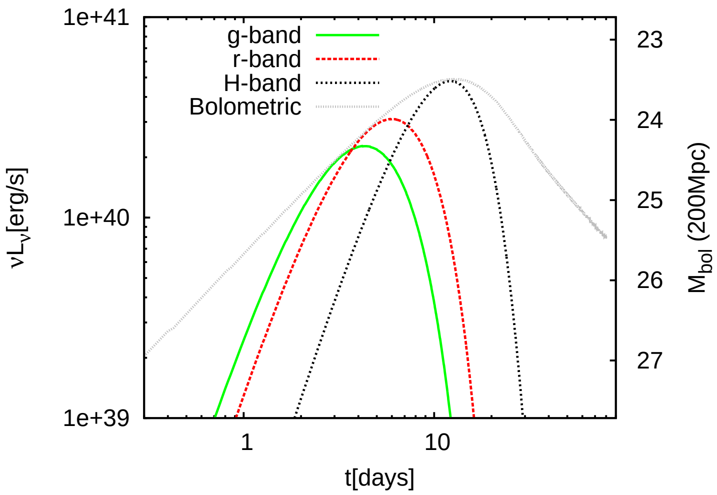

Figure 3.2: Light curve of kilonova of Li-Paczynsky model, of which the parameters of this model are $M_{\rm ej} = 0.01 M_\odot$, $v_{\rm ej} = 0.3c$, $f = 10^{-6}$,$\kappa = 10$ cm^2/g, respectively. The g, r, and H-band light curves are derived in the assumption of a black body spectrum.

where $\tau = t/t_c$, $\beta = v_{\rm ej}/c$, and $\tilde{U} = U/aT_1^4$, respectivley.

$$T_1 = \left(\frac{4\pi f^2 c^4}{3a^2\kappa^3 M_{\rm ej}}\right)^{1/8}, t_c = \left(\frac{3\kappa M_{\rm ej}}{4\pi v_{\rm ej}^2}\right)^{1/2}. \tag{3.8}$$

Here t_c is the time at which the ejecta satisfy the condition $\kappa\rho R_{\rm ej} = 1$, and thus, our approximation adopted here breaks down for $\tau > 1$.

The general solution of the homogeneous version of Eq. (3.7), which corresponds to the solution in the absence of the nuclear heating, is given by

$$\tilde{U}(\tau) = C_1 \frac{e^{-3\tau^2/8\beta}}{\tau^4}, \tag{3.9}$$

where C_1 is an integral constant. Note that the $1/\tau^4$ and $e^{-3\tau^2/8\beta}$ are the effects of the adiabatic cooling and the radiative cooling, respectively.

The peculiar solution of Eq. (3.7) is obtained as

$$\tilde{U}(\tau) = C_1 \frac{e^{-3\tau^2/8\beta}}{\tau^4} + \sqrt{\frac{8\beta}{3}} \frac{1}{\tau^4} Y\left(\sqrt{\frac{3}{8\beta}}\tau\right). \tag{3.10}$$

Here $Y(x)$ is the Dawson's integral defined by

$$Y(x) = e^{-x^2} \int_0^x e^{s^2} ds, \tag{3.11}$$

which behaves as $Y = x$ for $|x| \ll 1$ and has the maximum value 0.5410 at $x = 0.9241$. Even if the initial temperature is large as 10^{10}K, the second term in Eq. (3.10) dominates over the first term after $\tau \sim 10^{-4}$. This implies that the adiabatic cooling is so efficient that the ejecta forgets the initial condition. Neglecting the first term in Eq. (3.10), we obtain the luminosity of a kilonova as

$$L \simeq fc^3 \left(\frac{3\pi M_{\rm ej}}{4\kappa}\right)^{1/2} \sqrt{\frac{8\beta}{3}} Y \left(\sqrt{\frac{3}{8\beta}}\tau\right). \tag{3.12}$$

The luminosity has the maximum value

$$L_{\rm max} \simeq 3 \times 10^{40}\ {\rm erg/s} \left(\frac{\rm f}{10^{-6}}\right) \left(\frac{\kappa}{10\ {\rm cm/g}}\right)^{-1/2} \left(\frac{\rm M_{ej}}{0.01 \rm M_\odot}\right)^{1/2} \left(\frac{\rm v_{ej}}{\rm c/3}\right)^{1/2}, \tag{3.13}$$

at the time

$$t_{\rm max} \simeq 10\ {\rm days} \left(\frac{\kappa}{10\ {\rm cm/g}}\right)^{1/2} \cdot \left(\frac{M_{\rm ej}}{0.01 M_\odot}\right)^{1/2} \left(\frac{v_{\rm ej}}{c/3}\right)^{-1/2}. \tag{3.14}$$

The effective temperature at the peak can be evaluated as

$$T_{\rm eff} \simeq 1000\ {\rm K} \left(\frac{f}{10^{-6}}\right)^{1/4} \left(\frac{\kappa}{10\ {\rm cm/g}}\right)^{-1/8} \left(\frac{M_{\rm ej}}{0.01 M_\odot}\right)^{-1/8} \left(\frac{v_{\rm ej}}{c/3}\right)^{-1/8}. \tag{3.15}$$

This value of the effective temperature at the peak luminosity implies that the kilonova emission is bright in near-infrared. Figure 3.2 shows that the expected kilonova light curve in AB magnitude † derived from Eq. (3.12). In this figure, we plot the bolometric luminosity L and g, r, and H-band luminosity νL_ν, where we assume the Planck spectra. Note that the color evolution can be seen due to the adiabatic cooling. The expected kilonova spectrum becomes redder with time. This is a characteristic feature of kilonova emission, which may help us to distinguish kilonova emission from other astronomical phenomena.

Note that the above description of the compact binary merger ejecta is so simple. Microphysics such as the heating rate of the radioactive decays and the opacities play crucial role to understand kilonova emissions.

Furthermore the ejecta structure may affect kilonova emissions. In order to obtain more realistic ejecta structure, ejecta mass, and velocity profile, we need to perform numerical-relativity simulations of NS–NS and BH–NS mergers. In the next subsection, we briefly discuss the heating rate and opacity. In Chap. 7, we focus on the ejecta properties for NS–NS mergers based on the results of numerical relativity simulations.

3.2.2 Microphysics in NS–NS merger ejecta

In the previous subsection, we assumed the simple model for microphysics. Here we briefly summarize microphysics which play important role to understand kilonova emissions.

†The zero point of AB magnitude is set to be achromatic as $M_\nu^{\rm AB} = -48.60 - 2.5 \log f_\nu$, where f_ν is observed flux in cgs units.

Production of r-process elements
Lattimer and Schramm (1974) first pointed out that the compact binary merger NS–NS and BH–NS mergers can also produce r-process elements as an scenario of the origin of elements. After that, many authors study nucleaosynthesis in the ejecta of NS–NS mergers (Lattimer et al. 1977; Symbalisty and Schramm 1982; Meyer 1989; Freiburghaus et al. 1999; Goriely et al. 2011; Korobkin et al. 2012; Rosswog et al. 2013; Bauswein et al. 2013b). These theoretical studies have shown that almost nuclei in NS–NS merger ejecta are heavier than the iron group $A \geq 130$, where A is the mass number of nuclei.

Radioactive heating due to decay of r-process elements
The β-decay lifetime τ of a radioactive particle can be obtained by

$$\frac{1}{\tau(Q)} = \int_{m_e c^2}^{Q} \frac{2\pi}{\hbar} |\mathcal{M}_{fi}|^2 \frac{d\rho_f(Q, E_e)}{dE_e} dE_e, \tag{3.16}$$

where Q is the total energy of the decay, $\mathcal{M}_{fi}$ is the matrix elements of the decay, E_e is the energy of the electron, and ρ_f is the density of state of released particles. Here, we suppose that the matrix elemets do not depend on the energy. Because an electron and neutrino are ejected at the β-decay, the density of state can be written in the form

$$d\rho_f(Q, E_e) = \frac{4\pi p_e^2}{(2\pi\hbar)^3} \frac{dp_e}{dE_e} \frac{4\pi p_\nu^2}{(2\pi\hbar)^3} \frac{dp_\nu}{dQ} V^2 dE_e, \tag{3.17}$$

where p_e and p_ν are the momentum of an electron and neutrino, respectively. Note that the factor V^2 is cancelled out with the same factor in the matrix elements. Assuming $Q \gg m_e c^2$, the lifetime of the particle with Q can be described as

$$\frac{1}{\tau(Q)} \propto Q^5. \tag{3.18}$$

This dependence of the lifetime of the β-decay energy is called the Sargent's law.

Now we consider the heating rate of a statistical ensemble of β-decays (Colgate and White 1966). The heating rate per unit mass is given by

$$\epsilon(t) = \int_0^\infty Q \frac{f(Q)}{\tau(Q)} \exp(-t/\tau(Q)) dQ, \tag{3.19}$$

where $f(Q)$ is the distribution function. One supposes that flat distribution function $f(Q) \approx f_0$ for $Q \leq Q_{\max}$, where $Q_{\max}$ is the upper limit of the distribution. Substituting $\tau(Q) = t_0 Q^{-5}$ into Eq. (3.19), one can obtain the heating rate as

$$\epsilon(t) = \frac{\beta_0}{t_0} \left(\frac{t}{t_0}\right)^{-1.4}, \tag{3.20}$$

where β_0 is a constant. For the case that the number of radioactive nuclei is uniformly distributed in each energy scale, the power of the heating rate is -1.2 (see e.g. Colgate and McKee 1969). Although the above argument is quite simplified, the behavior of the

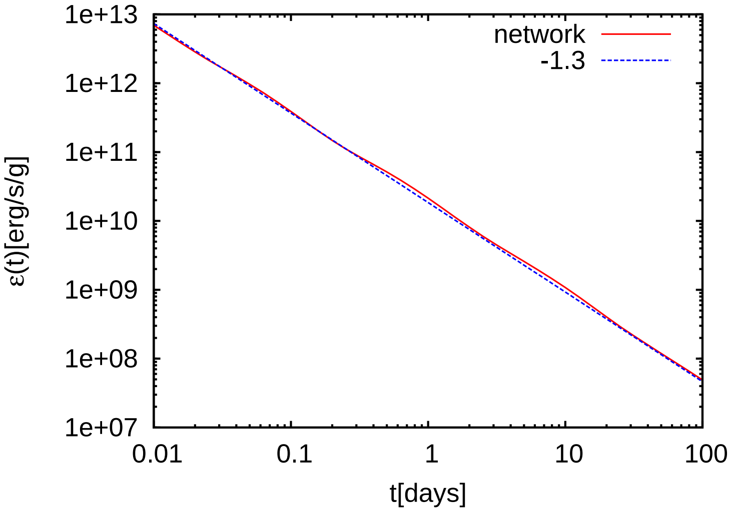

Figure 3.3: Heating rate due to β-decays of r-process elements. The red line shows the heating rate obtained by network calculation of nuclear reaction by S. Wanajo. The blue dashed line is line with the -1.3 power.

heating rate due to the β-decays of r-process elements can be understood as shown in Fig. 3.3.

Expansion Line Opacity

In NS–NS merger ejecta, the photon absorption due to the atomic transitions (bound-bound transitions) play an essential role to study kilonova emission as noted by Kasen et al. (2013); Tanaka and Hotokezaka (2013). Because heavy elements have many atomic levels in the temperature scale of kilonova and they are redshifted due to the expansion of ejecta, the opacity of NS–NS merger ejecta is significantly enhanced in the range from ultra-violet to near infrared wavelength. As a result, the opacity of NS–NS merger ejecta is large 100 times that of supernova ejecta, in which the opacities due the bound-bound transitions of the iron are dominated.

Here we briefly summarize the expansion opacity based on Karp et al. (1977). The cross section per unit frequency of a bound-bound transition denoted as the transition between a lower level l and upper level u, which is labeled by i $(l \rightarrow u)$,with a transition energy of $h\nu_i$ is given by

$$\sigma_{\nu_i}(\nu) = \frac{\pi e^2}{m_e c} X_l f_i \phi(\nu - \nu_i) \left(1 - \frac{g_l n_u}{g_u n_l}\right), \tag{3.21}$$

where X_i is the number fraction of the lower level, f_i is the oscillator strength of the transition i, $g_{l/u}$ is the statistical weight of the lower or higher level, $n_{l/u}$ is the number density of the lower or higher level, and $\phi(\nu - \nu_i)$ is the function of the line profile, which is normalized as $\int_0^\infty \phi d\nu = 1$. The last factor in Eq. (3.21) accounts for the stimulated emission of the transition of $u \to l$. For instance, the value of oscillator strength is $2^{13}/3^9 \approx 0.4$ for Lymann alpha and 10^{-1}–10^{-3} for 4f-4d transition of Lanthanide elements.

Here, we assume the homologously expanding ejecta $\vec{v}_{\rm exp} = \vec{r}/t$. In such expanding ejecta, the Sobolev's method can be used to compute the opacity. We assume (i) $v_{\rm th}/v_{\rm exp} \ll 1$, and (ii) $l_{\rm mfp}/c \ll t_{\rm exp}$, where $v_{\rm th}$ is the thermal velocity, $t_{\rm exp}$ is the expansion time, and $l_{\rm mfp}$ is the mean free path of photons in expanding ejecta.

The frequency of photons propagating in homologously expanding ejecta decreases along their path due to the Doppler shift. The evolution of a photon frequency is described by

$$\frac{d\nu}{dt} = -\frac{\nu}{t} + \mathcal{O}\left(\frac{v_{\rm ej}}{c}\right). \tag{3.22}$$

The photon emitted in the frequency ν_0 at r_0 is redshifted to $\nu(r) = \nu_0 + \Delta\nu$ at r. This gives $\Delta r \simeq ct \ln(1 + \Delta\nu/\nu)$, where $\Delta r = r - r_0$. Assuming that there are N lines in the frequency range $\nu(r) < \nu < \nu_0$ with a constant interval $\delta\nu$ and neglecting stimulated emissions, the optical depth is given by

$$\begin{aligned}
\tau_o(\Delta r) &= \int_{r_0}^{r} \sum_{i=1}^{N} \sigma_{\nu_i}(\nu) n dr, \\
&= \sum_{i=1}^{N} \frac{\pi e^2}{m_e c} \frac{g_l f_i}{g_0 \nu_i} n_0 c t e^{-E_l/k_B T}, \\
&\equiv \sum_{i}^{N} \kappa_i \rho c t \equiv \sum_{i}^{N} \tau_i,
\end{aligned} \tag{3.23}$$

where κ_i and τ_i are the opacity and optical depth for each line, respectively, g_0 is the statistical weight of the ground state of the ion, n_0 is the number density of the ion, and E_l is the energy level of lower energy state of the transition. Here we use $\phi(x) \simeq \delta(x)$ because of $v_{\rm th} \ll v_{\rm ej}$ and assume local thermodynamic equilibrium (LTE). This expression is called as the Sobolev optical depth for LTE. The mean free path of the photon is

$$l_{\rm mfp}(\nu) = \int_0^\infty e^{-\tau_o(s)} ds, \tag{3.24}$$

$$\sim ct \frac{\Delta\nu}{\nu} \frac{1}{\tau_1}, \tag{3.25}$$

where we assume $\tau_i \simeq \tau_1$. As a result, the line expansion opacity $\kappa_{\rm exp}$ can be evaluated as

$$\kappa_{\rm exp} = \frac{1}{\rho l_{\rm mfp}} \sim \kappa_1 \frac{\nu}{\delta\nu} = N\kappa_1, \tag{3.26}$$

where $\kappa_1 \simeq \kappa_i$. Note that the line expansion opacity is proportional to the number of the atomic lines, which is huge number for the ions of lanthanides $57 \leq Z \leq 71$. For instance, the first ionization state of Nd has 24,632,513 lines at the energy level of 5.52 eV (Kasen et al. 2013). Indeed, this number of lines is large and the energy level

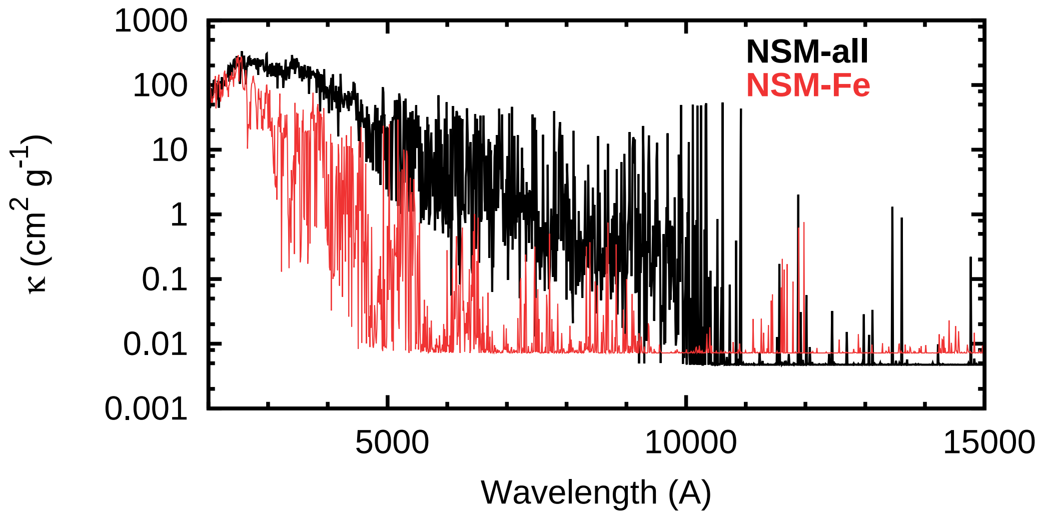

Figure 3.4: Comparison of opacities of NS–NS merger ejecta and of pure Fe ejecta at 3 days after the mass ejection for the mass shell with $v = 0.1c$. This figure is taken from Tanaka and Hotokezaka (2013).

is low compared to those of the first ionization state of Fe, of which the number of lines is 326,519 and its energy level is 7.90 eV (Kasen et al. 2013). Figure 3.4 shows that the opacity of r-process elements of NS-NS merger ejecta on the mass shell $v = 0.1c$ at 3 days after the merger (Tanaka and Hotokezaka 2013). The value of opacity has a maximum 100 cm^2/g around $\lambda \sim 3000$ Å (ultra-violet). Even in the near-infrared region (Z-band $\lambda \sim 10000$ Å), the opacity is still large. One can clearly see that the large opacity is composed with the superposition of many lines. Due to the complicated structure of the opacities of NS-NS merger ejecta, the expected spectrum is different from the black body spectrum. Therefore one has to perform radiative transfer simulations in order to obtain the spectrum and light curve in details (see Barnes and Kasen 2013; Tanaka and Hotokezaka 2013 for NS–NS merger ejecta and Tanaka et al. 2013 for BH–NS merger ejecta). Figure 3.5 shows the expected R-band light curve in Vega magnitude[‡].

3.2.3 Short GRB – Kilonova search

After the launch of *Swift* satellite, afterglows of short GRBs can be discovered despite of their short time scale. The detections of afterglows allow us to identify their host galaxies, and thus, the distance to the source can be estimated. Here we discuss characteristic short GRBs, which are interesting from the point of view of kilonovae (see also Kann et al. 2011).

[‡]Vega magnitude is the logarithmic measure of the flux f_ν erg/s/cm^2/Hz, of which the magnitude zero-point corresponds to the Vega.

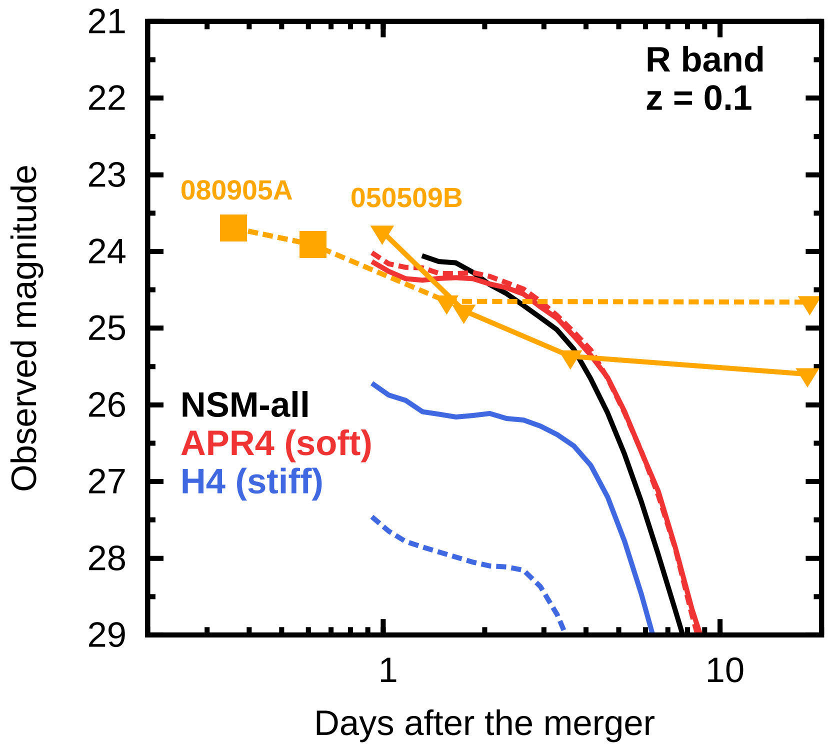

Figure 3.5: Expected R-band light curves at $z = 0.1$ in Vega magnitude taken from Tanaka and Hotokezaka (2013) and observed data (squares) and upper limits (triangles) of short GRB afterglows (GRB 050509B and GRB 080905A) taken from Kann et al. (2011). The black, red, and blue curve corresponds to the spherical ejecta model with ejecta mass of $0.01M_\odot$, APR4-120150, and H4-120150, respectively. The red and blue dashed curve corresponds to APR4-130140 and H4-130140, respectively (see Chap. 7 for these models). For the afterglow data, we use R-band magnitude corrected and shifted to $z = 0.1$ scale. This figure is taken from Tanaka and Hotokezaka (2013).

GRB 050509B

The short GRB 050509B is the first short GRB, for which a precise position measurement was made by *Swift* satellite (Bloom et al. 2006). Its host galaxy was turned out to be an elliptical galaxy at $z = 0.225$. It is the first evidence that at least some short GRBs are cosmological origin. The continuous observations have been done from 8 minutes to 8 days after the burst in optical to near-infrared. As a results, the upper limit was obtained as > 25.7 mag in R-band at ~ 1 day after the burst. This upper limit can constrain kilonova emissions, and thus, the compact binary mergers with massive ejecta $M_{\rm ej} > 0.01M_\odot$ may be excluded as the progenitor of GRB 050509B (see Fig. 3.5).

GRB 070724

The short GRB 070724A is associated with a very red near-infrared counterpart, of which the luminosity is bright as $K_s \simeq 20$ mag and $i \simeq 23.8$ mag at 2.3 hr after the burst, but with a faint optical counterpart (Berger et al. 2009; Kocevski et al. 2010). Berger et al. (2009) suggests the kilonova model as a possible origin of the near-infrared counterpart. However, it is difficult to reproduce such a fast time scale and extremely red color of the light curve with kilonova emission models.

GRB 080503

The short GRB 080503 is associated with a very bright extended emission which is about 30 times the gamma-ray fluence of the prompt emission (Perley et al. 2009). Meanwhile, the optical afterglow is very faint, e.g., 25 mag at 1 hr after the burst. This implies that the density of circumstellar matter is extremely low around the burst. Interestingly, the source is brighten again at ~ 1 day after the burst in optical. This can be a candidate of kilonova/macronova. However, reddening with time was not observed. It is not easy for kilonova models to explain the lack of reddening with time. Unfortunately, the redshift of this GRB is unknown. It prevents us further discussion of the 1 day re-brightening.

GRB 080905A

The short GRB 080905A is one of the most local short GRBs at $z = 0.1218$ [§] (Rowlinson et al. 2010). In optical observations, a faint optical afterglow was detected and upper limits are obtained in the late epoch ($>$ 1 days after the burst). These results give an upper limit on the ejecta mass $\lesssim 0.01 M_\odot$ (see Fig. 3.5).

GRB 130603B

The short GRB 130603B is the first short GRB, which the absorption spectrum is observed (de Ugarte Postigo et al. 2013). It allows us to determine the redshift of the burst $z = 0.356$. Furthermore, an electromagnetic transient associated with the burst is observed by *Hubble Space Telescope* (Tanvir et al. 2013; Berger et al. 2013). Combining these data and the other observational data taken by ground-based telescopes, there is an excess in near-infrared at 9 days after the burst. The observed time scale, luminosity, and color are quite consistent with the predicted kilonova emission model (Barnes and Kasen 2013; Tanaka and Hotokezaka 2013). This near-infrared excess may be the first detection of kilonova. We will give a further discussion on this event in Chap. 8.

3.2.4 GW–Kilonova search

A kilonova may be detected by surveys in optical and near infrared within the sky area localized by gravitational-wave observations. The first attempt had been done during LIGO and Virgo joint science run in 2009–2010 (The LIGO Scientific Collaboration and the Virgo Collaboration et al. 2013). They had performed follow-up observations of the

[§]GRB 061201 was reported to be associated with a galaxy at $z = 0.111$ with the offset of 17 arcsec (Stratta et al. 2007).

candidates of gravitational-wave events by using 13 telescopes with a relatively wide field of view. The range of the limiting R-band magnitude of the telescopes is 12–21 mag. Even though these telescopes have wide field of view, it is difficult to perform a survey in the total area of the large error circle of gravitational wave observations, typically 100 square degree. Therefore they had mostly observed only around large galaxies by using a source catalog. As a results, they give upper limits on kilonova events for each candidate of gravitational wave events.

In order to detect kilonova associated with a gravitational-wave signal, it is important to prepare the models of kilonova light curves. Figure 3.6 shows that the expected light curves in $ugrizJHK$-band in AB magnitude for an event occurring at 200 Mpc. As shown in the previous section, the expected kilonova spectrum becomes redder with time. As a result, the expected kilonova light curve has a peak in near infrared at the peak luminosity. We also show the detection thresholds of the several telescopes in Fig. 3.6. From this figure, we need at least a 4-m telescope in order to detect the kilonova as an electromagnetic counterpart of a gravitational-wave source.

3.3 Compact Binary Merger Remnant

Ejected material of a compact binary merger expands in circumstellar medium with a sub-relativistic velocity $\sim 0.1c$. For such a case, a strong shock is formed between the ejecta and circumstellar medium. Electrons around a shock wave may be accelerated to relativistic velocities. These electrons emit synchrotron radiation. Such an object can be strong radio emitter like radio supernovae, which are well explained synchrotron and synchrotron self-absorption models (Chevalier 1998). The synchrotron radiation from a compact binary merger remnant will be a detectable electromagnetic counterpart of a gravitational-wave event as first pointed out by Nakar and Piran (2011). In this section, we briefly summarize expected radio emissions from NS–NS merger ejecta.

3.3.1 Synchrotron radiation from compact binary merger remnants

Let us consider that the mildly relativistic ejecta with the mass $M_{\rm ej} \sim 0.01 M_{\odot}$ and velocity $\beta_{\rm ej} \sim 0.1c$ interacts with the circumstellar medium with the constant number density n. The ejecta freely expand as long as the mass of the swept material is smaller than the ejecta mass. The deceleration radius of the expanding ejecta is the radius where the mass of the swept material becomes comparable to the ejecta mass as

$$R_{\rm dec} = \left(\frac{3E}{4\pi n m_p c^2 \beta_{\rm ej,0}^2} \right)^{1/3} \approx 10^{18}\ {\rm cm}\ E_{50}^{1/3} n^{-1/3} \beta_{\rm ej,0,-1}^{-2/3}. \tag{3.27}$$

where $E = Mc^2\beta_{\rm ej,0}^2/2$ is the total energy, $\beta_{\rm ej,0}$ is the initial ejecta velocity. Beyond the deceleration radius, we approximately assume that the ejecta dynamics follow the Sedov-Taylor self-similar solution as

$$\beta_{\rm ej}(R) = \beta_{\rm ej,0}\begin{cases} 1 & (R \leq R_{\rm dec}), \\ \left(\frac{R}{R_{\rm dec}}\right)^{-3/2} & (R > R_{\rm dec}), \end{cases} \tag{3.28}$$

Electrons may be accelerated at the shock wave of the ejecta-circumstellar medium interaction. The shock wave also generates amplified magnetic fields. Here we assume the conversion efficiency of the internal energy of the shocked material into the energy of accelerated electrons and of amplified magnetic fields is $\epsilon_{\rm e} \sim 0.1$ and $\epsilon_{\rm B} \sim 0.1$, respectively. The distribution of the accelerated electrons is assumed to be $dN/d\gamma = N_0\gamma^{-p}$. The consideration of the total energy conservation leads the minimum Lorentz factor of the accelerated electrons $\gamma_m = \epsilon_{\rm e}\beta_{\rm ej}^2(p-2)m_e/(p-1)m_p$.

In order to calculate the synchrotron spectrum and light curve, there are two characteristic frequencies. One is the characteristic frequency corresponds to the synchrotron frequency of the electrons with minimum Lorentz factor as

$$\nu_m = \frac{3}{2}\gamma_m^2\frac{eB}{m_e c} \approx 10\ {\rm kHz}\ n^{1/2}\epsilon_{\rm B,-1}^{1/2}\epsilon_{\rm e,-1}^2\beta_{\rm ej,0,-1}^5. \tag{3.29}$$

Note that this frequency strongly depends on the value of $\beta_{\rm ej,0}$. Because of $\beta_{\rm ej}(t) \propto t^{-3/5}$ in the Sedov-Taylor phase, the evolution of ν_m is given by

$$\nu_m(t) \propto \begin{cases} {\rm const} & (R \leq R_{\rm dec}), \\ t^{-3} & (R > R_{\rm dec}). \end{cases} \tag{3.30}$$

The characteristic frequency of the self absorption is

$$\begin{aligned} \nu_a &= C_1 N_0^{\frac{2}{p+4}} R^{\frac{2}{p+4}} B^{\frac{p+2}{p+4}} \\ &\approx 0.1\ {\rm GHz}\ R_{18}^{\frac{2}{p+4}} n^{\frac{6+p}{2(p+4)}} \epsilon_{B,-1}^{\frac{2+p}{2(p+4)}} \epsilon_{e,-1}^{\frac{2(p-1)}{p+4}} \beta_{\rm ej,0,-1}^{\frac{5p-2}{p+4}}, \end{aligned} \tag{3.31}$$

where C_1 is a constant depending on p (Rybicki and Lightman 1979). Here we assume $p = 2.5$. Taking into account $R \propto t^{2/5}$ in the Sedov-Taylor phase, the evolution of ν_a is given by

$$\nu_a(t) \propto \begin{cases} t^{\frac{2}{p+4}} & (R \leq R_{\rm dec}), \\ t^{-\frac{3p-2}{4+p}} & (R > R_{\rm dec}). \end{cases} \tag{3.32}$$

It is worthy to note that $\nu_m < \nu_a$ is satisfied for NS–NS merger ejecta of which the ejecta velocity is nearly the escape velocity from the neutron star surface $\mathcal{O}(0.1c)$.

At the frequencies in optically thin region, the flux can be written as

$$F_\nu = F_m\left(\frac{\nu}{\nu_m}\right)^{-\frac{p-1}{2}}, \tag{3.33}$$

where

$$F_m = \frac{P_{\nu,\max}^{\rm tot}}{4\pi D_L^2} \approx 100 \text{ mJy } R_{18}^3 n^{3/2} \epsilon_{\rm B,-1} \beta_{\rm ej,0,-1} D_{L,27}^{-2}, \tag{3.34}$$

where D_L is the luminosity distance to the source. Therefore the evolution of the peak flux is

$$F_m(t) \propto \begin{cases} t^3 & (R \le R_{\rm dec}), \\ t^{3/5} & (R > R_{\rm dec}). \end{cases} \tag{3.35}$$

At the frequency in optically thick region, the synchrotron spectrum is given by

$$F_\nu = F_a \left(\frac{\nu}{\nu_a}\right)^{5/2}, \tag{3.36}$$

where

$$F_a \equiv F_{\nu_a} = F_m \left(\frac{\nu_a}{\nu_m}\right)^{-\frac{p-1}{2}} \tag{3.37}$$

From these consideration of the time evolution of the characteristic quantities, one obtain the expected light curves for a given observed frequency $\nu_{\rm obs}$. For optically thin regime $\nu_{\rm obs} > \nu_a$, the expected light curve is

$$F_{\nu_{\rm obs}}(t) \propto \begin{cases} t^3 & (R \le R_{\rm dec}), \\ t^{-\frac{15p-21}{10}} & (R > R_{\rm dec}). \end{cases} \tag{3.38}$$

For optically thick regime $\nu_{\rm obs} \le \nu_a$, the expected light curve is

$$F_{\nu_{\rm obs}}(t) \propto \begin{cases} t^2 & (R \le R_{\rm dec}), \\ t^{\frac{11}{10}} & (R > R_{\rm dec}). \end{cases} \tag{3.39}$$

Note that the flux rises until the deceleration radius in the high frequency. In low frequency $\nu < \nu_a$, the flux last to rise beyond the deceleration radius.

The radio flare for a hypothetical event at a distance of 200 Mpc, $E_0 \sim 10^{50}$ ergs with $n_0 = 1$ cm^{-3} may be strong enough to be observed by future-planned radio instruments (such as EVLA[¶], ASKAP[‖], MeerKAT[**] , and Apertif for which the root-mean square value of the background noise for one hour observation is smaller than 50 μJy as shown in Nakar and Piran 2011).

[¶]http://www.aoc.nrao.edu/evla/

[‖]http://www.atnf.csiro.au/projects/askap/

[**]http://www.ska.ac.za/meerkat/

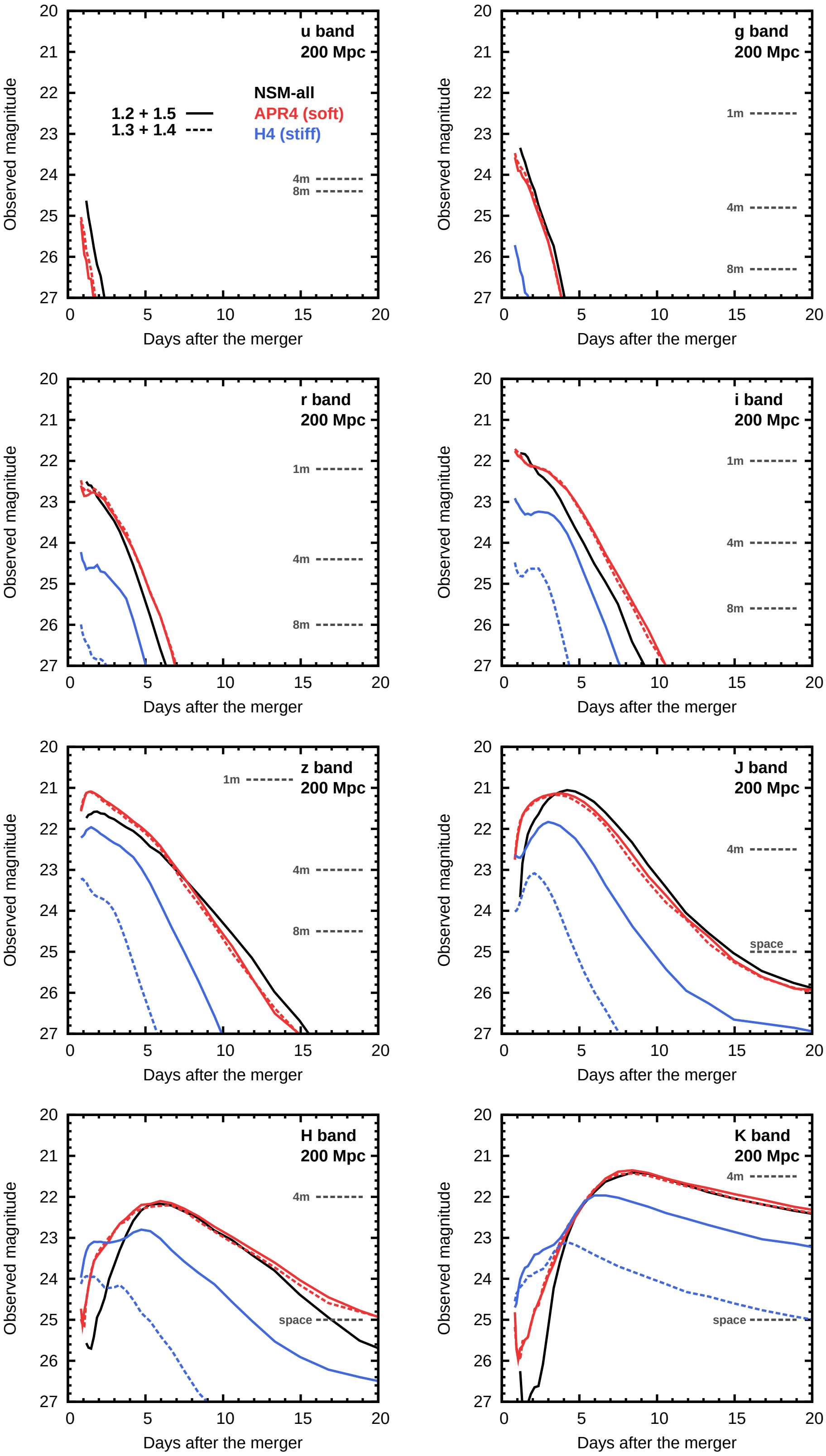

Figure 3.6: Expected *ugrizJHK*-band light curve (in AB magnitude). The distance to the NS–NS merger event is set to be 200 Mpc. Horizontal lines show the typical limiting magnitudes for wide-field telescopes (5σ with 10 minutes exposure). This figure is taken from Tanaka and Hotokezaka (2013).

Chapter 4

Set-up of numerical-relativity simulation

Numerical-relativity simulation, which solves an initial value problem of Einstein equation, is a powerful and unique tool to compute compact binary mergers. In this chapter, we summarize the formulation of numerical-relativity which is adopted our numerical code `SACRA`. We also describe the diagnostic tools in order to analyze numerical data and set up of our numerical simulation.

4.1 BSSN formalism

The initial value problem of Einstein equation can be solved with the decomposition of a globally hyperbolic spacetime $(\mathcal{M},\ g_{ab})$ into space $(\Sigma_t,\ \gamma_{ab},\ K_{ab})$ and time, where $\mathcal{M}$ is a real smooth manifold, g is a Lorentz metric, Σ_t is a Cauchy surface parameterized by a global time function t, γ_{ab} is an induced spatial metric on Σ_t, and K_{ab} is extrinsic curvature of Σ_t. This formulation is the so-called 3+1 formalism or Arnowitt-Deser-Misner (ADM) formalism (Arnowitt et al. 1959). In this formalism, one has twelve evolution equations for γ_{ab} and K_{ab} and four constraints, *Hamiltonian* constraint and *Momentum* constraint. In principle, the constraints are satisfied all the time, if they satisfied at the initial hypersurface (Wald 1984). However, the system is numerically unstable, and thus, the constraints are strongly violated in a numerical computation in the ADM formalism.

In order to overcome the numerical difficulty, several efforts have been made. One of the most successful formalism is the so-called Baumgarte-Shapiro-Shibata-Nakamura (BSSN) formalism (Shibata and Nakamura 1995; Baumgarte and Shapiro 1999). In this formalism, new variables are added to maintain the constraints. In particular, to solve new three variables Γ^i plays an important role to control the violation of the momentum constraint, which causes the crucial difficulty in ADM formalism.

It is worthy to note that the combination of the BSSN formalism and the moving puncture gauge is successful to compute the evolution of a binary black hole merger without black hole excision (Baker et al. 2006; Campanelli et al. 2006). For this reason, the BSSN formalism is widely used in numerical relativity.

4.1.1 The BSSN variables

In the original BSSN formalism (Shibata and Nakamura 1995; Baumgarte and Shapiro 1999), induced metric and extrinsic curvature are conformally decomposed as

$$\tilde{\gamma}_{ab} = e^{-4\phi}\gamma_{ab} \tag{4.1}$$

$$\tilde{A}_{ab} = e^{-4\phi}A_{ab}, \tag{4.2}$$

where $A_{ab} = K_{ab} - \gamma_{ab}K/3$, $K = \mathrm{tr}K_{ab}$, and ϕ is some scalar field. The new evolution variable $\tilde{\Gamma}^a \equiv -\partial_j\tilde{\gamma}^{aj}$ in order to keep the divergence of the conformal metric under control. Therefore the evolution variables are $(\tilde{\gamma}_{ab},\ \tilde{A}_{ab},\ \phi,\ K,\ \tilde{\Gamma}_a)$.

The puncture approach allows us to numerically treat an evolving black hole. In this approach, the metric on the initial hypersurface is decomposed as $\gamma_{ab} = (\psi_{\mathrm{BL}} + u)^4\delta_{ab}$, where $\psi_{\mathrm{BL}} = 1 + \sum_{i=1}^{n} m_i/(2r_i)$ is the Brill-Lindquist conformal factor, m_i is the mass of the black hole at a puncture i, r_i is the distance from a puncture i, and u is a scalar function which is finite on punctures. Therefore one can analytically treat the singular part of the metric. In order to avoid the singular forms $\mathrm{ln}r$ of ϕ on the punctures, Campanelli et al. (2006) introduced a new variable $\chi = \exp(-4\phi)$ $(W = \exp(-2\phi))$. To summarize, in the BSSN-moving puncture formalism, one solves the following 17 evolving variables $(\tilde{\gamma}_{ab},\ \tilde{A}_{ab}, \chi$ or $W,\ K,\ \tilde{\Gamma}_a)$.

4.1.2 The BSSN evolution equation

The evolution equations for these evolving variables can be obtained straightforwardly from the evolution equations in the ADM formalism. The evolution equations in the

BSSN formalism are written as

$$\left(\partial_t - \beta^k\partial_k\right)\tilde{\gamma}_{ij} = -2\alpha\tilde{A}_{ij} + \tilde{\gamma}_{ik}\partial_j\beta^k + \tilde{\gamma}_{jk}\partial_i\beta^k - \frac{2}{3}\tilde{\gamma}_{ij}\partial_k\beta^k \tag{4.3}$$

$$\begin{aligned}\left(\partial_t - \beta^k\partial_k\right)\tilde{A}_{ij} &= -W^2\left(D_iD_j\alpha - \frac{1}{3}\gamma_{ij}D^2\alpha\right) + W^2\alpha\left(R_{ij} - \frac{1}{3}\gamma_{ij}R\right)\\ &+\alpha\left(K\tilde{A}_{ij} - 2\tilde{A}_{ik}\tilde{A}^k_j\right) - 8\pi W^2\alpha\left(S_{ij} - \frac{1}{3}\gamma_{ij}S\right)\\ &+\tilde{A}_{ik}\partial_j\beta^k + \tilde{A}_{jk}\partial_i\beta^k - \frac{2}{3}\tilde{A}_{ij}\partial_k\beta^k.\end{aligned} \tag{4.4}$$

$$\left(\partial_t - \beta^k\partial_k\right)W = \frac{1}{3}W\left(\alpha K - \partial_k\beta^k\right) \tag{4.5}$$

$$\left(\partial_t - \beta^k\partial_k\right)K = -D^2\alpha + \alpha\left(\tilde{A}_{kl}\tilde{A}^{kl} + \frac{1}{3}K^2 + 4\pi(\rho + S)\right) \tag{4.6}$$

$$\begin{aligned}\left(\partial_t - \beta^k\partial_k\right)\tilde{\Gamma}^i &= -2\tilde{A}^{ik}\partial_k\alpha + 2\alpha\left(\tilde{\Gamma}^i_{kl}\tilde{A}^{kl} - 3W^{-1}\tilde{A}^{ik}\partial_kW - \frac{2}{3}\tilde{\gamma}^{ik}\partial_kK - 8\pi\tilde{\gamma}^{ik}j_k\right)\\ &+\tilde{\gamma}^{kl}\partial_k\partial_l\beta^i + \frac{1}{3}\tilde{\gamma}^{ik}\partial_k\partial_l\beta^l - \tilde{\Gamma}^l\partial_l\beta^i + \beta^k\partial_k\tilde{\Gamma}^i + \frac{2}{3}\tilde{\Gamma}^i\partial_k\beta^k,\end{aligned} \tag{4.7}$$

where α is the lapse function, β^i is the shift vector, D_i is the covariant derivtive associated with γ_{ij}, R_{ij} and R are the Ricci tensor and the scalar curvature. The matter fields $(\rho_{\rm H},\ j_\mu, S_{\mu\nu})$ are defined by

$$\rho_{\rm H} \equiv T^{\mu\nu}n_\mu n_\nu, \tag{4.8}$$

$$j_\mu \equiv -\gamma_{\mu\nu}T^{\nu\rho}n_\rho, \tag{4.9}$$

$$S_{\mu\nu} \equiv \gamma_{\mu\rho}\gamma_{\nu\lambda}T^{\rho\lambda}, \tag{4.10}$$

where n^μ is a unit normal vector on the hypersurface. The Ricci tensor can be divided into the radiation and non-radiation part as

$$R_{ij} = \tilde{R}_{ij} + R^W_{ij}, \tag{4.11}$$

where the radiation part

$$\begin{aligned}\tilde{R}_{ij} = -\frac{1}{2}\tilde{\gamma}^{kl}\partial_k\partial_l\tilde{\gamma}_{ij}\frac{1}{2}\left(\tilde{\gamma}_{ik}\partial_j\tilde{\Gamma}^k + \tilde{\gamma}_{jk}\partial_i\tilde{\Gamma}^k\right) + \frac{1}{2}\tilde{\Gamma}^{kl}_l\partial_k\tilde{\gamma}_{ij}\\ +\tilde{\Gamma}^{kl}_i\tilde{\Gamma}_{jkl} + \tilde{\Gamma}^{kl}_j\tilde{\Gamma}_{ikl} + \tilde{\Gamma}^{kl}_i\tilde{\Gamma}_{klj},\end{aligned} \tag{4.12}$$

and non-radiation part

$$R^W_{ij} = W^{-1}\tilde{D}_i\tilde{D}_jW + W^{-1}\tilde{\gamma}_{ij}\tilde{D}^2W - 2W^{-2}\tilde{\gamma}_{ij}\left(\tilde{D}^kW\right)\left(\tilde{D}_kW\right). \tag{4.13}$$

For solving the BSSN evolution equations, one has to specify the choice of the coordinate system, i.e., to specify $(\alpha,\ \beta^i)$ for each slice. According to Brügmann et al. (2008), a moving puncture gauge condition is given by

$$\left(\partial_t - \beta^k\partial_k\right)\alpha = -2\alpha K, \tag{4.14}$$

$$\left(\partial_t - \beta^k\partial_k\right)\beta^i = \frac{3}{4}B^i, \tag{4.15}$$

$$\left(\partial_t - \beta^k\partial_k\right)B^i = \left(\partial_t - \beta^i\partial_i\right)\tilde{\Gamma}^i - \eta_sB^i, \tag{4.16}$$

where B^i is an auxiliary variable and η_s is a parameter, which is typically set to be $\simeq 0.8/M$.

4.2 Hydrodynamics

4.2.1 Evolution equations

In general relativity, the matter fields satisfy the conservation law of baryon number density and energy-momentum tensor given by

$$\nabla_\mu J^\mu = 0, \quad \nabla_\mu T^{\mu\nu} = 0, \tag{4.17}$$

where $J^\mu = \rho u^\mu$ and the energy momentum tensor of ideal fluid is written as

$$T^{\mu\nu} = \rho h u^\mu u^\nu + P g^{\mu\nu}, \tag{4.18}$$

where ρ is the mass density, h is the specific enthalpy, u^μ is the four velocity, and P is the pressure. Equation (4.17) can be rewritten in the form of the ADM formalism

$$\begin{aligned}
\partial_t \rho_* + \partial_i \left(\rho_* v^i\right) &= 0, & (4.19)\\
\partial_t \left(\rho_* \hat{u}_i\right) + \partial_j \left(\rho_* \hat{u}_i v^j + P\alpha\sqrt{\gamma}\delta_i^j\right) &= P\partial_i \left(\alpha\sqrt{\gamma}\right) - \rho_* \left(hw\partial_i\alpha - \hat{u}_j\partial_i\beta^j + \frac{\alpha}{2hw}\hat{u}_j\hat{u}_k\partial_i\gamma^{jk}\right), & (4.20)\\
\partial_t \left(\rho_* \hat{e}\right) + \partial_i \left(\rho_* \hat{e} v^i + P\sqrt{\gamma}\left(v^i + \beta^i\right)\right) &= P\alpha\sqrt{\gamma}K - \rho_* \hat{u}_i\gamma^{ij}\partial_j\alpha + \frac{\rho_*\alpha}{hw}\hat{u}_i\hat{u}_j K^{ij}, & (4.21)
\end{aligned}$$

where we define new variables

$$\begin{aligned}
w &\equiv -n_\mu u^\mu = \alpha u^t, & (4.22)\\
v^i &\equiv \frac{u^i}{u^t}, & (4.23)\\
\rho_* &\equiv \rho\alpha\sqrt{\gamma}u^t, & (4.24)\\
\hat{u}_i &\equiv h u_i, & (4.25)\\
\hat{e} &\equiv h\alpha u^t - \frac{P}{\rho\alpha u^t}. & (4.26)
\end{aligned}$$

Here w is the Lorentz factor, v^i is the three velocity, and $(\rho_*,\ \hat{u}_i,\ \hat{e})$ are conserved variables in general relativistic hydrodynamics.

Note that Eqs. (4.19)–(4.21) are written in a conservation form as

$$\partial_t Q_a + \partial_i F_a^i = S_a. \tag{4.27}$$

For numerical computation of hydrodynamics, difficulties arise from the existence of discontinuities of dynamical variables, such as shock waves. In general relativistic hydrodynamics as well as Newtonian hydrodynamics, a conservation form allows us to treat discontinuities with a high-resolution shock capturing scheme or a high-resolution central scheme as shown by Banyuls et al. (1997) and Shibata and Font (2005), respectively. For numerical computation, it is essential to follow the disturbances of the fluid including shock waves, which propagate along lines so-called characteristics. In order to capture such characteristics, one transform Eq.(4.27) into the set of wave equations as

$$\partial_t Q_a + M^i_{ab}\partial_i Q_b = S_a, \tag{4.28}$$

where

$$M^i_{ab} \equiv \frac{\partial F^i_a}{\partial Q_b}. \tag{4.29}$$

This Jacobian matrix has information of characteristic speed of the fluid. The matrix can be diagonalized by a unitary matrix. The eigenvalues of the Jacobian matrix are needed to construct the flux at each cell boundary in numerical computation. In general relativistic hydrodynamics, the eigenvalues of the Jacobian matrix can be written as (Shibata 2003),

$$\lambda^i = \lambda^i_{\pm}, \quad v^i, \tag{4.30}$$

where

$$\lambda^i_{\pm} = \frac{1}{\alpha^2 - V_k V^k c_s^2} \times \tag{4.31}$$
$$\left[v^i\alpha^2(1-c_s^2) - \beta^i c_s^2(\alpha^2 - V_k V^k) \pm \alpha c_s \sqrt{(\alpha^2 - V_k V^k)\left(\gamma^{ii}(\alpha^2 - V_k V^k c_s^2) - (1-c_s^2)V^i V^i\right)}\right],$$

and

$$c_s^2 = \frac{1}{h}\left(\chi + \frac{P}{\rho^2}\kappa\right), \tag{4.32}$$

$$V^i = v^i + \beta^i, \tag{4.33}$$

$$\chi = \left.\frac{\partial P}{\partial \rho}\right|_{\epsilon}, \tag{4.34}$$

$$\kappa = \left.\frac{\partial P}{\partial \epsilon}\right|_{\rho}. \tag{4.35}$$

Here Eq. (4.32) is the relativistic local sound speed. In our numerical code `SACRA`, a high-resolution central scheme of Kurganov and Tadmor (2000) is adopted with a third-order piecewise parabolic spatial interpolation for reconstructing numerical fluxes.

In numerical simulations, the primitive variables ($\rho,\ u_i,\ \epsilon$) have to be calculated from the conserved variables ($\rho_*,\ \hat{u}_i,\ \hat{e}$). Here ϵ is the specific internal energy. In this procedure, one needs to know the Lorentz factor w. In order to obtain w, the algebraic equation $u_\mu u^\mu = -1$ has to be solved as

$$w^2 = 1 + \frac{\gamma^{ij}\hat{u}_i\hat{u}_j}{h(w)^2}. \tag{4.36}$$

This equation is solved by an iterative procedure.

Table 4.1: Parameters and key quantities for five piecewise polytropic EOSs and finite-temperature (Shen) EOSs employed so far. P_2 is shown in units of dyn/cm^2. $M_{\rm max}$ is the maximum-mass along the sequences of cold spherical neutron stars. $(R_{1.35}, \rho_{1.35})$, $(R_{1.5}, \rho_{1.5})$, $(R_{1.6}, \rho_{1.6})$, and $(R_{1.8}, \rho_{1.8})$ are the circumferential radius in units of km and the central density in units of g/cm^3 for $1.35M_\odot$, $1.5M_\odot$, $1.6M_\odot$, and $1.8M_\odot$ neutron stars, respectively. We note that the values of the mass, radius, and density listed for the piecewise polytropic EOSs are slightly different from those obtained in the original tabulated EOSs (see the text for the reason). MS1 is referred to as this name in Read et al. (2009), but in other references (e.g., Lattimer and Prakash 2004), it is referred to as MS0. We follow Read et al. (2009) in this thesis. The fitted parameters $(\log(P_2), \Gamma_1, \Gamma_2, \Gamma_3)$ are taken from Read et al. (2009).

EOS	$(\log(P_2), \Gamma_1, \Gamma_2, \Gamma_3)$	$M_{\rm max}(M_\odot)$	$R_{1.35}$	$\rho_{1.35}$	$R_{1.5}$	$\rho_{1.5}$	$R_{1.6}$	$\rho_{1.6}$	$R_{1.8}$	$\rho_{1.8}$
APR4	(34.269, 2.830, 3.445, 3.348)	2.20	11.1	8.9×10^{14}	11.1	9.6×10^{14}	11.1	10.1×10^{14}	11.0	11.4×10^{14}
SLy	(34.384, 3.005, 2.988, 2.851)	2.06	11.5	8.6×10^{14}	11.4	9.5×10^{14}	11.4	10.2×10^{14}	11.2	12.0×10^{14}
ALF2	(34.616, 4.070, 2.411, 1.890)	1.99	12.4	6.4×10^{14}	12.4	7.2×10^{14}	12.4	7.8×10^{14}	12.2	9.5×10^{14}
H4	(34.669, 2.909, 2.246, 2.144)	2.03	13.6	5.5×10^{14}	13.5	6.3×10^{14}	13.5	6.9×10^{14}	13.1	8.7×10^{14}
MS1	(34.858, 3.224, 3.033, 1.325)	2.77	14.4	4.2×10^{14}	14.5	4.5×10^{14}	14.6	4.7×10^{14}	14.6	5.1×10^{14}
Shen	(34.717, —, —, —)	2.20	14.5	4.4×10^{14}	14.4	4.9×10^{14}	14.4	5.8×10^{14}	14.2	6.7×10^{14}

4.2.2 Equation of state

The exact EOS for the high-density nuclear matter is still unknown (Lattimer and Prakash 2004), and hence, a numerical simulation employing a single particular EOS would not yield a scientific result. Simulations systematically employing a wide variety of possible hypothetical EOSs are required for exploring the merger of binary neutron stars. Nevertheless, the latest discoveries of a high-mass neutron star PSR J1614-2230 with mass $1.97 \pm 0.04M_\odot$ (Demorest et al. 2010) and PSR J0348+0432 with $2.01 \pm 0.04M_\odot$ (Antoniadis et al. 2013) significantly constrain EOSs of neutron-star matter to be chosen, because these suggest that the maximum allowed mass of (cold) spherical neutron stars for a given EOS (hereafter denoted by $M_{\rm max}$) has to be larger than $\sim 2M_\odot$. This indicates that the EOS should be rather stiff, although there are still many candidate EOSs (Lattimer and Prakash 2004).

The parameterized piecewise-polytropic EOS (Read et al. 2009) is useful to systematically study the dependence of the dynamical behavior of the merger on the EOS of the neutron-star matter. In this work, we employ a parameterized piecewise-polytropic EOS proposed by Read et al. (2009). This EOS is written in terms of four segments of polytropes

$$P = K_i \rho^{\Gamma_i} \qquad (\text{ for } \rho_i \le \rho < \rho_{i+1},\ 0 \le i \le 3), \tag{4.37}$$

where ρ is the mass density, P is the pressure, K_i is the polytropic constant, and Γ_i is the adiabatic index. We refer to the pressure in the form of Eq. (3) as the cold-part pressure, $P_{\rm cold}$. At each boundary of the piecewise polytropes, $\rho = \rho_i$, the pressure is required to be continuous, i.e., $K_i \rho_i^{\Gamma_i} = K_{i+1} \rho_i^{\Gamma_{i+1}}$. Read et al. (2009) determine these parameters in the following manner. First, they fix the EOS of the crust as $\Gamma_0 = 1.357$ and $K_0 = 3.594 \times 10^{13}$ in the cgs unit. Then they determine $\rho_2 = 1.85\rho_{\rm nucl}$ and $\rho_3 = 3.70\rho_{\rm nucl}$ where $\rho_{\rm nucl} = 2.7 \times 10^{14}$ g/cm^3 is the nuclear saturation density. With this preparation, they choose the following four parameters as a set of free parameters: $\{P_1, \Gamma_1, \Gamma_2, \Gamma_3\}$. Here P_1 is the pressure at $\rho = \rho_2$, and from this, K_1 and K_i are determined by $K_1 = P_1/\rho_2^{\Gamma_1}$ and $K_{i+1} = K_i \rho_i^{\Gamma_i - \Gamma_{i+1}}$. Therefore the EOS is specified by choosing the four parameters $\{P_1, \Gamma_1, \Gamma_2, \Gamma_3\}$.

In this work, we adopt 5 models of piecewise-polytropic EOS which describe the following EOSs based on nuclear theoretical calculations.

1. APR4: derived by a variational-method with the AV18 2-body potential, the UIX 3-body potential, and relativistic boost correction Akmal et al. 1998;
2. SLy: derived by using an effective potential approach of the Skyrme type (Douchin and Haensel 2001);
3. H4: derived by a relativistic mean-field approach including hyperons. The incompressibility, the effective mass, and the nucleon-meson coupling are chosen to be $K = 300$ MeV, $m_*/m_n = 0.72$, and $x_\sigma = 0.6$. Here m_n is the nucleon-mass (Lackey et al. 2006; Glendenning and Moszkowski 1991);
4. ALF2: a hybrid EOS which describes nuclear matter for a low density and color-flavor-locked quark matter for a high density. The transition density and the interaction parameter are chosen to be $\rho_c = 3\rho_{\rm nucl}$ and $c = 0.3$ (see Ref. (Alford et al. 2005));
5. MS: a relativistic mean-field approach. This EOS describes a neutron matter with pion condensation (Müller and Serot 1996).

Figure 8.1 plots the pressure as a function of the mass density for five piecewise polytropic EOSs as well as for Shen EOS.

In the numerical simulation, we used a modified version of the piecewise polytropic EOS to approximately take into account thermal effects. In this EOS, the pressure and specific internal energy are decomposed into cold and thermal parts as

$$P = P_{\rm cold} + P_{\rm th}\ ,\ \varepsilon = \varepsilon_{\rm cold} + \varepsilon_{\rm th}. \tag{4.38}$$

The cold parts of both variables are calculated using the original piecewise polytropic EOS from the primitive variable ρ, and then the thermal part of the specific internal energy is defined from ε as $\varepsilon_{\rm th} = \varepsilon - \varepsilon_{\rm cold}(\rho)$. Because $\varepsilon_{\rm th}$ vanishes in the absence of shock heating, it is regarded as the finite-temperature part determined by the shock heating in the present context. For the thermal part of the pressure and specific internal energy, a Γ-law ideal-gas EOS was adopted as

$$P_{\rm th} = (\Gamma_{\rm th} - 1)\rho\varepsilon_{\rm th}. \tag{4.39}$$

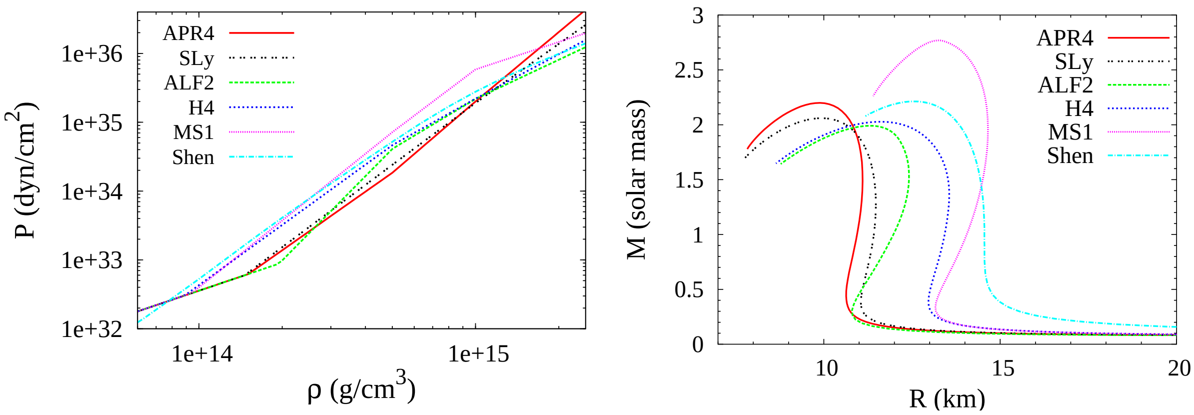

Figure 4.1: Pressure as a function of the mass density for six EOSs listed in Table 4.1 (left). Mass and radius of a cold-spherical neutron star for these EOSs (right). This figure is taken from Hotokezaka et al. (2013a)

Following the conclusion of a detailed study in Bauswein et al. (2010), $\Gamma_{\rm th}$ is chosen in the range $1.6-2.0$ with the canonical value 1.8. For several models, simulations were performed varying the value of $\Gamma_{\rm th}$ (see Table 6.1).

4.2.3 Artificial atmosphere

We put an artificial atmosphere of a small density outside of neutron stars because a vacuum is not allowed in any conservative hydrodynamics scheme. For instance, to obtain the velocity fields, the momentum density is divided by the density. An artificial atmosphere in numerical simulations should be as tenuous as possible, in order to avoid significant effects of the atmosphere on the motion of neutron stars and of ejected material from neutron stars. Here, we set the density profile of the atmosphere in the following rule

$$\rho_{\rm at} = \begin{cases} f_{\rm at}\ \rho_{\rm max} & (r \leq r_{\rm uni}), \\ f_{\rm at}\ \rho_{\rm max}(r/r_{\rm uni})^{-n} & (r \geq r_{\rm uni}), \end{cases} \tag{4.40}$$

where $\rho_{\rm max}$ denotes the maximum mass density of the neutron stars at the initial state $\lesssim 10^{15}$ g/cm^3. We typically set $f_{\rm at} = 10^{-10}$, $n = 3$, and $r_{\rm uni} = 16L_{min}$, where $2L_{\rm min}$ denotes the side length of the finest computational domain in the AMR algorithm. For MS1, a computational region is wider due to the large radii of neutron stars, and thus, we set $f_{\rm at} = 10^{-11}$ in order to reduce the total mass of the atmosphere. In there setting, the total mass of the atmosphere is less than $\sim 10^{-6}M_\odot$ or less for all cases. Such a value is less than the typical value of ejecta mass, which will be focused in Chap. 7

4.3 Initial data

4.3.1 Initial data of gravitational filed

We prepare NS–NS systems in quasi-equilibrium states for the initial condition of numerical simulations by using a spectral-method library, LORENE*. For solving constraint equations for the induced metric γ_{ij} and extrinsic curvature K_{ij}, the conformal thin-sandwich method is adopted. In this formalism, a certain time evolution is taken into account by specifying the time derivative of the conformal induced metric.

First, the induced metric γ_{ij} and the traceless part of the extrinsic curvature A_{ij} are conformally decomposed as

$$\gamma_{ij} = \psi^4 \hat{\gamma}_{ij}, \tag{4.41}$$

$$A^{ij} = \psi^{-10} \hat{A}^{ij}, \tag{4.42}$$

where ψ is the conformal factor. In conformally thin-sandwich formalism, a new variable $\hat{u}_{ij}$ is defined by

$$\hat{u}_{ij} \equiv \partial_t \hat{\gamma}_{ij}. \tag{4.43}$$

Using this valiable, $\hat{A}_{ij}$ can be rewritten as

$$\hat{A}^{ij} = \frac{\psi^6}{2\alpha}\left((\hat{L}\beta)^{ij} - \hat{u}^{ij}\right). \tag{4.44}$$

We describe the Hamiltonian and momentum constraints in terms of $\hat{u}_{ij}$ and β^i instead of $\hat{A}_{ij}$. ψ is solved by the Hamiltonian constraint as

$$\hat{D}^2\psi = \frac{1}{8}\hat{R} + \frac{1}{12}\psi^5 K^2 - \frac{1}{8}\psi^{-7}\hat{A}_{ij}\hat{A}^{ij} - 2\pi\psi^5\rho_{\mathrm{H}}, \tag{4.45}$$

$\hat{D}$ is the covariant derivative associated with $\hat{\gamma}_{ij}$ and $\hat{R}$ is the scalar curvature associated with $\hat{\gamma}_{ij}$. The momentum constraint becomes an elliptic equation of the shift vector as

$$\hat{D}_j(\hat{L}\beta)^{ij} - (\hat{L}\beta)^{ij}\hat{D}_j(\alpha\psi^{-6}) = \frac{4}{3}\alpha\hat{D}^i K + \alpha\psi^{-6}\hat{D}_j\left(\frac{\psi\hat{u}_{ij}}{\alpha}\right) + 16\pi\alpha\psi^4 j^i, \tag{4.46}$$

where

$$(\hat{L}\beta)^{ij} \equiv \hat{D}^i\beta^j + \hat{D}^j\beta^i - \frac{2}{3}\hat{\gamma}^{ij}\hat{D}_k\beta^k. \tag{4.47}$$

By using the evolution equation of K and specifying $\partial_t K$, we obtain an elliptic equation of $\alpha\psi$ as

$$\hat{D}^2(\alpha\psi) = \frac{1}{8}\alpha\psi\hat{R} + \frac{5}{12}\alpha\psi^{-3}K^2 + \frac{7}{8}\alpha\psi^{-7}\hat{A}_{ij}\hat{A}^{ij} - \psi^5(\partial_t - \pounds_\beta)K + 2\pi\alpha\psi^5(\rho_{\mathrm{H}} + 2S). \tag{4.48}$$

*LORENE webpage: http://www.lorene.obspm.fr/

Once the above equations is solved, one can obtain the conformally-weighted transverse traceless part of the extrinsic curvature via Eq. (4.44).

For initial value problem, four varaibles are determined by solving the four constraint equations and other variables are freely specifiable. In this formalism, there are 16 variables ($\hat{\gamma}_{ij},\ \hat{u}_{ij},\ K,\ \alpha,\ \beta^i,\ \psi$) in the constraint equations. In the original conformal thin-sandwich formalism, ($\hat{\gamma}_{ij},\ \hat{u}_{ij},\ K,\ \psi^6\alpha$) are chosen as a freely specifiable variables. ψ and β^i are determined by the Hamiltonian constraint and momentum constraint. In the extended conformal thin-sandwich formalism, $\partial_t K$ is chosen to be a freely specifiable variable instead of $\psi^6\alpha$. This version of the formalism is useful to construct quasiequilibrium configurations, such as initial data of an NS–NS system. Then we can adopt the conformally flat approximation $\hat{\gamma}_{ij} = f_{ij}$, the maximal slicing condition $K = 0$, and the preservation of them in time $\hat{u}_{ij} = 0$ and $\partial_t K = 0$, where f_{ij} is the flat metric. This choice the freely specifiable variables simplifies the constraint equations.

4.3.2 Initial data of hydrodynamical quantities

In order to construct initial data of an NS–NS quisi-equiribrium state, one has to compute hydrostationary configuration, which is associated with a helical symmetry. The helical Killing vector can be written as

$$\xi^\mu = \alpha n^\mu + \beta^\mu_{\rm rot}, \tag{4.49}$$

where $\beta^\mu_{\rm rot} = \beta^\mu + \Omega(\partial_\phi)^\mu$ and Ω is the angular frequency of a binary. For isentropic fluid, the conservation laws of fluids Eqs. (4.17) with the helical Killing vector can be rewritten as

$$D_i\left(\frac{h}{u^t} + \hat{u}_j V^j\right) + V^j(D_j\hat{u}_i - D_i\hat{u}_j) = 0, \tag{4.50}$$

$$D_i(\alpha u^t \rho V^i) = 0, \tag{4.51}$$

where D_i is the covariant derivative associated with γ_{ij}, $V^i = \gamma^i_a V^a$ is defined by the decomposition of the four vector as $u^a = u^t(\xi^a + V^a)$.

We further assume an irrotational binary, for which the vorticity of the fluid vanishes. Such a configuration is thought to be an astrophysically realistic configuration (Bildsten and Cutler 1992; Kochanek 1992). The vorticity tensor in general relativity is defined as

$$\omega_{ab} \equiv \gamma^\nu_a \gamma^\mu_b \left(\nabla_\mu h u_\nu - \nabla_\nu h u_\mu\right). \tag{4.52}$$

For fluid that satisfies $\omega_{ab} = 0$, one can introduce a velocity potential $\nabla_a\Phi = hu_a$. One can integrate Eq. (4.50) as

$$\frac{h}{u^t} + \hat{u}_j V^j = C, \tag{4.53}$$

where C is an integration constant. Using $u_a u^a = -1$, Eq. (4.53), and Eq. (4.51), one finally obtains

$$h^2 - \frac{1}{\alpha^2}\left(C + \beta^i_{\rm rot} D_i \Phi\right)^2 - D_i \Phi D^i \Phi = 0, \tag{4.54}$$

$$D_i D^i \Phi - D_i \left(\frac{C + \beta^j_{\rm rot} D_j \Phi}{\alpha^2} \beta^i_{\rm rot} \right) - \left(\frac{C + \beta^j_{\rm rot} D_j \Phi}{\alpha^2} \beta^i_{\rm rot} - D^i \Phi \right) D_i \ln \left(\frac{\alpha \rho}{h} \right) \tag{4.55}$$

These two equations determine h and Φ with a boundary condition at the stellar surface

$$\left(\frac{C + \beta^j_{\rm rot} D_j \Phi}{\alpha^2} \beta^i_{\rm rot} - D^i \Phi \right) D_i \rho = 0. \tag{4.56}$$

We choose the two different initial conditions with the different initial angular velocities. For the study of late inspiral phase, the orbital angular velocity of the initial configuration is chosen to be $M\omega_0 = 0.019$ ($f = 400$Hz for $M = 2.7 M_\odot$) in order to track more than 8 orbits. For the study of post-merger phases and mass ejection, the angular velocity of the initial configuration is chosen to be $M\omega_0 = 0.0221$.

4.3.3 Setup of AMR grids

An adaptive-mesh refinement (AMR) algorithm implemented in SACRA can prepare a fine-resolution domain in the vicinity of compact objects as well as a sufficiently wide domain that covers a local wave zone. The chosen AMR grids consist of a number of computational domains, each of which has the uniform, vertex-centered Cartesian grids with $(2N+1, 2N+1, N+1)$ grid points for (x, y, z) with the equatorial plane symmetry at $z = 0$. Since we chose that the grid spacing for three directions is identical, the shape of each AMR domain is a half cube. We chose $N = 60$ for the best resolved runs in this work, and all the results shown in the following were obtained with this resolution. We also performed simulations with smaller grid resolutions in order to check the convergence of the results.

We classify the domains of the AMR algorithm into two categories: one is a coarser domain, which covers a wide region including both neutron stars with its origin fixed at the approximate center of mass throughout the simulation. The other is a finer domain, two sets of which comove with two neutron stars and cover the region in their vicinity. We denote the side length of the largest domain, number of the coarser domains, and number of the finer domains by $2L$, l_c, and $2l_f$, respectively. For the simulations of Chap. **??**, $l_c = 3$ and $l_f = 4$. For the simulations of Chap. 6–Chpa. **??**, $l_c = 5$ and $l_f = 4$. The grid spacing for each domain is $h_l = L/(2^l N)$, where $l = 0 - l_{\rm max} (= l_c + l_f - 1)$ is the depth of each domain. In the following, we denote $L/2^{l_{\rm max}}$ by $L_{\rm min}$ and $h_{l_{\rm max}}$ by Δx.

Table 6.1 summarizes the parameters of the grid structure for the simulations of Chap. 6–**??**. For all the simulations, we chose $(l_c, l_f) = (5, 4)$, and L to be as $L/c \gtrsim 10$ ms. This implies that the material cannot escape from the computational domain in ~ 10 ms after the onset of the merger, even if it could move with the speed of light. In reality, the speed of most of the ejected material is smaller than $\sim 0.5c$, and thus, the material stays in the second coarsest level for more than 10 ms. L is also much larger than the gravitational wavelengths at the initial instant $\lambda_0 := \pi/\omega_0$. This implies that a spurious effect caused by outer boundaries when extracting gravitational waves is excluded in the present work more efficiently than in the previous works. The semi-major diameter of each neutron star is covered approximately by 100 grid points for $N = 60$.

4.4 Diagnoistic tools for numerical-data analysis

4.4.1 Mass, linear momenta, and angular momentum

We monitor the ADM mass $M_{\rm ADM}$, the linear momentum P_i, and the angular momenta J_i during the evolution. These parameters are defined by the integrals on two surfaces of a coordinate radius

$$M_{\rm ADM}(r) = \frac{1}{16\pi}\int_r \sqrt{\gamma}\gamma^{ij}\gamma^{kl}(\gamma_{ik,j} - \gamma_{ij,k})dS_l, \tag{4.57}$$

$$P_i(r) = \frac{1}{8\pi}\int_r \sqrt{\gamma}(K_i^j - K\gamma_i^j)dS_j, \tag{4.58}$$

$$J_i(r) = \frac{1}{8\pi}\epsilon_{ikl}\int_r \sqrt{\gamma}x^l(K^{jk} - K\gamma^{jk})dS_j, \tag{4.59}$$

where dS_l is the surface element and ϵ_{ijk} is the Levi-Civita symbol. Then, we extrapolate these quantities for $r \to \infty$ to obtain the asymptotic value.

We also monitor the total baryon mass

$$M_* = \int \rho u^t \sqrt{-g} d^3x, \tag{4.60}$$

where u^t is the time-component of the four velocity, and g is the determinant of the space-time metric. After the black hole formation, we calculate the torus mass defined by

$$M_{\rm torus} = \int_{r>r_{\rm AH}} \rho u^t \sqrt{-g} d^3x, \tag{4.61}$$

where $r_{\rm AH}$ is the coordinate radius of the apparent horizon.

4.4.2 Mass, energy, and moment of inertia of ejecta

To study dynamical mass ejection from an NS–NS merger, we define the followings quantities. Here, the ejected material is composed of a fluid element which is unbound by the gravitational potential of NS–NSs and an object formed after the merger. Thus, first of all, we have to determine which fluid elements are unbound. To assess this point for all the fluid elements, we calculate $u_\mu t^\mu = u_t$ at each grid point. Here, t^μ is a timelike vector

Table 4.2: List of the parameters of the initial condition for binaries chosen in numerical simulations: Total mass, mass ratio, masses of two components, initial value of angular velocity, and grid spacing Δx.

Model	$M(M_\odot)$	q	$M_A(M_\odot)$	$M_B(M_\odot)$	$M\omega_0$	Δx (km)
APR4-130160	2.90	0.813	1.30	1.60	0.026	0.172
APR4-140150	2.90	0.933	1.40	1.50	0.026	0.167
APR4-145145	2.90	1.000	1.45	1.45	0.026	0.166
APR4-130150	2.80	0.867	1.30	1.50	0.026	0.172
APR4-140140	2.80	1.000	1.30	1.50	0.026	0.167
APR4-120150	2.70	0.800	1.20	1.50	0.026	0.172
APR4-125145	2.70	0.862	1.25	1.45	0.026	0.174
APR4-130140	2.70	0.929	1.30	1.40	0.026	0.170
APR4-135135	2.70	1.000	1.35	1.35	0.026	0.169
APR4-120140	2.60	0.857	1.20	1.40	0.026	0.174
APR4-125135	2.60	0.926	1.25	1.35	0.026	0.174
APR4-130130	2.60	1.000	1.30	1.30	0.026	0.171
SLy-140140	2.80	1.000	1.40	1.40	0.026	0.174
SLy-120150	2.70	0.800	1.20	1.50	0.026	0.182
SLy-125145	2.70	0.862	1.25	1.25	0.026	0.181
SLy-130140	2.70	0.929	1.30	1.40	0.026	0.181
SLy-135135	2.70	1.000	1.35	1.35	0.026	0.177
SLy-130130	2.60	1.000	1.30	1.30	0.026	0.181
ALF2-140140	2.80	1.000	1.40	1.40	0.026	0.195
ALF2-120150	2.70	0.800	1.20	1.50	0.026	0.200
ALF2-125145	2.70	0.862	1.25	1.25	0.026	0.199
ALF2-130140	2.70	0.929	1.30	1.40	0.026	0.198
ALF2-135135	2.70	1.000	1.35	1.35	0.026	0.195
ALF2-130130	2.60	1.000	1.30	1.30	0.026	0.199
H4-130150	2.80	0.867	1.30	1.50	0.025	0.222
H4-140140	2.80	1.000	1.40	1.40	0.025	0.219
H4-120150	2.70	0.800	1.20	1.50	0.025	0.228
H4-125145	2.70	0.862	1.25	1.25	0.025	0.226
H4-130140	2.70	0.929	1.30	1.40	0.025	0.223
H4-135135	2.70	1.000	1.35	1.35	0.025	0.221
H4-120140	2.60	1.000	1.30	1.30	0.025	0.230
H4-125135	2.60	1.000	1.30	1.30	0.025	0.227
H4-130130	2.60	1.000	1.30	1.30	0.025	0.223
MS1-140140	2.80	1.000	1.40	1.40	0.025	0.237
MS1-120150	2.70	0.800	1.20	1.50	0.025	0.249
MS1-125145	2.70	0.862	1.25	1.25	0.025	0.244
MS1-130140	2.70	0.929	1.30	1.40	0.025	0.244
MS1-135135	2.70	1.000	1.35	1.35	0.025	0.242
MS1-130130	2.60	1.000	1.30	1.30	0.025	0.244

$(1,0,0,0)$ which is a Killing vector at spatial infinity. If $|u_t| > 1$, we consider that the fluid element there is unbound.

Then we calculate the total mass, total energy (excluding gravitational potential energy), and total internal energy of the fluid element of $|u_t| > 1$ by

$$
\begin{aligned}
M_{*\mathrm{esc}} &= \int_{|u_t|>1} \rho_* d^3x, &(4.62)\\
E_{\mathrm{tot,esc}} &= \int_{|u_t|>1} T_{\mu\nu} n^\mu n^\nu \sqrt{\gamma} d^3x \\
&= \int_{|u_t|>1} \rho_* e_* d^3x, &(4.63)\\
U_{\mathrm{esc}} &= \int_{|u_t|>1} \rho_* \varepsilon d^3x, &(4.64)
\end{aligned}
$$

where $T_{\mu\nu}$ is the stress-energy tensor,

$$T_{\mu\nu} = \rho h u_\mu u_\nu + P g_{\mu\nu}, \tag{4.65}$$

and n^μ is the unit timelike hypersurface normal. We note that the total energy is not uniquely defined by $E_{\mathrm{tot,esc}}$ for dynamical spacetimes, and thus, the total energy defined here should be considered as an approximate measure for it. We here choose this expression for simplicity. We then define kinetic energy approximately by

$$T_{*\mathrm{esc}} := E_{\mathrm{tot,esc}} - M_{*\mathrm{esc}} - U_{\mathrm{esc}}. \tag{4.66}$$

To approximately analyze the configuration of the ejected material, we also calculate the moments of inertia defined by

$$I_{ii,\mathrm{esc}} = \int_{|u_t|>1} \rho_* (x^i)^2 d^3x, \quad \text{(no sum for } i\text{)}, \tag{4.67}$$

and then, define

$$\bar{X} = \sqrt{\frac{I_{xx,\mathrm{esc}}}{M_{*\mathrm{esc}}}}, \quad \bar{Y} = \sqrt{\frac{I_{yy,\mathrm{esc}}}{M_{*\mathrm{esc}}}}, \quad \bar{Z} = \sqrt{\frac{I_{zz,\mathrm{esc}}}{M_{*\mathrm{esc}}}}, \tag{4.68}$$

and $\bar{R} = \sqrt{\bar{X}^2 + \bar{Y}^2}$. From $d\bar{R}/dt$ and $d\bar{Z}/dt$, we can determine the typical (average) velocity of the ejected material, which is denoted by $\bar{V}^R_{\mathrm{esc}}$ and $\bar{V}^Z_{\mathrm{esc}}$ in the following.

We consider a model that the configuration of the ejected material is approximated by an axisymmetric anisotropic shell of uniform density as

$$\rho = \begin{cases} \rho_{\mathrm{esc}} & \pi/2 - \theta_0 \le \theta \le \pi/2 + \theta_0 \\ & \quad \text{and } R_- \le r \le R_+, \\ 0 & \text{otherwise,} \end{cases} \tag{4.69}$$

where $\rho_{\rm esc}$, $R_\pm$, and θ_0 are time-varying parameters. In this case,

$$\begin{aligned} M_{*\rm esc} &= \frac{4\pi}{3}\rho_{\rm esc}(R_+^3 - R_-^3)\sin\theta_0, && (4.70)\\ \bar{R}^2 &= \frac{1}{5}\frac{R_+^5 - R_-^5}{R_+^3 - R_-^3}(3-\sin^2\theta_0), && (4.71)\\ \bar{Z}^2 &= \frac{1}{5}\frac{R_+^5 - R_-^5}{R_+^3 - R_-^3}\sin^2\theta_0. && (4.72)\end{aligned}$$

Thus for an axial ratio,

$$\eta_R = \frac{\bar{Z}}{\bar{R}}, \tag{4.73}$$

$\sin\theta_0$ is calculated as

$$\sin^2\theta_0 = \frac{3\eta_R^2}{1+\eta_R^2}. \tag{4.74}$$

Hence, from the axial ratio calculated for a numerical result of the ejected material, we can approximately define the extent in the θ direction; e.g., for $\eta_R = 0.4$ and 0.5, $\theta_0 \approx 40^\circ$ and 51°, respectively.

4.4.3 Extraction of gravitational waves

Gravitational waves are extracted by calculating the complex Weyl scalar Ψ_4 (Yamamoto et al. 2008) from which gravitational waveforms are determined by

$$h_+(t) - ih_\times(t) = -\lim_{r\to\infty}\int^t dt'\int^{t'} dt''\Psi_4(t'', r). \tag{4.75}$$

Here we omit arguments θ and ϕ. In the spherical coordinate (r, θ, ϕ), Ψ_4 can be expanded in the form

$$\Psi_4(t, r, \theta, \phi) = \sum_{lm}\Psi_4^{lm}(t, r)_{-2}Y_{lm}(\theta, \phi), \tag{4.76}$$

where ${}_{-2}Y_{lm}$ are spin-weighted spherical harmonics of weight -2 and Ψ_4^{lm} are expansion coefficients defined by this equation. In this work, we focus only on the $(l, |m|) = (2, 2)$ mode. The gravitational-wave phase $\phi_{\rm NR}$ is defined by

$$\Psi_4^{22}(t, r) = A_{22}(t, r)e^{i\phi_{\rm NR}(t,r)}, \tag{4.77}$$

where A_{22} denotes the amplitude and it is real. We evaluate Ψ_4 at a finite spherical-coordinate radius $r/M_\odot = 200$, 240, 300, and 400. To compare the waveforms extracted at different radii, we use the retarded time defined by

$$t_{\rm ret} = t - r_*. \tag{4.78}$$

Here, r_* is the tortoise coordinate defined by

$$r_* = r_{\rm A} + 2M\ln\left(\frac{r_{\rm A}}{2M} - 1\right), \tag{4.79}$$

where $r_{\rm A} = \sqrt{A/4\pi}$ with A being the proper surface area of the extraction sphere.

Chapter 5

Tidal effects in late stage of binary neutron star inspiral

We have discussed the analytic formulations for the orbital motion of compact binary systems in Chap. 2. These formulations break down in the late inspiral stage due to strong gravity. Furthermore, the late stage of an NS–NS inspiral ($f_{\rm GW} > 400$ Hz), nonlinear hydrodynamical effects play a crucial role for the evolution of the system (Lai et al. 1994). In addition, higher-PN tidal corrections may yield a pole-like behavior of the tidal interactions near the last unstable orbit (Bini et al. 2012). For better understanding of the precise motion and the waveforms in this late inspiral stage, numerical-relativity simulations are probably the best approach. Before proceeding with the detailed studies, we briefly mention the current status of this research field.

Recently, long-term simulations for NS–NS inspirals were performed by three groups (Baiotti et al. 2011; Thierfelder et al. 2011; Hotokezaka et al. 2011) aiming at the derivation of accurate gravitational waveforms for the late inspiral stage. Baiotti et al. (2010, 2011) performed numerical-relativity simulations employing a Γ-law EOS and compared the resulting waveforms of the *highest* resolution simulation with the analytic models calculated in the EOB and Taylor T4 formalisms. They suggested that the tidal effects might be significantly amplified by higher-PN tidal corrections even in the early inspiral phase.

Bernuzzi et al. (2012b,a) performed numerical-relativity simulations with Γ-law EOS ($\Gamma = 2$, and the compactness of a neutron star is 0.14). In Bernuzzi et al. (2012b), they studied the convergence of the numerical results for NS-NS inspirals. They concluded that the convergence of the simulation is second order up to contact. They also compared the resulting *extrapolated* waveform with that of the Taylor T4 formalism for the point-particle approximation and for including the tidal corrections. They found that the accumulated phase difference is about 1.5 radian at contact for a particular model of the NS–NS binary. In the subsequent paper (Bernuzzi et al. 2012a), they compared the waveform derived by the *highest* resolution simulation with the waveform calculated in the EOB formalism. They found that the EOB formalism including tidal corrections up to the next-to-next-to leading order is currently the most robust way to describe the waveform of NS–NS inspirals. In addition, they excluded the huge amplification of the tidal corrections suggested in Baiotti et al. (2011).

In this chapter, we study NS–NS inspirals by numerical-relativity simulations with three different EOSs and compare the *extrapolated* NR waveforms with those calculated in the EOB and Taylor T4 formalisms. Here we extrapolate numerical data with a new extrapolation procedure, the time and phase extrapolation. For studying the dependence of the tidal effects on the neutron-star matter EOS, we employ a piecewise-polytropic EOS of Read et al. (2009), which can approximately describe the EOS based on nuclear theoretical calculations and more realistic than Γ-law EOS adopted in Baiotti et al. (2011); Bernuzzi et al. (2012b,a). In this chapter, (i) we obtain the physical gravitational-wave phase by extrapolation; (ii) we then compare the *extrapolated* waveforms with those of the analytic models calculated in the Taylor T4 and EOB formalisms; (iii) we clarify the tidal effects on the gravitational-wave phase and show the validity of the analytic modeling in the late inspiral phase.

5.1 Data analysis of numerical-relativity simulations

The extrapolation with respect to the extraction radius and grid resolution plays a key role to obtain the physical waveforms in NS–NS inspirals from the results of numerical relativity simulations (see Table 5.1 for the initial conditions). Here, we focus in particular on deriving the accurate gravitational-wave phase by extrapolation because it carries the most important information in the matched filtering for data analysis. Thus, the goal of this section is to construct the extrapolated gravitational-wave phase.

5.1.1 Extrapolation to infinity

Because gravitational waves are extracted at finite radii (see Sec. 4.4.3), the extracted waveform does not fully agree with the waveform at infinity. In order to obtain the gravitational-wave phase at infinity, we first estimate the error due to the finite-radii extraction and then to extrapolate the gravitational-wave phase to infinity. For this purpose, we assume that the gravitational-wave phase is described by a polynomial Boyle et al. (2007),

$$\phi(t_{\rm ret}, r) = \phi^{(0)}(t_{\rm ret}) + \sum_{i=1}^{s} \frac{\phi^{(i)}(t_{\rm ret})}{r^i}. \tag{5.1}$$

Here, $\phi^{(0)}(t_{\rm ret})$ is considered to be the gravitational-wave phase extrapolated at $r \to \infty$, and $(s+1)$ is the number of extraction radii used. We determine it by extrapolating the gravitational-wave phases extracted at $r/M_\odot = 200,\ 240,\ 300,$ and 400.

Table 5.1: Key parameters for the initial models adopted in the present numerical simulation. M is the sum of the ADM masses of two neutron stars in isolation; ν is the symmetric mass ratio; M_0^{ADM} and J_0^{ADM} are the ADM mass and angular momentum of the system, respectively; M_* is the baryon mass; ω_0 is the angular velocity. We also show the setup of the grid structure of our AMR algorithm. $\Delta x = h_6 = L/(2^6 N)$ $(N = 60)$ is the grid spacing for the highest-resolution domain with L being the location of the outer boundaries for each axis. N specifies the grid size of the simulation with maximum $N = 60$. κ_2 is the parameter related to the tidal deformability. $\omega_{\mathrm{contact}}$ is the orbital angular velocity at contact of the two neutron stars (see Sec. V. B). Here we use the unit $M_\odot = 1$

Model	M	ν	M_0^{ADM}	J_0^{ADM}	M_*	$M\omega_0$	$\Delta x/M$	κ_2	$M\omega_{\mathrm{contact}}$	N
APR4	2.7	0.25	2.68	7.65	3.00	0.019	0.0438	62.3	0.151	(42,48,54,60)
H4	2.7	0.25	2.68	7.66	2.94	0.019	0.0560	215	0.112	(42,48,54,60)
MS1	2.7	0.25	2.68	7.67	2.92	0.019	0.0595	332	0.103	(42,48,54,60)
APR4-1215	2.7	0.24691358	2.68	7.28	3.01	0.0221	0.0438	65.8	0.151	(40,50,60)
H4-1215	2.7	0.24691358	2.68	7.56	2.94	0.019	0.0560	207	0.114	(40,50,60)

Figure 5.1 shows the differences among the hypothetically extrapolated gravitational-wave phases at infinity obtained by different numbers of extrapolation radius labeled by s. The curves labeled by $1 - 3(= s - 1)$ in Fig. 5.1 denote the differences between a radius-extrapolated gravitational-wave phase with the $(s - 1)$-th order polynomial and that with the s-th order one. Here, we set the phase difference to be zero at the merger. Note that the difference between the $(s-1)$-th and s-th order extrapolated gravitational-wave phases accumulates mainly just after the contact of the two stars and its value is less than about 0.5 radian. In this work, we do not pay attention to the gravitational-wave phase after contact of the two stars. As shown in the next subsection, furthermore, this accumulated gravitational-wave phase difference of the radius extrapolation is much smaller than the magnitude of other error sources. Therefore, here, we neglect the phase error associated with the finite-radius extraction, and use the resolution-extrapolated gravitational-wave phase with the extracted radius $r/M_\odot = 400$ as the extrapolated wave phase. We note however that in a high-resolution study, the error associated with the finite-radius extraction could be comparable to or smaller than the error due to the finite grid resolution.

5.1.2 Extrapolation to infinite resolution

A numerical waveform is derived as a solution of discretized Einstein's equations and hydrodynamics equations. Associated with the finite differencing, a truncation error

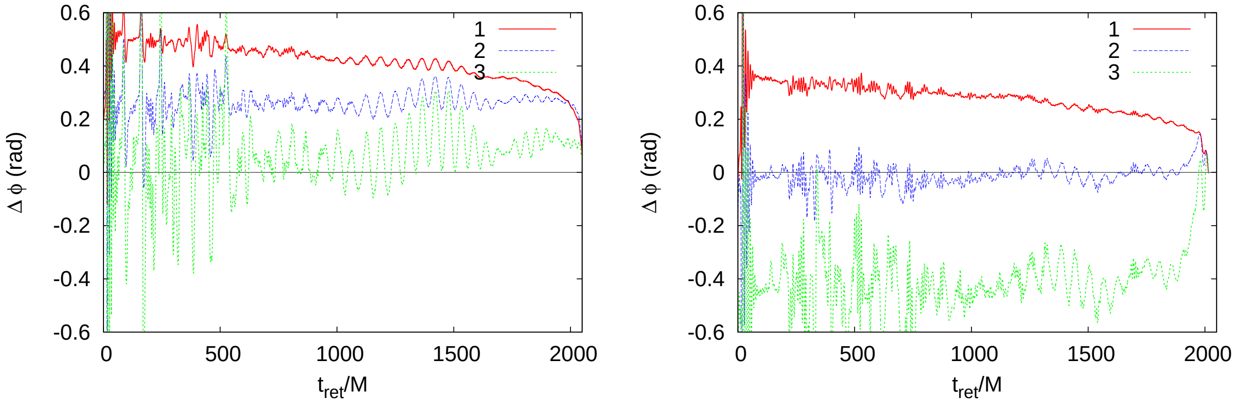

Figure 5.1: The phase errors for APR4 (left) and H4 (right). The curve 1 denotes the difference between the gravitational-wave phase extracted at $r/M_\odot = 400$ and an extrapolated gravitational-wave phase obtained using the data at $r/M_\odot = 300$ and 400. The curve 2 denotes the difference between the extrapolated gravitational-wave phase obtained using the data at $r/M_\odot = 300$ and 400 and that obtained using the data at $r/M_\odot = 240,\ 300$, and 400. The curve 3 denotes the difference between the extrapolated gravitational-wave phase obtained using the data at $r/M_\odot = 240,\ 300,$ and 400 and that obtained using the data at $r/M_\odot = 200,\ 240,\ 300,$ and 400. This figure is taken from Hotokezaka et al. (2013c).

is yielded. For the purpose of comparing the numerical waveform with the analytical waveforms, we have to obtain a hypothetically physical waveform by extrapolating the numerical waveform obtained in the finite grid resolution for the limit of the infinite grid resolution. The order of the convergence of our NR simulation with respect to the grid spacing is found to be about 1.8. Because the order of the convergence has an uncertainty, we conservatively assume that the order of the convergence is $1.8{\pm}0.2$ in the following (see also Bernuzzi et al. 2012b).

For understanding the convergence property of the numerical results, we check the convergence for the evolution of the gravitational-wave frequency performing simulations with four different grid resolutions (see Fig. 5.2 for gravitational-wave angular velocity). Here, we refer to the data for $N = (42, 48, 54, 60)$ as (A, B, C, D). Although the gravitational-wave frequencies agree with each other at $t_{\rm ret} = 0$, their subsequent evolution disagrees with each other. Obviously, the gravitational-wave frequency in the lower grid resolution evolves more rapidly than that in the higher grid resolution. The rapid evolution for the lower-resolution simulations may be ascribed to larger numerical dissipation of the angular momentum.

One can find the similarity among four curves of the gravitational-wave frequency for the different grid resolutions and this enables us to obtain an extrapolated waveform. To show this similarity, we normalize the time variable by using the time at the onset of the

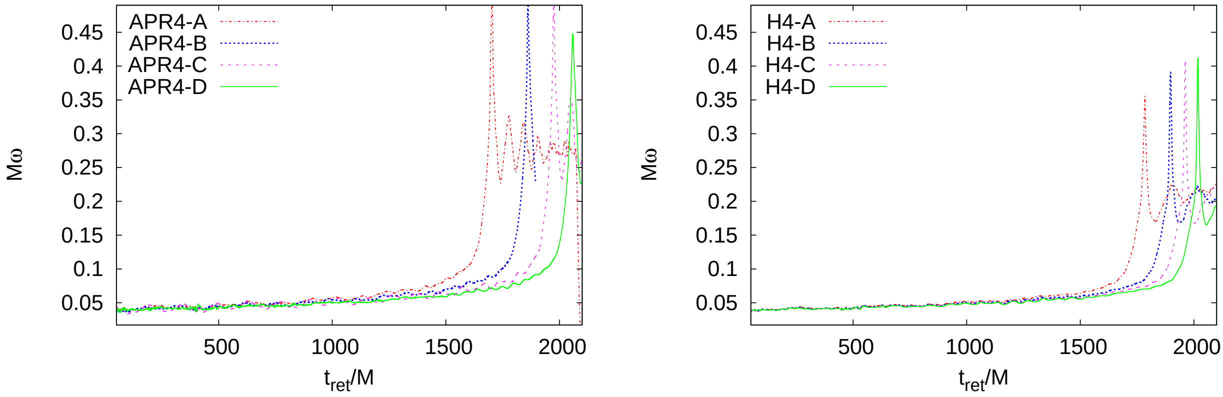

Figure 5.2: The evolution of gravitational-wave angular velocity for four different resolutions for APR4 (left panel) and H4 (right panel). The curves with marks A, B, C, and D denote the results for the simulations with $N = (42, 48, 54, 60)$, respectively. This figure is taken from Hotokezaka et al. (2013c).

merger, which is defined by $t_m(\Delta x) = t|_{\omega_{\max}}(\Delta x)$:

$$t \to \tilde{t}(t) = \frac{t}{\Lambda(\Delta x)}. \tag{5.2}$$

Here, $\Lambda(\Delta x) = t_m(0)/t_m(\Delta x)$, Δx is the grid spacing of the simulation ($\propto N^{-1}$), and $t_m(0)$ is the extrapolated merger time. For obtaining the extrapolated merger time, we assume that the merger time as a function of grid resolutions is described by a binomial

$$t_m(\Delta x) = t_m(0) + K(\Delta x)^n, \tag{5.3}$$

where $t_m(0)$, n, and K are constants which are determined by the least-square fitting method. We find that the best fitted value of n is ≈ 1.8 with a dispersion ~ 0.2, and thus, we set the order of the convergence n is to be 1.8 ± 0.2. The resulting fitted values for $n = (1.6, 1.8, 2.0)$ are $t_m(0) = (2521M, 2452M, 2397M)$ for APR4, $t_m(0) = (2391M, 2274M, 2238M)$ for H4, and $t_m = (2145M, 2145M, 2091M)$ for MS1. We define the rescaled gravitational-wave frequency by

$$\tilde{\omega}(t, \Delta x) \equiv \omega(\tilde{t}(t), \Delta x). \tag{5.4}$$

The evolution curves of the rescaled gravitational-wave frequency $\tilde{\omega}$ for the different grid resolutions agree with each other, as shown in the upper two panels of Fig. 5.3 (here, we set $n = 1.8$). The differences among the rescaled gravitational-wave frequencies of the different grid resolutions are within $\sim 10\%$ for APR4 and $\sim 5\%$ for H4, as shown in the lower panels of Fig. 5.3. Therefore, we conclude that the numerical results for the gravitational-wave frequency (angular velocity) is written in the form

$$\tilde{\omega}(t, \Delta x) = \tilde{\omega}(t, 0) + \omega_{\rm r}(t, \Delta x), \tag{5.5}$$

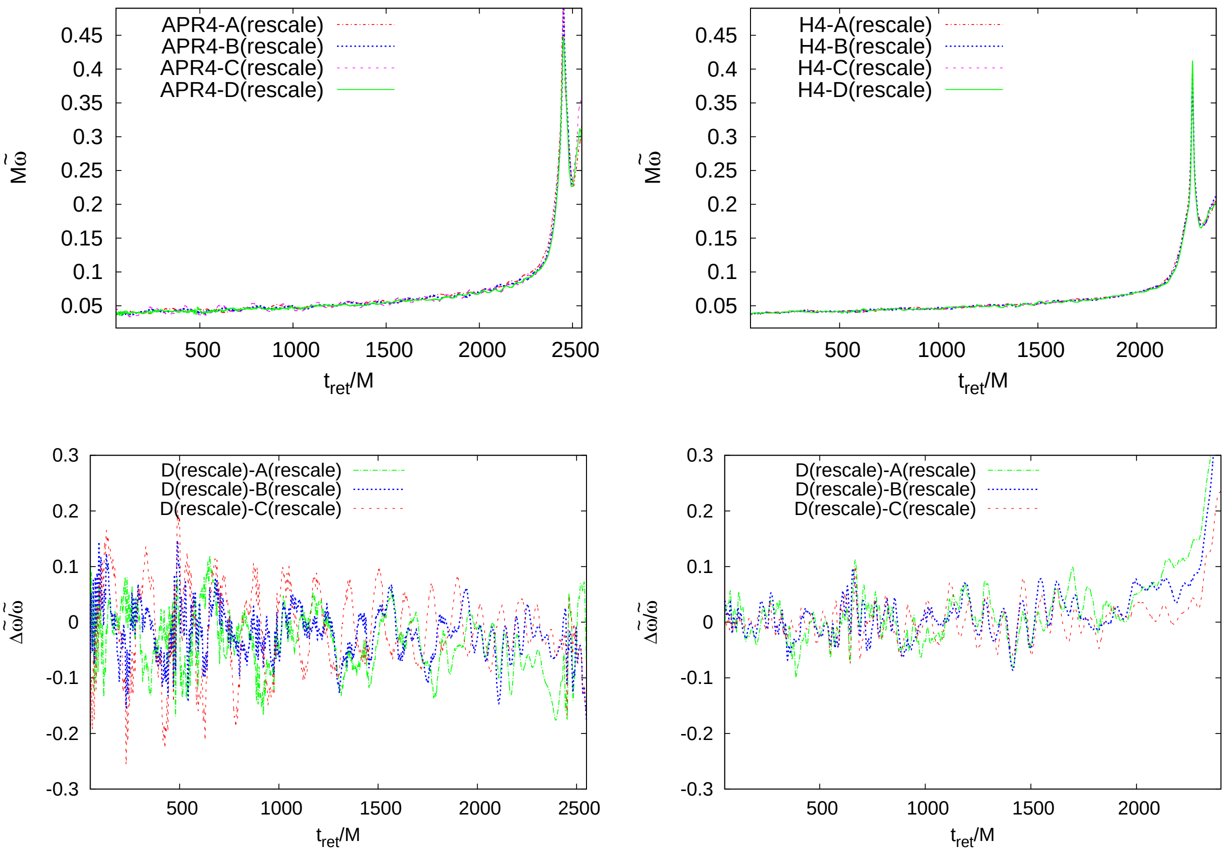

Figure 5.3: Convergence of the rescaled gravitational-wave angular velocity. *Upper panels*: the evolution curves of the rescaled gravitational-wave angular velocity for APR4 (left panel) and H4 (right panel). *Lower panels*: the difference in the rescaled gravitational-wave frequency between different resolutions for APR4 (left panel) and H4 (right panel). Here we choose $n = 1.8$. This figure is taken from Hotokezaka et al. (2013c).

where $\omega_{\rm r}(t, \Delta x)$ is a function that depends on the grid resolution, which should have been eliminated systematically by extrapolation. However, because the value of $\omega_{\rm r}(t, \Delta x)$ randomly fluctuates, it cannot be eliminated by extrapolation at each given moment as shown in lower panels in Fig. 5.3. Thus, the extrapolated gravitational-wave frequency can be only approximately obtained by simply rescaling the time variable of the simulations.

We proceed to extrapolate the rescaled gravitational-wave phase, which will be compared with the gravitational-wave phases derived in the PN and EOB approaches in the next section. We define the rescaled gravitational-wave phase as

$$\tilde{\phi}(t, \Delta x) \equiv \int_0^t \tilde{\omega}(t', \Delta x) dt'. \tag{5.6}$$

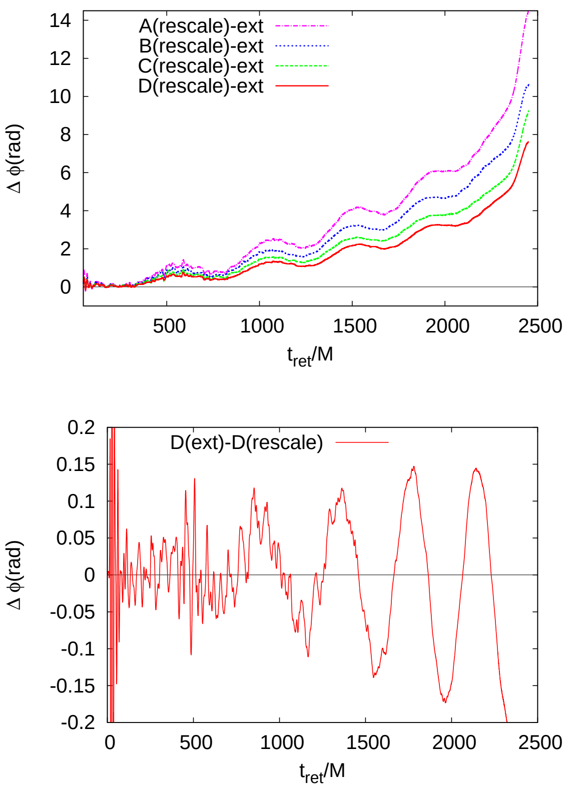

Figure 5.4: Convergence of the gravitational-wave phase for APR4 (left) and H4 (right). In the upper panels, the curves show the phase differences between the extrapolated gravitational-wave phase and the rescaled numerical results. Here, we set the order of the convergence n to be 1.8 for deriving the extrapolated gravitational-wave phase. In the lower panels, the curves show the difference between the rescaled gravitational-wave phase in the resolution D and the extrapolated gravitational-wave phase which is obtained by extrapolating the rescaled gravitational-wave phases of the resolution A, B, and C to the resolution D. This figure is taken from Hotokezaka et al. (2013c).

Substituting Eq. (5.4) into this equation yields

$$\tilde{\phi}(t,\Delta x) = \Lambda(\Delta x)\phi(\tilde{t},\Delta x), \tag{5.7}$$

and combining Eq. (5.5) and Eq. (5.6) yields

$$\tilde{\phi}(t,\Delta x) = \tilde{\phi}(t,0) + \int_0^t \epsilon(t',\Delta x)dt', \tag{5.8}$$

where $\tilde{\phi}(t,0)$ is the extrapolated gravitational-wave phase. Assuming the second term in the right-hand side of this equation can be described as $\phi_{\rm r}(t)\Delta x^n$, we obtain

$$\Lambda(\Delta x)\phi(\tilde{t},\Delta x) = \tilde{\phi}(t,0) + \phi_{\rm r}(t)\Delta x^n. \tag{5.9}$$

Here $\tilde{\phi}(t,0)$ and $\phi_{\rm r}(t)$ are functions which are determined by the least-square fitting of the numerical data $\phi_{\rm NR}(\tilde{t},\Delta x)$. We again set the order of the convergence n to be 1.8 ± 0.2.

Figure 5.5 shows the evolution curves of the extrapolated gravitational-wave phase for the different EOS.

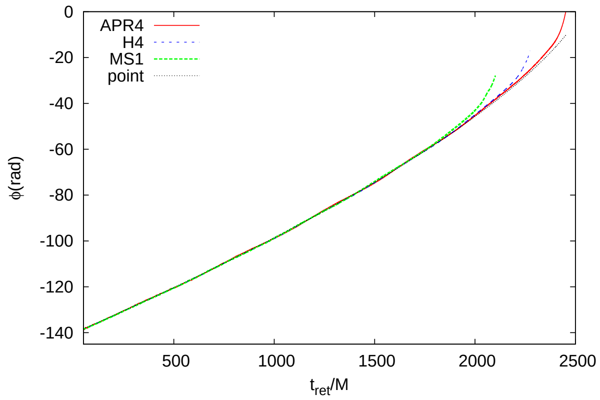

Figure 5.5: The extrapolated gravitational-wave phase for the three EOSs. Here, we set the order of the convergence to be 1.8. This figure is taken from Hotokezaka et al. (2013c).

The differences in the rescaled gravitational-wave phase $\tilde{\phi}_{\rm NR}(t,\Delta x)$ obtained for runs with the different grid resolutions and the extrapolated gravitational-wave phase $\tilde{\phi}(t,0)$ for $n=1.8$ are shown in Fig. 5.4. The accumulated difference between the extrapolated gravitational-wave phase and that of the highest grid resolution is ~ 8 radian for APR4 and ~ 3 radian for H4 at the onset of the merger. These values imply that the simulation for the neutron star which has the larger radius is relatively well convergent. These phase differences are much larger than the possible error in the gravitational-wave phase associated with the finite-radius extraction, $\lesssim 0.5$ radian. Thus, we conclude that the resolution extrapolation of the gravitational-wave phase is essential to construct the extrapolated physical waveform for our current numerical-relativity simulations. The lower panels in Fig. 5.4 show the difference between the gravitational-wave phase of the resolution D, $\tilde{\phi}_{\rm NR}(t,\Delta x_{\rm D})$, and the one which is obtained by extrapolating the gravitational-wave phase of the resolutions A, B, and C to the resolution D, $\tilde{\phi}(t,\Delta x_{\rm D})$. The difference $\Delta\phi$ is within 0.15 radian up to the merger. Here, this error is caused mainly by a modulation associated with an unphysical orbital eccentricity. The upper panels of Fig. 5.6 show the evolution curves of the extrapolated gravitational-wave phase for the different choice of n.

For the brief check of the validity of the extrapolation, we calculate the dispersion $\sigma(t)$ of the extrapolation as

$$\sigma(t)^2 = \frac{1}{N_{\rm R}}\sum_{i=1}^{N_{\rm R}}\left(\tilde{\phi}(t,\Delta x_i) - \tilde{\phi}_{\rm NR}(t,\Delta x_i)\right)^2, \tag{5.10}$$

where $\tilde{\phi}_{\rm NR}(\tilde{t},\Delta x_i)$ is the rescaled gravitational-wave phase of the numerical data, $i=1\sim N_{\rm R}$ denote the numerical run with the different grid resolutions, e.g. $N=(42,48,54,60)$, and N_{R} is the total number of them, e.g. $N_{\mathrm{R}} = 4$. As shown later, the value of the dispersion is in the range 0.01 radian (in the early part) to 0.4 radian (just before the merger). We regard this dispersion as an error due to the resolution extrapolation. Hereafter we use only the extrapolated quantities and omit the tilde of them.

5.2 Comparison between numerical and analytical results

Matching Procedure

In the analysis, we first match an early part of the gravitational-wave phase obtained by extrapolating numerical results, $\phi_{\mathrm{NR}}(t)$, with that of the analytic ones, $\phi_{\mathrm{PN}}(t)$ (the wave phase derived in the PN calculation) and $\phi_{\mathrm{EOB}}(t)$ (the wave phase derived in the EOB calculation), by minimizing the following quantity,

$$\int_{t_1}^{t_2} (\Delta\phi(t))^2 \, dt = \int_{t_1}^{t_2} \left(\phi_{\mathrm{NR}}(t) - \phi_{\mathrm{PN/EOB}}(t - t_{\mathrm{s}}) - \phi_{\mathrm{s}}\right)^2 dt, \tag{5.11}$$

where ϕ_{s} and t_{s} are the fitting parameters. The initial and final time of the integral, t_1 and t_2, are chosen as follows. As shown in the previous section, the curve of the extrapolated gravitational-wave phase obtained from the results of NR simulations has modulation due to the orbital eccentricity. Thus, (t_1, t_2) are chosen to cover a range between two adjacent local maxima or local minima of the curve in an early part of the gravitational-wave phase. This choice of the matching region allows us to match the gravitational-wave phase numerically obtained with the PN/EOB phases smoothly using the least-square fitting. Here, we choose the two adjacent local minima as the matching boundaries as follows: $(t_1, t_2) = (583M, 1030M)$ for APR4 (which corresponds to $M\omega \in [0.042 : 0.048]$), $(t_1, t_2) = (550M, 1000M)$ for H4 (which corresponds to $M\omega \in [0.042 : 0.046]$), and $(t_1, t_2) = (550M, 960M)$ for MS1.

Comparison

We compare ϕ_{NR} with $\phi_{\mathrm{PN/EOB}}$ which are calculated in several levels of the approximation. The middle panels of Fig. 5.6 show the difference between ϕ_{NR} and ϕ_{EOB} in which tidal effects up to the next-to-leading order are included. The error bars show the dispersion associated with the least-square fitting in the extrapolation procedure, which is defined by Eq. (41). The three curves show the gravitational-wave phase difference for the three assumed orders of the convergence $n = (1.6, 1.8, 2.0)$. The phase differences are modulated with an amplitude about 0.4 radian due to the unphysical orbital eccentricity. We regard this modulation as a systematic error, which is denoted by the horizontal dashed lines. For comparison, we also plot the gravitational-wave angular velocity evolution in the bottom of Fig. 5.6. Figure 5.7–5.8 shows the difference between $\phi_{\rm NR}$ and $\phi_{\rm PN/EOB}$ which are calculated in several levels of the approximation.

In the early stage of the inspiral, i.e., before the time $t_{\rm ret}/M \lesssim 1500$ ($M\omega \lesssim 0.054$) for APR4, $t_{\rm ret}/M \lesssim 1300$ ($M\omega \lesssim 0.05$) for H4, and $t_{\rm ret}/M \lesssim 1200$ ($M\omega \lesssim 0.049$) for MS1, we find that $\phi_{\rm NR}$ is consistent with $\phi_{\rm PN/EOB}$ for any levels of the approximation. In this stage, the point-mass approximation works well and the PN and EOB approaches appear to describe NS-NS inspirals well even if tidal effects are not taken into account. It is difficult to verify a clear signature of the tidal effects in this early stage due to the modulation of the numerical data and the weakness of the tidal effects.

After the early stage of the inspiral, the binary system proceeds to a tidally-dominated inspiral phase where the tidal interaction becomes strong. In this late inspiral stage, one can see that the difference between $\phi_{\rm NR}$ and $\phi_{\rm PN/EOB}$ gradually increases. $\phi_{\rm NR}$ is larger than $\phi_{\rm PN/EOB}$ for a given moment, implying binaries in NR simulations evolve faster than those in the PN and EOB calculations.

After the time $t_{\rm ret}/M \sim 2300$ ($M\omega \sim 0.09$) for APR4, $t_{\rm ret}/M \sim 2100$ ($M\omega \sim 0.08$) for H4, and $t_{\rm ret}/M \sim 1950$ ($M\omega \sim 0.075$) for MS1, the difference between $\phi_{\rm NR}$ and $\phi_{\rm EOB}$ rapidly increases with time. This corresponds to the transition from the inspiral to the plunge. The orbital angular velocity when two neutron stars come into contact, $M\omega_{\rm contact}$, is approximately defined by Damour et al. (2012)

$$M\omega_{\rm contact} = 2\left(\frac{M_A}{M}\frac{1}{C_A} + \frac{M_B}{M}\frac{1}{C_B}\right)^{-3/2}. \tag{5.12}$$

At the moment of the contact, the accumulated gravitational-wave phase difference between $\phi_{\rm NR}$ and $\phi_{\rm EOB}$ including the tidal effects up to the next-to-leading order is ~ 3.3 radian (2.5%) for APR4, ~ 1.9 radian (1.7%) for H4, and ~ 2.1 radian (2.0%) for MS1. If the correction is up to the next-to-next-to-leading order, the phase difference is ~ 2.6 radian (2.0%) for APR4, ~ 1.4 radian (1.3%) for H4, and ~ 1.1 radian (1.1%) for MS1. We find that the EOB approach including the tidal effects up to the next-to-next-to-leading order yields currently the best model for the late stage of NS-NS inspirals. However, the tidal effects are still underestimated for the final inspiral orbit even for the best model of the analytic approaches. Thus, for constructing better waveforms in NS-NS inspirals, this rapid evolution of the gravitational-wave phase should be taken into account.

We compare our results of MS1, of which the compactness is $C = 0.138$, with the results of Bernuzzi et al. (2012b), in which a neutron-star with $C = 0.14$ is employed. Both results show that the difference between the extrapolated gravitational-wave phase of NR and that of T4 without tidal effects is about 3 radian at contact ($M\omega \sim 0.1$), in the case that the alignment is performed after the first orbit (Bernuzzi et al. 2012b). Therefore our results are consistent with the results of Bernuzzi et al. (2012b).

Figure 5.10 and Fig. 5.11 show the snapshots of the density contour of NS-NS inspirals for APR4 and H4. Here we focus on Fig. 5.11 as an example. The upper left panel of

Fig. 5.11 plots the density profile of the binary at an early inspiral stage. At this time, the neutron stars have a spherical shape. The ellipticity of the neutron star, which is defined by the ratio of the semi-major axis a_1 to the semi-minor axis a_2 of the star on the equatorial plane, is approximately unity.

The upper right panel of Fig. 5.11, at $M\omega = 0.056$, plots the configuration of the binary at which the tidal effects seem to be small but cannot be neglected. For this plot, the ellipticity of the star is ~ 1.05. After this time, the binary system proceeds to the tidally-dominated inspiral phase. In the lower left panel of Fig. 5.11, two neutron stars are obviously deformed due to the strong tidal fields; the ellipticity of the neutron star is ~ 1.17. The snapshot around the plunge is shown in the lower right panel of Fig. 5.11. Soon after the onset of the plunge, the two neutron stars contact and the ellipticity is ~ 1.23.

We also note that the ellipticity of the neutron star rapidly increases after the stage at $M\omega = 0.056$. This evolution of the ellipticity is consistent with the semianalytic, Newtonian results Lai et al. (1994). Note that the value of the ellipticity defined here depends on the coordinate system. We here assumed that the coordinate distortion is small because of our choice of the spatial gauge condition.

Finally, we show the difference between the extrapolated gravitational-wave phase and the gravitational-wave phase derived in the PN and EOB approaches for unequal-mass systems APR4-1215 and H4-1215: see Fig. 5.9 . Here, we choose the matching region $(t_1, t_2) = (520M, 1020M)$ for APR4-1215 and $(t_1, t_2) = (600M, 1080M)$ for H4-1215. This figure shows that the feature of the curves for the unequal-mass system is qualitatively the same as those of the equal-mass system, and the magnitude of the phase difference between $\phi_{\rm NR}$ and $\phi_{\rm PN/EOB}$ is also as large as that for the equal-mass case.

5.3 Conclusions

We have explored the property of gravitational waves emitted in the late stage of NS–NS inspirals. To derive the physical waveform from numerical data obtained by numerical-relativity simulations, we carefully performed the radius and resolution extrapolation of the waveforms. Then, we found that the resolution extrapolation is crucial in our present study. Specifically, the accumulated difference between the gravitational-wave phase in the highest grid resolution run and the resolution-extrapolated gravitational-wave phase is ~ 8 radian for APR4 and ~ 3 radian for H4. These values imply that the simulation for the NS–NS inspiral with more compact neutron stars has worse convergence. For the simulation with more compact neutron stars , one needs to perform a higher resolution simulation to derive an accurate waveform. Therefore a sophisticated procedure for the extrapolation is needed to derive an accurate waveform for compact neutron stars. We found that the time-rescaling is a robust prescription for deriving the resolution-extrapolated gravitational-wave phase $\phi_{\rm NR}$.

We have compared $\phi_{\rm NR}$ with $\phi_{\rm PN/EOB}$, which are derived from the Taylor T4 approximant of the PN formalism and the EOB formalism. Both of the analytic approaches are capable of including the tidal effects. We found that $\phi_{\rm NR}$ is consistent with $\phi_{\rm PN/EOB}$ in the early part of the inspiral. On the other hand, in the very late part of the inspiral, $\phi_{\rm NR}$ evolves more rapidly than $\phi_{\rm PN/EOB}$. The EOB approach including the tidal corrections up to the next-to-next-to-leading order is currently the best approach for describing the late stage of NS–NS inspirals. However, the estimated accumulated difference between $\phi_{\rm NR}$ and $\phi_{\rm EOB}$ is ~ 2.6 radian for APR4, ~ 1.9 radian for H4, and ~ 1.1 radian for MS1 at the moment of contact of the two neutron stars. Therefore we conclude that the tidal effects are still underestimated in the EOB approach including the tidal corrections up to the next-to-next-to-leading order. We also found that this result is independent of the EOS and mass ratio.

Here we make a comparison of our results with the earlier results. We found the absence of the large amplification of the tidal effects in the early inspiral phase suggested in Baiotti et al. (2011), if the resolution extrapolation is taken into account. In the late inspiral phase, the amplification of the tidal effects is observed. This agrees with the earlier results (Baiotti et al. 2011; Bernuzzi et al. 2012b). In particular, for the MS1 ($C \sim 0.14$), the value of the phase difference between the extrapolated gravitational-wave phase and that of Taylor T4 without tidal effects is consistent with the results of Bernuzzi et al. (2012b), which employed a neutron star with $C = 0.14$.

In order to extract the tidal deformability of a neutron star efficiently and faithfully from a signal of gravitational waves, one has to prepare a theoretical template of gravitational waves which should be accurate enough up to the onset of the merger. Our present study suggests that the EOB approach including up to the next-to-next-to-leading order tidal correction yields currently the best result. However, for the final orbit, there is still room for the improvement. In the current prescription for incorporating the tidal effects, the adiabatic approximation is assumed for the tidal deformation. For the very close orbits, however, this approximation breaks down; for example, the presence of the dynamical tidal lag (which is seen in Figs. 5.10 and 5.11) cannot be reproduced. If a more sophisticated formalism in which such effects are taken into account can be developed, the accuracy of the analytic modeling could be improved. There is also the issue on the side of numerical relativity. For constructing an analytic model of the gravitational waveform in NS-NS inspirals with a high accuracy, one always calibrates the model waveform by comparing it with the numerical result. This implies that a high-accuracy numerical waveform is necessary. To achieve a high accuracy, one needs to perform high-accuracy simulations than the present ones. One of the keys for improving the accuracy is to reduce the orbital eccentricity in future.

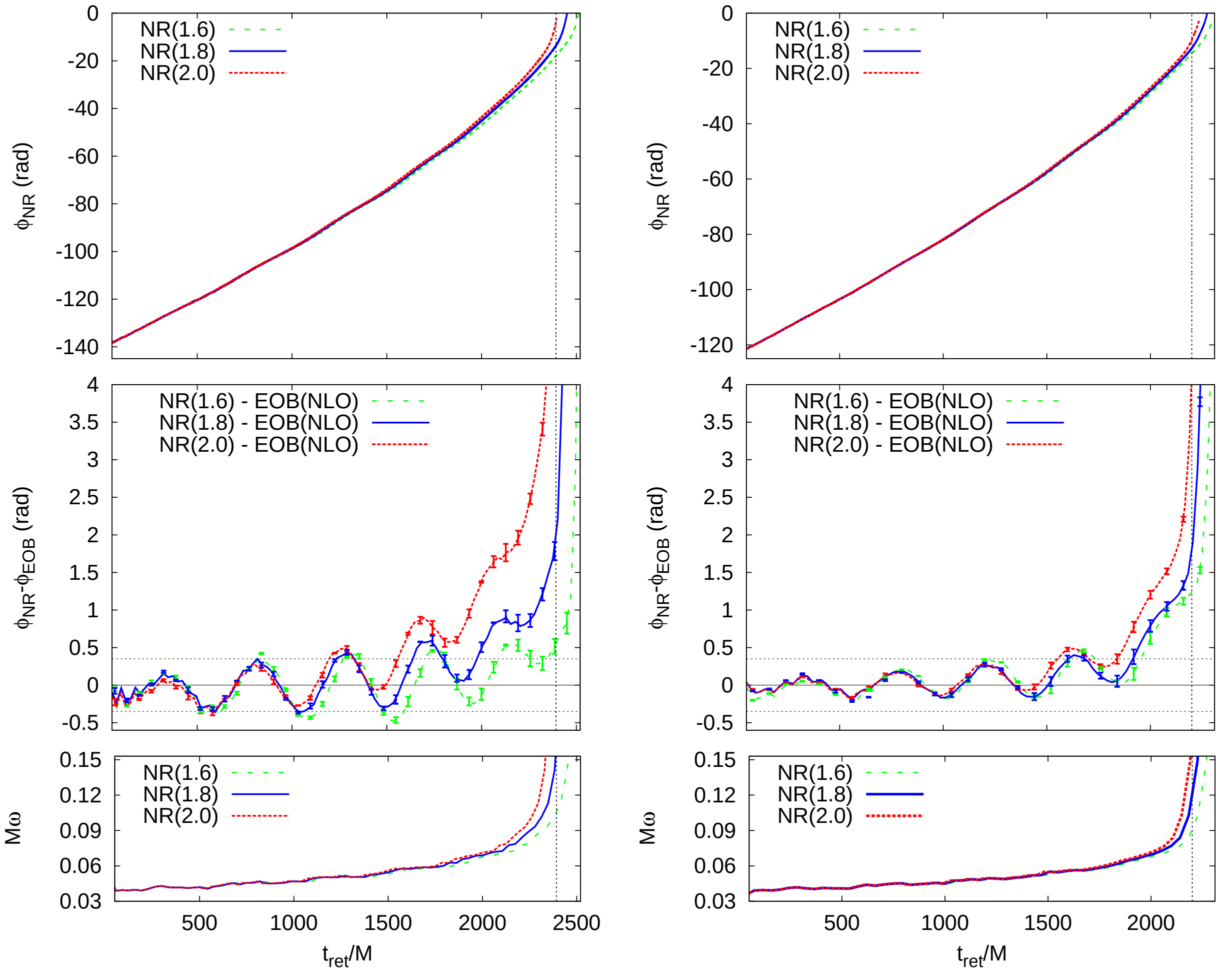

Figure 5.6: Gravitational-wave phase (top panels), difference between $\phi_{\rm NR}$ and $\phi_{\rm EOB}$ (middle panels), and gravitational-wave angular velocity (bottom panels) for APR4 (left panels) and H4 (right panels). EOB(NLO) denotes the effective-one-body formalism including the tidal effects up to the next-to leading order. We show the curves for the three orders of the convergence, $n = (1.6, 1.8, 2.0)$. The horizontal dashed lines in the middle panels denote the uncertainty due to the modulation of the numerical data. The vertical dashed lines denote the time at contact of the two stars for the case of the order of the convergence is 1.8. This figure is taken from Hotokezaka et al. (2013c).

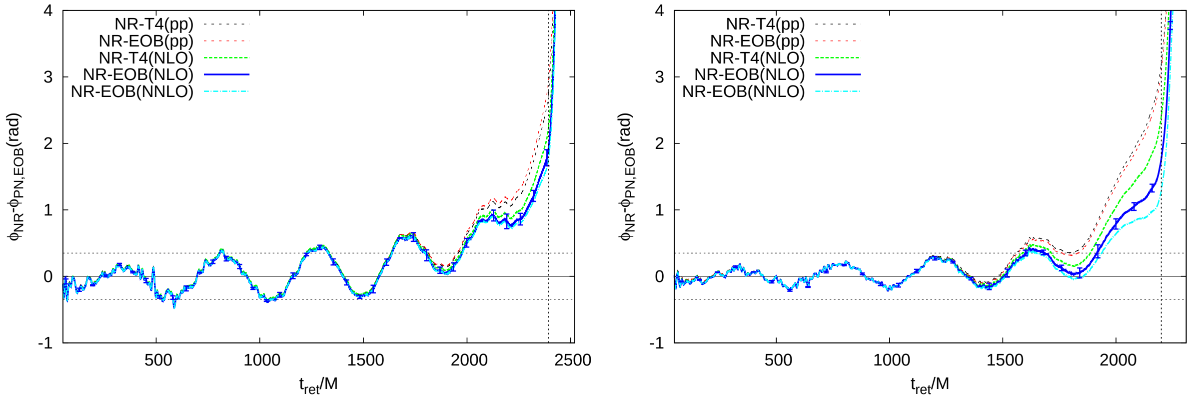

Figure 5.7: Phase difference between $\phi_{\rm NR}$ and$\phi_{\rm PN/EOB}$ for APR4 (left) and for H4 (right). In this figure, we set the order of the convergence to be 1.8 for obtaining the extrapolated gravitational-wave phase. T4(pp) and EOB(pp) denote the Taylor T4 approximant and the effective-one-body formalism without the tidal corrections. Here, we only display the error bars of the curve NR-EOB(NLO). However, other curves also have the same amount of the error. This figure is taken from Hotokezaka et al. (2013c).

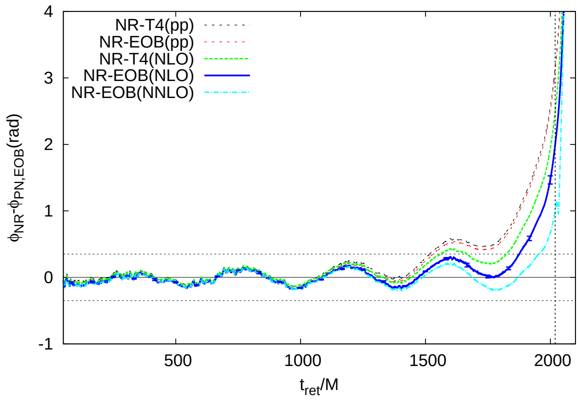

Figure 5.8: The same as Fig. 5.7 but for MS1. This figure is taken from Hotokezaka et al. (2013c).

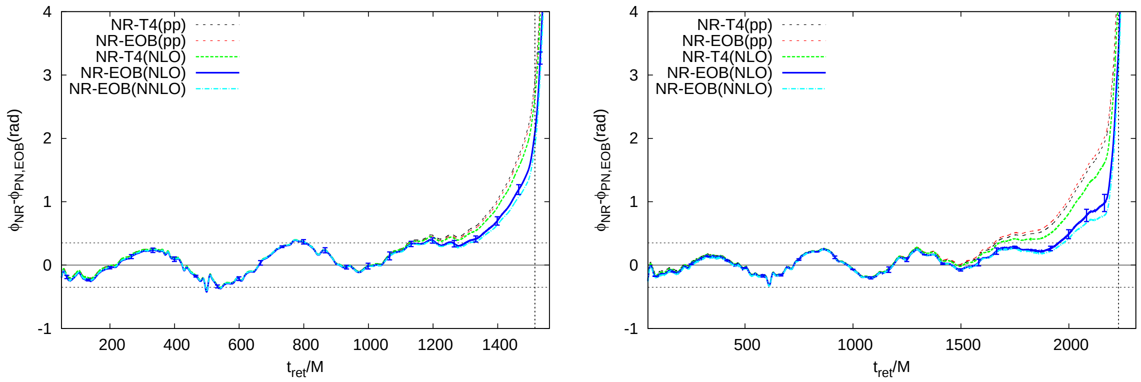

Figure 5.9: Difference between $\phi_{\rm NR}$ and $\phi_{\rm PN/EOB}$ for APR4-1215 (left panel) and for H4-1215 (right panel). Here we choose $n = 1.8$. This figure is taken from Hotokezaka et al. (2013c).

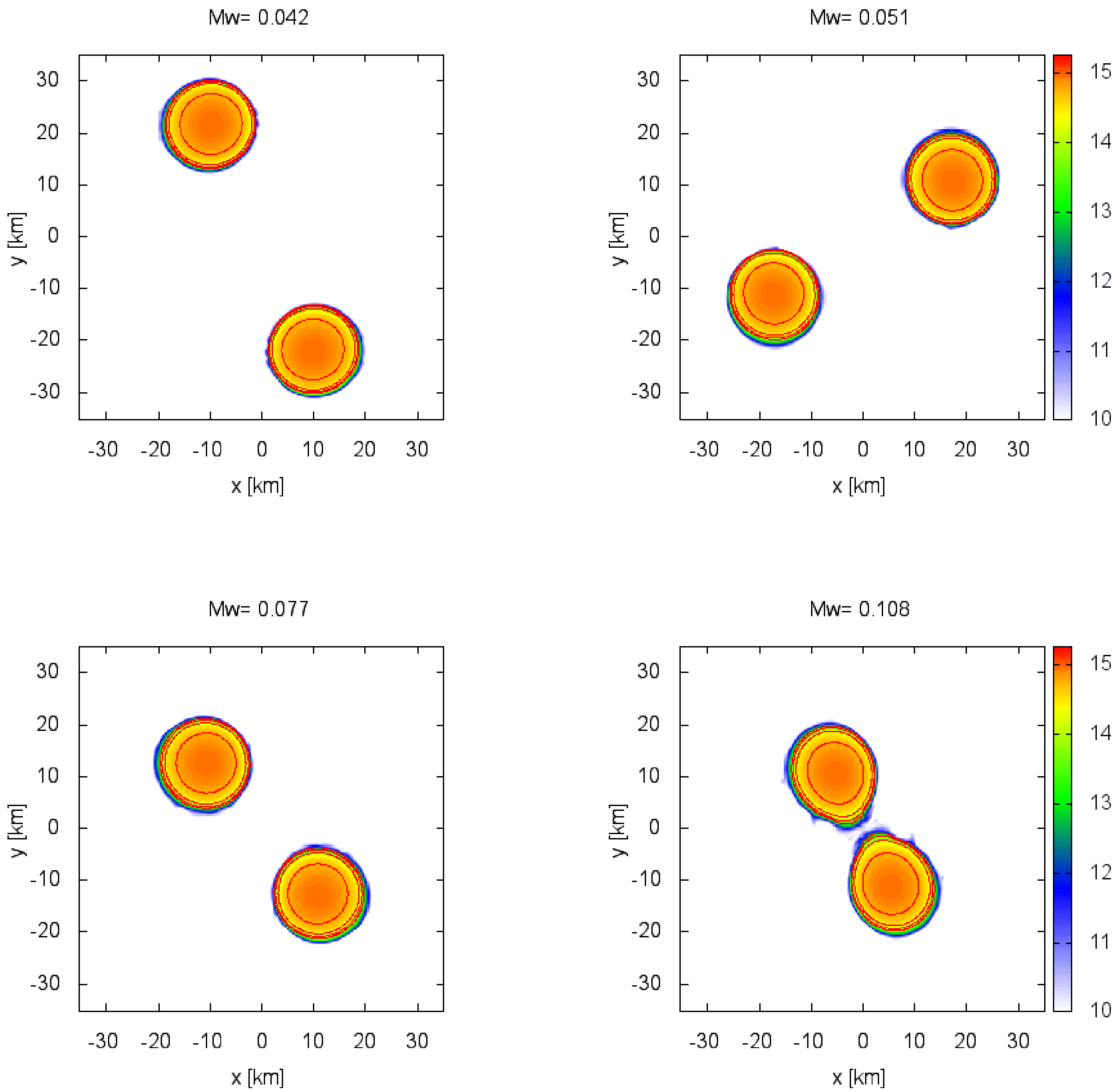

Figure 5.10: Snapshots of the orbital-plane density profile of NS-NS binaries in close orbits for APR4. The color denotes the density in units of $\log\rho(\mathrm{g/cm^3})$. This figure is taken from Hotokezaka et al. (2013c).

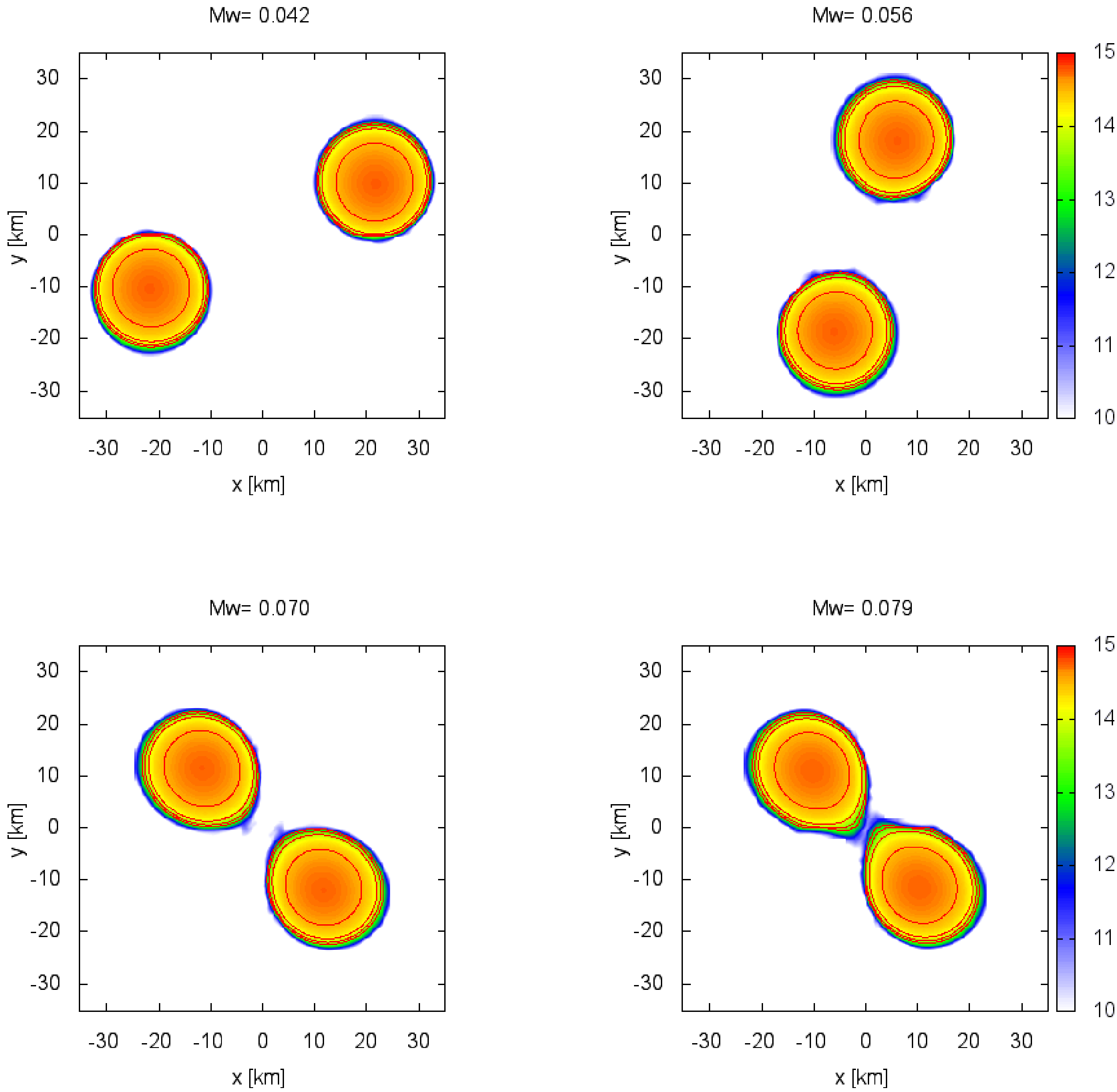

Figure 5.11: The same as Fig.5.10 but for H4. This figure is taken from Hotokezaka et al. (2013c).

Chapter 6

Evolution and gravitational waveform of binary neutron star merger remnant

There is a variety of evolutionary paths after an NS–NS merger, depending on the total mass, mass ratio, and EOS. In particular, a massive neutron star is likely to be formed after an NS–NS merger. The possible formation of a massive neutron star is supported by the novel discoveries of the two solar-mass neutron stars with white dwarf companions, which indicate that the EOS of neutron-star matter is stiff enough to support a two-solar mass neutron star. These discoveries motivate us to study massive neutron star formation after an NS–NS merger. In the former of this chapter, we are concerned about the formation and evolution of a massive neutron star after an NS–NS merger and dependence of them on the total mass, mass ratio, and EOS (Kiuchi et al. 2009; Hotokezaka et al. 2011, 2013a).

A rapidly rotating massive neutron star formed after a merger emits gravitational waves due to its non-axisymmetric shape. The gravitational-wave signal from a massive neutron star contains valuable information regarding the EOS of neutron-star matter (Shibata 2005; Hotokezaka et al. 2011; Sekiguchi et al. 2011b; Bauswein and Janka 2012; Bauswein et al. 2012, 2013a; Hotokezaka et al. 2013a). However, the modeling of waveforms and as well as method how to analyze gravitational-wave signal from a massive neutron star are still under debate. In the latter part chapter, we summarize the properties of gravitational waveforms of massive neutron stars and discuss a phenomenological waveform describing the numerical waveforms of post-merger phase.

6.1 Fate of binary neutron star merger

A sequence of spherical neutron stars has the maximum mass state. Beyond the maximum mass $M_{\rm max}$, there is no equilibrium configuration of them. Although the total mass of an NS–NS binary M may exceed the maximum mass of a non-rotating cold neutron star, a

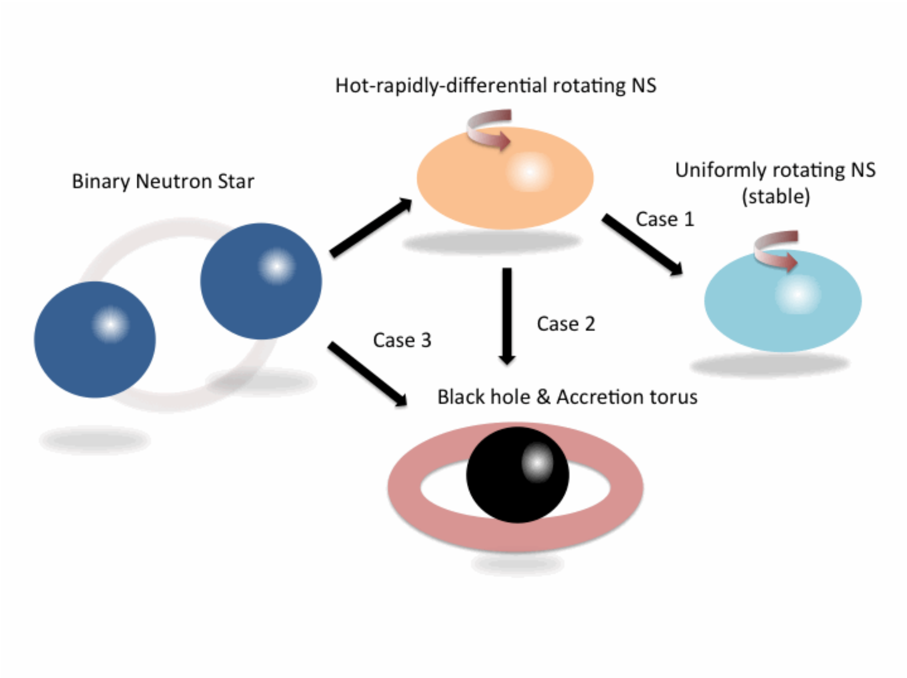

Figure 6.1: Evolutionary paths of NS–NS mergers.

massive neutron star can be formed after a merger, depending on the total mass, mass ratio, and EOS. In the post-merger stage, the evolutionary path of an NS–NS merger is classified into the following three cases (the schematic illustration is shown in Fig. 6.1).

1. A supermassive neutron star is formed ($M < M_{\rm crit,2}$).

2. A hypermassive neutron star temporary is formed ($M_{\rm crit,1} < M < M_{\rm crit,2}$).

3. A black hole is promptly formed ($M_{\rm crit,1} < M$).

Here, a supermassive neutron star (SMNS) is defined as a *uniformly* rotating neutron star with mass of $\geq M_{\rm max}$. The maximum mass of an SMNS is determined by the spin rate at which the mass element at the equator rotates with the (general relativistic) Kepler velocity and further speed-up would lead to mass shedding. The value of the maximum mass of an SMNS can reach $15-20\%$ larger than that of a non-rotating neutron star (Cook et al. 1996).

The merger of an NS–NS does not result in a uniformly rotating neutron star just after the merger, but in a *differentially* rotating neutron star. The inner region of a remnant massive neutron star rotates faster than its envelope. The angular velocity in the inner region can be larger than the Kepler velocity as found in Shibata and Uryū (2000). Differential rotation could support a massive neutron star of which the mass is larger than the maximum mass of an SMNS (Baumgarte et al. 2000). Such a massive neutron star is called a hypermassive neutron star (HMNS). An HMNS eventually collapses to a

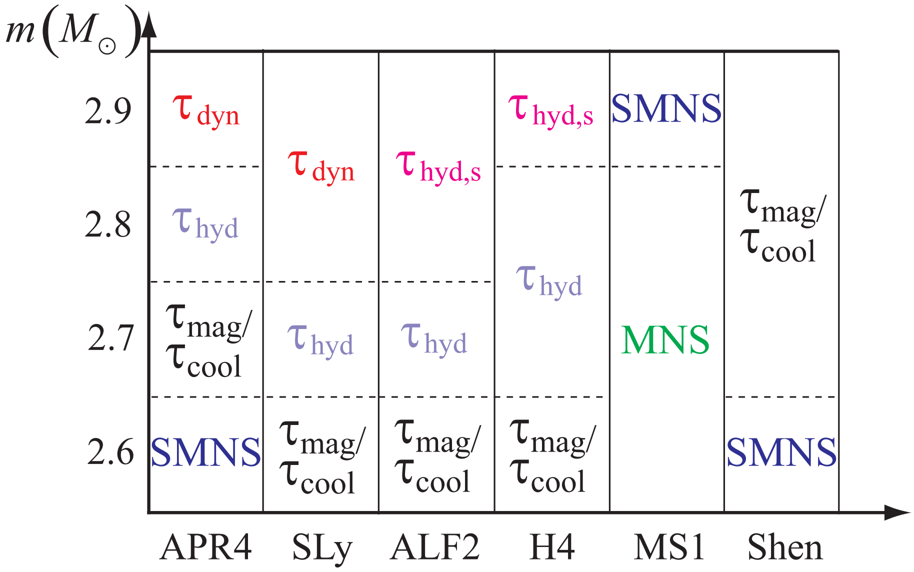

Figure 6.2: The evolution time scale of the system in the plane composed of EOSs and total mass. $\tau_{\rm dyn}$: A black hole is formed in the dynamical time scale after the onset of the merger. $\tau_{\rm hyd}$: A HMNS is formed and its lifetime is determined by the hydrodynamical angular-momentum transport time scale. $\tau_{\rm hyd,s}$: The same as for $\tau_{\rm hyd}$ but the lifetime is shorter than $\sim 10\,$ms. $\tau_{\rm mag}/\tau_{\rm cool}$: A HMNS is formed and its lifetime would be determined by the time scale of angular-momentum transport by some magnetohydrodynamics effects or by the neutrino cooling time scale. The evolution time scale for a given total mass depends weakly on the mass ratio. For MS1, only the MNS or SMNS is formed for $m \leq 2.9 M_\odot$. For APR4 and Shen, the remnant for the $m \lesssim 2.6 M_\odot$ case is likely to be a SMNS (not HMNS). This figure is taken from Hotokezaka et al. (2013a).

black hole on the time scales of angular momentum losses driven by either gravitational-wave emission, hydrodynamical process, or magnetic fields. Because thermal pressure may contribute to support an HMNS (Hotokezaka et al. 2011; Bauswein et al. 2010; Kaplan et al. 2013), neutrino cooling also plays an important role to understand the delayed collapse of an HMNS.

The problem of whether an HMNS is formed or not after an NS–NS merger is not easy to answer, because the HMNS formation depends on merger dynamics. Numerical relativity is unique tool to study the problem by computing an NS–NS merger for given component masses, an equation of state (EOS) of neutron-star matter. In this thesis, we focus in particular on the EOSs, of which the maximum mass of spherical neutron star is larger than $2M_\odot$.

6.1.1 Supermassive neutron star and black hole formation

The critical mass of an SMNS formation $M_{\rm crit,2}$ corresponds to the maximum mass of an SMNS, which is determined from the equilibrium sequence of a *uniformly* rotating neutron star for a given EOS. Because the maximum mass of an SMNS is 15%—20% larger than that of non-rotating neutron star, an NS–NS merger with a total mass of $2.7M_\odot$ can result in an SMNS for an EOS of which the maximum mass of a non-rotating neutron star is $\gtrsim 2.3M_\odot$.

The critical mass of a black hole formation $M_{\rm crit,1}$ is not determined from equilibrium considerations, because the distribution of density and angular momentum just after the merger depends on the dynamics of the merger. The value of $M_{\rm crit,1}$ may be proportional to the maximum mass of a given EOS as

$$M_{\rm crit,1} = kM_{\rm max}, \tag{6.1}$$

where k is a constant which depends on EOSs. By using numerical relativity simulations of equal mass NS–NS mergers for 6 EOSs, we find that the value of k is in the range (Hotokezaka et al. 2011)

$$1.3 \lesssim k \lesssim 1.7. \tag{6.2}$$

For an NS–NS merger with more compact neutron stars, the value of k is smaller than that with less compact neutron stars. For instance, the value of k is ~ 1.3 and ~ 1.7 for APR4 ($R_{1.35} = 11.42$ km) and PS ($R_{1.35} = 15.47$ km), respectively.

Bauswein et al. (2013a) have surveyed the value of k for 12 EOSs, which can support a non-rotating neutron star with mass of $\sim 2M_\odot$. They have shown that the value of k is in the range $1.3 \leq k \leq 1.6$. They have also found k is well described as a function of $C^*_{1.6} = (GM_{\rm max})/(c^2 R_{1.6})$, where $R_{1.6}$ is the radius of a neutron star with the mass of $1.6M_\odot$ *. The function can be described as

$$k = j \cdot C^*_{1.6} + a, \tag{6.3}$$

where $j = -3.359$ and $a = 2.315$ are constants which are determined by a fitting. They have shown that the correlation between k and $C^*_{1.6}$ holds with an error of a few per cent. Therefore the maximum mass can be measured through Eqs.(6.1, 6.3), once one has succeeded to determine $M_{\rm crit,1}$ by using gravitational-wave observations from NS–NS mergers.

6.1.2 Hypermassive neutron star formation and evolution

An HMNS is probably formed for the case of an NS–NS merger with a total mass in the typical mass range 2.6–2.8$M_\odot$ (see Table. 1.1), for an EOS of which maximum mass of

*$R_{1.6}$ is chosen instead of $R_{\rm max}$, because $R_{1.6}$ may be more measurable than $R_{\rm max}$ by future observations.

non-rotating neutron star is $\sim 2M_\odot$ as shown above. If degree of the differential rotation of an HMNS is reduced by angular momentum transport, an HMNS becomes unstable against gravitational collapse. There are several processes of angular momentum and energy losses. We discuss the time scales of these processes in the followings.

Hydrodynamical process

An HMNS has a non-axisymmetric shape, e.g., double-core structure or bar-like structure, which induce non-axisymmetric gravitational fields. A torque due to the rotation of non-axisymmetric gravitational fields is exerted to matter in the envelope of a non-axisymmetric HMNS. The magnitude of a gravitational torque can be estimated the torque exerted on the Lindblad resonance (Goldreich and Tremaine 1979; see also Hirata 2011 for the formulation in general relativity)

$$\tau_{\rm hyd} \sim 10^{-2}{\rm s}\ \omega_4 \left(\frac{\rho_{\rm L}}{10^{12}{\rm g/cm^3}}\right)^{-1}, \tag{6.4}$$

where ω is the angular velocity of the HMNS and $\rho_{\rm L}$ is the density at the radius of the Lindblad resonance. Although this evaluation of the torque is valid for the gravitational interaction between a non-axisymmetric central star and a thin disk, this time scale may be correct as shown later. Note that a gravitational torque is efficient only when an HMNS has a non-axisymmetric shape. The shape of an HMNS approaches to be axisymmetric with decreasing its angular momentum as discussed in the next section. Thus hydrodynamical process of angular momentum transport may be important just after the onset of a merger.

Gravitational-wave emission

Gravitational waves are burstly emitted by a massive neutron star, when it has non-axisymmetric shape. The gravitational waves carry away angular momentum from a MNS. The quadratic formula for the angular momentum loss of a system is given by

$$\frac{{\rm d}S_i^{\rm GW}}{{\rm d}t} = \frac{2G}{5c^5}\epsilon_{ijk} < \ddot{I}_{km}^{\rm TT}\dddot{I}_{mj}^{\rm TT} > \tag{6.5}$$

$$\tau_{\rm GW} \sim 3\times10^{-1}s\ R_{\rm HMNS,6}^{-2}\omega_4^{-4}\epsilon_{\rm def,-1}^{-1}\left(\frac{M}{2.7M_\odot}\right)^{-1}, \tag{6.6}$$

where $\epsilon_{\rm def}$ is a deformation parameter of a HMNS defined by $\epsilon_{\rm def} = (I_{xx}^{\rm TT} - I_{yy}^{\rm TT})/(I_{xx}^{\rm TT} + I_{yy}^{\rm TT})$.

Magnetohydrodynamical process

Magnetic fields play a crucial role for the angular momentum transport in a remnant massive neutron star. There are two possible processes of the angular momentum transport, which are achieved in the presence of magnetic fields. First, magnetic wind effects transport the angular momentum of the inner core to the outer envelope of a HMNS on the Alfven time scale as

$$\tau_{\rm wind} \sim \frac{R_{\rm HMNS}}{v_{\rm A}} \sim 10^{-1}{\rm s}\ \rho_{15}^{1/2} B_{15}^{-1} R_{\rm HMNS,6}, \tag{6.7}$$

where $R_{\rm HMNS}$ is the typical radius of an HMNS, B is the typical magnitude of the radial component of magnetic fields, and $v_{\rm A}$ is the Alfven velocity given by $\simeq B/\sqrt{4\pi\rho}$.

The other process of angular momentum transport is the magnetorotational instability (MRI) (Balbus and Hawley 1998, 1991). The MRI may act as a viscous torque which may be described by the effective viscous parameter

$$\nu_{\rm vis} \sim \alpha_{\rm vis} \frac{c_{\rm s}^2}{\omega}, \tag{6.8}$$

where $\alpha_{\rm vis}$ is the so-called α parameter which may be 0.01-0.1 (Balbus and Hawley 1998), $c_{\rm s}$ is the typical sound velocity of order of $\sim 0.1c$, and ω is the typical angular velocity $\sim 10^4$rad/s. Assuming the above typical values, the time scale of the MRI can be estimated as

$$\tau_{\rm MRI} \sim \frac{R_{\rm HMNS}^2}{\nu_{\rm vis}} \sim 10^{-1}{\rm s}\ R_{\rm HMNS,6}^2 \omega_4 \left(\frac{\alpha_{\rm vis}}{0.01}\right)^{-1} \left(\frac{c_{\rm s}}{0.1c}\right)^{-2}. \tag{6.9}$$

The time scale of the MRI does not depend on the magnitude of magnetic fields. This process may dominate over the magnetic windings as long as the magnetic field strength is $\ll 10^{15}$G. However the value of $\alpha_{\rm vis}$ is uncertain in the HMNS formed after a NS–NS merger. In order to explore the nature of the MRI in NS–NS mergers, high-resolution simulations of general relativistic magnetohydrodynamics are needed.

It is wothy to note that both the magnetic wind effect and MRI work as long as differential rotation is present even in the absence of a non-axisymmetric shape of a remnant massive neutron star. Therefore, the collapse of an HMNS is inevitable on the time scale of the magnetohydrodynamical processes.

Viscous process

Shear viscosity can destroy differential rotation and redistribute angular momentum in a HMNS. The viscosity due to the transport of momentum of neutrons acts on a time scale (Flowers and Itoh 1979; Cutler and Lindblom 1987)

$$\tau_{\rm vis} \sim 10^{10}{\rm s}\ T_{10}^2 \left(\frac{M_{\rm HMNS}}{2M_\odot}\right)^{9/2} \left(\frac{C_{\rm HMNS}}{0.2}\right)^{-23/4}, \tag{6.10}$$

where $C_{\rm HMNS}$ is the compactness of the HMNS. The time scale of the viscosity in an HMNS is much longer than that of the magnetic fields. Therefore the effects of viscosity are negligible for HMNS evolution.

Neutrino cooling

The thermal pressure also contributes to support an HMNS, because the temperature of an HMNS reaches several MeV. The maximum mass of such an hot neutron star is 10–30 % larger than that of a cold neutron star. Because neutrinos carry the thermal energy away from an HMNS, the HMNS may collapse into a black hole due to the loss of thermal energy. The time scale of neutrino cooling can be estimated as

$$\tau_{\rm cool} \sim 1{\rm s}\ \rho_{15} \left(\frac{T}{10{\rm MeV}}\right) \left(\frac{\epsilon_\nu^{\rm HMNS}}{10^{33}{\rm erg/s/cm^3}}\right)^{-1}, \tag{6.11}$$

where $\epsilon_\nu^{\rm HMNS}$ is the neutrino emissivity of an HMNS and T is the temperature. The typical values are taken from Sekiguchi et al. (2011a).

Dipole radiation

Magnetic fields with a coherent large scale structure exert a torque to a rotating magnetized star. The time scale of the dipole radiation is evaluated as

$$\tau_{\rm dip} \sim 10^3{\rm s}\ \omega_4^{-2} R_6^{-4} B_{15}^{-2} \left(\frac{M_{\rm HMNS}}{2.7M_\odot}\right) \tag{6.12}$$

Note that the dipole radiation carry away the rotational energy from an SMNS. As a result, the SMNS collapses into a black hole.

Note that the angular momentum transports play a crucial role not only for the evolution of an HMNS, but also for the formation of the accretion torus surrounding a black hole. After the gravitational collapse of an HMNS, the envelope which has gained sufficient angular momentum remains outside of the black hole. This correlation between HMNS lifetimes and amounts of accretion torii is found in our simulations as shown in Table 6.1.

Figure 6.2 shows the evolutionary paths of an NS–NS merger for a given total mass and EOS, based on the results of our numerical relativity simulations. Here we classify the remnant objects into several cases: a direct collapse denoted by $\tau_{\rm dyn}$, HMNS, SMNS, and a stable massive neutron star. HMNS formation cases are further classified into subgroups depends on their lifetime scales. $\tau_{\rm hyd}$ ($\tau_{\rm hyd,s}$) denotes an HMNS formation which the lifetime of the HMNS is longer (shorter) than 10 ms. This lifetime is determined by the angular momentum transport through hydrodynamical processes. $\tau_{\rm mag}/\tau_{\rm cool}$ denotes an HMNS formation which the HMNS does not collapse into a black hole due to the angular momentum transport through the hydrodynamical processes, e.g., the HMNS becomes an axisymmetric configuration. However, degree of differential rotation still exists. Therefore the HMNS is expected to be collapse due to the angular momentum transport through magnetic fields or loss of thermal energy through the neutrino cooling. These two processes are beyond our numerical simulations.

6.2 Dynamics of remnant massive neutron stars

Evolution of maximum density

Table 6.1: List of the simulation models in which a MNS is formed. The model is referred to as the name "EOS"-"M_A" "M_B"; e.g., the model employing APR4, $M_A = 1.3M_\odot$, and $M_B = 1.4M_\odot$ is referred to as model APR4-130140. Second – fourth columns show the adiabatic index for the thermal pressure for the piecewise polytropic EOS and masses of two components. The last three columns show the numerical results; approximate lifetime of the massive neutron star that was found in our simulation time, the mass of disks surrounding the remnant black hole, and final gravitational mass of the system. — denotes that the lifetime of the massive neutron star is much longer than 30 ms and we did not find black-hole formation in our simulation time. The disk mass is measured at 10 ms after the formation of the black hole. We note that a black hole is formed soon after the onset of the merger with $M \geq 2.9M_\odot$ for APR4 and with $M \geq 2.8M_\odot$ for SLy. For ALF2 with $M = 2.9M_\odot$, a massive neutron star is formed after the merger but its lifetime is quite short, < 5 ms.

Model	$\Gamma_{\rm th}$	$M_A(M_\odot)$	$M_B(M_\odot)$	Lifetime (ms)	disk mass ($M_\odot$)	final mass ($M_\odot$)
APR4-130150	1.8	1.30	1.50	30	0.12	2.69
APR4-140140	1.8	1.30	1.50	35	0.12	2.69
APR4-120150	1.6, 1.8, 2.0	1.20	1.50	—	—	2.60, 2.59, 2.59
APR4-125145	1.8	1.25	1.45	—	—	2.60
APR4-130140	1.8	1.30	1.40	—	—	2.60
APR4-135135	1.6, 1.8, 2.0	1.35	1.35	—	—	2.59, 2.61, 2.60
APR4-120140	1.8	1.20	1.40	—	—	2.52
APR4-125135	1.8	1.25	1.35	—	—	2.53
APR4-130130	1.8	1.30	1.30	—	—	2.53
SLy-120150	1.8	1.20	1.50	10	0.12	2.60
SLy-125145	1.8	1.25	1.45	15	0.14	2.60
SLy-130140	1.8	1.30	1.40	15	0.11	2.60
SLy-135135	1.8	1.35	1.35	10	0.08	2.58
SLy-130130	1.8	1.30	1.30	—	—	2.51
ALF2-145145	1.8	1.45	1.45	2	0.04	2.84
ALF2-140140	1.8	1.40	1.40	5	0.07	2.72
ALF2-120150	1.8	1.20	1.50	45	0.31	2.63
ALF2-125145	1.8	1.25	1.25	40	0.23	2.63
ALF2-130140	1.8	1.30	1.40	10	0.12	2.63
ALF2-135135	1.8	1.35	1.35	15	0.17	2.62
ALF2-130130	1.8	1.30	1.30	—	—	2.54
H4-130160	1.8	1.30	1.60	5	0.12	2.83
H4-145145	1.8	1.45	1.45	5	0.03	2.81
H4-130150	1.8	1.30	1.50	20	0.25	2.72
H4-140140	1.8	1.40	1.40	10	0.03	2.72
H4-120150	1.6, 1.8, 2.0	1.20	1.50	—	—	2.65, 2.64, 2.64
H4-125145	1.8	1.25	1.25	—	—	2.63
H4-130140	1.8	1.30	1.40	—	—	2.62
H4-135135	1.6, 1.8, 2.0	1.35	1.35	15, 25, 35	0.08, 0.08, 0.08	2.62, 2.62, 2.62
H4-120140	1.8	1.30	1.30	—	—	2.54
H4-125135	1.8	1.30	1.30	—	—	2.55
H4-130130	1.8	1.30	1.30	—	—	2.53
MS1-130160	1.8	1.30	1.60	—	—	2.85
MS1-145145	1.8	1.45	1.45	—	—	2.85
MS1-140140	1.8	1.40	1.40	—	—	2.75
MS1-120150	1.8	1.20	1.50	—	—	2.65
MS1-125145	1.8	1.25	1.25	—	—	2.66
MS1-130140	1.8	1.30	1.40	—	—	2.66
MS1-135135	1.8	1.35	1.35	—	—	2.65
MS1-130130	1.8	1.30	1.30	—	—	2.56
Shen-120150	—	1.20	1.50	—	—	2.64
Shen-125145	—	1.25	1.45	—	—	2.61
Shen-130140	—	1.30	1.40	—	—	2.63
Shen-135135	—	1.35	1.35	—	—	2.62
Shen-140140	—	1.40	1.40	—	—	2.74
Shen-150150	—	1.50	1.50	—	—	2.95
Shen-160160	—	1.60	1.60	10	0.10	3.12

Figure 6.3 shows the evolution of the maximum density of NS–NS mergers for the cases that a massive neutron star is formed. At soon after the merger, The maximum density rapidly increases due to a strong compression, which is induced by the existence of the large radial infall velocity of a coalescing NS–NS. The radial infall velocity reaches $\sim 10\%$ of the tangential velocity because of the back reaction of gravitational-wave emissions, a strong gravity, , and a hydrodynamic instability of close binary configurations (Lai et al. 1994).

After the first contraction of merging neutron stars, a bounce occurs for the case of $M < M_{\rm crit,1}$. The maximum density, in turn, begins to oscillate and gradually increases in average sense. The amplitude of the oscillation decreases with time. The increase rate of the maximum density is larger for the larger amplitude of the oscillation, because the deformation of the massive neutron star induced by the oscillation enhances the angular momentum transport from the inner core to the outer envelope via the hydrodynamical process.

The oscillation of the maximum density lasts for $\sim$ 10 times the oscillation period. After that, the maximum density secularly increases due to the angular momentum loss of the inner core. In some cases, the maximum density suddenly increases, e.g., APR4-130150 in the upper left panel of Fig. 6.3. This indicates that an HMNS collapses to a black hole at the moment. The amplitude of the oscillation depends on the total mass of an NS–NS for a given EOS. For a merger of a more massive NS–NS, the amplitude of the oscillation is larger.

Evolution of shape of a remnant neutron star

A massive neutron star formed after the merger is rapidly rotating and non-axisymmetric (cf. Figs. 6.4 and 6.5). The merger process depends on the mass ratio, and total mass, and EOS. The mass ratio, in particular, becomes a key ingredient for determining the evolution process of the density profile and the configuration of a massive neutron star in a quasistationary state. Here, we pay special attention to the dependence of the evolution of the massive neutron star configuration on the binary mass ratio.

First, we summarize the evolution process of a massive neutron star for equal-mass cases (see Fig. 6.4). For this case, a massive neutron star composed of two cores is formed soon after the onset of the merger irrespective of the EOSs. Then, due to the loss of their angular momentum by the hydrodynamical angular-momentum transport and gravitational-wave emission, the shape changes gradually to an ellipsoidal one, and the ellipticity decreases with time. Here, the time scale of the angular-momentum loss depends on the EOS (the compactness of massive neutron stars). For soft EOSs APR4 and SLy for which the amplitude of an excited quasiradial oscillation is large in the early evolution stage of a massive neutron star (see Fig. 6.3). The time scale of the angular-momentum loss is short ($\sim 10\,$ms). For stiff EOSs H4, MS1, and Shen, the time scale is rather long. For these stiff EOSs, the evolution time scale from the two-core shape to the spheroidal shape is relatively long $> 10\,\mathrm{ms}$. These facts can be found from Fig. 6.3, and also Fig. 4 of Sekiguchi et al. (2011a).

For unequal-mass cases, the evolution process of a remnant massive neutron star configuration is different from that for equal-mass cases. To make the difference clear, we focus here on the case of $M_A = 1.2M_\odot$ and $M_B = 1.5M_\odot$ (see Fig. 6.5). For this case, the configuration of a massive neutron star changes with the dynamical time scale in the early evolution stage. The reason is as follows: In the merger stage, the less-massive neutron star is tidally deformed and its outer part is stripped during the merger. Then, the stripped material forms an envelope of the remnant massive neutron star, while the core of the less-massive neutron star interacts with the core of the massive companion. As a result, the massive neutron star is composed of two asymmetric cores (see the first two panels of Fig. 6.5). Because the gravity of the less-massive core is much weaker than that of the massive one, the less-massive core behaves as a satellite that is significantly and dynamically deformed by the massive core, varying its shape with time. Eventually, the shape of the massive neutron star becomes approximately spheroidal shape (see the third panel of Fig. 6.5).

All these evolution processes of massive neutron stars are well reflected in their gravitational waveforms. In the next section, we will summarize the properties of waveforms of gravitational waves from remnant massive neutron stars.

6.3 Gravitational Waveforms from remnant massive neutron stars

A massive neutron star formed after an NS–NS merger emits gravitational waves because of its non-axisymmetric shape as mentioned in the previous section. The gravitational-wave signal from a massive neutron star contains abundant information of neutron-star matter. In this section, we show gravitational waveforms and discuss the correlation between waveforms and physical parameters of an NS–NS system.

6.3.1 Waveforms

Figure 6.6–6.10 show the gravitational waveforms obtained with numerical relativity simulations for various total masses, mass ratios, and EOSs. Each panel displays a waveform Dh_+/M and its frequency, simultaneously. A gravitational-wave amplitude and frequency gradually increase before the merger of two neutron stars, the so-called chirp signal. After the merger, the waveforms emitted by a massive neutron star are rich in variety, depending on the total mass, mass ratio, and EOS.

Amplitude

Broadly speaking, the amplitude of the gravitational waves emitted by a massive neutron star decreases with time because the shape of a massive neutron star approaches to be axisymmetric due to the angular momentum transport via the hydrodynamical process and gravitational-wave emission.

At the onset of a merger, a gravitational-wave amplitude has a maximum value. In turn, the amplitude becomes very small, because merged neutron stars are compressed in a small volume due to a strong gravity and its shape is nearly spherical at the moment. At the same time, gravitational-wave frequency has the maximum value. If the total mass M is less than $M_{\rm crit,1}$, a massive neutron star is formed and emits gravitational waves at the frequency 2–4 kHz.

Roughly speaking, the frequency of gravitational waves from a remnant massive neutron star corresponds to its rotational frequency. Therefore the modulation in gravitational-wave frequency implies the existence of a radial oscillation of a massive neutron star. Such oscillation lasts for $\sim$ 5ms. The amplitude of the oscillation is larger for the case that the total mass M is close to the critical mass $M_{\rm crit,1}$, because the remnant HMNS is the unstable configuration. Note that the frequency of gravitational waves from a massive neutron star gradually increases due to gravitational contraction.

6.3.2 Characteristic frequency and neutron star radius

A characteristic frequency of the gravitational-wave signal from a remnant massive neutron star is related to the radius of merging neutron stars (Bauswein and Janka 2012; Bauswein et al. 2012). Here we discuss this topic in more details.

A characteristic frequency is defined in both the Fourier domain and the time domain. A characteristic frequency in the Fourier domain is defined as the frequency at a Fourier peak in Fourier spectra. Figure 6.11 shows the Fourier spectra of the gravitational-wave signals shown in Fig. 6.6–6.10. Each Fourier spectrum has a sharp peak, which corresponds to the rotational frequency of a massive neutron star. A characteristic frequency in the Fourier domain is useful to discuss the detectability of the signals, because the amplitude of a Fourier peak can be easily compared with the detector noise curves, as shown in Fig. 6.11. However, a Fourier spectrum has several peaks in some cases. For such a case, the value of the characteristic frequency is unclear.

A characteristic frequency in the time domain is defined as

$$f_{\rm ave} := \frac{\displaystyle\int_{t_{\rm c}}^{t_{\rm f}} f|h|dt}{\displaystyle\int_{t_{\rm c}}^{t_{\rm f}} |h|dt}, \tag{6.13}$$

where we use $|h| = (h_+^2 + h_\times^2)^{1/2}$ as the weight factor in order to take into account the gravitational-wave power. To take the average of a characteristic frequency, we use a time window between $t_{\rm c}$ and $t_{\rm f}$, where $t_{\rm c}$ and $t_{\rm f}$ are the coalescence time and the time at the end the time window, respectively. In order to estimate uncertainties in the value of characteristic frequencies, the physical dispersion of f is defined by

$$\sigma_f^2 := \frac{\displaystyle\int_{t_\mathrm{c}}^{t_\mathrm{f}} (f - f_\mathrm{ave})^2 |h| dt}{\displaystyle\int_{t_\mathrm{c}}^{t_\mathrm{f}} |h| dt}. \tag{6.14}$$

A characteristic frequency in the time domain has no ambiguity, in contrast to that in the Fourier domain. However, the dispersion is enhanced due to oscillation of a massive neutron star in the early phase ($\leq$ 5ms after a merger).

We show characteristic frequencies in both the Fourier domain and the time domain in Table 6.3.2. For Fourier peaks, two or three values are shown for the case that the Fourier spectrum has multiple peaks. For characteristic frequencies in the time domain, we adopt three different durations of time windows $t_\mathrm{f} - t_\mathrm{c} = (5,\ 10,\ 20)$ ms.

As pointed out in Bauswein and Janka (2012); Bauswein et al. (2012), we also find that a certain correlation exists between the characteristic frequency and a stellar radius of a cold spherical neutron star in isolation. Figure 6.12 plots the frequency of the Fourier spectrum peak as a function of the neutron-star radius of mass $1.8M_\odot$ (upper panels) and $1.6M_\odot$ (lower panels) for a given EOS (denoted by $R_{1.8}$ and $R_{1.6}$ in units of km) for $M = 2.7M_\odot$ (left panels) and $2.6M_\odot$ (right panels) †. For $M = 2.7M_\odot$ case, we also plot the Fourier spectrum peak of the results of Bauswein and Janka (2012); Bauswein et al. (2012) for comparison ‡. The dotted curves are

$$f = (4.0 \pm 0.3)\,\mathrm{kHz}\left(\frac{(R_{1.8}/\mathrm{km}) - 2}{8}\right)^{-3/2}, \tag{6.15}$$

for the upper left panel,

$$f = (3.85 \pm 0.15)\,\mathrm{kHz}\left(\frac{(R_{1.8}/\mathrm{km}) - 2}{8}\right)^{-3/2}, \tag{6.16}$$

for the upper right panel,

$$f = (4.15 \pm 0.35)\,\mathrm{kHz}\left(\frac{(R_{1.6}/\mathrm{km}) - 2}{8}\right)^{-3/2}, \tag{6.17}$$

†It should be noted that irrespective of the mass ratio, the chirp mass defined by $(M_A M_B)^{3/5} M^{-1/5}$ is approximately equal to the value for the equal-mass system, $2^{-6/5}M$, within 1% error for $0.8 \leq q \leq 1$. Thus, we may approximately consider that the plots of Fig. 6.12 are the plots for a given value of the chirp mass. In the data analysis of the chirp signal of gravitational waves, the chirp mass will be determined accurately but the mass ratio may not be Cutler and Flanagan (1994); Poisson and Will (1995). For this reason, we generated Fig. 6.12 for a given value of m irrespective of the mass ratio.

‡Here we choose only the data of which the maximum mass of given EOSs is larger than $1.97M_\odot$ (see details in Table II of Bauswein and Janka (2012); Bauswein et al. (2012)).

for the lower left panel, and

$$f = (3.95 \pm 0.25)\,\mathrm{kHz}\left(\frac{(R_{1.6}/\mathrm{km}) - 2}{8}\right)^{-3/2}, \tag{6.18}$$

for the lower right panel. These curves approximately show the upper and lower limits of the characteristic frequency. We note that the subtraction factor of -2 for $R_{1.8}$ and $R_{1.6}$ is empirically needed to capture the upper and lower limits for the star of radius $\sim 11\,\mathrm{km}$. The reason seems to be due to the fact that general relativistic corrections play an important role for the small value of the neutron-star radius. The reason why $R_{1.8}$ is employed is that we found it a better choice to get a clear correlation between the peak frequency and a neutron-star radius for our results. The choice of $R_{1.6}$ is done following (Bauswein and Janka 2012; Bauswein et al. 2012). In both cases, our results of the correlation between the characteristic frequency and a stellar radius are largely consistent with the results of Bauswein and Janka (2012); Bauswein et al. (2012) within the uncertainty represented with the dotted curves.

For the figure, we plotted all the values of the peak frequency when we found multiple peaks; for some models, we plotted 2 or 3 points. We also plotted all the data irrespective of the values of Γ_{th} for APR4 and H4. Possible unknown dispersion associated with the shock heating effect is taken into account in these plots. Nevertheless, we still find a clear correlation for the choice of $R_{1.8}$. In particular for the lower-mass models ($M = 2.6M_{\odot}$), the dispersion is quite small. This figure suggests that if we can determine the peak frequency accurately, we will be able to constrain the radius of the neutron star with the uncertainty of $\sim 1\,\mathrm{km}$. However, it is also found that it is not easy to reduce the estimation error to $\ll 1\,\mathrm{km}$, because of the presence of the systematic dispersion of the peak frequency.

The peak frequencies are associated with the major frequencies of the quasiperiodic oscillation of gravitational waves emitted by a massive neutron star as found in Figs. 6.6 – 6.10. However, as already mentioned, the (non-axisymmetric) oscillation frequency of the massive neutron stars changes during the evolution due to a quasiradial oscillation (which changes the peak frequency as $R_{\mathrm{MNS}}^{-3/2}$) and to the secular dissipation processes of their angular momentum, and hence, the major frequencies change with time, resulting in the broadening of the peak or appearance of the multiple peaks (e.g., the spectra for APR4-135135, APR4-130140, H4-120150, ALF2-130130, and ALF2-120150). This broadening is not very large for particular models such as equal-mass models of some EOSs (see a discussion in the last paragraph of this section), and thus, for these particular cases, the characteristic frequency may be determined with a small dispersion. However, in general, the broadening value is $\sim 10\%$ of the peak frequencies which is $\sim 2 - 3.5\,\mathrm{kHz}$. Therefore, it will not be easy to strictly determine the peak frequencies from the Fourier spectrum. This situation will bring a serious problem in the real data analysis, in which the noise level is by several 10 percent as large as the signal amplitude; the peak will not be determined strictly due to the presence of many fake peaks and spurious broadening.

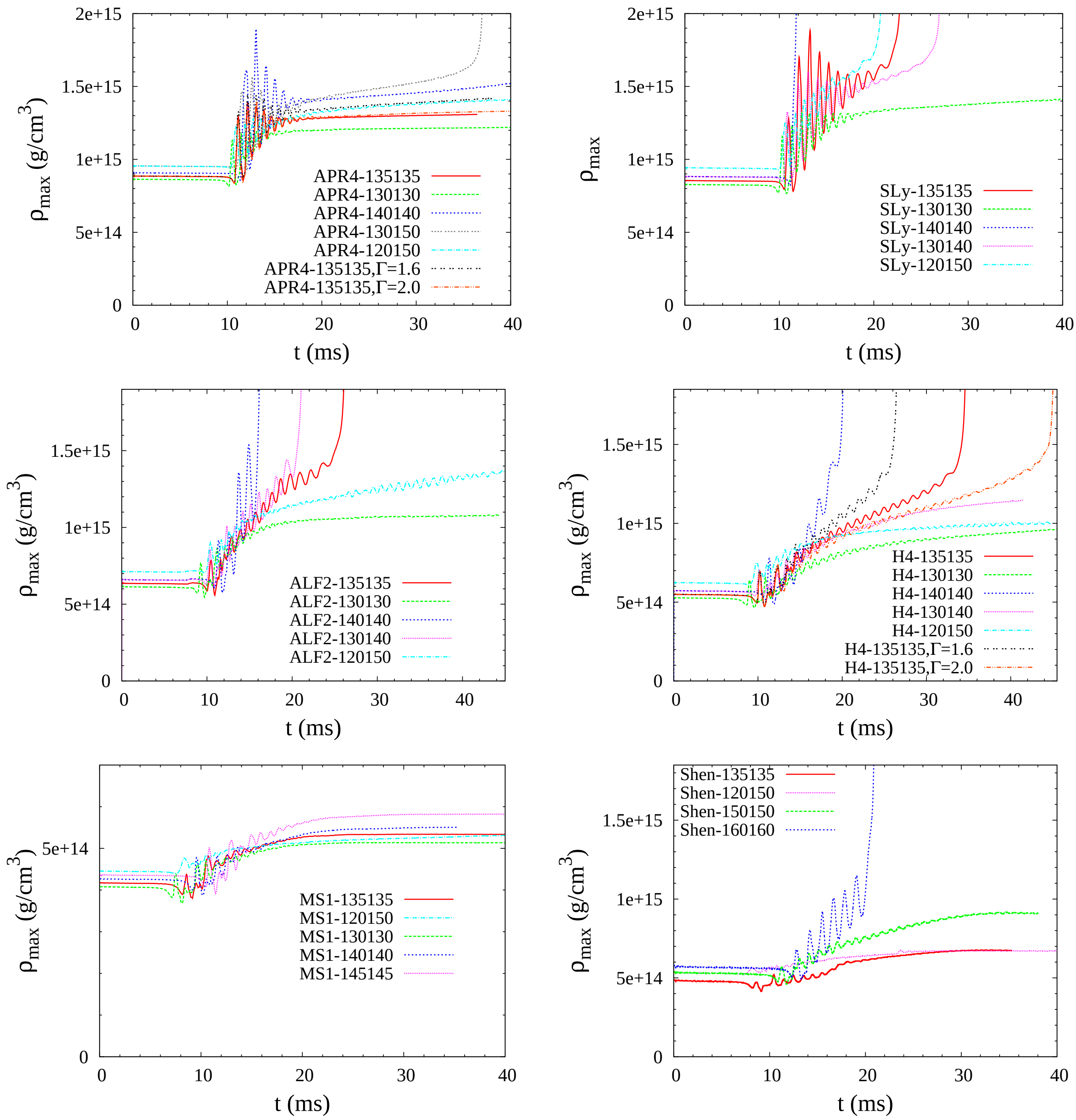

Figure 6.3: Maximum density as a function of time for APR4 (top left), SLy (top right), ALF2 (middle left), H4 (middle right), MS1 (bottom left), and Shen (bottom right) EOSs with several values of binary mass. Note that Γ for the panel of APR4 and ALF2 denotes $\Gamma_{\rm th}$ and the absence of Γ value means that $\Gamma_{\rm th} = 1.8$. For APR4-140140 and ALF2-120150, we confirmed that a black hole was eventually formed at $t \sim 47\,\mathrm{ms}$ and $52\,\mathrm{ms}$. This figure is taken from Hotokezaka et al. (2013a).

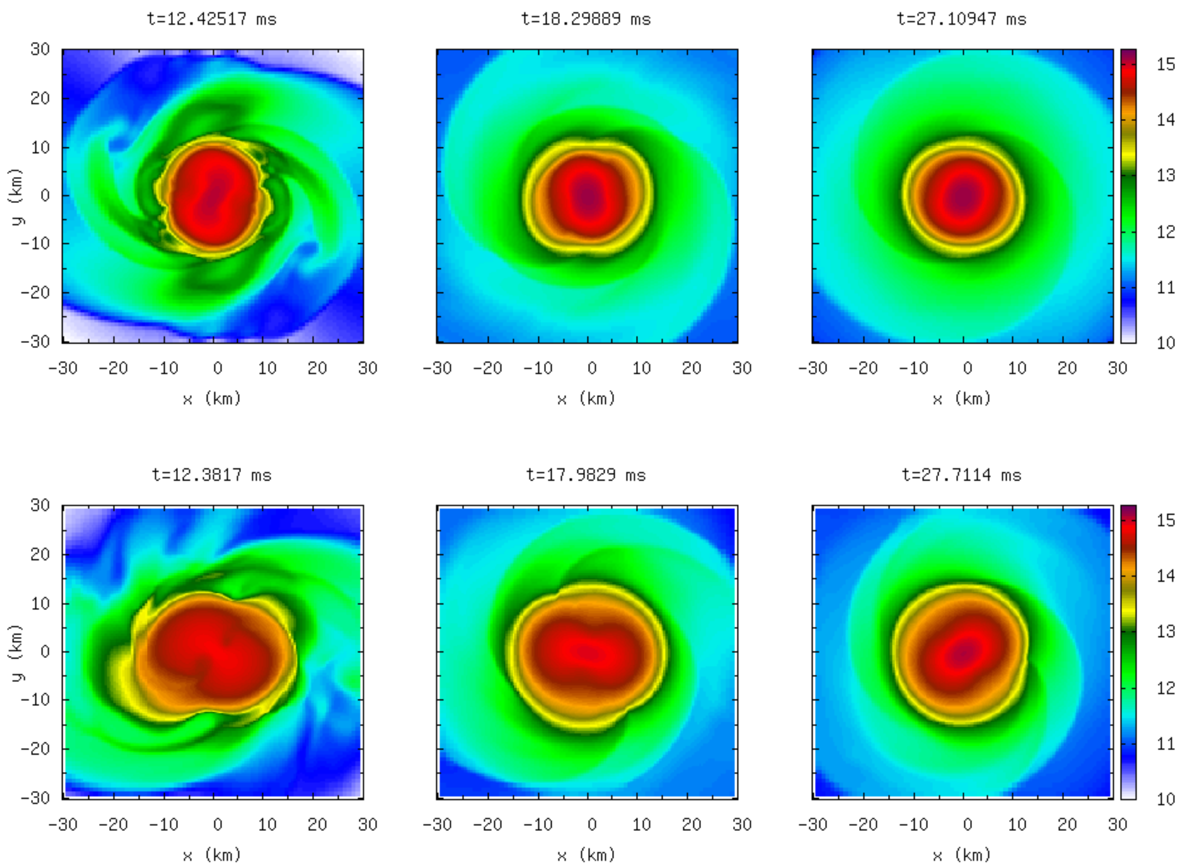

Figure 6.4: Snapshots of the density profile in the equatorial plane at selected time slices for equal-mass models APR4-135135 (upper panel) and H4-135135 (lower panel) with $\Gamma_{\rm th} = 1.8$. This figure is taken from Hotokezaka et al. (2013a).

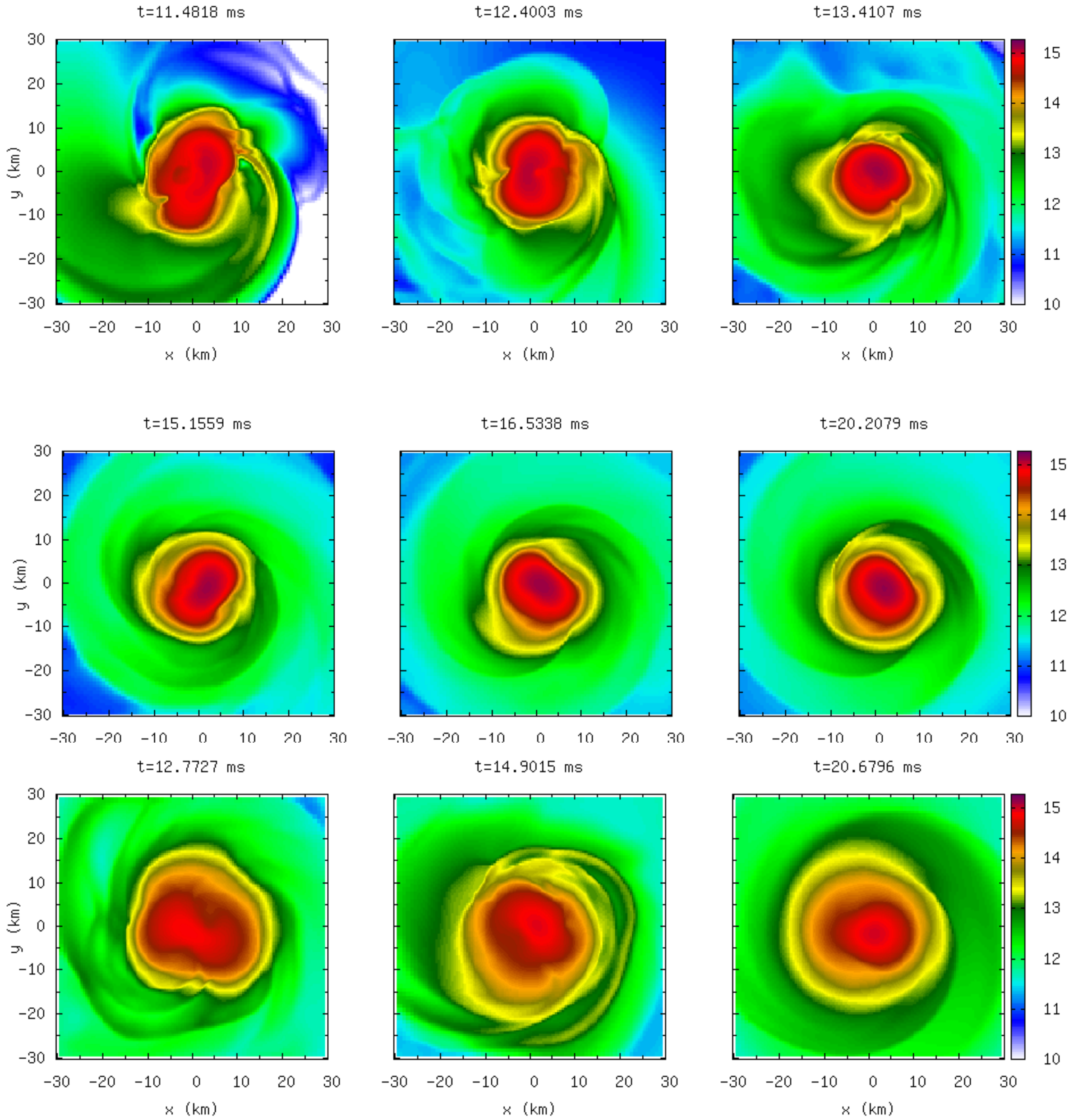

Figure 6.5: The same as Fig. 6.4 but for unequal-mass models APR4-120150 (upper and middle panels) and H4-120150 (bottom panel). This figure is taken from Hotokezaka et al. (2013a).

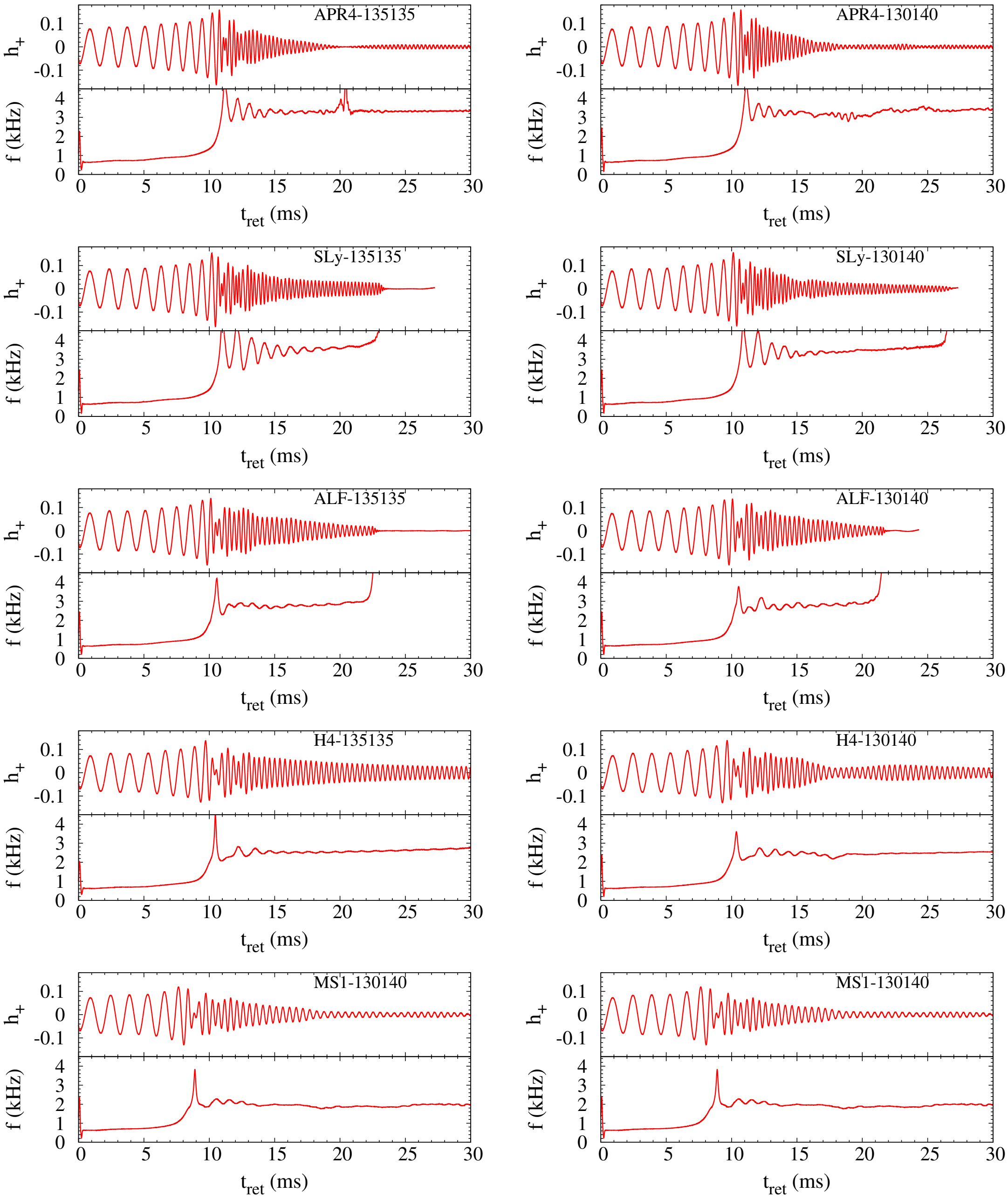

Figure 6.6: Gravitational waves (h_+D/M) and the frequency of gravitational waves f (kHz) as functions of retarded time for models $M_A = M_B = 1.35M_\odot$ and $(M_A, M_B) = (1.30M_\odot, 1.40M_\odot)$ with APR4 (top row), SLy (second row), ALF2 (third row), H4 (fourth row), and MS1 (bottom row). For SLy and ALF2, a black hole is eventually formed for $t_{\rm ret} < 30\,$ms. For all the models, $\Gamma_{\rm th} = 1.8$. The vertical axis of the gravitational waveforms shows the non-dimensional amplitude, h_+D/M, with D being the distance to the source. Spikes in the curves of $f(t)$ (for the plot of APR4-135135 and MS1-135135) are not physical; these are generated when the gravitational-wave amplitude is too low to determine the frequency accurately. This figure is taken from Hotokezaka et al. (2013a).

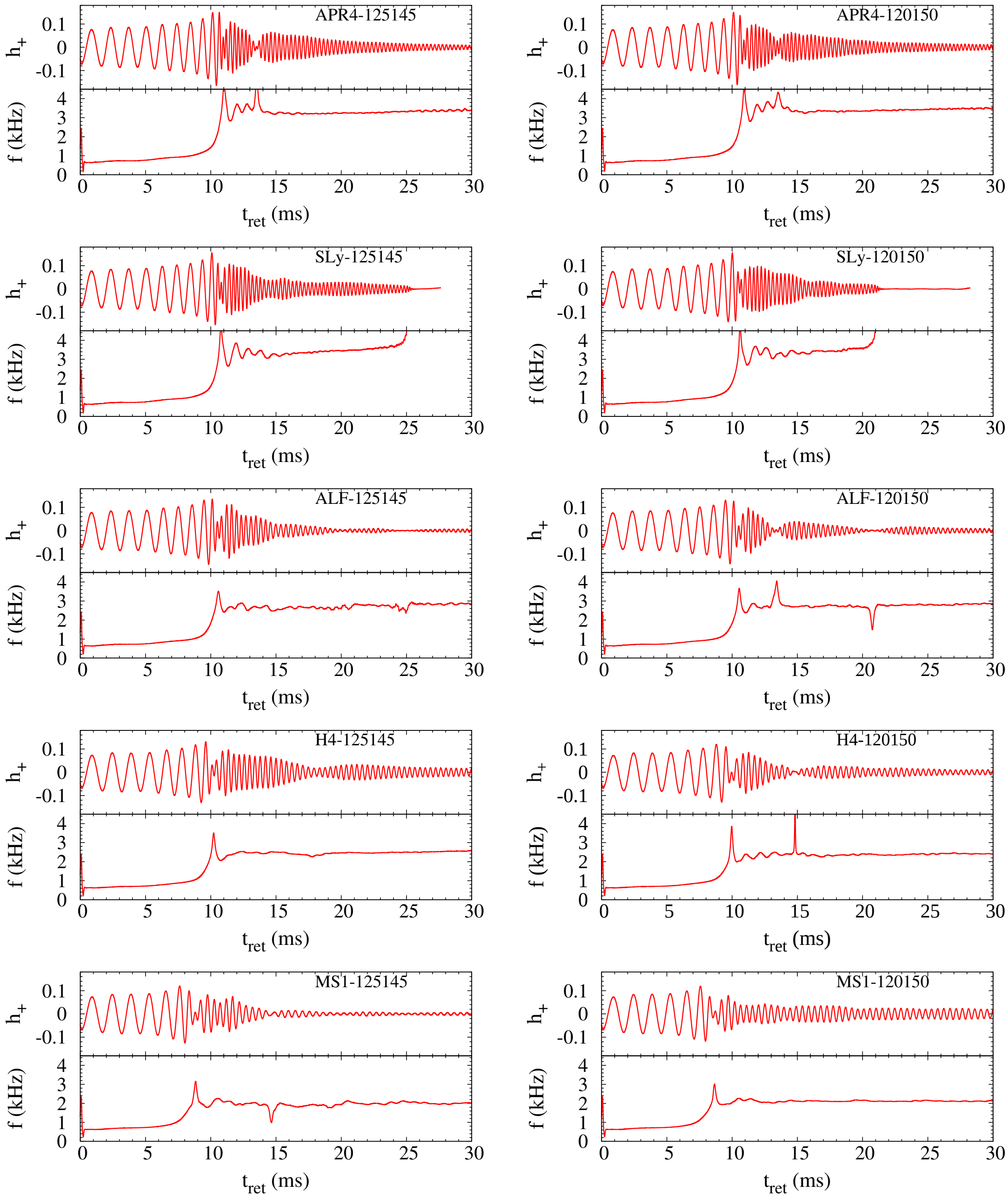

Figure 6.7: The same as Fig. 6.6 but for $(M_A, M_B) = (1.25M_\odot, 1.45M_\odot)$ (left) and $(1.20M_\odot, 1.50M_\odot)$ (right). This figure is taken from Hotokezaka et al. (2013a).

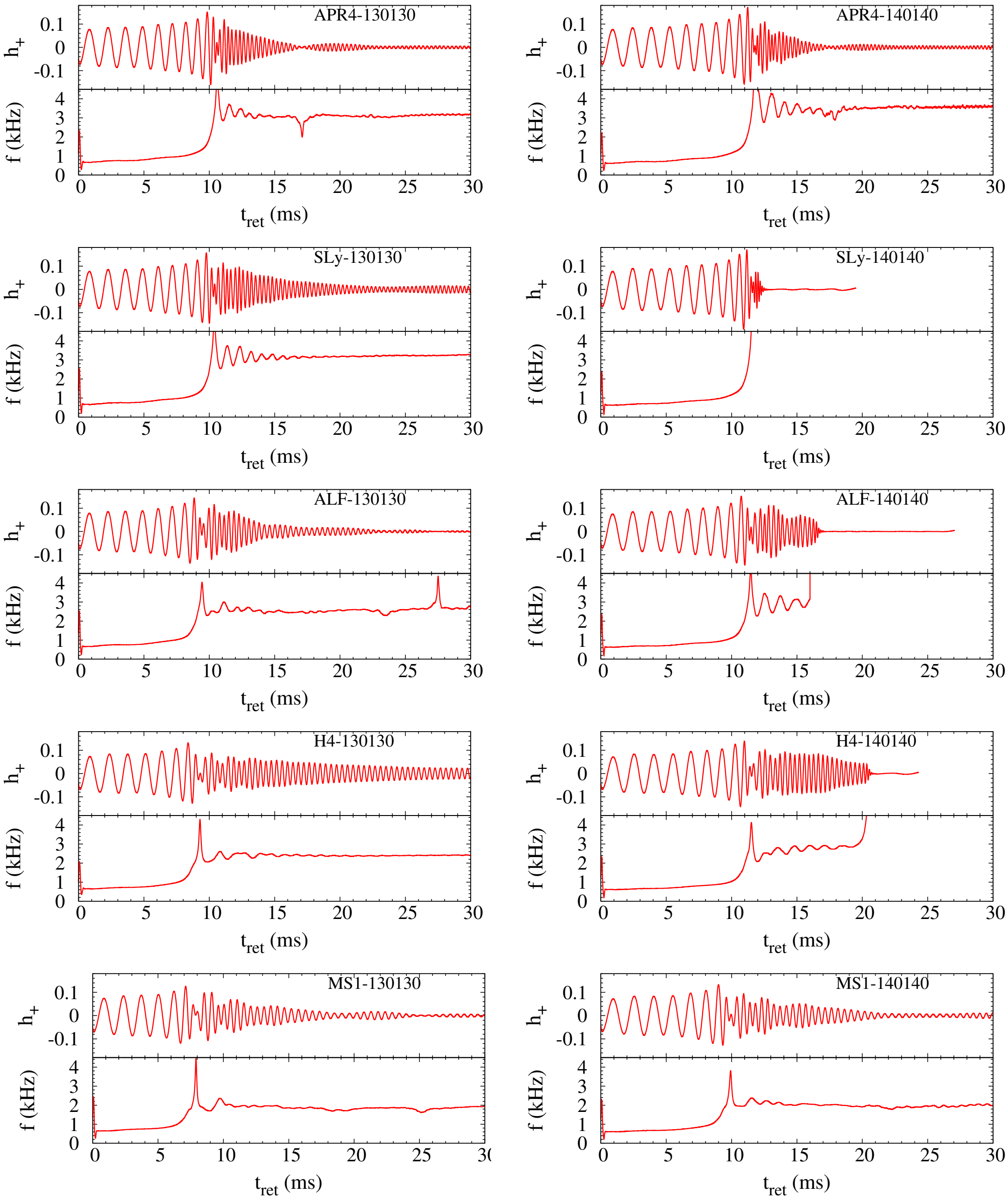

Figure 6.8: The same as Fig. 6.6 but for $M_A = M_B = 1.3M_\odot$ (left) and $M_A = M_B = 1.4M_\odot$ (right). This figure is taken from Hotokezaka et al. (2013a).

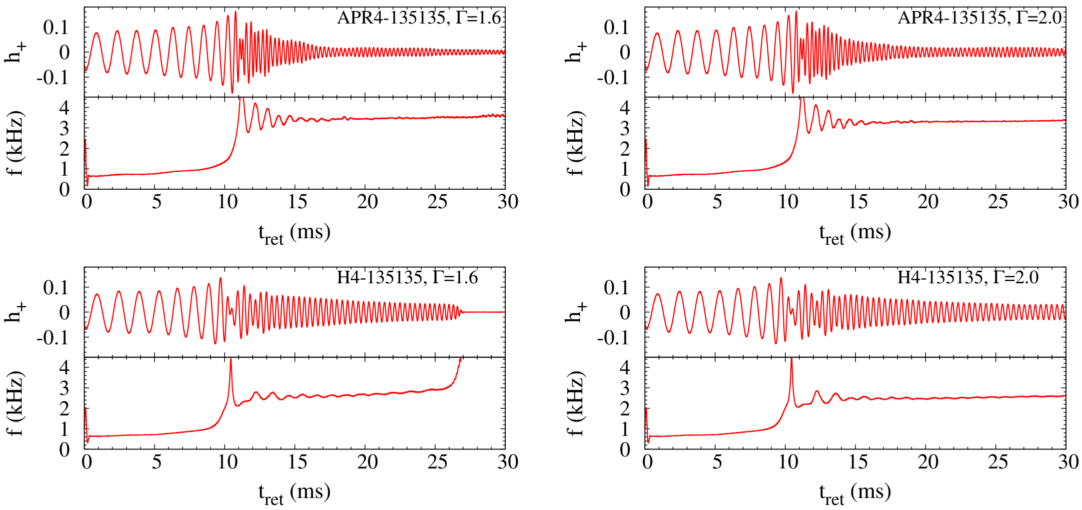

Figure 6.9: The same as Fig. 6.6 but for $M_A = M_B = 1.35M_\odot$ and $\Gamma_{\rm th} = 1.6$ (left) and 2.0 (right) with APR4 (upper row) and H4 (lower row) EOSs. This figure is taken from Hotokezaka et al. (2013a).

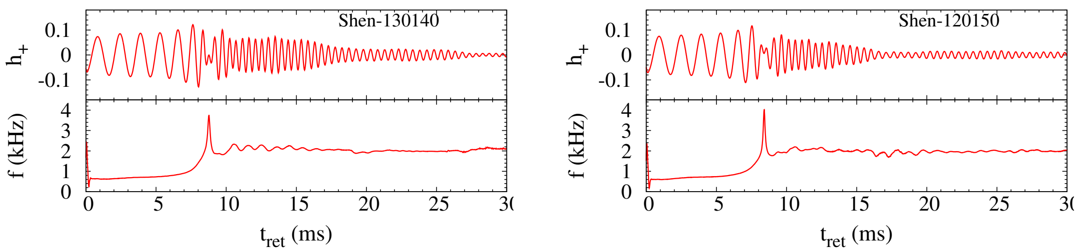

Figure 6.10: The same as Fig. 6.6 but for Shen EOSs with $(M_A, M_B) = (1.3M_\odot, 1.4M_\odot)$ and $(1.2M_\odot, 1.5M_\odot)$. This figure is taken from Hotokezaka et al. (2013a).

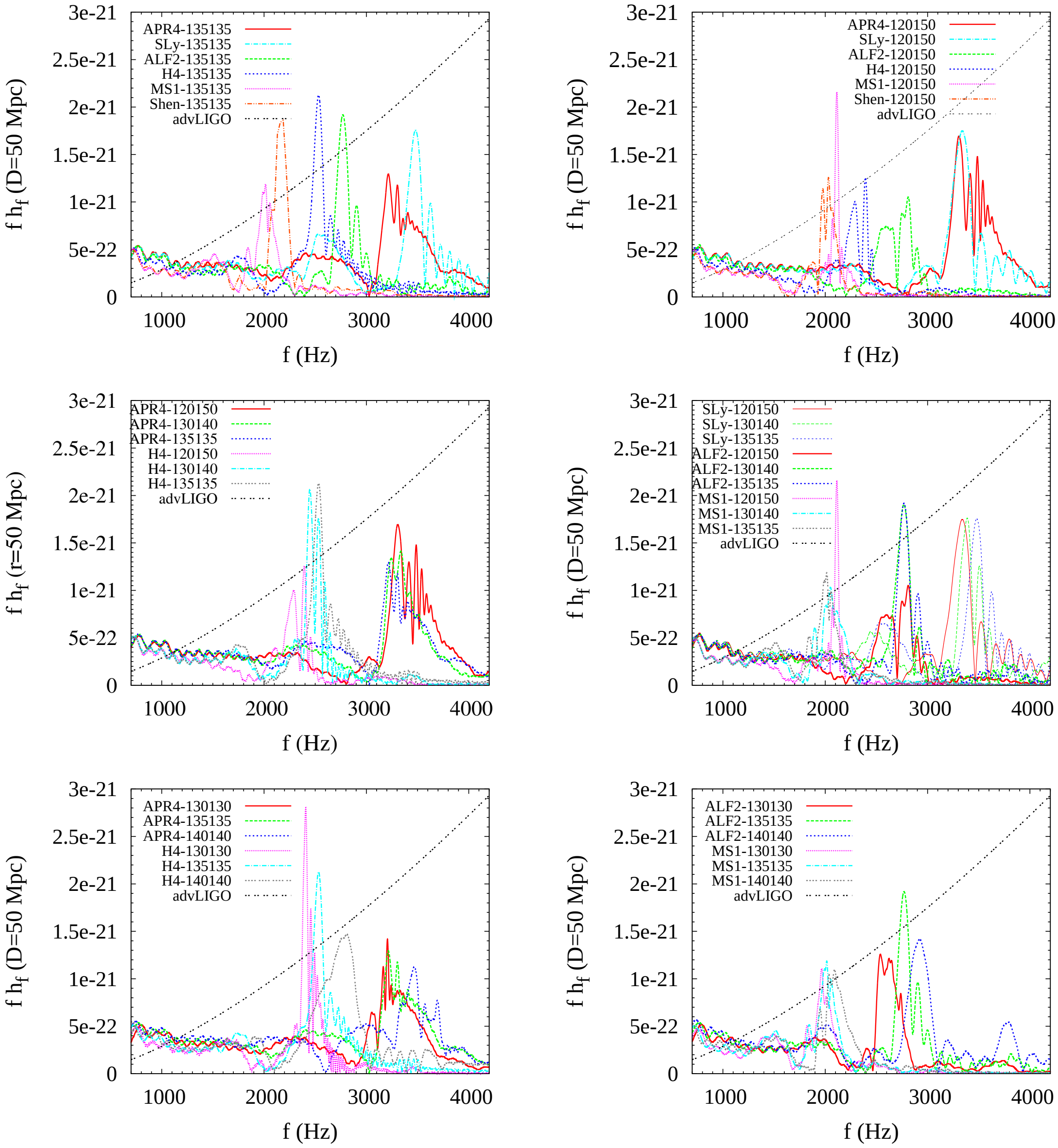

Figure 6.11: Fourier spectra of gravitational waves for some of results shown in Figs. 6.6 – 6.10: Top left; for $M_A = M_B = 1.35M_\odot$ with $\Gamma_{\rm th} = 1.8$ and with five piecewise polytropic and Shen EOSs: Top right; the same as top left but for $M_A = 1.2M_\odot$ and $M_B = 1.5M_\odot$: Middle left; for three mass ratios with $M = 2.7M_\odot$, $\Gamma_{\rm th} = 1.8$, and with APR4 and H4: Middle right; the same as middle left but for SLy, ALF2, and MS1: Bottom left; for equal-mass models with $M = 2.6$, 2.7, and $2.8M_\odot$, $\Gamma_{\rm th} = 1.8$, and with APR4 and H4: Bottom right; the same as bottom left but for ALF2 and MS1. The amplitude is shown for the hypothetical event at a distance of $D = 50\,$Mpc along the direction perpendicular to the orbital plane (the most optimistic direction). The black dot-dot curve is the noise spectrum of the advanced LIGO with an optimistic configuration for the detection of high-frequency gravitational waves (see https://dcc.ligo.org/cgi-bin/DocDB/ShowDocument?docid=2974). This figure is taken from Hotokezaka et al. (2013a).

Table 6.2: Characteristic frequencies of gravitational waves emitted by MNSs which are determined by two different methods: Fourier peak denotes the peak frequencies of the effective amplitude $h(f)f$. $f_{\rm ave,5ms}$, $f_{\rm ave,10ms}$, and $f_{\rm ave,20ms}$ denote the results for Eq. (6.13) with 5, 10, and 20 ms time integration after the formation of the MNSs, — denotes that the lifetime of MNSs is shorter than the corresponding integration time. The deviation of $f_{\rm ave}$ shown here denotes σ_f. The multiple values shown for the Fourier peak imply that we found many peaks for which their peak values of $h(f)f$ are larger than 80% of its maximum value. $f^{\rm fit}_{\rm ave,10ms}$ denote the averaged frequency calculated from the best-fit results of formulae (6.21) – (6.23). The last four columns show the maximum values of $\mathcal{M}$ for a fitting procedure with the number of parameters, $N_{\rm p}$ = 13, 12, 11, and 10 (see Sec. 6.3.3).

Model	$\Gamma_{\rm th}$	Fourier peak (kHz)	$f_{\rm ave,5ms}$ (kHz)	$f_{\rm ave,10ms}$ (kHz)	$f_{\rm ave,20ms}$ (kHz)	$f^{\rm fit}_{\rm ave,10ms}$ (kHz)	$\mathcal{M}_{N_{\rm p}=13}$	$\mathcal{M}_{N_{\rm p}=12}$	$\mathcal{M}_{N_{\rm p}=11}$	$\mathcal{M}_{N_{\rm p}=10}$
APR4-130150	1.8	3.40	3.48 ± 0.47	3.46 ± 0.37	3.49 ± 0.33	3.39 ± 0.29	0.910	0.894	0.894	0.883
APR4-140140	1.8	3.47	3.59 ± 0.64	3.57 ± 0.58	3.53 ± 0.44	3.59 ± 0.59	0.968	0.968	0.967	0.965
APR4-120150	1.6	3.31 3.54	3.47 ± 0.30	3.44 ± 0.27	—	3.44 ± 0.24	0.963	0.962	0.959	0.945
APR4-120150	1.8	3.31,3.43	3.44 ± 0.30	3.41 ± 0.24	3.41 ± 0.21	3.41 ± 0.23	0.959	0.959	0.954	0.951
APR4-120150	2.0	3.18	3.32 ± 0.32	3.27 ± 0.26	3.27 ± 0.22	3.16 ± 0.20	0.924	0.924	0.919	0.919
APR4-125145	1.8	3.23	3.36 ± 0.31	3.31 ± 0.25	3.31 ± 0.23	3.20 ± 0.18	0.930	0.930	0.926	0.907
APR4-130140	1.8	3.28,3.31,3.40	3.30 ± 0.29	3.27 ± 0.28	3.29 ± 0.26	3.26 ± 0.26	0.982	0.982	0.981	0.968
APR4-135135	1.6	3.45	3.46 ± 0.42	3.45 ± 0.37	3.46 ± 0.30	3.44 ± 0.33	0.970	0.967	0.967	0.942
APR4-135135	1.8	3.21,3.30	3.31 ± 0.41	3.28 ± 0.37	3.28 ± 0.34	3.27 ± 0.33	0.970	0.969	0.969	0.947
APR4-135135	2.0	3.29,3.37	3.35 ± 0.39	3.33 ± 0.34	3.33 ± 0.29	3.29 ± 0.17	0.952	0.952	0.947	0.947
APR4-120140	1.8	3.14	3.15 ± 0.21	3.13 ± 0.19	3.12 ± 0.18	3.11 ± 0.16	0.982	0.981	0.981	0.972
APR4-125135	1.8	3.20	3.22 ± 0.25	3.19 ± 0.24	—	3.15 ± 0.17	0.975	0.975	0.974	0.963
APR4-130130	1.8	3.21	3.22 ± 0.28	3.19 ± 0.26	3.18 ± 0.24	3.18 ± 0.28	0.974	0.970	0.965	0.958
SLy-120150	1.8	3.34	3.31 ± 0.26	3.35 ± 0.24	—	3.32 ± 0.19	0.984	0.983	0.979	0.979
SLy-125145	1.8	3.32	3.29 ± 0.32	3.32 ± 0.27	—	3.31 ± 0.28	0.969	0.957	0.948	0.948
SLy-130140	1.8	3.39	3.35 ± 0.47	3.36 ± 0.40	—	3.38 ± 0.42	0.965	0.959	0.958	0.913
SLy-135135	1.8	3.48	3.41 ± 0.58	3.46 ± 0.48	—	3.47 ± 0.47	0.963	0.952	0.946	0.893
SLy-130130	1.8	3.16	3.17 ± 0.34	3.16 ± 0.29	3.18 ± 0.26	3.16 ± 0.28	0.988	0.988	0.987	0.972
ALF2-140140	1.8	2.92	2.93 ± 0.42	—	—	2.90 ± 0.34	0.980	0.955	0.952	0.911
ALF2-120150	1.8	2.74,2.82,2.87	2.70 ± 0.19	2.71 ± 0.16	2.73 ± 0.15	2.61 ± 0.20	0.924	0.916	0.916	0.907
ALF2-125145	1.8	2.65	2.66 ± 0.14	2.66 ± 0.13	2.67 ± 0.13	2.63 ± 0.09	0.985	0.985	0.985	0.985
ALF2-130140	1.8	2.77	2.73 ± 0.19	2.75 ± 0.17	—	2.75 ± 0.12	0.981	0.979	0.978	0.977
ALF2-135135	1.8	2.77	2.74 ± 0.17	2.76 ± 0.15	—	2.74 ± 0.12	0.989	0.989	0.981	0.981
ALF2-130130	1.8	2.54,2.63,2.65	2.58 ± 0.18	2.56 ± 0.16	2.56 ± 0.15	2.55 ± 0.12	0.978	0.975	0.973	0.972

Model	$\Gamma_{\rm th}$	Fourier peak (kHz)	$f_{\rm ave,5ms}$ (kHz)	$f_{\rm ave,10ms}$ (kHz)	$f_{\rm ave,20ms}$ (kHz)	$f^{\rm fit}_{\rm ave,10ms}$ (kHz)	$\mathcal{M}_{N_{\rm p}=13}$	$\mathcal{M}_{N_{\rm p}=12}$	$\mathcal{M}_{N_{\rm p}=11}$	$\mathcal{M}_{N_{\rm p}=10}$
H4-130160	1.8	2.72	2.64 ± 0.26	—	—	2.64 ± 0.26	0.973	0.965	0.963	0.942
H4-145145	1.8	2.90,2.96	2.97 ± 0.56	—	—	2.93 ± 0.49	0.965	0.965	0.942	0.941
H4-130150	1.8	2.45,2.56	2.44 ± 0.17	2.45 ± 0.15	2.54 ± 0.17	2.42 ± 0.09	0.958	0.956	0.956	0.952
H4-140140	1.8	2.75,2.81	2.63 ± 0.23	2.77 ± 0.41	—	2.69 ± 0.22	0.975	0.975	0.966	0.951
H4-120150	1.6	2.22,2.32,2.38	2.28 ± 0.16	2.29 ± 0.14	2.31 ± 0.14	2.30 ± 0.03	0.980	0.977	0.977	0.966
H4-120150	1.8	2.29,2.39	2.30 ± 0.18	2.31 ± 0.15	2.33 ± 0.14	2.28 ± 0.09	0.955	0.955	0.955	0.939
H4-120150	2.0	2.30	2.24 ± 0.15	2.22 ± 0.14	2.26 ± 0.12	2.22 ± 0.08	0.983	0.980	0.980	0.973
H4-125145	1.8	2.44	2.41 ± 0.15	2.41 ± 0.13	2.44 ± 0.11	2.39 ± 0.13	0.981	0.981	0.980	0.980
H4-130140	1.8	2.43,2.52	2.42 ± 0.17	2.42 ± 0.15	2.44 ± 0.13	2.40 ± 0.13	0.968	0.968	0.967	0.966
H4-135135	1.6	2.59	2.49 ± 0.19	2.54 ± 0.16	—	2.54 ± 0.15	0.985	0.968	0.966	0.960
H4-135135	1.8	2.53	2.44 ± 0.20	2.48 ± 0.16	2.54 ± 0.17	2.48 ± 0.14	0.984	0.982	0.978	0.963
H4-135135	2.0	2.49	2.39 ± 0.21	2.43 ± 0.17	2.47 ± 0.15	2.44 ± 0.14	0.977	0.977	0.972	0.972
H4-120140	1.8	2.34,2.37,2.43	2.30 ± 0.15	2.30 ± 0.14	2.33 ± 0.13	2.32 ± 0.06	0.948	0.948	0.947	0.912
H4-125135	1.8	2.26	2.29 ± 0.17	2.27 ± 0.14	2.26 ± 0.12	2.28 ± 0.14	0.973	0.971	0.971	0.966
H4-130130	1.8	2.31	2.35 ± 0.18	2.38 ± 0.14	2.38 ± 0.11	2.37 ± 0.12	0.982	0.982	0.980	0.980
MS1-130160	1.8	2.12	2.07 ± 0.15	2.06 ± 0.13	—	2.02 ± 0.14	0.967	0.967	0.965	0.956
MS1-145145	1.8	2.11	2.12 ± 0.15	2.09 ± 0.13	—	2.09 ± 0.12	0.979	0.979	0.978	0.978
MS1-140140	1.8	2.04,2.09	2.09 ± 0.14	2.07 ± 0.12	2.05 ± 0.12	2.06 ± 0.12	0.972	0.972	0.968	0.964
MS1-120150	1.8	2.11	2.08 ± 0.11	2.09 ± 0.09	2.10 ± 0.07	2.08 ± 0.10	0.987	0.987	0.987	0.983
MS1-125145	1.8	2.02,2.08	2.02 ± 0.14	1.99 ± 0.15	1.99 ± 0.14	1.97 ± 0.16	0.959	0.959	0.955	0.953
MS1-130140	1.8	2.05	2.06 ± 0.14	2.02 ± 0.13	2.00 ± 0.13	2.03 ± 0.11	0.978	0.976	0.975	0.973
MS1-135135	1.8	1.99,2.02,2.05	1.98 ± 0.17	1.96 ± 0.15	1.95 ± 0.14	2.00 ± 0.22	0.951	0.951	0.941	0.935
MS1-130130	1.8	1.96	1.94 ± 0.18	1.93 ± 0.15	1.91 ± 0.15	1.96 ± 0.22	0.950	0.950	0.948	0.943
Shen-120150	—	1.97,2.03	2.02 ± 0.15	2.00 ± 0.13	2.00 ± 0.12	2.01 ± 0.07	0.985	0.977	0.977	0.977
Shen-125145	—	2.10,2.18	2.15 ± 0.17	2.17 ± 0.15	2.15 ± 0.13	2.16 ± 0.12	0.972	0.966	0.964	0.963
Shen-130140	—	2.09,2.12	2.08 ± 0.18	2.09 ± 0.14	2.06 ± 0.15	2.07 ± 0.14	0.972	0.971	0.971	0.967
Shen-135135	—	2.18	2.18 ± 0.18	2.23 ± 0.14	2.21 ± 0.11	2.27 ± 0.06	0.971	0.969	0.967	0.967
Shen-140140	—	2.28	2.29 ± 0.26	2.28 ± 0.19	2.27 ± 0.16	2.31 ± 0.05	0.989	0.989	0.989	0.989
Shen-150150	—	2.29	2.22 ± 0.24	2.13 ± 0.18	2.11 ± 0.16	2.25 ± 0.12	0.989	0.989	0.989	0.984
Shen-160160	—	2.49	2.38 ± 0.37	2.51 ± 0.50	—	2.49 ± 0.20	0.943	0.943	0.930	0.919

6.3.3 Modeling waveforms from massive neutron star remnants

In this subsection, we attempt to construct a phenomenological waveforms for gravitational waves from remnant massive neutron stars. The phenomenological waveforms may be useful to understand the dependence of the waveforms on the physical parameters, such as total mass, mass ratio, and EOS. In addition, the phenomenogical waveforms will be helpful to analyze gravitational-wave signals from remnant massive neutron stars for future gravitational-wave detectors.

In order to construct such a phenomenological waveform, we need to prepare the fitting formulae for the waveforms obtained from numerical relativity simulations. There are two conflicting requirements for the fitting formulae:

- Various numerical waveforms should be well fitted universally by the fitting formulae.
- The fitting formulae should be controlled by minimal numbers of free parameters, to minimize the computational costs for the fitting parameter survey procedures. In addition, the risk of unphysical fitting is decreased with smaller numbers of free parameters.

For this purpose, we have to find an optimized fitting formula that is described by an optimized number of parameters. In order to discover the optimized fitting formula, we introduce a fitting formula that reproduces many characteristic properties of numerical waveforms as a first step. Then, the number of free parameters will be reduced while keeping the matching degree as high as possible.

The universal features of gravitational waveforms emitted by remnant massive neutron stars are summarized as follows:

1. The frequency of gravitational waves reaches a maximum peak soon after the onset of a merger. A damping oscillation, in turn, lasts several oscillation periods. The frequency eventually settles into a constant value, although a long-term secular change associated with the change in the state of massive neutron stars is present.
2. Soon after the onset of the merger, the amplitude of gravitational waves becomes very low. Subsequently, the amplitude steeply increases, and then, it decreases either monotonically or with modulations.
3. The damping time scale of the amplitude is of the order of 10 ms for most massive neutron star model.

The fact (3) implies that the emissivity of gravitational waves of massive neutron stars is in general high for the first ~ 10 ms after their formation. Hence, in order to save the

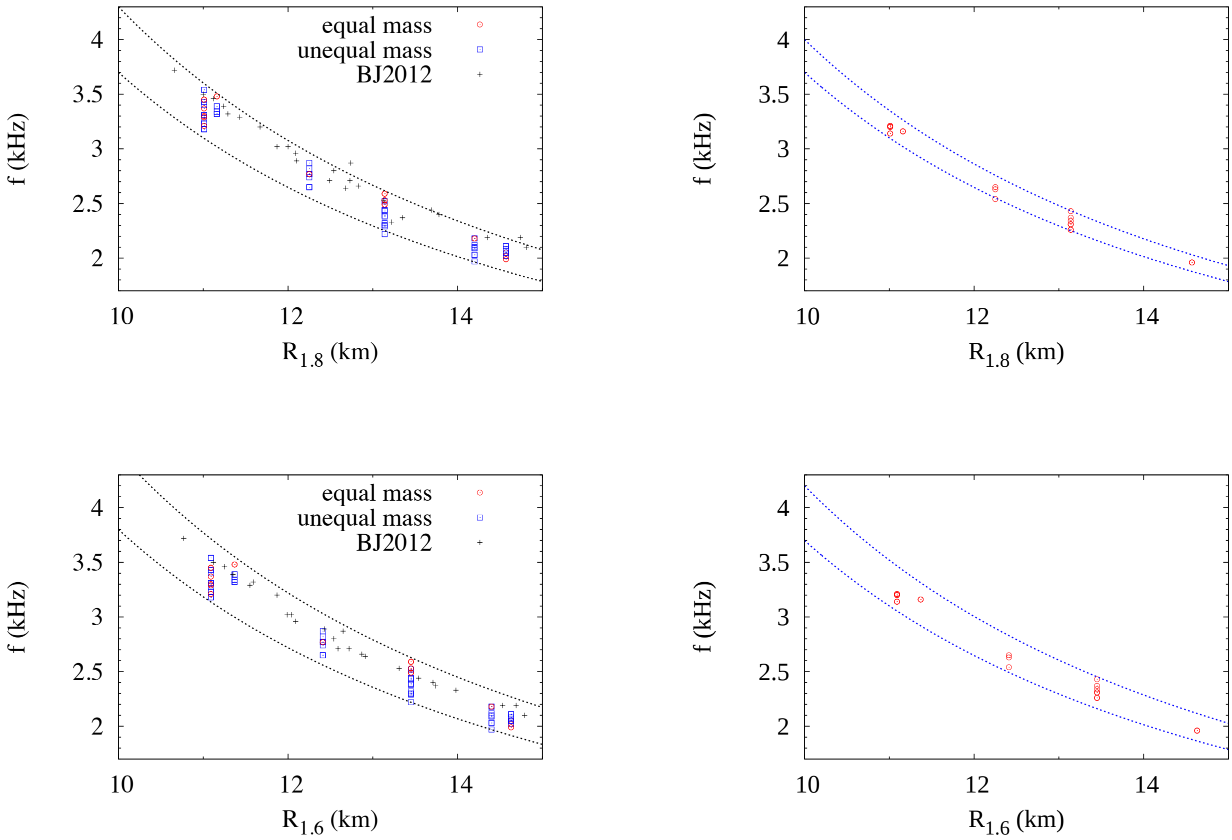

Figure 6.12: The frequency of the Fourier spectrum peak as a function of the neutron-star radius of $M = 1.8M_{\odot}$ (upper panels) and $M = 1.6M_{\odot}$ (lower panels) with a given EOS for $M = 2.7M_{\odot}$ (left panels) and $2.6M_{\odot}$ (right panels). In the right panels, we plotted all the data (equal-mass and unequal-mass data) using the same symbol. In the left panels, the cross symbols denote the data of Bauswein and Janka (2012). This figure is taken from Hotokezaka et al. (2013a).

search costs, we focus on gravitational-wave signals in this time range by using a window function

$$W(t) := \begin{cases} 1 & \text{for } t_c \leq t \leq t_f, \\ 0 & \text{otherwise,} \end{cases} \tag{6.19}$$

where $t = t_c$ is the coalescence time when the frequency peak is reached and t_f is the time at the end of a time window. In the following, we set the origin of time to be $t_c = 0$ for simplicity.

Taking into account the characteristic properties of gravitational waves listed above, we first introduce a fitting formula that contains 13 free parameters as follows. Using the fact that a complex function of any gravitational-wave signal, $h(t)$, can be uniquely

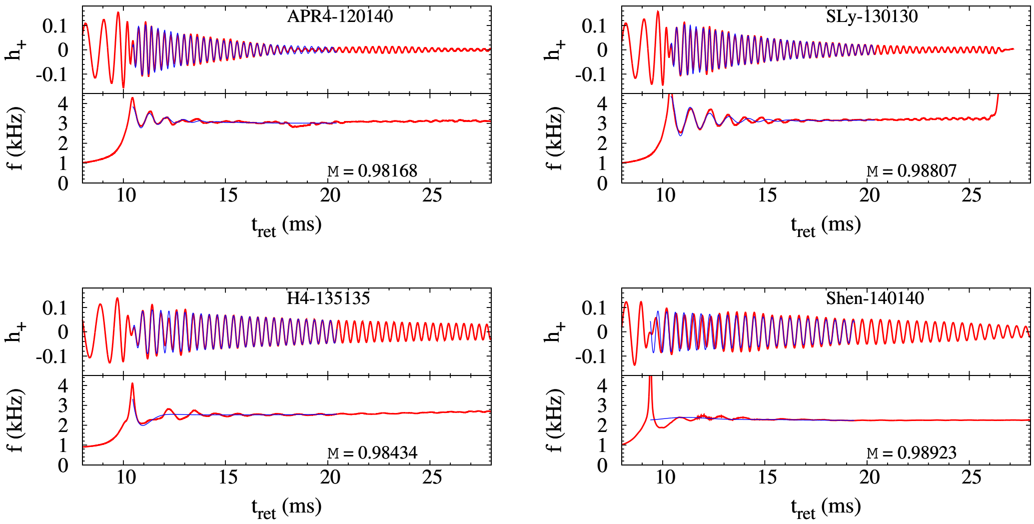

Figure 6.13: Comparison of numerical waveforms with their fitting results for APR4-120140, SLy-130130, H4-135135 with $\Gamma_{\rm th} = 1.8$, and Shen-140140. Gravitational waves (h_+D/M) and the frequency of gravitational waves f (kHz) as functions of retarded time are plotted. The red curves are numerical waveforms, as in Fig. 6.6, while the blue segment curves are the corresponding fitting functions with the best-fit parameters. The numerical value written in the lower right corner of each panel is the value of $\mathscr{M}$. This figure is taken from Hotokezaka et al. (2013a).

decomposed into a pair of real function $AP(t)$ and $PP(t)$ as

$$h(t) = AP(t)\exp\left[-i\,PP(t)\right], \tag{6.20}$$

we consider the following forms of fitting formulae,

$$h_{\rm fit}(t) \;=\; AP_{\rm fit}(t)\exp\left[-i\,PP_{\rm fit}(t)\right], \tag{6.21}$$

where

$$\begin{aligned} AP_{\rm fit}(t) &= \left[a_1\exp\left(-\frac{t}{a_{\rm d}}\right)+a_0\right] \\ &\quad\times\left(\frac{1}{1+\exp\left[(t-a_{\rm co})/t_{\rm cut}\right]}\right) \\ &\quad\times\left[1-\exp\left(-\frac{t}{a_{\rm ci}}\right)\right], \end{aligned} \tag{6.22}$$

$$\begin{aligned} PP_{\rm fit}(t) &= p_0+p_1t+p_2t^2+p_3t^3 \\ &+ \exp\left(-\frac{t}{p_{\rm d}}\right)\left[p_{\rm c}\cos(p_{\rm f}t)+p_{\rm s}\sin(p_{\rm f}t)\right]. \end{aligned} \tag{6.23}$$

Equation (6.22) shows that we model the fitting function for the amplitude part in terms of three parts:

1. $a_1e^{-t/a_{\rm d}}+a_0$ denotes the evolution for the amplitude which is assumed to be composed of an exponentially damping term and a constant term. a_0, a_1, and $a_{\rm d}$ are free parameters that should be determined by a fitting procedure.

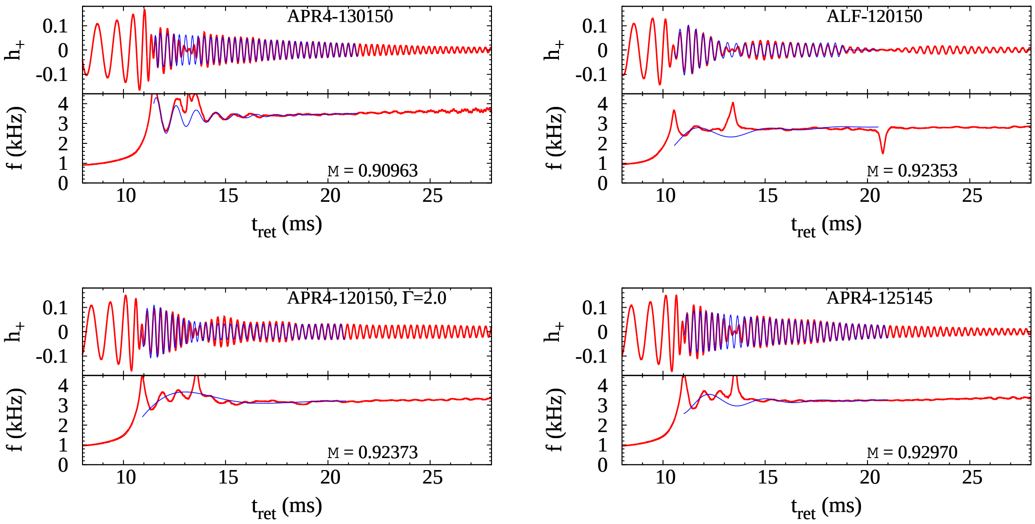

Figure 6.14: The same as Fig. 6.13 but for APR4-130150, ALF2-120150, APR4-120150 (with $\Gamma_{\rm th} = 2.0$), and APR4-125145. This figure shows that our fitting formula (6.21) is relatively poor at fitting the modulating feature in the amplitude. This figure is taken from Hotokezaka et al. (2013a).

2. $[1 + \exp\{(t - a_{\rm co})/t_{\rm cut}\}]^{-1}$ denotes a cutoff term that specifies a time interval of a high-amplitude stage with $a_{\rm co}$ being the center of the cutoff time and $t_{\rm cut}$ being the time scale for the shutdown. $a_{\rm co} < 10\,{\rm ms}$ for the case that a black hole is formed within 10 ms after the formation of a MNS. $a_{\rm co}$ is determined in the fitting process, while $t_{\rm cut}$ is a parameter that should be manually chosen and fixed; we here choose it to be 0.1 ms for simplicity.

3. $1 - \exp(-t/a_{\rm ci})$ is a steeply increasing function for $t \gtrsim t_i$ with $a_{\rm ci}$ being the growth time scale. The reason for introducing this term is that at $t = t_i = 0$, the amplitude of gravitational waves is universally low, but after this moment, the amplitude steeply increases and the time scale depends on the total mass, mass ratio, and EOS.

The fitting function for the amplitude contains five free parameters (a_0, a_1, $a_{\rm d}$, $a_{\rm co}$, $a_{\rm ci}$) which is determined by a fitting procedure. Note that we do not take into account the effects of modulation in amplitude in this fitting formula. To include them, we have to significantly increase the number of free parameters. However, these parameters increase the search costs, and hence, we neglect them.

Equation 6.23 shows the fitting function for the frequency evolution in terms of a secularly evolving terms $p_0+p_1t+p_2t^2+p_3t^3$ and damping oscillation terms $e^{-t/p_d}\,[p_c \cos(p_f t) + p_s \sin(p_f t)]$. Here the fitting function contains eight free parameters which should be determined by a fitting procedure.

Thus, in total, there are 13 parameters to be determined, and we denote them by $\vec{\rm Q}$

in the following. We here stress that 13 parameters are the maximally necessary ones in our present fitting procedure. In the following, we ask whether it is possible to reduce the number as small as possible.

6.3.4 Determining the model parameters

Fitting procedure

First, we focus on the fitting formula that contains 13 parameters and describe how we determine these parameters. For the determination, it might be natural to define the following function

$$\mathscr{M}(h_{\rm fit}) := \frac{(h_{\rm NR}, h_{\rm fit})}{\sqrt{(h_{\rm NR}, h_{\rm NR})(h_{\rm fit}, h_{\rm fit})}}, \tag{6.24}$$

and consider to maximize the absolute value of this function. Here, $(\ \cdot\ ,\ \cdot\ )$ is the inner product defined in the time domain by

$$(a, b) := \mathrm{Re}\left(\int_{t_i}^{t_f} a(t) b^*(t)\, dt\right), \tag{6.25}$$

and we note that the maximum value of $\mathscr{M}(h_{\rm fit})$ is unity.

One problem to be pointed out is that Eq. (6.24) has a freedom of the scale transformation as $h_{\rm fit} \to C h_{\rm fit}$ with C being an arbitrary constant, and hence, the amplitude of the fitting function cannot be determined by maximizing $\mathcal{M}$. Thus, as an alternative, we define the following *cost function*,

$$\begin{aligned} C_{\rm C}(h_{\rm fit}) \ &:= \ -\mathscr{M}(h_{\rm fit}) \\ &\qquad + \frac{[(h_{\rm NR}, h_{\rm NR}) - (h_{\rm fit}, h_{\rm fit})]^2}{(h_{\rm NR}, h_{\rm NR})^2}, \end{aligned} \tag{6.26}$$

and consider to minimize this function. Here, the second term is in a sense the normalization factor by which the ambiguity in the amplitude of $h_{\rm fit}$ is fixed. We note that by the minimization of $C_{\rm C}$, we can obtain $h_{\rm fit}$ that maximizes $\mathscr{M}$ and also the amplitude of $h_{\rm fit}$ that agrees approximately with that of $h_{\rm NR}$.

Minimizing $C_{\rm C}(h_{\rm fit})$ is not straightforwardly achieved because the fitting formula has a lot of local minima in the 13-dimensional parameter space. We decompose the cost function into two cost functions

$$C_{\rm P}(h_{\rm fit}) \ := \ \int_{t_i}^{t_f} AP_{\rm NR}^2 (PP_{\rm NR} - PP_{\rm fit})^2 dt, \tag{6.27}$$

$$C_{\rm A}(h_{\rm fit}) \ := \ \int_{t_i}^{t_f} (AP_{\rm NR} - AP_{\rm fit})^2 dt, \tag{6.28}$$

where $AP_{\rm NR}$ and $PP_{\rm NR}$ are amplitude and phase parts of $h_{\rm NR}$, respectively, which are obtained by the decomposition defined in Eq. (6.20). Then, we perform the minimization procedure in terms of $C_{\rm P}$ and $C_{\rm C}$ (see Hotokezaka et al. 2013a for the algorithm of the fitting procedure).

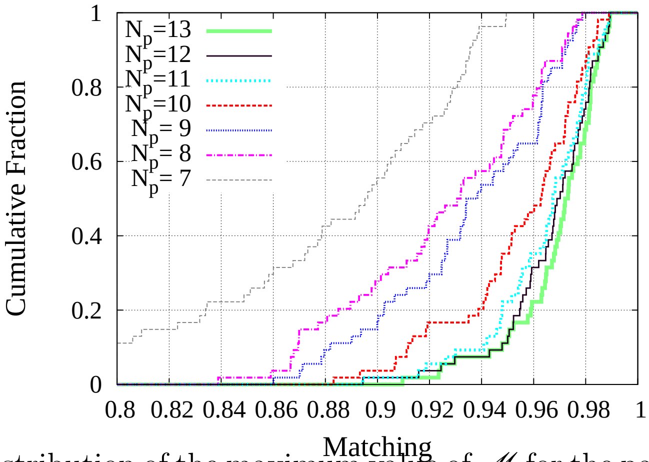

Figure 6.15: Cumulative distribution of the maximum value of $\mathscr{M}$ for the parameter fitting with the number of parameters $N_{\rm p} = 7-13$. The horizontal axis denotes the maximum value of matching, $\mathscr{M}$, and the vertical axis shows the cumulative fraction of the models whose maximum fitting value is less than $\mathscr{M}$. This figure is taken from Hotokezaka et al. (2013a).

6.3.5 Fitting result

Figure 6.15 shows the cumulative distribution for the maximum value of $\mathscr{M}$. Here, see the plot for $N_{\rm p} = 13$ that denotes the cumulative distribution for the case of the 13-parameter fitting (see also the column of $\mathcal{M}_{N_{\rm p}=13}$ in Table 6.3.2 which lists the maximum values of $\mathscr{M}$ for all the numerical waveforms). This plot shows that for $\sim 90\%$ of the waveforms, the maximum value of $\mathscr{M}$ is larger than 0.95. Also for all the waveforms, the maximum value of $\mathscr{M}$ is larger than 0.90.

Figure 6.13 compares numerical waveforms with their fitting results for four models, for all of which the value of $\mathscr{M}$ is larger than 0.98. For these models, the amplitude of gravitational waves emitted by a massive neutron star decreases monotonically with time and the corresponding frequency is approximately constant only with small modulation. For such waveforms, the fitting can be well achieved in our fitting formula.

By contrast, the fitting is not as well achieved for the case that the amplitude significantly modulates with time in the early phase of the MNS evolution. Figure 6.14 shows the sample for such cases. For all the models picked up in this figure, the amplitude increases with time from $t = t_i$ and reaches a high value. Then, the amplitude once damps at $t - t_i = 2$–$5\,$ms, and subsequently, quasi-periodic gravitational waves with slowly decreasing amplitude are emitted. This type of gravitational waveform is often found for the case of asymmetric binaries with APR4 and ALF2. Nevertheless, the value of $\mathscr{M}$ is still larger than 0.9.

We notice that the fitting formula, which are constructed with the data for 10 ms duration, could reproduce longer data as well (e.g., 20 ms data). Indeed, the value of $\mathscr{M}$

Model	$f^{\rm low}_{\rm ave,10ms}$ (kHz)	$f^{\rm middle}_{\rm ave,10ms}$ (kHz)	$f^{\rm high}_{\rm ave,10ms}$ (kHz)	$\mathcal{M}_{\rm low}$	$\mathcal{M}_{\rm middle}$	$\mathcal{M}_{\rm high}$
APR4-120150	3.31 ± 0.23	3.28 ± 0.23	3.41 ± 0.24	0.964	0.972	0.959
APR4-135135	3.40 ± 0.36	3.34 ± 0.36	3.28 ± 0.37	0.970	0.981	0.970
ALF2-120150	2.68 ± 0.13	2.78 ± 0.15	2.71 ± 0.16	0.991	0.975	0.924
ALF2-135135	2.82 ± 0.21	2.82 ± 0.19	2.76 ± 0.15	0.988	0.990	0.989
H4-120150	2.27 ± 0.12	2.28 ± 0.14	2.31 ± 0.15	0.986	0.984	0.964
H4-135135	2.51 ± 0.14	2.52 ± 0.14	2.48 ± 0.16	0.982	0.990	0.984

Table 6.3: The resolution study for the characteristic frequency $f_{\rm ave,10ms}$ and the maximum values of $\mathcal{M}$ for APR4, ALF2, and H4 EOSs with $M_A = M_B = 1.35M_\odot$ and $(M_A, M_B) = (1.2M_\odot, 1.5M_\odot)$. Here the number of parameters is set to be $N_{\rm p} = 13$.

for 20 ms duration data with the fitting formula is only 1% smaller than the value of $\mathscr{M}$ listed in Table 6.3.2 for the compact neutron-star models, APR4, SLy, and ALF2. For the less compact neutron-star models, the value of $\mathscr{M}$ is still $1 \sim 10\%$ smaller than the value listed in Table 6.3.2. For the softer EOSs, the duration of high-amplitude gravitational waves is relatively short as $\lesssim 10$ ms. Thus the longer data do not contribute much to the matching. This is the reason that the value of $\mathcal{M}$ depends weakly on the duration of the data. For the stiffer EOSs, in particular, for H4, the duration of high-amplitude gravitational waves is longer as $\gtrsim 10$ ms. For such gravitational waves, the matching parameters have to be reconstructed for the longer-duration data.

Before closing this subsection, we comment on the convergence of the value of $\mathscr{M}$. For the case that the gravitational waveform has the modulation of the amplitude, the value of $\mathscr{M}$ is lower for the higher-resolution simulations, because the modulation of the amplitude is more distinctive for the higher-resolution simulations (see details in Appendix A). Therefore the value of $\mathscr{M}$ is likely to be overestimated for the waveforms which have the large modulation.

6.3.6 Reduction of the number of free parameters

The number of free parameters for the fitting procedure should be smaller for constructing a robust fitting formula. Here we attempt to reduce the number of free parameters from $N_{\rm p} = 13$ to $N_{\rm p} = 2$ by fixing the parameters of which the maximum value of $\mathscr{M}$ is relatively independent. In order to determine which parameter should be fixed, we define a quality function $q(\vec{Q}')$ for a subset of parameters $\vec{Q}' \subset \vec{Q}$, where $\vec{Q}$ is a vector in the 13-dimensional parameter space. $q(\vec{Q}')$ is defined as the worst value among the maximum values of $\mathscr{M}$ for the all numerical waveforms when the fitting is performed with $\vec{Q}'$ as

$$q(\vec{Q}') := \min_{\rm NR\ models}[\mathscr{M}(h_{\rm fit})]. \tag{6.29}$$

We consider that the quality of a fitting formula is better for the larger value of $q(\vec{Q}')$. In Table. 6.4, free parameters and $q(\vec{Q}')$ are listed for each fitting formula with different

	phase part								amplitude part					quality
$N_\mathrm{p} = 2$							p_1	p_0						0.0274881661358768
$N_\mathrm{p} = 3$							p_1	p_0				a_d		0.4753105281276069
$N_\mathrm{p} = 4$			p_c				p_1	p_0				a_d		0.5908178259595284
$N_\mathrm{p} = 5$			p_c				p_1	p_0	a_ci			a_d		0.6750096266165332
$N_\mathrm{p} = 6$			p_c				p_1	p_0	a_ci			a_d	a_1	0.7053957819403283
$N_\mathrm{p} = 7$			p_c			p_2	p_1	p_0	a_ci			a_d	a_1	0.7305212430130907
$N_\mathrm{p} = 8$	p_d		p_c			p_2	p_1	p_0	a_ci			a_d	a_1	0.8388076222568087
$N_\mathrm{p} = 9$	p_d		p_c			p_2	p_1	p_0	a_ci		a_0	a_d	a_1	0.8600728396291507
$N_\mathrm{p} = 10$	p_d	p_f	p_c			p_2	p_1	p_0	a_ci		a_0	a_d	a_1	0.8831675719064657
$N_\mathrm{p} = 11$	p_d	p_f	p_c		p_3	p_2	p_1	p_0	a_ci		a_0	a_d	a_1	0.8943981384792208
$N_\mathrm{p} = 12$	p_d	p_f	p_c	p_s	p_3	p_2	p_1	p_0	a_ci		a_0	a_d	a_1	0.8943981384792208
$N_\mathrm{p} = 13$	p_d	p_f	p_c	p_s	p_3	p_2	p_1	p_0	a_ci	a_co	a_0	a_d	a_1	0.9096283876761225

Table 6.4: The sets of free parameters in the chosen fitting formulae with $N_\mathrm{p} = 2-13$.

number of free parameters.

Table 6.3.2 lists the maximum values of $\mathcal{M}$ for the cases of $N_\mathrm{p} = 10$ to 13 parameters (see the columns $\mathcal{M}_{N_\mathrm{p}=10}$ to $\mathcal{M}_{N_\mathrm{p}=13}$). This table obviously shows that the maximum values of $\mathcal{M}$ are approximately identical for $N_\mathrm{p} = 12$ and $N_\mathrm{p} = 13$ (except for APR4-130150 and ALF-140140). Therefore, the cumulative distributions for these two cases are approximately identical as found in Fig. 6.14 (see the plots for $N_\mathrm{p} = 12$ and 13). This implies that the search procedure may well be performed in the fitting formula with 12 free parameters fixing a_co, which might be a redundant parameter.

We further perform the reduction, and construct reduced fitting formulae with 2 to 11 free parameters ($N_\mathrm{p} = 2-11$). We list the sets of the parameters for $N_\mathrm{p} = 2-13$ in Table 6.4. Figure 6.15 shows the cumulative distribution of $\mathscr{M}$ for the formulae with $N_\mathrm{p} = 7-13$. This figure indicates that the reduced formula with $N_\mathrm{p} = 11-13$ have approximately the same quality, giving $\mathscr{M} > 0.9$ for more than 98% of the waveforms. The reduced formula with $N_\mathrm{p} = 8-10$ have gradually decreasing quality, giving $\mathscr{M} > 0.9$ for $\gtrsim 80\%$ of the waveforms. Then, there is a substantial quality gap between $N_\mathrm{p} = 7$ and $N_\mathrm{p} = 8$. This occurs when p_d is fixed to its standard value.

The last two columns of Table 6.3.2 also list the values of $\mathcal{M}_{M_\mathrm{p}=11}$ and $\mathcal{M}_{M_\mathrm{p}=10}$. Comparing these data with $\mathcal{M}_{M_\mathrm{p}=13}$ also shows that the reduced formula with $N_\mathrm{p} = 11$ has the quality that is approximately the same as that for $N_\mathrm{p} = 13$. This implies that we may reduce the number of the parameters to 11 by fixing the values of the other parameters to be the standard values. We may further reduce the number of free parameters to 10 if we can allow the matching with $\mathscr{M} < 0.9$ for $\sim 5\%$ of the waveforms.

6.4 Conclusion

In this chapter, we studied the formation and evolution of the remnant object of an NS–NS merger. In order to take into account uncertainties due to the unknown EOS of neutron-star matter, we adopted different EOSs which are stiff enough to support massive neutron stars $\gtrsim 2M_\odot$ (Demorest et al. 2010; Antoniadis et al. 2013). As a result, we obtained the following conclusions for the remnant object of an NS–NS merger:

- a HMNS or SMNS is likely to be formed in the NS–NS merger with the canonical mass range of NS–NS systems, $2.6M_\odot \leq M \leq 2.8M_\odot$.
- Just after the merger, a remnant massive neutron star has a rapidly rotating non-axisymmetric core, which emits gravitational waves.
- The angular momentum transport due to the gravitational torque between a non-axisymmetric core and its envelope drives the collapse of the HMNS in the first several milliseconds.

These results suggest that an NS–NS merger with the typical total mass of the observed NS–NS systems results in an HMNS or SMNS. The remnant HMNS and SMNS will eventually collapse into a black hole through some time scale, such as the time scale of hydrodynamical angular momentum transport, magnetohydrodynamical angular momentum transport, and neutrino cooling, depending on the total mass and EOS. Therefore there should be varieties in the nature of post-NS–NS merger phase. These facts should be taken into account to study the central engine of short GRBs.

We also showed that a massive neutron star formed after a merger emit gravitational waves, which might be observable by future gravitational-wave detectors. Note that the waveforms strongly reflect the dynamics of a remnant massive neutron star. In particular, these gravitational waves have a characteristic frequency, which corresponds to a rotational frequency of a remnant massive neutron star. We showed that the characteristic frequency strongly correlate to the radius of the merging neutron stars with errors of 10%. This result is basically consistent with the results previously obtained by Bauswein and Janka (2012); Bauswein et al. (2012).

A phenomenological waveform for gravitational waves emitted from a remnant massive neutron star was constructed by fitting the waveforms obtained by our numerical relativity simulations with a fitting formula. We found a fitting formula which well describes numerical waveforms with 13 parameters. The mismatch between the best-fitted waveform and the numerical waveform is less than 10%. We attempted to reduce the number of free parameters in the fitting formula. We found that the fitting formula works even for the 10 free parameters. The phenomenological waveform will be useful to analyze gravitational waves emitted a remnant massive neutron star in future.

Chapter 7

Mass ejection from binary neutron star mergers

Mass ejection from a NS–NS merger play a crucial role to study electromagnetic counterparts of merger events, because the expected brightness of signals sensitively depends on the ejecta mass (see Chap. 3 for details). Due to the non-linearity of the ejection mechanism at the merger, numerical simulations of NS–NS mergers are required in order to compute the properties of mass ejection. Importantly, the amount of ejecta mass can vary by an order of magnitude, depending on the mass of a binary and the EOS of neutron-star matter. Therefore it is important to understand such dependences, in order to fully understand mass ejection of a merger. In this chapter, we systematically study dynamical mass ejection of NS–NS mergers.

7.1 Dynamical mass ejection

7.1.1 Mass ejection: massive neutron star formation case

As we mentioned in the pervious chapter, an NS–NS merger with a stiff EOS and with a canonical total mass in the range of $2.6 - 2.8 M_\odot$ (see Table 1.1), a remnant massive neutron star is often formed with a lifetime much longer than the dynamical timescale ~ 0.1 ms and its rotation period ~ 1 ms; the lifetime is always longer than 10 ms for the most models employed in this chapter. In this section, we focus on the mass ejection in the case of HMNS formation.

Figures 7.1 – 7.3 display snapshots of the density contours of the merger for the models APR4-135135, APR4-120150, and H4-120150, respectively. The first and second rows of these figures show the ejecta profile on the equatorial plane of the binary orbit with the scale of 100 km and 1000 km, respectively. The third and fourth rows of these figures show the ejecta on the meridional plane of the system. In all the cases, the strong mass ejection can be found for the first several milliseconds after the onset of the merger. The velocity profile on the scale of 1000 km is homologous $\vec{v} \propto \vec{r}$ and the value of the velocity at the ejecta head is $\sim 0.5c$. Note that the ejecta expand not only on the equatorial plane but also on the meridional plane, as can be seen in these figures. Such a spheroidal shape of ejecta is consistent with the results of other numerical simulations taking into account the general relativistic effects (Oechslin et al. 2007; Bauswein et al. 2013b). Figure 7.4 and 7.5 show the specific internal energy $\epsilon_{\rm th}$ on the equatorial plane (upper panels) and the meridional plane (lower panels). On the equatorial plane, hot regions are formed at the front of the spiral arms. On the meridional plane, hot regions are formed above the HMNS due to the collision between the HMNS and fall beck material on the rotational axis. In the followings, we will discuss the mechanisms of mass ejection in NS–NS mergers.

Figures 7.1 – 7.3 indicate that there are two important processes for mass ejection. The first one is the heating by shocks formed at the onset of the merger at the interface of two neutron stars. This process occurs in particular for the equal-mass and slightly asymmetric binaries, i.e., the case that the less massive neutron star does not strongly disrupted by the companion star. The shocked material is pushed outward by the thermal pressure generated by the shock Subsequently, it expands outwards with rotation, and eventually forms spiral arms on the equatorial plane. This component subsequently gains angular momentum due to the torque exerted by the non-axisymmetric gravity of the HMNS, and a fraction of the material eventually gains the kinetic energy that is large enough to escape from the central remnant.

A stronger shock appears to play basically a positive role for increasing the amount of the ejected material. A stronger shock is formed for softer EOSs or for binaries composed of more compact neutron stars because of larger approaching velocities at the merger. This point will be in more detail described in Sec. 7.1.1. A strong shock could be also formed for binaries with the total mass close to the critical value for the collapse to a black hole even for stiff EOSs, because a high-density state is realized by the strong gravity.

The secondly important process for mass ejection is a gravitational torque as the following two ways. At the merger of an asymmetric binary, the less massive neutron star is elongated by the torque exerted by the more massive neutron star. In turn, some fraction of material in the tail of elongated neutron star gains sufficient angular momentum to escape from the system. After the merger, as already mentioned in the previous chapter, the formed HMNS is always highly non-axisymmetric and rapidly rotating. The gravitational torque induced by the non-axisymmetric HMNS causes the angular momentum transport. Thus, it works as a rotating engine that exerts a torque and supplies angular momentum to the material surrounding the HMNS.

In the early mass ejection caused by the torque of the HMNS, the typical velocity of escaping material in this early stage is quite high $\sim 0.5 - 0.8c$ (compare the locations of the head of the ejected materials in Figs. 7.1 – 7.3). The maximum velocity is larger for the EOS that yields smaller-radius neutron stars; for APR4, it is $\sim 0.8c$ and for MS1, it is $\sim 0.5c$. This also depends on the mass ratio for models with a large radius (for models

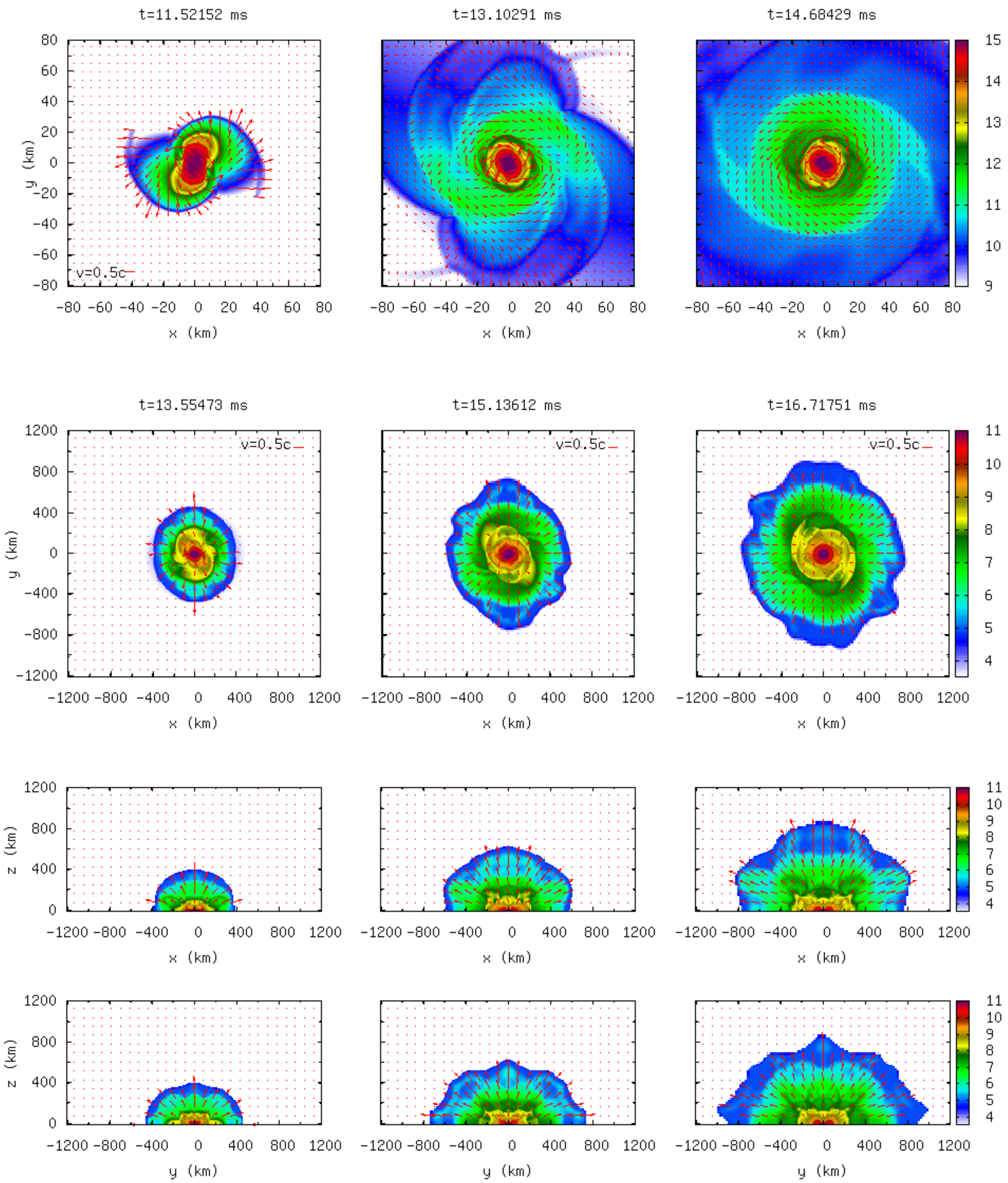

Figure 7.1: Snapshots of the density profile for the merger of binary neutron stars for model APR4-135135. The first row shows the density profiles in the equatorial plane and in the central region, and second – fourth ones show the density profile for a wide region in the x-y, x-z, and y-z planes. This figure is taken from Hotokezaka et al. (2013b).

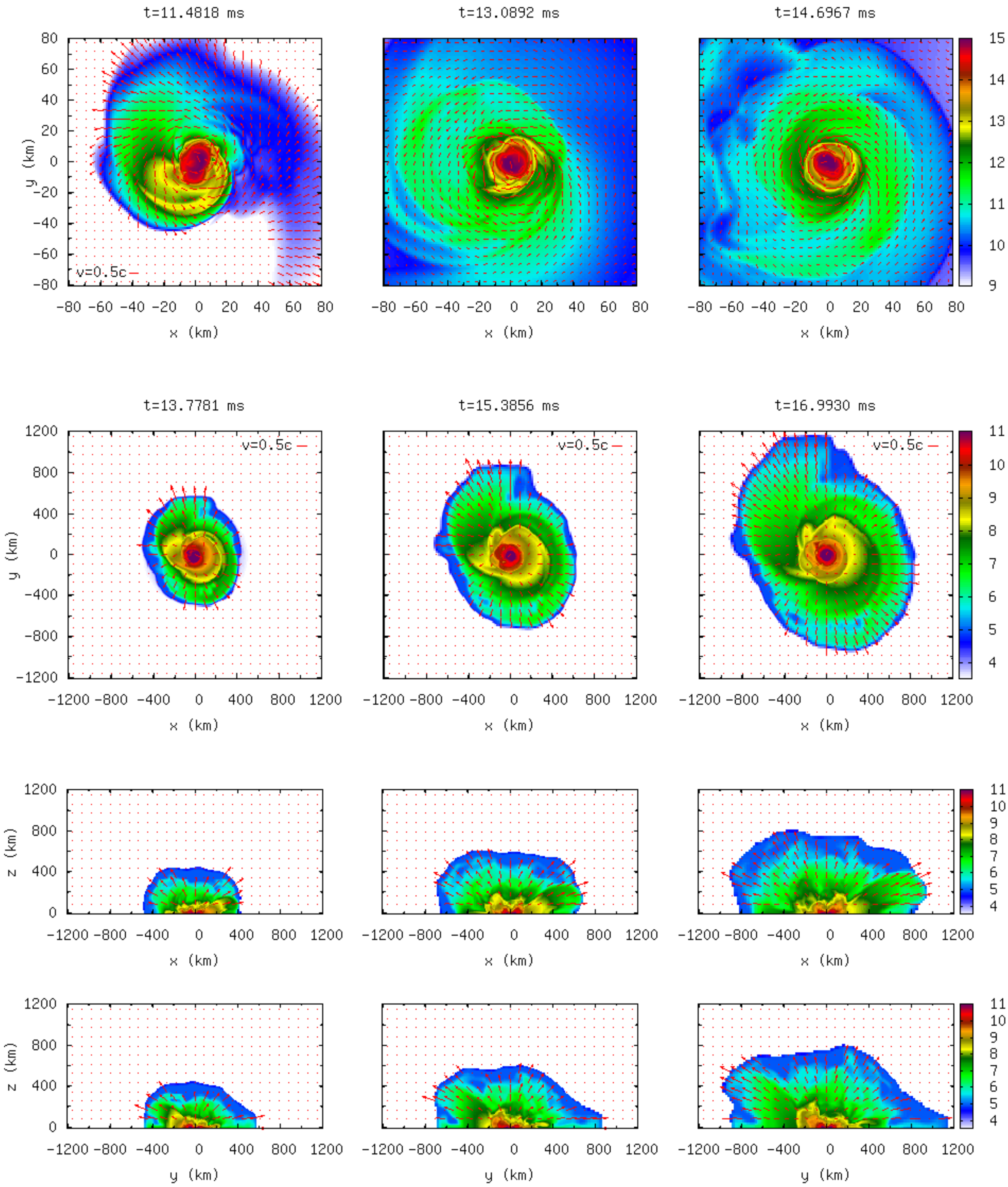

Figure 7.2: The same as Fig. 7.1, but for model APR4-120150. This figure is taken from Hotokezaka et al. (2013b).

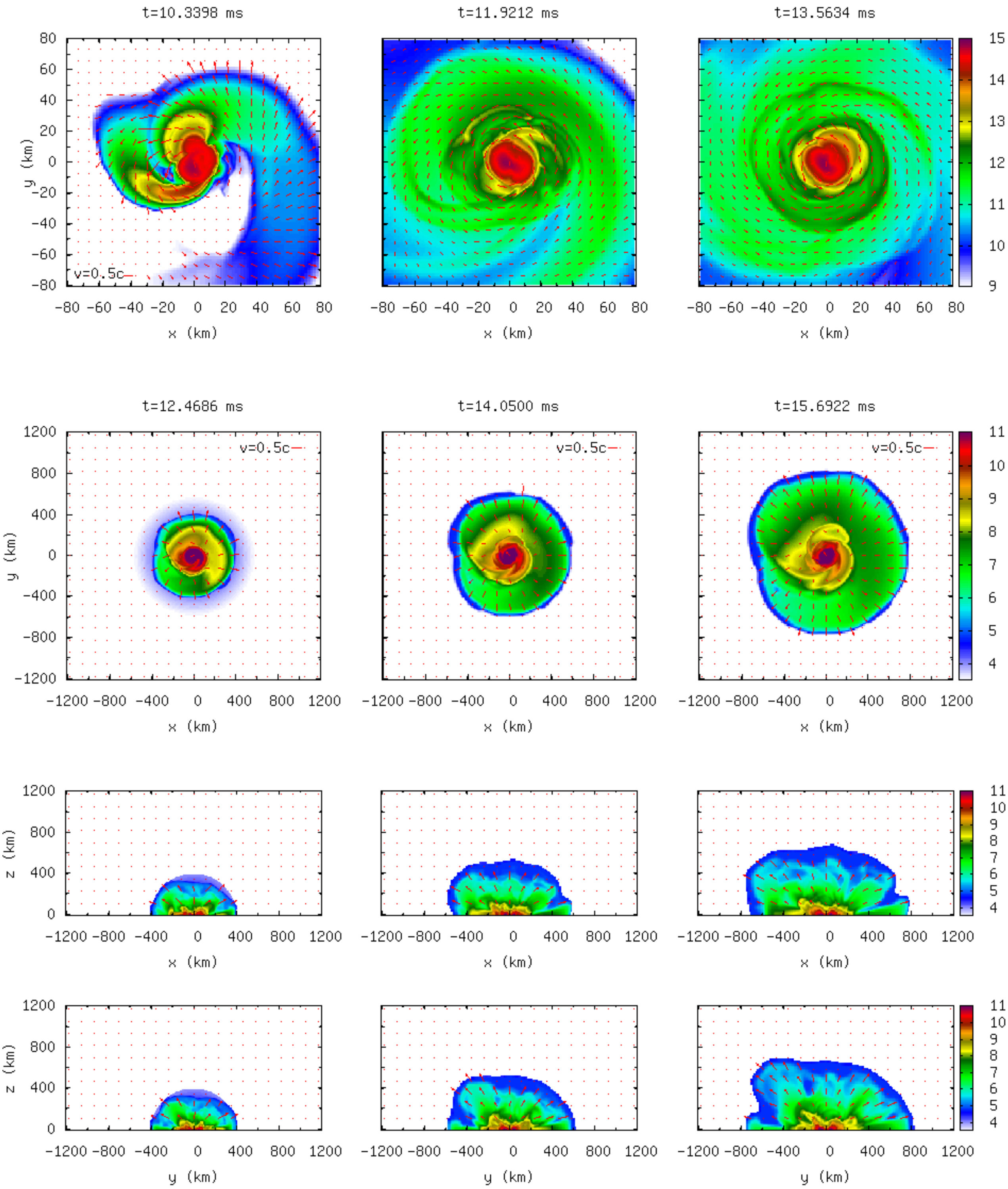

Figure 7.3: The same as Fig. 7.1 but for models H4-120150. This figure is taken from Hotokezaka et al. (2013b).

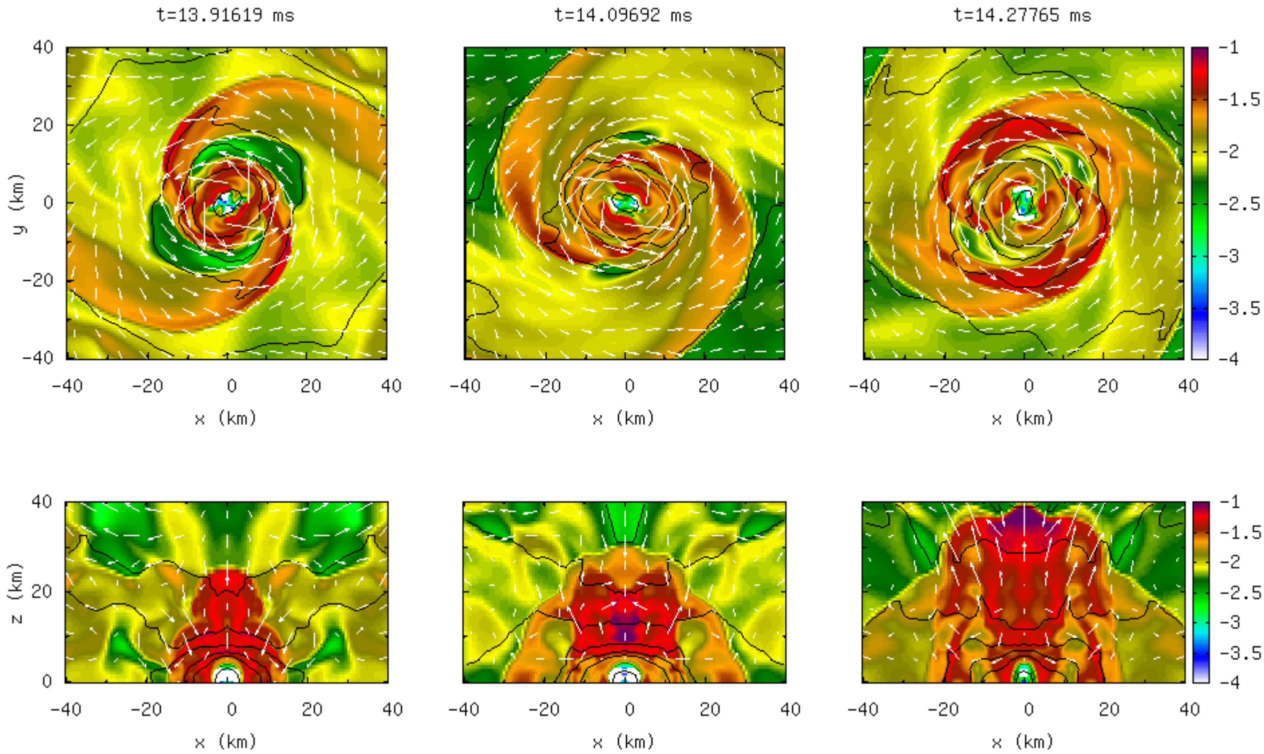

Figure 7.4: Snapshots of the thermal part of the specific internal energy ($\varepsilon_{\rm th}$) profile in the vicinity of HMNSs on the equatorial (top) and x-z (bottom) planes for an equal-mass model APR4-135135. The mass density contours are overplotted for every decade from 10^{15} g/cm^3. This figure is taken from Hotokezaka et al. (2013b).

of H4 and MS1).

In the later phase, mass ejection appears to occur by the combination of shock heating and a torque from the HMNS. Continuous shock heating occurs in the envelope of the HMNS in the presence of spiral arms, as can be seen in Figs. 7.4 and 7.4. a fraction of the material gains large kinetic energy. In addition, the material in the outer region gains the torque from the HMNS. By this process, the material is gradually ejected from the system in a quasispherical manner; the anisotropy of the configuration of the ejected material is not as large as that of the material ejected in the early stage. This indicates that the shock heating plays a relatively important role. The average velocity of escaping material in this process is sub-relativistic $\sim 0.15 - 0.25c$ (see Table 7.1.2).

In summary, mass ejection of an NS–NS merger occurs as the following manner.

1. At an NS–NS merger, the material between the interface of the two neutron stars gains energy through a shock heating due to the bounce of HMNS formation. The material in the tail of the less massive neutron star also gains energy and angular momentum through the gravitational torque exerted by the more massive neutron star.

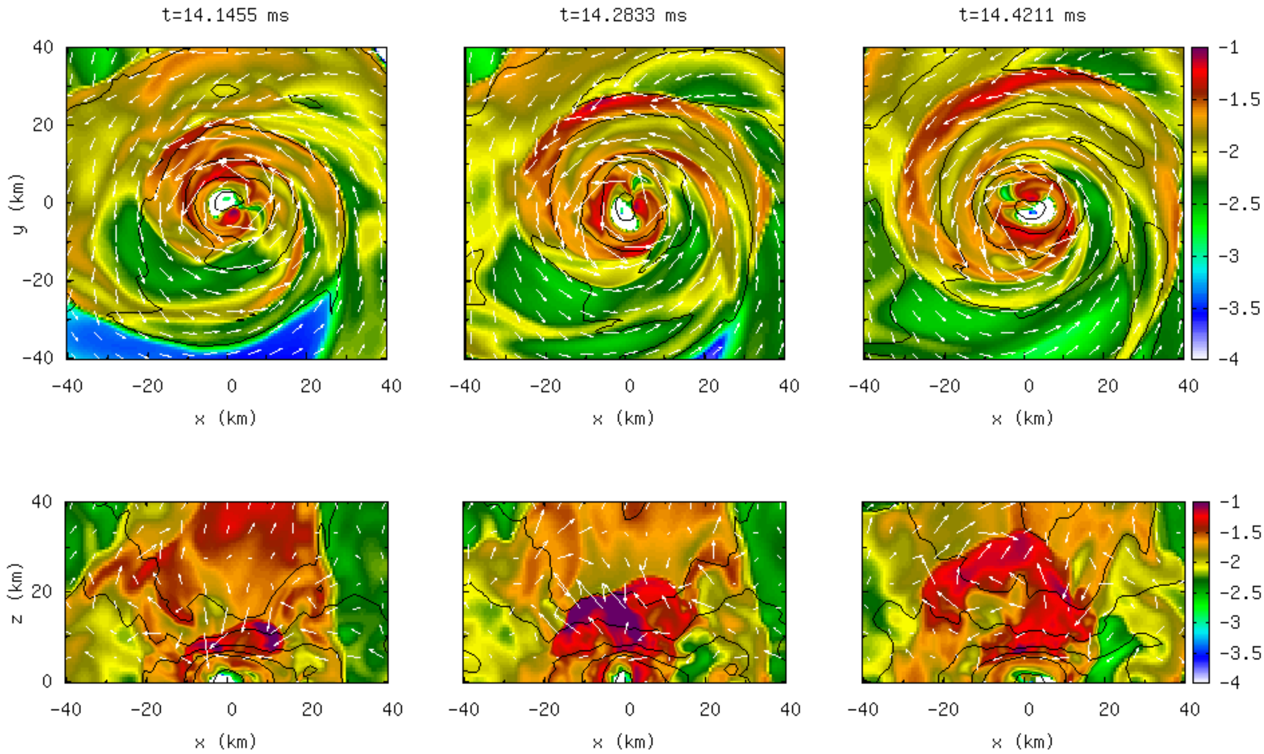

Figure 7.5: The same as Fig. 7.5, but for an unequal-mass model APR4-120150. This figure is taken from Hotokezaka et al. (2013b).

2. A fraction of material which gains energy through the two processes escapes from the system. The other material remains to be bounded by the gravitational potential of the central object.

3. An HMNS continue to eject the material in the envelope through the shock heating and gravitational torque.

In the mass ejection process, these nonlinearly coupled effects (shock heating and torque by the HMNS) play a substantial role. As a result, the amount of the ejected material depends on the EOS, the total mass of the system, and the mass ratio in a nonlinear manner. Thus, a small change (associated, e.g., with the grid resolution, the initial orbital separation, configuration of the atmosphere, and presence or absence of the π symmetry for equal-mass binaries) results in $\sim 10-30\%$ change in the mass and kinetic energy of the ejected material; this fluctuation is in general small, $\sim 10\%$, for APR4 and MS1, moderate $\sim 10-20\%$ for ALF2, and $\sim 30\%$, for H4, for unequal-mass binaries. For the equal-mass case, the convergence is relatively poor because a strong shock often occurs at the merger and plays an important role in the mass ejection (note that shocks are computed by the first-order accuracy in the spatial grid resolution). For some models (such as ALF2-135135 and MS1-135135), the ejected mass increases steeply with the grid resolution, and the results in this thesis might give the lower bound.

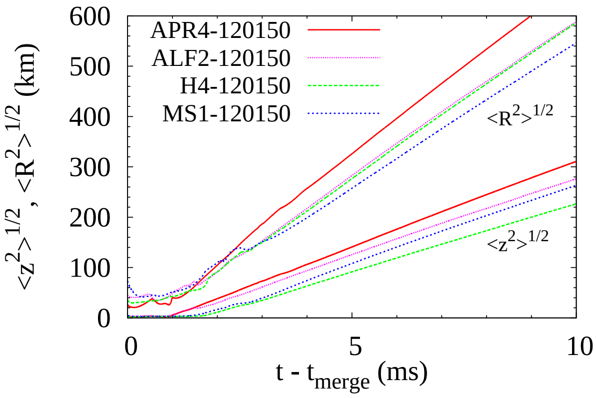

Figure 7.6: $\bar{R}(=\langle R^2\rangle^{1/2})$ and $\bar{Z}(=\langle z^2\rangle^{1/2})$ as functions of time for APR4-120150, ALF2-120150, H4-120150, and MS1-120150. This figure is taken from Hotokezaka et al. (2013b).

In the following subsections, we describe the properties of the ejected material in more detail.

Average velocity of ejected material

Figure 7.6 plots $\bar{R}$ and $\bar{Z}$ as functions of time for APR4-120150, ALF2-120150, H4-120150, and MS1-120150. Note that $d\bar{R}/dt$ and $d\bar{Z}/dt$ may be considered as the average velocity of the ejected material in the cylindrical and vertical directions, respectively. This shows that the ejected material expands with an approximately constant sub-relativistic velocity $\sim 0.15 - 0.25c$ for $t - t_{\rm merger} \gtrsim 2$ ms in the cylindrical direction and the velocity in the vertical direction is $0.4 - 0.5$ times as large as that in the cylindrical direction. This suggests that the vertical thickness angle of the ejected material, θ_0, is $\sim 40 - 50°$. This indicates that the ejected material expands in a moderately anisotropic manner. Note that the velocity in the cylindrical direction is primarily caused by the tidal torque exerted by the HMNS, while the velocity in the vertical direction is primarily caused by the shock heating. This implies that both effects play an important role.

The velocity in the later phase, $t - t_{\rm merge} \gtrsim 3$ ms, clearly depends on the EOS as shown in Fig. 7.6. The value of the ejecta velocity is larger for the merger of more compact neutron stars. Roughly speaking, this is because the typical ejecta velocity reflects the escape velocity of merging neutron stars, of which the value is larger for more compact neutron stars. Specifically, a more compact state is realized in the HMNS: (i) a strong shock associated with the compression by a strong gravity and a subsequent large-amplitude oscillation occurs, resulting in an efficient mass ejection, and (ii) the HMNS is a stronger supplier of the torque to its surrounding material.

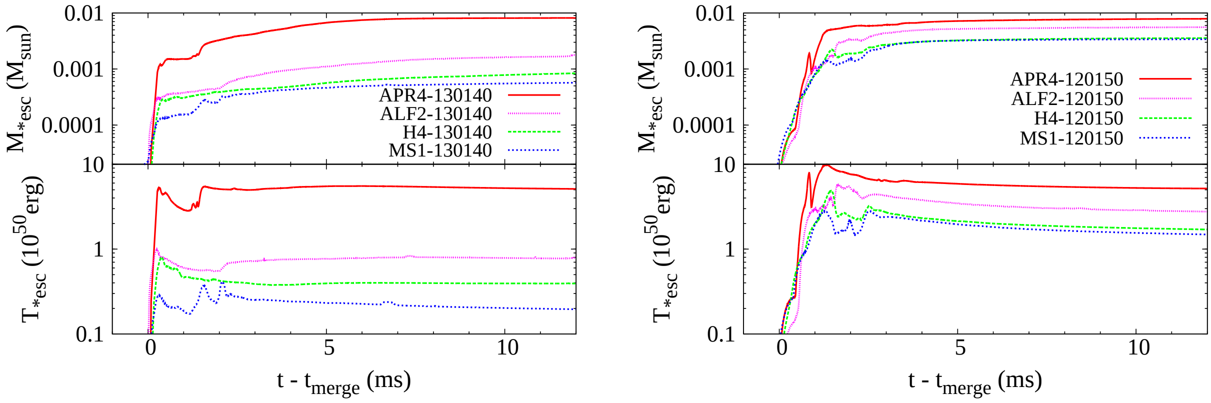

Figure 7.7: $M_{*\rm esc}$ and $T_{*\rm esc}$ as a function of $t - t_{\rm merge}$ (left) for models APR4-130140, ALF2-130140, H4-130140, MS1-130140, and (right) for models APR4-120150, ALF2-120150, H4-120150, MS1-120150. This figure is taken from Hotokezaka et al. (2013b).

Dependence on EOS

Figure 7.7 plots the total mass and kinetic energy of the ejected material as a function of $t - t_{\rm merge}$ for the four EOS models; for the left and right panels, the masses of two neutron stars are $(1.3M_\odot, 1.4M_\odot)$ and $(1.2M_\odot, 1.5M_\odot)$, respectively. Note that the mass ejection lasts over 5 ms after the merger in all the cases. This figure shows that the mass and kinetic energy of the ejected material depend strongly on the EOS. More specifically, for a given total mass, the merger of more compact neutron stars ejects a larger amount of material as long as an HMNS is formed. This dependence is consistent with the results obtained by Bauswein et al. (2013b), but it is not trivial to understand because the following reason. As we have already mentioned, the material which ejected at early phase of the merger is originated from the following two parts, the tidal tail of the less massive neutron star and the interface between the two neutron stars. The amount of the tidal tail component is expected to be larger for the merger of less compact neutron stars, because the less compact star can be easily disrupted. On the other hand, the amount of the interface component is expected to be larger for the merger of more compact neutron stars, because the two stars have a larger approaching velocity, which enhances shock heating.

Keeping this in mind, our results imply that the ejecta originated from the interface between the two stars significantly contribute to the ejecta mass, because the merger of compact neutron stars ejects a larger amount of material. Therefore we can conclude that the general relativistic effects are essential to compute the ejecta mass and kinetic energy, because such a compact neutron star cannot be treated with Newtonian hydrodynamics simulations.

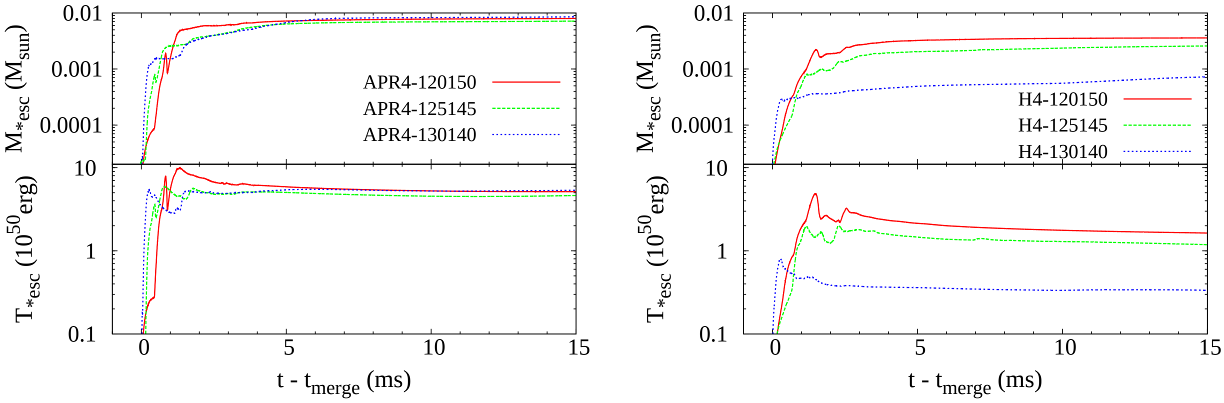

Figure 7.8: $M_{*\rm esc}$ and $T_{*\rm esc}$ as functions of $t-t_{\rm merge}$ (left) for models APR4-120150, APR4-125145, APR4-130140, and (right) for models H4-120150, H4-125145, H4-130140. This figure is taken from Hotokezaka et al. (2013b).

Dependence of the ejected material on the mass ratio and total mass

The mass and kinetic energy of the material ejected from the HMNS depend on the mass ratio of an NS–NS. Figure 7.8 plots $M_{*\rm esc}$ and $T_{*\rm esc}$ as a function of $t - t_{\rm merge}$ for APR4 and H4 with three mass ratios and with the total mass $2.7M_\odot$. For the models with H4, the total mass and kinetic energy of the ejected material increase with decreasing the mass ratio, e.g., the total mass and kinetic energy for $q = 0.8$ are by a factor of ~ 5 and 7 larger than those for $q = 0.933$ and $q = 1$ with $m = 2.7M_\odot$. Essentially the same results are found for the models with ALF2 and MS1 with $q < 1$ (see Table 7.1.2). By contrast, for the models with APR4, the total mass and kinetic energy depend weakly on the mass ratio for $m = 2.7M_\odot$. These facts indicate that:

- the asymmetry of the component masses of an NS–NS enhances the mass ejection through the angular momentum transport via the tidal torque for relatively stiff EOS such as ALF2, H4 and MS1 (although there is some exception; see the result of model MS1-135135).

- the amount of the ejected material depends very weakly on the mass ratio for the canonical total mass $\sim 2.6 - 2.8M_\odot$ for a relatively soft EOS, APR4, which yields a small-radius neutron star.

The mass and kinetic energy of the ejected material depends also on the total mass of the system. For APR4, ALF2, and H4, these quantities are larger for more massive system (see Table 7.1.2). This property is consistent with the fact that these quantities are larger for an EOS that yields compact neutron stars. Namely, for the larger mass, the system can be in general more compact, and also the resulting HMNS is more compact, more rapidly rotate, and quasiradially oscillate with a larger amplitude, which enhance the mass ejection from an HMNS.

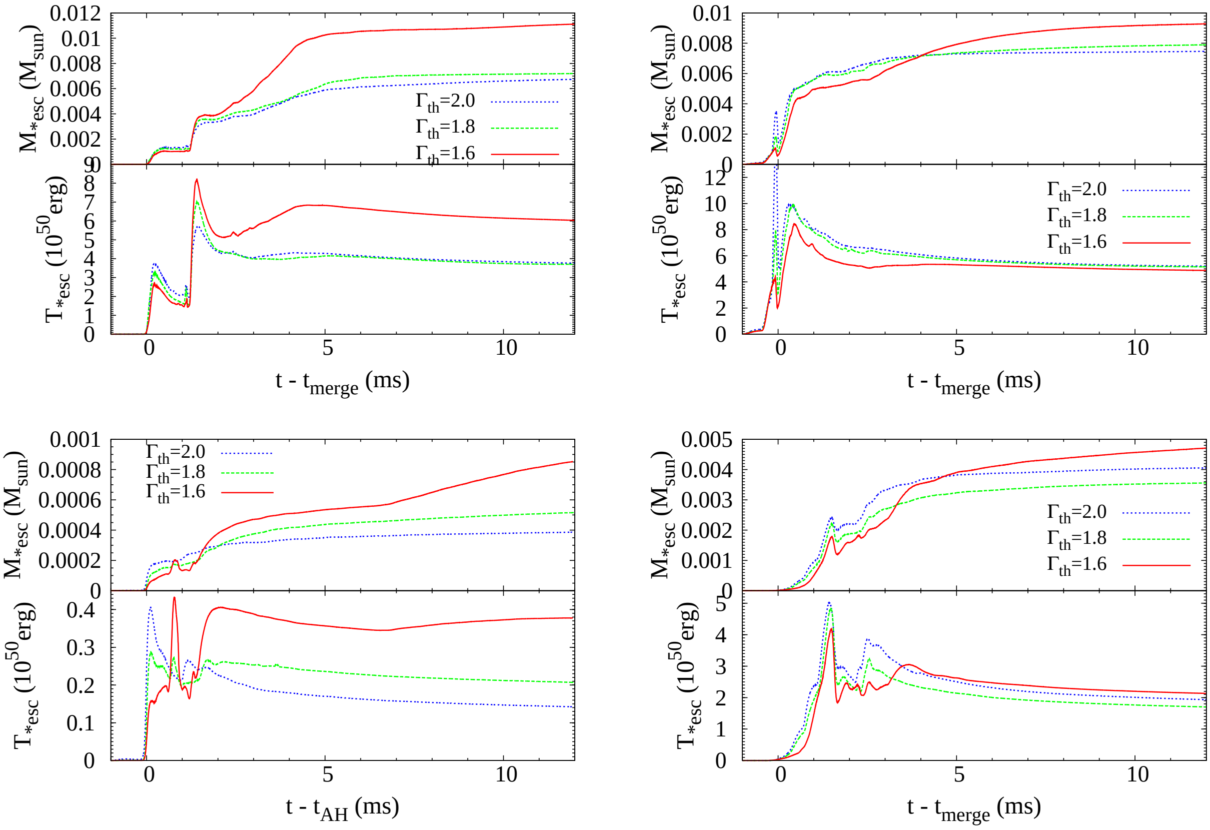

Figure 7.9: $M_{*\rm esc}$ and $T_{*\rm esc}$ as functions of $t - t_{\rm merge}$ (left) for models APR4-135135 (top left), APR4-120150 (top right), H4-135135 (bottom left), and H4-120150 (bottom right) with $\Gamma_{\rm th} = 2.0$, 1.8, and 1.6. This figure is taken from Hotokezaka et al. (2013b).

For MS1 for which neutron stars and HMNSs are not very compact, the quantities of the ejected material do not change systematically. For MS1-140140, the quantities of the ejected material is much smaller than those for MS1-135135 and as small as those for MS1-130140. The possible reason is that the HMNS formed for MS1-140140 is slightly more compact than that for MS1-135135, and the mass ejection is suppressed by the trapping effect. This suggests that for these mass ranges, a slight change in the compactness significantly affects the efficiency of the mass ejection.

Note that these dependences of the ejecta mass on the total mass is true only when a long-lived HMNS is formed after the merger. For a short-lived HMNS formation case, the most of the bounded material around the HMNS can not gain energy and angular momentum enough to escape from the central remnant.

Dependence on $\Gamma_{\rm th}$

The mass and kinetic energy for the ejected material depend also on the value of $\Gamma_{\rm th}$. The possible reason is described as follows.

For larger values of $\Gamma_{\rm th}$, one might expect that the mass ejection is more efficient because the effect of shock heating is stronger. However, the HMNS becomes less compact for the larger value of $\Gamma_{\rm th}$ because of the contribution of large thermal pressure. As a result, although the outward velocity of the material caused by the shock heating is initially larger for the larger values of $\Gamma_{\rm th}$, the subsequent gain of the kinetic energy via the shock heating could be smaller. Therefore, the total amount of mass and kinetic energy of the ejecta depend on these two competing nonlinear processes. Therefore the amount of the ejected material does not depend monotonically on the value of $\Gamma_{\rm th}$. In the following, we discuss this fact in more details.

Figure 7.9 compares the evolution of the total mass and kinetic energy for $\Gamma_{\rm th} = 1.6$, 1.8, and 2.0 for models APR4-135135, APR4-120150, H4-135135, and H4-120150. All the panels of Fig. 7.9 clearly show that for the early time, $t - t_{\rm merge} \lesssim 1.5$ ms for APR4-135135 and H4-135135, $\lesssim 5$ ms for APR4-120150 and H4-120150, these two quantities are larger for the larger value of $\Gamma_{\rm th}$. Namely the stronger shock heating associated with the larger value of $\Gamma_{\rm th}$ plays an important role. However, after the early time, the mass tends to be larger for the smaller value of $\Gamma_{\rm th}$. In particular, for $\Gamma_{\rm th} = 1.6$, the total amount of mass of ejecta increases with time. Thus, a long-term mass ejection process works for the smaller values of $\Gamma_{\rm th}$, and this mechanism is remarkable for $\Gamma_{\rm th} = 1.6$.

For APR4-120150 and H4-120150, the mass of the ejected material is largest for $\Gamma_{\rm th} = 1.6$. However, the kinetic energy depends weakly on the value of $\Gamma_{\rm th}$. This implies that although more materials are ejected, the gained kinetic energy is not very large for $\Gamma_{\rm th} = 1.6$.

The dependence of the mass and kinetic energy of the ejected material on $\Gamma_{\rm th}$ is qualitatively similar for APR4 and H4. This indicates that the properties summarized in this subsection would hold irrespective of the EOS.

Before closing this subsection, we compare our results with the results obtained by Bauswein et al. (2013b) from point of view of the dependence of mass ejection on $\Gamma_{\rm th}$. Bauswein et al. (2013b) performed numerical simulations of NS–NS mergers employing zero-temperature EOSs, which include thermal effects as the ideal gas EOS with $\Gamma_{\rm th}$. They chose $\Gamma_{\rm th} = (1.5,\ 1.8,\ 2.0)$. As a result, they found the ejecta mass is large for the case of $\Gamma = 1.5$. This tendency is consistent with our results. They also pointed out that the ideal gas EOS with $\Gamma_{\rm th} = 1.5$ quantitatively agrees with the results obtained with the finite-temperature EOS.

7.1.2 Mass ejection: black hole formation case

We briefly summarize the properties of mass ejection for the case that a black hole is promptly formed after the onset of the merger. In this study, the prompt formation of a black hole occurs only for APR4 with the total mass $2.9M_\odot$.

For these models, the mass ejection primarily occurs at the instance of the merger, i.e., during a short duration before the formation of a black hole. Because a black hole

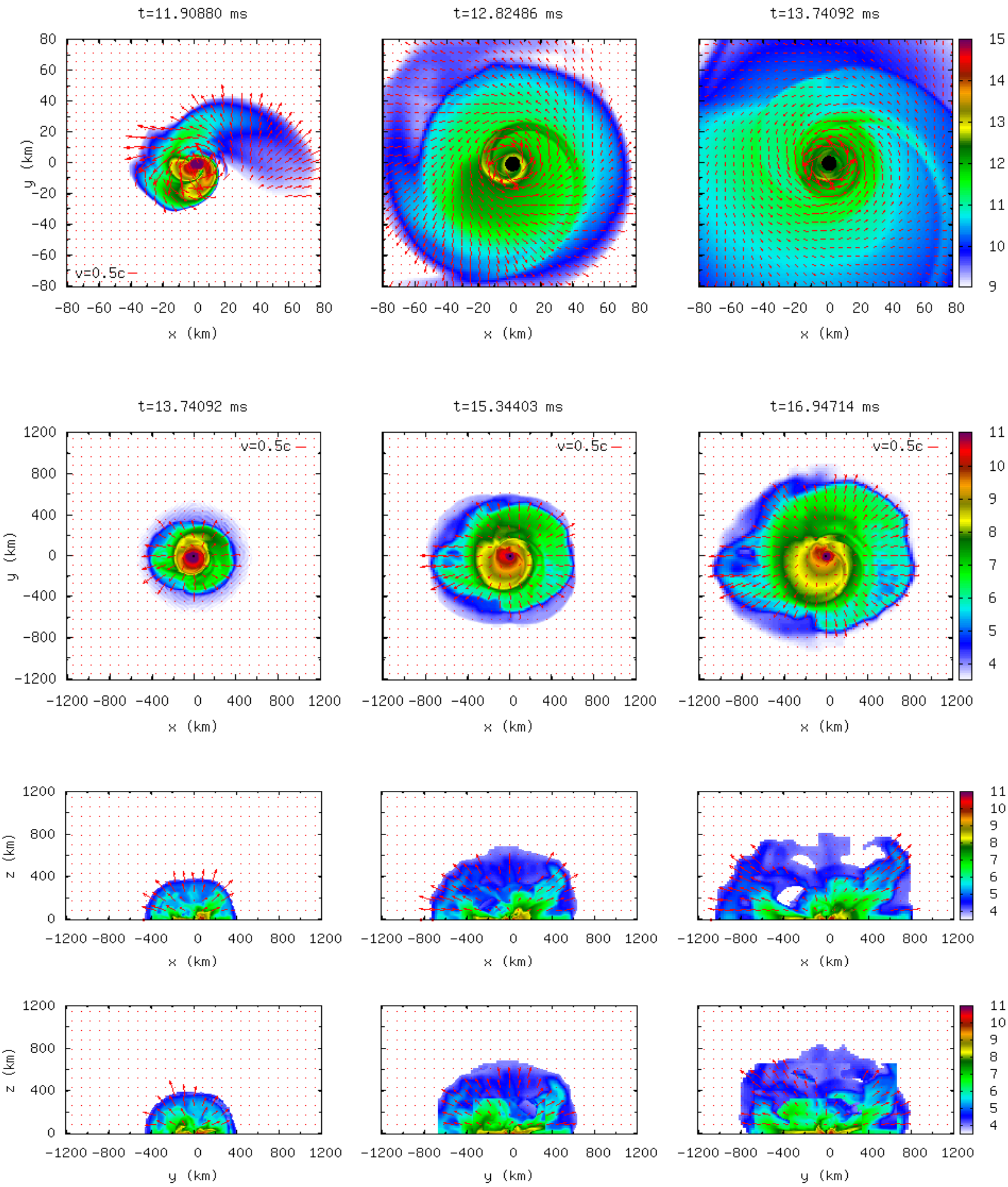

Figure 7.10: The same as Fig. 7.1 but for high-mass and unequal-mass model APR4-130160. The filled black circles in the middle and right panels of the top row denote black holes. This figure is taken from Hotokezaka et al. (2013b).

is promptly formed, a shock-heated region at the interface of two neutron stars is soon swallowed by the black hole, and thus, the shock heating does not play a primary role in the mass ejection. A significant mass ejection occurs for the case that the mass asymmetry is present, and the mass ejection is induced by a tidal torque. In the presence of mass asymmetry, the less-massive neutron star is tidally elongated during the merger, and a fraction of the tidally elongated neutron-star material gains a sufficient torque from the merged object just before the formation of a black hole and gets the escape velocity. For models APR4-140150 and APR4-130160, this gain of the angular momentum is large enough to eject materials of mass $\sim 6 \times 10^{-4} M_{\odot}$ and $2 \times 10^{-3} M_{\odot}$, respectively (see Table 7.1.2). Figure 7.10 shows the snapshot of the density contours of the model APR4-130160. Ejecta expands mainly on the equatorial plane compared to the HMNS formation cases.

In the direct black hole formation cases, disks are also formed, and their mass (for material bounded by the black hole) is $0.03 M_{\odot}$ and $0.002 M_{\odot}$, respectively. The values for the mass ejection depend only very weakly on the grid resolution with the fluctuation within 10% level. The reason is that strong shocks do not play an important role in the mass ejection mechanism.

The average velocity of the ejected material for these cases is $\sim 0.3c$ and larger than that in the case of the HMNS formation. The reason is that the mass ejection is caused primarily by the tidal interaction at the onset of the merger, and for this case, the induced velocity is larger than that by subsequent long-term shock heating. Because the tidal interaction plays a primary role, the material is ejected primarily in the direction of the equatorial plane. The motion to the z direction is also induced by shock heating that occurs when spiral arms surrounding the black hole collide each other. However, this is a secondary effect. Hence, for the case that a black hole is promptly formed from an asymmetric binary, the value of θ_0 is $30 - 35°$ which is smaller than those for the case of the HMNS formation for which $\theta_0 = 40 - 50°$.

For the equal-mass binary, the total amount of mass of ejecta is quite small $\sim 10^{-4} M_{\odot}$ (see Table 7.1.2), because of the absence of the asymmetry and of the lack of the time during which the material located in the outer region gains the torque from the merged object (note that most of the fluid elements of binary neutron stars just before the onset of the merger do not have the specific angular momentum large enough to escape from the black hole formed Shibata and Uryū 2000). In this case, the disk mass surrounding the black hole is also quite small, $\sim 10^{-4} M_{\odot}$. This is consistent with the previous finding (Shibata et al. 2005).

7.2 Summary and Discussion

We studied dynamical mass ejection from NS–NS mergers by using numerical relativity simulations. For this purpose, we adopted the wide numerical grids $\sim$ 3000 km and a

Table 7.1: Summary of numerical results. The remnant, the total mass, $M_{*\mathrm{esc}}$, the kinetic energy, $T_{*\mathrm{esc}}$, the R and Z components of the average velocity of escaping material, and $\bar{V}^R_{\mathrm{esc}}$ and $\bar{V}^Z_{\mathrm{esc}}$ of the ejected material The total mass, kinetic energy, and average velocity are measured at ≈ 10 ms after the onset of the merger. The remnant is judged at ≈ 30 ms after the onset of the merger. All the results shown are those in the run with $N = 60$ and our standard setting of atmosphere. The mass and kinetic energy of the ejected material have the uncertainty of order 10%.

Model	Γ_{th}	Remnant	$M_{*\mathrm{esc}}(10^{-3}M_\odot)$	$T_{*\mathrm{esc}}(10^{50}\mathrm{ergs})$	$\bar{V}^R_{\mathrm{esc}}/c$	$\bar{V}^Z_{\mathrm{esc}}/c$
APR4-130160	1.8	BH	2.0	1.5	0.24	0.08
APR4-140150	1.8	BH	0.6	0.9	0.35	0.12
APR4-145145	1.8	BH	0.1	< 0.1	0.29	0.13
APR4-130150	1.8	HMNS→BH	12	8.5	0.23	0.12
APR4-140140	1.8	HMNS→BH	14	10	0.22	0.15
APR4-120150	1.6	HMNS	9	5	0.20	0.10
APR4-120150	1.8	HMNS	8	5.5	0.23	0.11
APR4-120150	2.0	HMNS	7.5	5.5	0.24	0.12
APR4-125145	1.8	HMNS	7	4.5	0.22	0.11
APR4-130140	1.8	HMNS	8	5	0.19	0.12
APR4-135135	1.6	HMNS	11	6	0.19	0.13
APR4-135135	1.8	HMNS	7	4	0.19	0.12
APR4-135135	2.0	HMNS	5	3	0.19	0.13
APR4-120140	1.8	HMNS	3	2	0.21	0.12
APR4-125135	1.8	HMNS	5	3	0.18	0.10
APR4-130130	1.8	HMNS	2	1	0.19	0.10
SLy-140140	1.8	BH	0.5	0.7	0.35	0.18
SLy-120150	1.8	HMNS→BH	9	6	0.33	0.15
SLy-125145	1.8	HMNS→BH	8	5.5	0.32	0.16
SLy-130140	1.8	HMNS → BH	9.5	6.5	0.27	0.17
SLy-135135	1.8	HMNS → BH	20	12	0.23	0.15
SLy-130130	1.8	HMNS	4.5	2	0.23	0.15

Model	$\Gamma_{\rm th}$	Remnant	$M_{*\rm esc}(10^{-3}M_\odot)$	$T_{*\rm esc}(10^{50}\rm ergs)$	$\bar{V}^R_{\rm esc}/c$	$\bar{V}^Z_{\rm esc}/c$
ALF2-140140	1.8	HMNS→BH	2.5	1.5	0.21	0.13
ALF2-120150	1.8	HMNS	5.5	3	0.21	0.10
ALF2-125145	1.8	HMNS	3	1.5	0.20	0.10
ALF2-130140	1.8	HMNS → BH	1.5	0.8	0.16	0.11
ALF2-135135	1.8	HMNS → BH	2.5	1.5	0.22	0.12
ALF2-130130	1.8	HMNS	2	1.0	0.19	0.10
H4-130150	1.8	HMNS→BH	3	2	0.19	0.10
H4-140140	1.8	HMNS→BH	0.3	0.2	0.17	0.13
H4-120150	1.6	HMNS	4.5	2	0.19	0.10
H4-120150	1.8	HMNS	3.5	2	0.21	0.09
H4-120150	2.0	HMNS	4	2	0.21	0.09
H4-125145	1.8	HMNS	2	1.5	0.19	0.10
H4-130140	1.8	HMNS	0.7	0.4	0.18	0.10
H4-135135	1.6	HMNS→BH	0.7	0.4	0.21	0.11
H4-135135	1.8	HMNS→BH	0.5	0.2	0.19	0.11
H4-135135	2.0	HMNS	0.4	0.2	0.20	0.10
H4-120140	1.8	HMNS	2.5	1	0.19	0.10
H4-125135	1.8	HMNS	0.6	0.3	0.18	0.10
H4-130130	1.8	HMNS	0.3	0.1	0.16	0.10
MS1-140140	1.8	MNS	0.6	0.2	0.13	0.09
MS1-120150	1.8	MNS	3.5	1.5	0.19	0.10
MS1-125145	1.8	MNS	1.5	0.8	0.19	0.11
MS1-130140	1.8	MNS	0.6	0.2	0.17	0.09
MS1-135135	1.8	MNS	1.5	0.6	0.14	0.08
MS1-130130	1.8	MNS	1.5	0.5	0.15	0.08

low-density artificial atmosphere. As result, we obtained the following conclusions:

- the ejecta mass is in the range of 10^{-4}–$10^{-2} M_\odot$ and the ejecta velocity is in the range of 0.1–0.5c, for the various total masses, mass ratios, and EOSs.
- both the tidal torque and shock heating play an important role for mass ejection.
- for a given EOS, the ejecta mass increases with total mass of a binary, as long as a long-lived HMNS is formed after the merger.
- for a given mass, an NS–NS merger with a softer EOS produces a larger amount of ejecta, as long as a long-lived HMNS is formed after the merger.
- ejecta have a spheroidal shape rather than a disk-like shape except for the case of direct formation of a black hole.

Note that HMNS formation plays an important role to understand dynamical mass ejection of an NS–NS merger. Depending on the total mass, the amount of ejecta mass varies by more than two orders of magnitude even for a given EOS. Furthermore, the amount of the ejecta mass varies by at least an order of magnitude for a given total mass, depending on the EOS. These facts prevent us to predict the brightness and time scale of kilonova and radio flare with small uncertainties because these depend sensitively on the ejecta mass and velocity as already stated in Chap. 3.

A spheroidal structure of NS–NS merger ejecta should interacts with a relativistic jet, which may produce a GRB. Our numerical simulations show that the ejecta on the rotational axis are sufficiently dense compared to the hypothetical structure employed in the previous study (Aloy et al. 2005). Such dense material prevents the jet propagation. As a result, there might be the case that a relativistic jet could not break out of a ejecta surface and results in a failed GRB. Such phenomena should be studied in future.

Chapter 8

Kilonova candidate associated with the short GRB 130603B

A kilonova candidate was observed as a near-infrared counterpart of the short GRB 130603B. The observed brightness, time scale, and color are largely consistent with the expected kilonova emissions of the simple NS–NS merger models (Kasen et al. 2013; Barnes and Kasen 2013; Tanaka and Hotokezaka 2013; Grossman et al. 2013). In this chapter, we explore the possible progenitor models of GRB 130603B by comparing numermical-relativity and radiative transfer simulations with the observed data.

8.1 Observations: GRB 130603B

GRB 130603B was detected on June 03, 2013, at 15:49:14 UT by the Burst Alert Telescope onboad the *Swift* satellite (Melandri et al. 2013). The burst had a duration $T_{90} = 0.18 \pm 0.02$ s in the 15–350 keV (Berthelmy et al. 2013). Follow-up observations of the bursts determined the host galaxy at $z = 0.3565$ (Cucchiara et al. 2013; de Ugarte Postigo et al. 2013). GRB 130603B is the first short GRB with the absorption spectrum of the afterglow. As result, the isotropic-equivalent gamma-ray energy is $E_{\gamma,\mathrm{iso}} \approx 2.1 \pm 0.2 \times 10^{51}$ erg in the range 20 keV–10 MeV in rest-frame (Frederiks and the Konus-Wind team 2013). Furthermore, the continuous observations of the afterglow in X-ray, optical, near infrared, and radio specified the jet break at ≈ 0.47 days after the burst (Tanvir et al. 2013; Berger et al. 2013; de Ugarte Postigo et al. 2013; Fong et al. 2013). The jet opening angle is estimated as $\theta_j \approx 4$–8° and the resulting beaming-corrected gamma-ray energy and kinetic energy are estimated $E_\gamma \approx 0.5$–2×10^{49} erg and $E_K \approx 0.1$–1.6×10^{49} erg, respectively (Fong et al. 2013).

Remarkably, *Hubble Space Telescope* detected an excess in near-infrared at ~ 9 days after the burst and gave an upper limit at ~ 30 days after the burst (Tanvir et al. 2013; Berger et al. 2013). The near-infrared excess and deep upper limits in r-band at ~ 9 days and in H-band at ~ 30 days after the burst are consistent with the expected kilonova

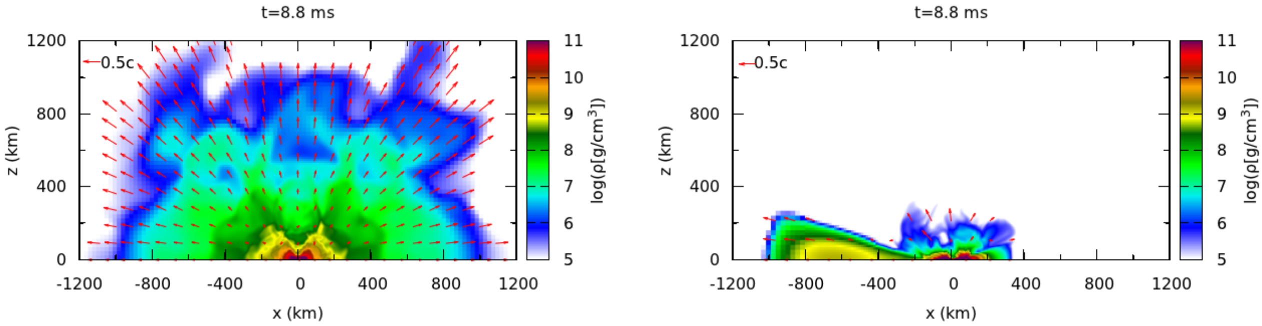

Figure 8.1: The mass density profiles on the meridional plane for the NS-NS (SLy, $M_{\rm tot} = 2.7M_\odot$, $Q = 1.0$) and BH-NS (H4, $Q = 3$, $\chi = 0.75$) models at 8.8 ms after the onset of the merger. The red arrows show the velocity profiles of the ejecta. This figure is taken from Hotokezaka et al. (2013d).

emission models (Kasen et al. 2013; Barnes and Kasen 2013; Tanaka and Hotokezaka 2013; Grossman et al. 2013). Therefore these observations might be the first detection of kilonova, and thus, it could be a direct evidence of the compact binary merger hypothesis of short GRBs.

8.2 Mass ejection: NS–NS vs BH–NS

The brightness and time scale of a kilonova emission depend on the global properties of the ejecta such as the mass, expansion velocity, and morphology as shown in Eq. (3.13) and (3.14). Using the observed data of the near-infrared excess, Berger et al. (2013) estimated the ejecta mass and expansion velocity under the assumption of spherically expanding ejecta. These properties of the ejecta depend on the type of the progenitor (NS–NS or BH–NS), on the parameters of the progenitor models such as mass and spin of the two objects, and on the EOS of neutron-star matter. Recent numerical simulations of compact binary mergers have explored the ejecta properties (Rosswog et al. 1999; Oechslin et al. 2007; Hotokezaka et al. 2013b; Bauswein et al. 2013b; Rosswog 2013; Foucart et al. 2013; Lovelace et al. 2013; Kyutoku et al. 2013; Deaton et al. 2013). By these numerical studies, we can estimate the dependences of the ejecta properties on the parameters of the progenitor models and on EOSs. Here we employ the NS–NS merger ejecta as shown in Chap. 7 and the BH–NS merger ejecta computed by Kyutoku et al. 2014 in preparation.

For NS–NS mergers, we choose the total gravitational mass of the binary $M = 2.6M_\odot - -2.8M_\odot$ and the mass ratio* $Q = 1.0 - 1.25$ (see Table 7.1.2). For BH–NS mergers, the

*The mass ratio is defined by $Q = M_A/M_B$ with $M_A \geq M_B$, where M_A and M_B are the component gravitational mass of the neutron star $M_{\rm NS}$ is fixed to be $1.35M_\odot$ and the mass ratio is chosen to be $Q = 3 - 7$. The nondimensional spin parameter of the black hole χ is chosen as $\chi = 0.75$. We also perform the simulations for $Q = 7$ and $\chi = 0.5$. These parameters, ejecta masses $M_{\rm ej}$, and averaged ejecta velocities $\langle v_{\rm ej}\rangle/c$ of the progenitor models are summarized in Table 8.1.

The morphologies of the ejecta for NS–NS and BH–NS mergers are compared in Fig. 8.1. This figure plots the profiles of the density and velocity fields at 8.8 ms after the onset of the merger. Note that the ejecta velocities are in the small range between $\sim 0.1c$ and $\sim 0.3c$, because those are roughly equal to the escape velocities from the neutron stars, which do not depend sensitively on the progenitor models. However, the total mass and morphology of the ejecta depend sensitively on the progenitor models. In the following, we briefly summarize these properties of the NS–NS and BH–NS ejecta.

Table 8.1: Parameters of the progenitor models and their ejecta properties.

EOS	type	$R_{1.35}$	$M_{\rm tot}/M_\odot$	Q	χ	$M_{\rm ej}/10^{-2}M_\odot$	$\langle v_{\rm ej}\rangle/c$
APR4	NS–NS	11.1	2.6–2.9	1.0–1.25	–	0.01–1.4	0.22–0.27
SLy	NS–NS	11.4	2.6–2.8	1.0–1.25	–	0.8–2	0.2–0.26
ALF2	NS–NS	12.4	2.6–2.8	1.0–1.25	–	0.15–0.55	0.22–0.24
H4	NS–NS	13.6	2.6–2.8	1.0–1.25	–	0.03–0.4	0.18–0.26
MS1	NS–NS	14.4	2.6–2.8	1.0–1.25	–	0.06–0.35	0.18–0.2
APR4	BH–NS	11.1	5.4–10.8	3.0–7.0	0.75	0.05–1	0.23–0.27
ALF2	BH–NS	12.4	5.4–10.8	3.0–7.0	0.75	2.0–4.0	0.25–0.29
H4	BH–NS	13.6	5.4–10.8	3.0–7.0	0.75	4.0–5.0	0.24–0.29
MS1	BH–NS	14.4	5.4–10.8	3.0–7.0	0.75	6.5–8.0	0.25–0.3
APR4	BH–NS	11.1	10.8	7.0	0.5	$\lesssim 10^{-4}$	–
ALF2	BH–NS	12.4	10.8	7.0	0.5	0.02	0.27
H4	BH–NS	13.6	10.8	7.0	0.5	0.3	0.29
MS1	BH–NS	14.4	10.8	7.0	0.5	1.7	0.3

NS-NS ejecta. As shown in Fig. 8.1, the NS-NS ejecta have spheroidal shape rather than a torus or a disk irrespective of Q and EOS as long as an HMNS is formed after the merger (see Chap. 7 for ejecta properties in details).

Numerical simulations of NS–NS mergers show that the total amount of ejecta is in a range 10^{-4}–$10^{-2}M_\odot$ depending on $M_{\rm tot}$, Q, and EOS (see the left panel of Fig. 8.2). The more compact neutron star models with soft EOSs produce the larger amounts of ejecta, because the impact velocities and subsequent shock heating effects at merger are larger.

masses of a binary.

More specifically, the amounts of the ejecta are

$$
\begin{aligned}
&10^{-4} \lesssim M_{\rm ej}/M_\odot \lesssim 2\times 10^{-2} \quad \text{(soft EOSs)},\\
&10^{-4} \lesssim M_{\rm ej}/M_\odot \lesssim 5\times 10^{-3} \quad \text{(stiff EOSs)}.
\end{aligned} \tag{8.1}
$$

BH–NS ejecta. Tidal disruption of a neutron star results in the anisotropic mass ejection for a BH–NS merger (Kyutoku et al. 2013). As a result, the ejecta concentrate near the binary orbital plane as shown in the right panel of Fig. 8.1, and its shape is like a disk or crescent.

The amounts of the ejecta for BH–NS models are smaller for the more compact neutron star models with the fixed values of χ and Q as shown in the right panel of Fig. 8.2. This is because the tidal disruption occurs in a less significant manner. This dependence of the BH-NS ejecta on the compactness of neutron stars is opposite to the NS–NS ejecta.

More specifically, the amounts of the ejecta are

$$
\begin{aligned}
5\times 10^{-4} &\lesssim M_{\rm ej}/M_\odot \lesssim 10^{-2} \quad \text{(soft EOSs)},\\
4\times 10^{-2} &\lesssim M_{\rm ej}/M_\odot \lesssim 7\times 10^{-2} \quad \text{(stiff EOSs)},
\end{aligned} \tag{8.2}
$$

for $\chi = 0.75$ and $3 \leq Q \leq 7$. For $\chi = 0.5$, the ejecta mass is smaller than that for $\chi = 0.75$. Only the stiff EOS models can produce large amounts of ejecta more than $0.01M_\odot$ for $\chi = 0.5$ and $Q = 7$.

Both for NS–NS and BH–NS merger models, winds driven by neutrino/viscous/nuclear-recombination heating or magnetic field from the central object might provide ejecta in addition to the dynamical ejecta (Dessart et al. 2009; Wanajo and Janka 2012; Kiuchi et al. 2012; Fernández and Metzger 2013). However, it is not easy to estimate the amount of the wind ejecta, because it depends strongly on the condition of the remnant formed after the merger. In this work, we focus only on the dynamical ejecta.

8.3 Radiative transfer simulations for the ejecta

For the NS–NS and BH–NS merger models described in the previous section, we perform radiative transfer simulations to obtain the light curves of the radioactively powered emission from the ejecta using the three-dimensional, time-dependent, multi-frequency Monte Carlo radiative transfer code (Tanaka and Hotokezaka 2013). For a given density structure of the ejecta and elemental abundances, this code computes the emission in the ultraviolet, optical, and near-infrared wavelength ranges by taking into account the detailed r-process opacities. In this work, we include r-process elements with $Z \geq 40$ assuming the solar abundance ratios by Simmerer et al. (2004). More details of the radiation transfer simulations are described in Tanaka and Hotokezaka (2013); Tanaka et al. (2013).

The heating rate from the radioactive decay of r-process elements is one of the important ingredients of the radiative transfer simulations. As a fiducial-heating model, we

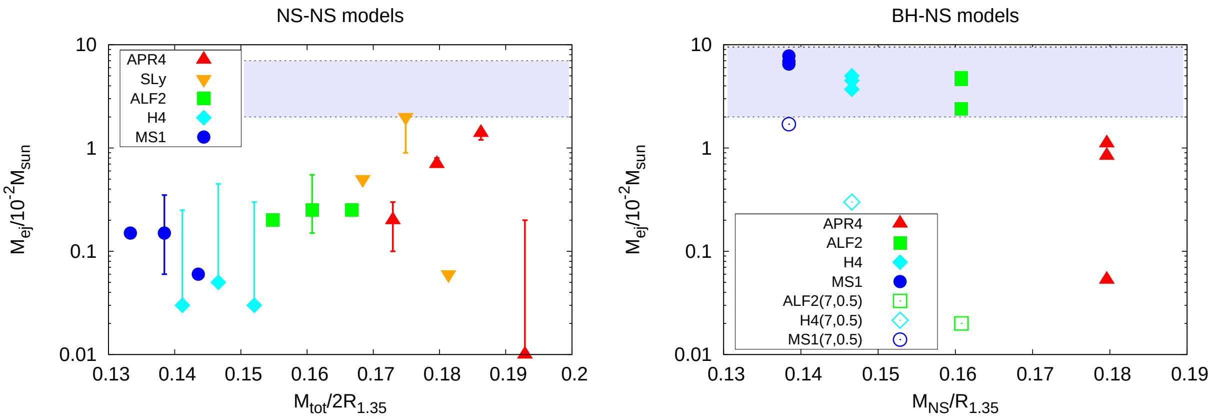

Figure 8.2: Ejecta masses as a function of the compactness of the neutron star, which is defined by $GM_{\rm tot}/2R_{1.35}c^2$ and $GM_{\rm NS}/R_{1.35}c^2$ for NS–NS and BH–NS models, respectively. Left panel: NS–NS models. Each point shows the ejecta mass for the equal mass cases. Error bars denote the dispersion of the ejecta masses due to the various mass ratios. Right panel: BH–NS models. The filled and open symbols correspond to the models with $(Q, \chi) = (3\text{–}7, 0.75)$ and $(7, 0.5)$, respectively. The blue shaded region in each panel shows the allowed ejecta masses to reproduce the observed near-infrared excess of GRB 130603B, $0.02 \lesssim M_{\rm ej}/M_\odot \lesssim 0.07$ and $0.02 \lesssim M_{\rm ej}/M_\odot \lesssim 0.1$ for NS-NS and BH-NS models, respectively. The lower and upper bounds are imposed by the hypothetical high- and low-heating models, respectively. This figure is taken from Hotokezaka et al. (2013d).

employ the heating rate computed with the abundance distribution that reproduces the solar r-process pattern (see Tanaka et al. 2013 for more detail). Heating is due to β-decays only, which increase the atomic numbers from the neutron-rich region toward the β-stability line without changing the mass number A. This heating rate is in reasonable agreement with those from previous nucleosynthesis calculations (Metzger et al. 2010; Goriely et al. 2011; Grossman et al. 2013) except for the first several seconds.

We note that there could exist quantitative uncertainties in the heating rate as well as in the opacities. As an example, the heating rate would be about a factor 2 higher if the r-process abundances of $A \sim 130$ (or those produced with the electron fraction of $Y_e \sim 0.2$) were dominant in the ejecta (Metzger et al. 2010; Grossman et al. 2013). To take into account such uncertainties, we also consider the cases in which the light curves of mergers are twice and half as luminous (high- and low-heating models; only explicitly shown for the NS–NS models in Fig. 3) as those computed with the fiducial-heating model.

8.4 Light curves and possible progenitor models

The computed light curves and observed data in r and H-band are compared in Fig. 8.3. The left panel of Fig. 8.3 shows the light curves of the NS–NS merger models SLy ($Q =$

1.0, $M_{\rm ej} = 0.02M_\odot$) and H4 ($Q = 1.25$, $M_{\rm ej} = 4 \times 10^{-3}M_\odot$) for reference. Here the total mass of the progenitor is chosen to be $M = 2.7M_\odot$. We plot three light curves derived with the fiducial- (the middle curves), high- (the upper curves), and low-heating models (the lower curves). We expect that the realistic light curves may lie within the shaded regions. For the NS–NS models, the computed r-band light curves are fainter than 30 mag. The right panel of Fig. 8.3 shows the light curves of the BH–NS merger models, MS1 ($M_{\rm ej} = 0.07M_\odot$), H4 ($M_{\rm ej} = 0.05M_\odot$), and APR4 ($M_{\rm ej} = 0.01M_\odot$) with $(Q,\ \chi) = (3,\ 0.75)$. For these cases, we employ the fiducial-heating model. Note that the r-band light curves of the BH-NS models reach ~ 27 mag, which implies that the light curves of the BH-NS models are bluer than those of the NS-NS models. This is because the energy from the radioactive decay is deposited to a small volume for the BH–NS models (see Tanaka et al. 2013 in details). As shown in Fig. 6 of Kasen et al. (2013, see also Fig. 15 of Tanaka and Hotokezaka 2013), the opacity of r-process elements depends strongly on the temperature, and thus the time after the merger. The small bumps in the H-band light curves of BH–NS models are caused by this time-dependent opacity.

There are expected to be uncertainties associated with the difference in the morphology between the models of the same progenitor type but different masses and spins. Moreover, the light curves may also depend on the viewing angle. However, these uncertainties are not large enough to affect significantly our results (see Tanaka and Hotokezaka 2013; Tanaka et al. 2013 for details).

We now translate these results into the progenitor models, such as mass ratio, black hole spin, and EOS.

NS–NS models. The NS–NS models for GRB 130603B should have ejecta of mass $\gtrsim 0.02M_\odot$. This is consistent with that derived by Berger et al. (2013). This value strongly constrains the NS-NS models because the amount of the ejecta is at most $\sim 0.02M_\odot$ for an NS–NS merger within the plausible mass range of the observed NS–NS systems (see Table 1.1) Specifically, as shown in the left panel of Fig. 8.2, such a large amount of ejecta can be obtained only for the soft EOS models in which an HMNS with lifetime $\gtrsim 10$ ms is formed after the merger. For the stiff EOS models, the amount of the ejecta is at most $4 \times 10^{-3}M_\odot$. Thus we conclude that the ejecta of the NS–NS models with soft EOSs ($R_{1.35} \lesssim 12$ km) are favored as the progenitor of GRB 130603B.

BH–NS models. The observed data in the H-band is consistent with the BH–NS models which produce the ejecta of $\sim 0.05M_\odot$ in our fiducial-heating model. Such a large amount of ejecta can be obtained with only the stiff EOSs ($R_{1.35} \gtrsim 13.5$ km) for the case of $\chi = 0.75$ and $3 \leq Q \leq 7$ as shown in the right panel of Fig. 8.2. For the soft EOS models, the total amount of ejecta reaches only $0.01M_\odot$ as long as $\chi \leq 0.75$, which hardly reproduces the observed near-infrared excess. Thus the models with stiff EOSs are favored for the BH–NS merger models as long as with $0.5 \leq \chi \leq 0.75$ and $3 \leq Q \leq 7$ as the progenitor model of GRB 130603B. It is worthy to note that any BH–NS models with $\chi \leq 0.5$ and $Q \geq 7$ are unlikely to reproduce the observed near-infrared excess.

8.5 Conclusion and Discussion

We explored possible progenitor models of the electromagnetic associated with the *Swift* short GRB 130603B. This electromagnetic may have been powered by the radioactive decay of r-process elements, the so-called kilonova. We analyzed the dynamical ejecta of NS–NS and BH–NS mergers for the progenitor models of this event. For computing the expected light curves, we carried out the radiative transfer simulations using the density and velocity structures obtained from the numerical-relativity simulations with several total masses, mass ratios, and EOSs. Depending on these quantities, the total amount of ejecta mass varies by orders of magnitude $10^{-4}M_\odot$ to $10^{-2}M_\odot$ for the NS–NS models and $10^{-5}M_\odot$ to $10^{-1}M_\odot$ for the BH–NS models. The expected light curves for the BH–NS models are bluer than those for the NS–NS models due to the morphology effects. Our findings are as follows:

- There are progenitor models that can reproduce the observed near-infrared excess within the realistic parameter ranges for both NS–NS and BH–NS models.
- The observed data suggest that the required ejecta mass is at least $\sim 0.02M_\odot$ for NS–NS mergers. For BH–NS mergers, the required ejecta mass would be ~ 0.02–$0.1M_\odot$ taking into account the uncertainty in the heating rate and opacities. Such a large amount of material is ejected when an HMNS with its lifetime $\gtrsim 10$ ms is formed after the merger for the NS–NS models and when the neutron star is tidally disrupted for the BH–NS models.
- The soft EOS models are favored for NS–NS models as the progenitor of GRB 130603B. On the contrary, the stiff EOS models are favored for BH–NS models with the mass ratio $3 \leq Q \leq 7$ and the nondimensional spin parameter of the black hole $0.5 \leq \chi \leq 0.75$. Furthermore, for $\chi \leq 0.5$, any BH–NS models with $Q \geq 7$ are unlikely to produce the required amount of ejecta.

The above values of ejecta mass are consistent with the results of a spherically expanding ejecta model (Berger et al. 2013). Note that our results may be valid as long as the mass ejection due to winds is subdominant.

In future, the observations of gravitational waves from compact binary mergers within ~ 200 Mpc will provide the masses of the binaries and their types. Combining the observations of the gravitational-wave and electromagnetic signals, it will be possible to constrain more stringently the progenitor models, in particular EOSs, of such events.

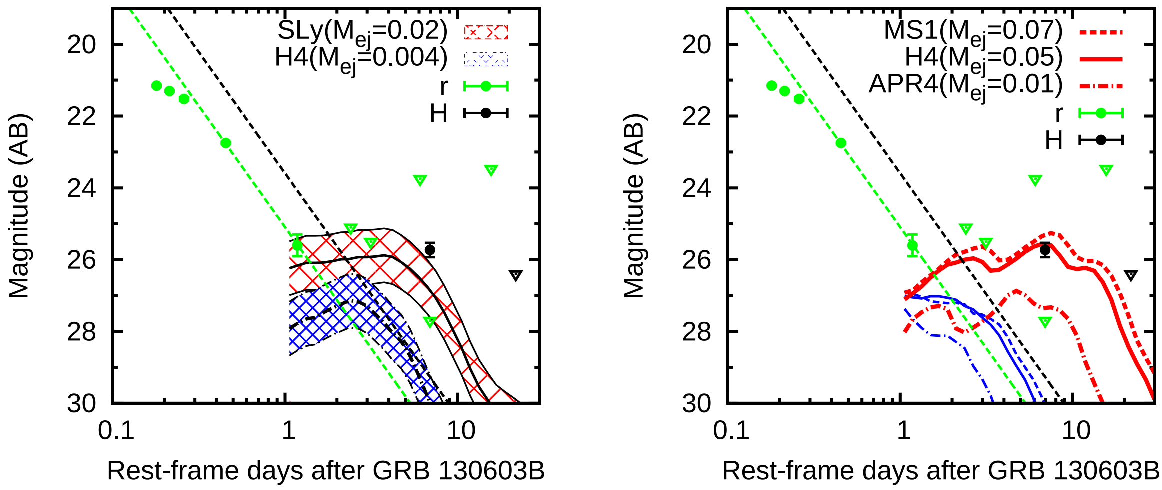

Figure 8.3: Predicted light curves for NS–NS and BH–NS models. Left panel: NS–NS models. The dashed, solid, and dot-dashed curves show the H-band light curves for the models: SLy ($Q = 1.0,\ M_{\rm ej} = 0.02M_{\odot}$), H4 ($Q = 1.25,\ M_{\rm ej} = 4 \times 10^{-3}M_{\odot}$), respectively. The total mass of the progenitor is fixed to be $2.7M_{\odot}$. The upper, middle, and lower curves for each model correspond to the high-, fiducial- and low-heating models. Right panel: BH-NS models. The dashed, solid, and dot-dashed curves show the models MS1 ($M_{\rm ej} = 0.07M_{\odot}$), H4 ($M_{\rm ej} = 0.05M_{\odot}$), and APR4 ($M_{\rm ej} = 0.01M_{\odot}$), respectively. Here only the fiducial-heating models are shown. The thin and thick lines denote the r and H-band light curves. Here we set $(Q,\ \chi) = (3,\ 0.75)$. The observed data (filled circles), upper limits (triangles), and the light curves (dashed lines) of the afterglow model of GRB 130603B in r and H-band are plotted (Tanvir et al. 2013; de Ugarte Postigo et al. 2013). The observed point in r-band at 1 days after the GRB is consistent with the afterglow model. The key observations for a kilonova are the observed H-band data at 7 days after the GRB, which exceed the H-band light curve of the afterglow model, and the upper limit in H-band at 22 days after the GRB. These data suggest the existence of a kilonova associated with GRB 130603B. This figure is taken from Hotokezaka et al. (2013d).

Chapter 9

Summary and Future directions

Progress in the development of numerical relativity allows us to compute dynamical spacetime and hydrodynamics. In this thesis, we apply numerical relativity to the systematical study of NS–NS merger, where numerical simulations of NS–NS merger are performed with several total masses, mass ratios, and EOSs of neutron-star matter. The main aim of this thesis is to model both gravitational-wave and electromagnetic signals based on the results of our numerical relativity simulations. This kind of studies is needed in the era of the second-generation ground based gravitational-wave detectors.

The former part of the thesis is devoted to the studies of waveforms of gravitational waves from NS–NS mergers. A late-inspiral phase, merger phase, and post-merger phase of NS–NS systems contain information about the EOS of neutron-star matter. We will be able to extract this information via gravitational-wave observations. For this purpose, the waveforms which are accurate enough to be used as template waveforms are needed in these phases. We attempt to model waveforms by using numerical relativity simulations:

- The long-term waveforms (about 9 orbits) in the late NS–NS inspiral phase are computed with four different grid resolutions. By using these data, the extrapolated gravitational-wave phases are obtained. Then we find that the numerical error due to the finite differencing is the dominant error, e.g., $\gtrsim 0.1$ radian for gravitational-wave phases.

- The extrapolated waveforms are compared with the waveforms obtained by analytical computations. Here we adopt the post-Newtonian formalism and effective one body formalism, where both the formalisms include the tidal effects of the quadrupole deformation of neutron stars. As a result, we find that the phase evolution of the extrapolated waveforms is rapid compared to that of the analytic waveforms. The difference between them is 1–2 radian at the contact of an NS–NS. This value is still larger than the phase difference due to the higher order tidal corrections. Furthermore, the modulation of gravitational-wave phase due to the residual eccentricity of the initial data prevents us to accurately extrapolate a numerical waveform and compare that with the analytic waveforms.

- A massive neutron star can be a strong gravitational-wave emitter in the post-merger phase. Our numerical simulations suggest that such a massive neutron star survives for NS–NS mergers with the typical mass range $2.6M_{\odot} \leq M \leq 2.8M_{\odot}$. The characteristic frequency of gravitational waves of a remnant massive neutron star has a strong correlation with the radius of neutron stars.

- We construct a phenomenological waveform of post-merger phase, which contains 13 free parameters to fit the various waveforms obtained by numerical relativity simulations. The mismatch between the best-fitted waveform and the numerical waveform is less than 10%.

The latter part of the thesis is devoted to the studies of electromagnetic counterparts of NS–NS mergers, which will be helpful to determine the positions of gravitational-wave sources which are precise enough to locate the gravitational-wave events within their host galaxies. Some electromagnetic signals are speculated to be associated with mass ejection at NS–NS mergers, e.g., a kilonova, a radio-flare of a merger remnant, and extended emissions in X-ray. In order to study properties of mass ejection in full general relativity, we perform numerical relativity simulations with a relatively wide computational domain. We further study the expected light curves of a kilonova based on the radiative transfer simulations. Our results are as follows:

- The ejecta mass is in the range of 10^{-4}–$10^{-2}M_{\odot}$ and the ejecta velocity is in the range of 0.1–0.5c, for the various total masses, mass ratios, and EOSs. For a given EOS, the ejecta mass increases with total mass of a binary, as long as a long-lived HMNS is formed after the merger. For a given mass, an NS–NS merger with a softer EOS produces a larger amount of ejecta, as long as a long-lived HMNS is formed after the merger.

- A kilonova candidate associated with the short GRB 130603B is compared with our numerical relativity simulations. As a result, we find that there are models of which brightness, time scale, and color are consistent with the observed data and upper limits. More specifically, NS–NS merger models with soft EOS and BH–NS merger models are the candidate of the progenitor of the short GRB 130603B.

We now discuss the future directions of this research field. In order to achieve measurement of the finite-size of a neutron star with gravitational-wave observations, we have to do the followings:

- High-accuracy numerical simulations of NS–NS mergers of which uncertainties of accumulated phase difference in last 10 orbits due to finite differencing and residual eccentricities is less than ~ 0.05 radian should be performed.

- Analytical waveforms up to post-4 Newtonian terms are needed.
- Measurability of tidal deformability parameters should be estimated with more sophisticated ways, e.g., Markov-chain Monte-Carlo methods.
- Detectability of signals of a remnant massive neutron star should be evaluated.
- A map between the parameters contained in a phenomenological waveform of a massive neutron star and physical parameters such as the mass and EOS should be investigated.

Future directions of the research about electromagnetic signals from compact bianry mergers are as follows:

- The full opacity table should be prepared in order to compute a complete spectrum of kilonova emissions. This is crucial to confirm the kilonova discovery.
- The distribution of electron fraction of the ejecta should be explored, which will allow us to evaluate more precise heating rate and opacities for kilonova emissions.
- The possible contributions of wind-mass ejection should be studied.
- Dynamical interaction between a relativistic jet and NS–NS merger ejecta should be explored to fully understand the NS–NS merger scenario of short GRBs.

Acknowledgements

I am deeply grateful to Prof. Masaru Shibata for his continuous help and support. I appreciate Dr. Koutarou Kyutoku for computing initial data for my numerical simulations. I also appreciate Dr. Hirotada Okawa for improving the numerical code `SACRA` and managing the computational environments.

I would like to appreciate Prof. Takashi Nakamura for faithful discussions and countinuous encouragement. I am also grateful to Prof. Testuya Shiromizu, Prof. Kazuyuki Omukai, Prof. Takahiro Tanaka, Prof. Misao Sasaki, Prof. Jiro Soda, Prof Masaki Ando, Prof. Yudai Suwa, Prof. Naoki Seto, Prof. Yoshiyuki Yamada, and Prof. Tsutomu Kobayashi for helpful discussions of astrophysics and relativity. I also appreciate to Prof. Toshitaka Tasumi and Prof. Akira Ohnishi for faithful discussions of neutron stars.

I am grateful to Dr. Yuichiro Sekiguchi, Dr. Kenta Kiuchi, Dr. Takayuki Murnushi and Prof. Keisuke Taniguchi for in-depth discussions of numerical relativity and gravitational waves. I also appreciate Prof. Masaomi Tanaka, Prof. Kunihito Ioka, Dr. Shinya Wanajo, Dr. Hiroki Nagakura, and Dr. Kazumi Kashiyama for faithfull discussions of high-energy astrophysics. I am also grateful to Mr. Daisuke Nakauchi and Mr. Tomoya Kinugawa for faithful discussions of binary evolution. Finally, I would like to thank Mr. Kohei Inayoshi, Mr. Kazuyuki Sugimura, Mr. Soichiro Isoyama, Mr. Yusuke Korai, and Mr. Doleman Youri for helpful discussions and encouragement.

Appendix A Synchrotron radiation

Here we briefly review the basic concepts of the synchrotron radiation based on Rybicki and Lightman (1979). For a relativistic electron with the Lorentz factor γ which is moving in magnetic fields B with the pitch angle α, the frequency of the gyration is given by $\omega_B = eB/\gamma m_e c$. Such a relativistic electron emits the radiation with the total power

$$P = \frac{4}{3}\sigma_{\rm T} c\beta^2\gamma^2\frac{B^2}{8\pi}, \tag{1}$$

where $\sigma_{\rm T}$ is the Thomson cross section and β is the velocity of the electron. Here we take an average of the pitch angle. Due to relativistic beaming, an observer can see only the photon emitted in $\Delta\theta \sim 2/\gamma$, and thus the observer receives the photons emitted during $\Delta t \simeq 2/(\gamma\omega_B \sin\alpha)$. Then the arrival time can be written $\Delta t_{\rm A} \simeq \Delta t/(2\gamma^2 \sin\alpha)$. Therefore an observer detects the radiation with the characteristic frequency given by

$$\omega_{\rm c} = \frac{3}{2}\gamma^3\omega_B \sin\alpha. \tag{2}$$

By using the characteristic frequency, the emission power of a relativistic electron can be written as

$$P(\omega) = \frac{\sqrt{3}}{2\pi}\frac{e^3 B\sin\alpha}{m_e c^2}F\left(\frac{\omega}{\omega_c}\right) \tag{3}$$

where $F(x)$ is described the modified Bessel function of 5/3 order $K_{5/3}$ as $F(x) \equiv x\int_x^\infty K_{5/3}(\xi)d\xi$. The asymptotic forms of $F(x)$ are

$$F(x) \propto \begin{cases} x^{1/3} & (x \ll 1), \\ x^{1/2}e^{-x} & (x \gg 1). \end{cases} \tag{4}$$

The function F(x) has a maximum at $x = 0.29$, and thus, the power spectrum of the synchrotron radiation of an electron has a peak around the characteristic frequency ν_m. Roughly speaking, the maximum value of the power can be evaluated as

$$P_{\nu,\max}(\gamma) \simeq \frac{P(\gamma)}{\omega_c(\gamma)/3} = \frac{2m_e c^2\sigma_{\rm T} B}{3e}. \tag{5}$$

It is worthy to note that this value does not depend on the Lorentz factor of a relativistic electron.

Now we consider the spectrum of the synchrotron emission of the relativistic electrons with the power law index p, .i.e., the distribution function of the relativistic electrons is given by $N(\gamma)d\gamma = N_0\gamma^{-p}d\gamma$. For such a case, the spectrum is given by

$$P^{\rm tot}(\omega) = C\int_{\gamma_m}^\infty F\left(\frac{\omega}{\omega_c}\right)\gamma^{-p}d\gamma. \tag{6}$$

Here we assume that their is a minimum Lorentz factor γ_m of the distribution of the relativistic electrons and we denote the ω_m is the characteristic frequency of the electrons with γ_m. For the relativistic electron accelerated at the relativistic shock, the minimum Lorentz factor of electrons can be given by $\epsilon_e \Gamma(p-2)/(p-1) m_e/m_p$, where ϵ_e is the conversion efficiency of the energy density behind the shock into the energy density of the accelerated electrons, Γ is the Lorentz factor of the shocked fluid (Sari et al. 1998). As long as the frequency is larger than ω_m, the spectrum of the synchrotron radiation is

$$P_\nu^{\rm tot} \propto \nu^{-(p-1)/2}. \tag{7}$$

For $\omega < \omega_m$, the spectrum of the synchrotron radiation is

$$P_\nu^{\rm tot} \propto \nu^{1/3}. \tag{8}$$

Because of Eq. (5), the maximum value of a spectrum is

$$P_{\nu,\rm max}^{\rm tot} \simeq \frac{2 m_e c^2 \sigma_{\rm T} B N_e}{e}, \tag{9}$$

where N_e is the total number of relativistic electrons.

The above discussion about the spectrum of the synchrotron radiation is assumed to be the optically thin limit. However, one often encounters optically thick cases. Here we argue the spectrum of the synchrotron radiation in the optically thick regime, in which the emission is determined at $\tau_\nu \approx 1$

For the low frequency $h\nu \ll \gamma m_e c^2$, the absorption coefficient can be written as

$$\alpha_\nu = -\frac{c^2}{8\pi\nu^2} \int d\gamma P(\nu,\gamma) \gamma^2 \frac{\partial}{\partial \gamma} \left[\frac{N(\gamma)}{\gamma^2} \right]. \tag{10}$$

Here we consider two cases for the relativistic electron distribution function $N(\gamma)$: (i) a thermal distribution $N(\gamma) \propto \gamma^2 e^{-\gamma m_e c^2/kT}$, (ii) a power law distribution $N(\gamma) \propto \gamma^{-p}$ in the frequency $\nu > \nu_m$, and (iii) a power law distribution $N(\gamma) \propto \gamma^{-p}$ in the frequency $\nu \lesssim \nu_m$. For the case (i), The distribution leads

$$\alpha_\nu^{\rm th} = \frac{c^2}{8\pi\nu^2 kT} \int_0^\infty N(\gamma) P(\nu,\gamma) d\gamma = \frac{j_\nu}{2\nu^2 kT}, \tag{11}$$

where j_ν is the emissivity defined by

$$j_\nu = \frac{1}{4\pi} \int_0^\infty N(\gamma) P(\nu,\gamma) d\gamma. \tag{12}$$

The source function $S_\nu \equiv j_\nu/\alpha_\nu$ is obtained, for the case (i),

$$S_\nu \propto \nu^2, \tag{13}$$

This form is the famous Reyleigh-Jeans law.

For the case (ii), the absorption coefficient can be wrriten as

$$\alpha_\nu^{\rm p} \simeq \frac{(p+2)c^2}{8\pi\nu^2} \int_0^\infty \frac{N(\gamma)}{\gamma} P(\nu,\gamma) d\gamma \propto \nu^{-(p+4)/2}, \tag{14}$$

and thus

$$S_\nu \propto \nu^{5/2}, \tag{15}$$

where Eq. (7) is used for the emissivity of the synchrotron radiation of relativistic electrons with the power law distribution.

For the case (iii),

$$\alpha_\nu^{\mathrm{p}} \simeq \frac{(p+2)c^2}{8\pi\nu^2}\int_{\gamma_m}^{\infty}\frac{N(\gamma)}{\gamma}P(\nu,\gamma)d\gamma \propto \nu^{-5/3}\gamma_m^{-p-2/3}. \tag{16}$$

The source function can be obtained as

$$S_\nu \propto \nu^2\gamma_m. \tag{17}$$

As long as γ_m is independent of the frequency, and thus, one obtains the source function $S_\nu \propto \nu^2$, which is again the Reyleigh-Jeans law.

Note that the absorption coefficient is larger for photons with the lower frequency for the both cases. Therefore the self-absorption effects has to be taken into account, when one focuses on the synchrotron light curve and spectrum at lower frequencies. In most synchrotron radiation models of GRB afterglows, only a power-law distribution of electrons is taken into account. In such cases, the spectral index of the synchrotron radiation is $-(p-1)/2$ for the optically thin and $\omega > \omega_m$ case, 1/3 for the optically thin and $\omega < \omega_m$ case, 5/2 for the optically thick and $\omega > \omega_m$ case, and 2 for the optically thick and $\omega < \omega_m$ case.

Bibliography

J. Abadie, B. P. Abbott, R. Abbott, M. Abernathy, T. Accadia, F. Acernese, C. Adams, R. Adhikari, P. Ajith, B. Allen, and et al. TOPICAL REVIEW: Predictions for the rates of compact binary coalescences observable by ground-based gravitational-wave detectors. *Classical and Quantum Gravity*, 27(17):173001, September 2010. doi: 10.1088/0264-9381/27/17/173001.

J. Abadie, B. P. Abbott, R. Abbott, T. D. Abbott, M. Abernathy, T. Accadia, F. Acernese, C. Adams, R. Adhikari, C. Affeldt, and et al. Search for gravitational waves from low mass compact binary coalescence in LIGO's sixth science run and Virgo's science runs 2 and 3. Phys. Rev. D, 85(8):082002, April 2012. doi: 10.1103/PhysRevD.85.082002.

A. Akmal, V. R. Pandharipande, and D. G. Ravenhall. Equation of state of nucleon matter and neutron star structure. Phys. Rev. C, 58:1804–1828, September 1998. doi: 10.1103/PhysRevC.58.1804.

M. Alford, M. Braby, M. Paris, and S. Reddy. Hybrid Stars that Masquerade as Neutron Stars. ApJ, 629:969–978, August 2005. doi: 10.1086/430902.

M. A. Aloy, H.-T. Janka, and E. Müller. Relativistic outflows from remnants of compact object mergers and their viability for short gamma-ray bursts. A&A, 436:273–311, June 2005. doi: 10.1051/0004-6361:20041865.

J. Antoniadis, P. C. C. Freire, N. Wex, T. M. Tauris, R. S. Lynch, M. H. van Kerkwijk, M. Kramer, C. Bassa, V. S. Dhillon, T. Driebe, J. W. T. Hessels, V. M. Kaspi, V. I. Kondratiev, N. Langer, T. R. Marsh, M. A. McLaughlin, T. T. Pennucci, S. M. Ransom, I. H. Stairs, J. van Leeuwen, J. P. W. Verbiest, and D. G. Whelan. A Massive Pulsar in a Compact Relativistic Binary. *Science*, 340:448, April 2013. doi: 10.1126/science.1233232.

R. Arnowitt, S. Deser, and C. W. Misner. Dynamical structure and definition of energy in general relativity. *Phys. Rev.*, 116:1322–1330, Dec 1959. doi: 10.1103/PhysRev.116.1322. URL `http://link.aps.org/doi/10.1103/PhysRev.116.1322`.

L. Baiotti, T. Damour, B. Giacomazzo, A. Nagar, and L. Rezzolla. Analytic Modeling of Tidal Effects in the Relativistic Inspiral of Binary Neutron Stars. *Physical Review Letters*, 105(26):261101, December 2010. doi: 10.1103/PhysRevLett.105.261101.

L. Baiotti, T. Damour, B. Giacomazzo, A. Nagar, and L. Rezzolla. Accurate numerical simulations of inspiralling binary neutron stars and their comparison with effective-one-body analytical models. Phys. Rev. D, 84(2):024017, July 2011. doi: 10.1103/PhysRevD.84.024017.

J. G. Baker, J. Centrella, D.-I. Choi, M. Koppitz, and J. van Meter. Gravitational-Wave Extraction from an Inspiraling Configuration of Merging Black Holes. *Physical Review Letters*, 96(11):111102, March 2006. doi: 10.1103/PhysRevLett.96.111102.

S. A. Balbus and J. F. Hawley. A powerful local shear instability in weakly magnetized disks. I - Linear analysis. II - Nonlinear evolution. ApJ, 376:214–233, July 1991. doi: 10.1086/170270.

S. A. Balbus and J. F. Hawley. Instability, turbulence, and enhanced transport in accretion disks. *Reviews of Modern Physics*, 70:1–53, January 1998. doi: 10.1103/RevModPhys.70.1.

F. Banyuls, J. A. Font, J. M. A. Ibanez, J. M. A. Marti, and J. A. Miralles. Numerical {3+1} General Relativistic Hydrodynamics: A Local Characteristic Approach. ApJ, 476:221, February 1997. doi: 10.1086/303604.

J. Barnes and D. Kasen. Effect of a High Opacity on the Light Curves of Radioactively Powered Transients from Compact Object Mergers. ApJ, 775:18, September 2013. doi: 10.1088/0004-637X/775/1/18.

T. W. Baumgarte and S. L. Shapiro. Numerical integration of Einstein's field equations. Phys. Rev. D, 59(2):024007, January 1999. doi: 10.1103/PhysRevD.59.024007.

T. W. Baumgarte, S. L. Shapiro, and M. Shibata. On the Maximum Mass of Differentially Rotating Neutron Stars. ApJ, 528:L29–L32, January 2000. doi: 10.1086/312425.

A. Bauswein and H.-T. Janka. Measuring Neutron-Star Properties via Gravitational Waves from Neutron-Star Mergers. *Physical Review Letters*, 108(1):011101, January 2012. doi: 10.1103/PhysRevLett.108.011101.

A. Bauswein, H.-T. Janka, and R. Oechslin. Testing approximations of thermal effects in neutron star merger simulations. Phys. Rev. D, 82(8):084043, October 2010. doi: 10.1103/PhysRevD.82.084043.

A. Bauswein, H.-T. Janka, K. Hebeler, and A. Schwenk. Equation-of-state dependence of the gravitational-wave signal from the ring-down phase of neutron-star mergers. Phys. Rev. D, 86(6):063001, September 2012. doi: 10.1103/PhysRevD.86.063001.

A. Bauswein, T. W. Baumgarte, and H.-T. Janka. Prompt Merger Collapse and the Maximum Mass of Neutron Stars. *Physical Review Letters*, 111(13):131101, September 2013a. doi: 10.1103/PhysRevLett.111.131101.

A. Bauswein, S. Goriely, and H.-T. Janka. Systematics of Dynamical Mass Ejection, Nucleosynthesis, and Radioactively Powered Electromagnetic Signals from Neutron-star Mergers. ApJ, 773:78, August 2013b. doi: 10.1088/0004-637X/773/1/78.

E. Berger. Short-Duration Gamma-Ray Bursts. *ArXiv e-prints*, November 2013.

E. Berger, S. B. Cenko, D. B. Fox, and A. Cucchiara. Discovery of the Very Red Near-Infrared and Optical Afterglow of the Short-Duration GRB 070724A. ApJ, 704:877–882, October 2009. doi: 10.1088/0004-637X/704/1/877.

E. Berger, W. Fong, and R. Chornock. An r-process Kilonova Associated with the Short-hard GRB 130603B. ApJ, 774:L23, September 2013. doi: 10.1088/2041-8205/774/2/L23.

S. Bernuzzi, A. Nagar, M. Thierfelder, and B. Brügmann. Tidal effects in binary neutron star coalescence. Phys. Rev. D, 86(4):044030, August 2012a. doi: 10.1103/PhysRevD.86.044030.

S. Bernuzzi, M. Thierfelder, and B. Brügmann. Accuracy of numerical relativity waveforms from binary neutron star mergers and their comparison with post-Newtonian waveforms. Phys. Rev. D, 85(10):104030, May 2012b. doi: 10.1103/PhysRevD.85.104030.

S. D. Berthelmy, W. H. Baumgartner, N. Cummings J. R. Gehrels, H. A. Krimm, A. Y Lien, Markwardt C. B., Melandri A., Palmer D. M., Sakamoto T., Sato G., Stamatikos M., Tueller J. Ukwatta T. N., and the Swift team. GRB 130603B: Swift-BAT refined analysis. *GCN circular*, 2013.

L. Bildsten and C. Cutler. Tidal interactions of inspiraling compact binaries. ApJ, 400: 175–180, November 1992. doi: 10.1086/171983.

D. Bini, T. Damour, and G. Faye. Effective action approach to higher-order relativistic tidal interactions in binary systems and their effective one body description. Phys. Rev. D, 85(12):124034, June 2012. doi: 10.1103/PhysRevD.85.124034.

T. Binnington and E. Poisson. Relativistic theory of tidal Love numbers. Phys. Rev. D, 80(8):084018, October 2009. doi: 10.1103/PhysRevD.80.084018.

J. S. Bloom, J. X. Prochaska, D. Pooley, C. H. Blake, R. J. Foley, S. Jha, E. Ramirez-Ruiz, J. Granot, A. V. Filippenko, S. Sigurdsson, A. J. Barth, H.-W. Chen, M. C. Cooper, E. E. Falco, R. R. Gal, B. F. Gerke, M. D. Gladders, J. E. Greene, J. Hennanwi, L. C. Ho, K. Hurley, B. P. Koester, W. Li, L. Lubin, J. Newman, D. A. Perley, G. K. Squires, and W. M. Wood-Vasey. Closing in on a Short-Hard Burst Progenitor: Constraints from Early-Time Optical Imaging and Spectroscopy of a Possible Host Galaxy of GRB 050509b. ApJ, 638:354–368, February 2006. doi: 10.1086/498107.

M. Boyle, D. A. Brown, L. E. Kidder, A. H. Mroué, H. P. Pfeiffer, M. A. Scheel, G. B. Cook, and S. A. Teukolsky. High-accuracy comparison of numerical relativity simulations with post-Newtonian expansions. Phys. Rev. D, 76(12):124038, December 2007. doi: 10.1103/PhysRevD.76.124038.

O. Bromberg, E. Nakar, T. Piran, and R. Sari. Short versus Long and Collapsars versus Non-collapsars: A Quantitative Classification of Gamma-Ray Bursts. ApJ, 764:179, February 2013. doi: 10.1088/0004-637X/764/2/179.

Bernd Brügmann, José A. González, Mark Hannam, Sascha Husa, Ulrich Sperhake, and Wolfgang Tichy. Calibration of moving puncture simulations. *Phys. Rev. D*, 77:024027, Jan 2008. doi: 10.1103/PhysRevD.77.024027. URL `http://link.aps.org/doi/10.1103/PhysRevD.77.024027`.

A. Buonanno and T. Damour. Effective one-body approach to general relativistic two-body dynamics. Phys. Rev. D, 59(8):084006, April 1999. doi: 10.1103/PhysRevD.59.084006.

A. Buonanno and T. Damour. Transition from inspiral to plunge in binary black hole coalescences. Phys. Rev. D, 62(6):064015, September 2000. doi: 10.1103/PhysRevD.62.064015.

M. Burgay, N. D'Amico, A. Possenti, R. N. Manchester, A. G. Lyne, B. C. Joshi, M. A. McLaughlin, M. Kramer, J. M. Sarkissian, F. Camilo, V. Kalogera, C. Kim, and D. R. Lorimer. An increased estimate of the merger rate of double neutron stars from observations of a highly relativistic system. Nature, 426:531–533, December 2003. doi: 10.1038/nature02124.

M. Campanelli, C. O. Lousto, P. Marronetti, and Y. Zlochower. Accurate Evolutions of Orbiting Black-Hole Binaries without Excision. *Physical Review Letters*, 96(11):111101, March 2006. doi: 10.1103/PhysRevLett.96.111101.

R. A. Chevalier. Synchrotron Self-Absorption in Radio Supernovae. ApJ, 499:810, May 1998. doi: 10.1086/305676.

S. A. Colgate and C. McKee. Early Supernova Luminosity. ApJ, 157:623, August 1969. doi: 10.1086/150102.

S. A. Colgate and R. H. White. The Hydrodynamic Behavior of Supernovae Explosions. ApJ, 143:626, March 1966. doi: 10.1086/148549.

G. B. Cook, S. L. Shapiro, and S. A. Teukolsky. Testing a simplified version of Einstein's equations for numerical relativity. Phys. Rev. D, 53:5533–5540, May 1996. doi: 10.1103/PhysRevD.53.5533.

A. Cucchiara, J. X. Prochaska, D. Perley, S. B. Cenko, J. Werk, A. Cardwell, J. Turner, Y. Cao, J. S. Bloom, and B. E. Cobb. Gemini Spectroscopy of the Short-hard Gamma-Ray Burst GRB 130603B Afterglow and Host Galaxy. ApJ, 777:94, November 2013. doi: 10.1088/0004-637X/777/2/94.

C. Cutler and É. E. Flanagan. Gravitational waves from merging compact binaries: How accurately can one extract the binary's parameters from the inspiral waveform\? Phys. Rev. D, 49:2658–2697, March 1994. doi: 10.1103/PhysRevD.49.2658.

C. Cutler and L. Lindblom. The effect of viscosity on neutron star oscillations. ApJ, 314: 234–241, March 1987. doi: 10.1086/165052.

T. Damour. Coalescence of two spinning black holes: An effective one-body approach. Phys. Rev. D, 64(12):124013, December 2001. doi: 10.1103/PhysRevD.64.124013.

T. Damour and A. Nagar. Relativistic tidal properties of neutron stars. Phys. Rev. D, 80(8):084035, October 2009. doi: 10.1103/PhysRevD.80.084035.

T. Damour and A. Nagar. Effective one body description of tidal effects in inspiralling compact binaries. Phys. Rev. D, 81(8):084016, April 2010. doi: 10.1103/PhysRevD.81.084016.

T. Damour, A. Nagar, and L. Villain. Measurability of the tidal polarizability of neutron stars in late-inspiral gravitational-wave signals. Phys. Rev. D, 85(12):123007, June 2012. doi: 10.1103/PhysRevD.85.123007.

A. de Ugarte Postigo, C. C. Thoene, A. Rowlinson, R. Garcia-Benito, A. J. Levan, J. Gorosabel, P. Goldoni, S. Schulze, T. Zafar, K. Wiersema, R. Sanchez-Ramirez, A. Melandri, P. D'Avanzo, S. Oates, V. D'Elia, M. De Pasquale, T. Kruehler, A. J. van der Horst, D. Xu, D. Watson, S. Piranomonte, S. Vergani, B. Milvang-Jensen, L. Kaper, D. Malesani, J. P. U. Fynbo, Z. Cano, S. Covino, H. Flores, S. Greiss, F. Hammer, O. E. Hartoog, S. Hellmich, C. Heuser, J. Hjorth, P. Jakobsson, S. Mottola, M. Sparre, J. Sollerman, G. Tagliaferri, N. R. Tanvir, M. Vestergaard, and R. A. M. J. Wijers. The host galaxy and environment of a neutron star merger. *arXiv:1308.2984*, August 2013.

M. B. Deaton, M. D. Duez, F. Foucart, E. O'Connor, C. D. Ott, L. E. Kidder, C. D. Muhlberger, M. A. Scheel, and B. Szilagyi. Black Hole-Neutron Star Mergers with a Hot Nuclear Equation of State: Outflow and Neutrino-Cooled Disk for a Low-Mass, High-Spin Case. *arXiv:1304.3384*, April 2013.

P. B. Demorest, T. Pennucci, S. M. Ransom, M. S. E. Roberts, and J. W. T. Hessels. A two-solar-mass neutron star measured using Shapiro delay. Nature, 467:1081–1083, October 2010. doi: 10.1038/nature09466.

L. Dessart, C. D. Ott, A. Burrows, S. Rosswog, and E. Livne. Neutrino Signatures and the Neutrino-Driven Wind in Binary Neutron Star Mergers. ApJ, 690:1681–1705, January 2009. doi: 10.1088/0004-637X/690/2/1681.

F. Douchin and P. Haensel. A unified equation of state of dense matter and neutron star structure. A&A, 380:151–167, December 2001. doi: 10.1051/0004-6361:20011402.

D. Eichler, M. Livio, T. Piran, and D. N. Schramm. Nucleosynthesis, neutrino bursts and gamma-rays from coalescing neutron stars. Nature, 340:126–128, July 1989. doi: 10.1038/340126a0.

A. J. Faulkner, M. Kramer, A. G. Lyne, R. N. Manchester, M. A. McLaughlin, I. H. Stairs, G. Hobbs, A. Possenti, D. R. Lorimer, N. D'Amico, F. Camilo, and M. Burgay. PSR J1756-2251: A New Relativistic Double Neutron Star System. ApJ, 618:L119–L122, January 2005. doi: 10.1086/427776.

M. Favata. Systematic parameter errors in inspiraling neutron star binaries. *ArXiv e-prints*, October 2013.

R. Fernández and B. D. Metzger. Delayed outflows from black hole accretion tori following neutron star binary coalescence. MNRAS, August 2013. doi: 10.1093/mnras/stt1312.

É. É. Flanagan and T. Hinderer. Constraining neutron-star tidal Love numbers with gravitational-wave detectors. Phys. Rev. D, 77(2):021502, January 2008. doi: 10.1103/PhysRevD.77.021502.

E. Flowers and N. Itoh. Transport properties of dense matter. II. ApJ, 230:847–858, June 1979. doi: 10.1086/157145.

W. Fong and E. Berger. The Locations of Short Gamma-Ray Bursts as Evidence for Compact Object Binary Progenitors. ApJ, 776:18, October 2013. doi: 10.1088/0004-637X/776/1/18.

W.-f. Fong, E. Berger, B. D. Metzger, R. Margutti, R. Chornock, G. Migliori, R. J. Foley, B. A. Zauderer, R. Lunnan, T. Laskar, S. J. Desch, K. J. Meech, S. Sonnett, C. M. Dickey, A. M. Hedlund, and P. Harding. Short GRB 130603B: Discovery of a jet break in the optical and radio afterglows, and a mysterious late-time X-ray excess. *arXiv:1309.7479*, September 2013.

F. Foucart, M. B. Deaton, M. D. Duez, L. E. Kidder, I. MacDonald, C. D. Ott, H. P. Pfeiffer, M. A. Scheel, B. Szilagyi, and S. A. Teukolsky. Black-hole-neutron-star mergers at realistic mass ratios: Equation of state and spin orientation effects. Phys. Rev. D, 87(8):084006, April 2013. doi: 10.1103/PhysRevD.87.084006.

D. B. Fox, D. A. Frail, P. A. Price, S. R. Kulkarni, E. Berger, T. Piran, A. M. Soderberg, S. B. Cenko, P. B. Cameron, A. Gal-Yam, M. M. Kasliwal, D.-S. Moon, F. A. Harrison, E. Nakar, B. P. Schmidt, B. Penprase, R. A. Chevalier, P. Kumar, K. Roth, D. Watson, B. L. Lee, S. Shectman, M. M. Phillips, M. Roth, P. J. McCarthy, M. Rauch, L. Cowie, B. A. Peterson, J. Rich, N. Kawai, K. Aoki, G. Kosugi, T. Totani, H.-S. Park, A. MacFadyen, and K. C. Hurley. The afterglow of GRB 050709 and the nature of the short-hard γ-ray bursts. Nature, 437:845–850, October 2005. doi: 10.1038/nature04189.

D. Frederiks and the Konus-Wind team. GRB 130603B: rest-frame energetics in gamma-rays. *GCN circular*, 2013.

C. Freiburghaus, S. Rosswog, and F.-K. Thielemann. R-Process in Neutron Star Mergers. ApJ, 525:L121–L124, November 1999. doi: 10.1086/312343.

T. J. Galama, P. M. Vreeswijk, J. van Paradijs, C. Kouveliotou, T. Augusteijn, H. Böhnhardt, J. P. Brewer, V. Doublier, J.-F. Gonzalez, B. Leibundgut, C. Lidman, O. R. Hainaut, F. Patat, J. Heise, J. in't Zand, K. Hurley, P. J. Groot, R. G. Strom, P. A. Mazzali, K. Iwamoto, K. Nomoto, H. Umeda, T. Nakamura, T. R. Young, T. Suzuki, T. Shigeyama, T. Koshut, M. Kippen, C. Robinson, P. de Wildt, R. A. M. J. Wijers, N. Tanvir, J. Greiner, E. Pian, E. Palazzi, F. Frontera, N. Masetti, L. Nicastro, M. Feroci, E. Costa, L. Piro, B. A. Peterson, C. Tinney, B. Boyle, R. Cannon, R. Stathakis, E. Sadler, M. C. Begam, and P. Ianna. An unusual supernova in the error box of the γ-ray burst of 25 April 1998. Nature, 395:670–672, October 1998. doi: 10.1038/27150.

H. Gao, B. Zhang, X.-F. Wu, and Z.-G. Dai. Possible high-energy neutrino and photon signals from gravitational wave bursts due to double neutron star mergers. Phys. Rev. D, 88(4):043010, August 2013. doi: 10.1103/PhysRevD.88.043010.

N. Gehrels, C. L. Sarazin, P. T. O'Brien, B. Zhang, L. Barbier, S. D. Barthelmy, A. Blustin, D. N. Burrows, J. Cannizzo, J. R. Cummings, M. Goad, S. T. Holland, C. P. Hurkett, J. A. Kennea, A. Levan, C. B. Markwardt, K. O. Mason, P. Meszaros, M. Page, D. M. Palmer, E. Rol, T. Sakamoto, R. Willingale, L. Angelini, A. Beardmore, P. T. Boyd, A. Breeveld, S. Campana, M. M. Chester, G. Chincarini, L. R. Cominsky, G. Cusumano, M. de Pasquale, E. E. Fenimore, P. Giommi, C. Gronwall, D. Grupe, J. E. Hill, D. Hinshaw, J. Hjorth, D. Hullinger, K. C. Hurley, S. Klose, S. Kobayashi,

C. Kouveliotou, H. A. Krimm, V. Mangano, F. E. Marshall, K. McGowan, A. Moretti, R. F. Mushotzky, K. Nakazawa, J. P. Norris, J. A. Nousek, J. P. Osborne, K. Page, A. M. Parsons, S. Patel, M. Perri, T. Poole, P. Romano, P. W. A. Roming, S. Rosen, G. Sato, P. Schady, A. P. Smale, J. Sollerman, R. Starling, M. Still, M. Suzuki, G. Tagliaferri, T. Takahashi, M. Tashiro, J. Tueller, A. A. Wells, N. E. White, and R. A. M. J. Wijers. A short γ-ray burst apparently associated with an elliptical galaxy at redshift z = 0.225. Nature, 437:851–854, October 2005. doi: 10.1038/nature04142.

B. Giacomazzo and R. Perna. Formation of Stable Magnetars from Binary Neutron Star Mergers. ApJ, 771:L26, July 2013. doi: 10.1088/2041-8205/771/2/L26.

N. K. Glendenning and S. A. Moszkowski. Reconciliation of neutron-star masses and binding of the Lambda in hypernuclei. *Physical Review Letters*, 67:2414–1417, October 1991. doi: 10.1103/PhysRevLett.67.2414.

P. Goldreich and S. Tremaine. The excitation of density waves at the Lindblad and corotation resonances by an external potential. ApJ, 233:857–871, November 1979. doi: 10.1086/157448.

J. Goodman. Are gamma-ray bursts optically thick? ApJ, 308:L47–L50, September 1986. doi: 10.1086/184741.

S. Goriely, A. Bauswein, and H.-T. Janka. r-process Nucleosynthesis in Dynamically Ejected Matter of Neutron Star Mergers. ApJ, 738:L32, September 2011. doi: 10.1088/2041-8205/738/2/L32.

D. Grossman, O. Korobkin, S. Rosswog, and T. Piran. The longterm evolution of neutron star merger remnants II: radioactively powered transients. *ArXiv e-prints*, July 2013.

D. Hilditch, S. Bernuzzi, M. Thierfelder, Z. Cao, W. Tichy, and B. Brügmann. Compact binary evolutions with the Z4c formulation. Phys. Rev. D, 88(8):084057, October 2013. doi: 10.1103/PhysRevD.88.084057.

T. Hinderer. Tidal Love Numbers of Neutron Stars. ApJ, 677:1216–1220, April 2008. doi: 10.1086/533487.

C. M. Hirata. Lindblad resonance torques in relativistic discs - I. Basic equations. MNRAS, 414:3198–3211, July 2011. doi: 10.1111/j.1365-2966.2011.18617.x.

K. Hotokezaka, K. Kyutoku, H. Okawa, M. Shibata, and K. Kiuchi. Binary neutron star mergers: Dependence on the nuclear equation of state. Phys. Rev. D, 83(12):124008, June 2011. doi: 10.1103/PhysRevD.83.124008.

K. Hotokezaka, K. Kiuchi, K. Kyutoku, T. Muranushi, Y.-i. Sekiguchi, M. Shibata, and K. Taniguchi. Remnant massive neutron stars of binary neutron star mergers: Evolution process and gravitational waveform. Phys. Rev. D, 88(4):044026, August 2013a. doi: 10.1103/PhysRevD.88.044026.

K. Hotokezaka, K. Kiuchi, K. Kyutoku, H. Okawa, Y.-i. Sekiguchi, M. Shibata, and K. Taniguchi. Mass ejection from the merger of binary neutron stars. Phys. Rev. D, 87(2):024001, January 2013b. doi: 10.1103/PhysRevD.87.024001.

K. Hotokezaka, K. Kyutoku, and M. Shibata. Exploring tidal effects of coalescing binary neutron stars in numerical relativity. Phys. Rev. D, 87(4):044001, February 2013c. doi: 10.1103/PhysRevD.87.044001.

K. Hotokezaka, K. Kyutoku, M. Tanaka, K. Kiuchi, Y. Sekiguchi, M. Shibata, and S. Wanajo. Progenitor Models of the Electromagnetic Transient Associated with the Short Gamma Ray Burst 130603B. ApJ, 778:L16, November 2013d. doi: 10.1088/2041-8205/778/1/L16.

R. A. Hulse and J. H. Taylor. Discovery of a pulsar in a binary system. ApJ, 195:L51–L53, January 1975. doi: 10.1086/181708.

N. Ivanova, S. Justham, X. Chen, O. De Marco, C. L. Fryer, E. Gaburov, H. Ge, E. Glebbeek, Z. Han, X.-D. Li, G. Lu, T. Marsh, P. Podsiadlowski, A. Potter, N. Soker, R. Taam, T. M. Tauris, E. P. J. van den Heuvel, and R. F. Webbink. Common envelope evolution: where we stand and how we can move forward. A&A Rev., 21:59, February 2013. doi: 10.1007/s00159-013-0059-2.

K. Iwamoto, P. A. Mazzali, K. Nomoto, H. Umeda, T. Nakamura, F. Patat, I. J. Danziger, T. R. Young, T. Suzuki, T. Shigeyama, T. Augusteijn, V. Doublier, J.-F. Gonzalez, H. Boehnhardt, J. Brewer, O. R. Hainaut, C. Lidman, B. Leibundgut, E. Cappellaro, M. Turatto, T. J. Galama, P. M. Vreeswijk, C. Kouveliotou, J. van Paradijs, E. Pian, E. Palazzi, and F. Frontera. A hypernova model for the supernova associated with the γ-ray burst of 25 April 1998. Nature, 395:672–674, October 1998. doi: 10.1038/27155.

B. A. Jacoby, P. B. Cameron, F. A. Jenet, S. B. Anderson, R. N. Murty, and S. R. Kulkarni. Measurement of Orbital Decay in the Double Neutron Star Binary PSR B2127+11C. ApJ, 644:L113–L116, June 2006. doi: 10.1086/505742.

D. A. Kann, S. Klose, B. Zhang, S. Covino, N. R. Butler, D. Malesani, E. Nakar, A. C. Wilson, L. A. Antonelli, G. Chincarini, B. E. Cobb, P. D'Avanzo, V. D'Elia, M. Della Valle, P. Ferrero, D. Fugazza, J. Gorosabel, G. L. Israel, F. Mannucci, S. Piranomonte, S. Schulze, L. Stella, G. Tagliaferri, and K. Wiersema. The Afterglows of Swift-era Gamma-Ray Bursts. II. Type I GRB versus Type II GRB Optical Afterglows. ApJ, 734:96, June 2011. doi: 10.1088/0004-637X/734/2/96.

J. D. Kaplan, C. D. Ott, E. P. O'Connor, K. Kiuchi, L. Roberts, and M. Duez. The Influence of Thermal Pressure on Hypermassive Neutron Star Merger Remnants. *ArXiv e-prints*, June 2013.

A. H. Karp, G. Lasher, K. L. Chan, and E. E. Salpeter. The opacity of expanding media - The effect of spectral lines. ApJ, 214:161–178, May 1977. doi: 10.1086/155241.

D. Kasen, N. R. Badnell, and J. Barnes. Opacities and Spectra of the r-process Ejecta from Neutron Star Mergers. ApJ, 774:25, September 2013. doi: 10.1088/0004-637X/774/1/25.

L. E. Kasian. *Radio observations of two binary pulsars.* PhD thesis, The University of British Columbia, 2012.

C. Kim, V. Kalogera, and D. R. Lorimer. The Probability Distribution of Binary Pulsar Coalescence Rates. I. Double Neutron Star Systems in the Galactic Field. ApJ, 584: 985–995, February 2003. doi: 10.1086/345740.

K. Kiuchi, Y. Sekiguchi, M. Shibata, and K. Taniguchi. Long-term general relativistic simulation of binary neutron stars collapsing to a black hole. Phys. Rev. D, 80(6): 064037, September 2009. doi: 10.1103/PhysRevD.80.064037.

K. Kiuchi, K. Kyutoku, and M. Shibata. Three-dimensional evolution of differentially rotating magnetized neutron stars. Phys. Rev. D, 86(6):064008, September 2012. doi: 10.1103/PhysRevD.86.064008.

D. Kocevski, C. C. Thöne, E. Ramirez-Ruiz, J. S. Bloom, J. Granot, N. R. Butler, D. A. Perley, M. Modjaz, W. H. Lee, B. E. Cobb, A. J. Levan, N. Tanvir, and S. Covino. Limits on radioactive powered emission associated with a short-hard GRB 070724A in a star-forming galaxy. MNRAS, 404:963–974, May 2010. doi: 10.1111/j.1365-2966.2010.16327.x.

C. S. Kochanek. Coalescing binary neutron stars. ApJ, 398:234–247, October 1992. doi: 10.1086/171851.

C. S. Kochanek and T. Piran. Gravitational Waves and gamma -Ray Bursts. ApJ, 417: L17, November 1993. doi: 10.1086/187083.

O. Korobkin, S. Rosswog, A. Arcones, and C. Winteler. On the astrophysical robustness of the neutron star merger r-process. MNRAS, 426:1940–1949, November 2012. doi: 10.1111/j.1365-2966.2012.21859.x.

C. Kouveliotou, C. A. Meegan, G. J. Fishman, N. P. Bhat, M. S. Briggs, T. M. Koshut, W. S. Paciesas, and G. N. Pendleton. Identification of two classes of gamma-ray bursts. ApJ, 413:L101–L104, August 1993. doi: 10.1086/186969.

M. Kramer, I. H. Stairs, R. N. Manchester, M. A. McLaughlin, A. G. Lyne, R. D. Ferdman, M. Burgay, D. R. Lorimer, A. Possenti, N. D'Amico, J. M. Sarkissian, G. B. Hobbs, J. E. Reynolds, P. C. C. Freire, and F. Camilo. Tests of General Relativity from Timing the Double Pulsar. *Science*, 314:97–102, October 2006. doi: 10.1126/science.1132305.

A. Kurganov and E. Tadmor. New High-Resolution Central Schemes for Nonlinear Conservation Laws and Convection-Diffusion Equations. *Journal of Computational Physics*, 160:241–282, May 2000. doi: 10.1006/jcph.2000.6459.

K. Kyutoku, K. Ioka, and M. Shibata. Ultrarelativistic electromagnetic counterpart to binary neutron star mergers. *ArXiv e-prints*, September 2012.

Koutarou Kyutoku, Kunihito Ioka, and Masaru Shibata. Anisotropic mass ejection from black hole-neutron star binaries: Diversity of electromagnetic counterparts. *Phys. Rev. D*, 88:041503, Aug 2013. doi: 10.1103/PhysRevD.88.041503. URL `http://link.aps.org/doi/10.1103/PhysRevD.88.041503`.

B. D. Lackey, M. Nayyar, and B. J. Owen. Observational constraints on hyperons in neutron stars. Phys. Rev. D, 73(2):024021, January 2006. doi: 10.1103/PhysRevD.73.024021.

D. Lai, F. A. Rasio, and S. L. Shapiro. Hydrodynamic instability and coalescence of binary neutron stars. ApJ, 420:811–829, January 1994. doi: 10.1086/173606.

J. M. Lattimer and M. Prakash. The Physics of Neutron Stars. *Science*, 304:536–542, April 2004. doi: 10.1126/science.1090720.

J. M. Lattimer and M. Prakash. What a Two Solar Mass Neutron Star Really Means. *ArXiv e-prints*, December 2010.

J. M. Lattimer and D. N. Schramm. Black-hole-neutron-star collisions. ApJ, 192:L145–L147, September 1974. doi: 10.1086/181612.

J. M. Lattimer, F. Mackie, D. G. Ravenhall, and D. N. Schramm. The decompression of cold neutron star matter. ApJ, 213:225–233, April 1977. doi: 10.1086/155148.

L.-X. Li and B. Paczyński. Transient Events from Neutron Star Mergers. ApJ, 507: L59–L62, November 1998. doi: 10.1086/311680.

D. R. Lorimer. Binary and Millisecond Pulsars. *Living Reviews in Relativity*, 11:8, November 2008. doi: 10.12942/lrr-2008-8.

D. R. Lorimer, I. H. Stairs, P. C. Freire, J. M. Cordes, F. Camilo, A. J. Faulkner, A. G. Lyne, D. J. Nice, S. M. Ransom, Z. Arzoumanian, R. N. Manchester, D. J. Champion, J. van Leeuwen, M. A. Mclaughlin, R. Ramachandran, J. W. Hessels, W. Vlemmings,

A. A. Deshpande, N. D. Bhat, S. Chatterjee, J. L. Han, B. M. Gaensler, L. Kasian, J. S. Deneva, B. Reid, T. J. Lazio, V. M. Kaspi, F. Crawford, A. N. Lommen, D. C. Backer, M. Kramer, B. W. Stappers, G. B. Hobbs, A. Possenti, N. D'Amico, and M. Burgay. Arecibo Pulsar Survey Using ALFA. II. The Young, Highly Relativistic Binary Pulsar J1906+0746. ApJ, 640:428–434, March 2006. doi: 10.1086/499918.

G. Lovelace, M. D. Duez, F. Foucart, L. E. Kidder, H. P. Pfeiffer, M. A. Scheel, and B. Szilágyi. Massive disc formation in the tidal disruption of a neutron star by a nearly extremal black hole. *Classical and Quantum Gravity*, 30(13):135004, July 2013. doi: 10.1088/0264-9381/30/13/135004.

R. S. Lynch, P. C. C. Freire, S. M. Ransom, and B. A. Jacoby. The Timing of Nine Globular Cluster Pulsars. ApJ, 745:109, February 2012. doi: 10.1088/0004-637X/745/2/109.

A. Melandri, W. H. Baumgartner, D. N. Burrows, J. R Cummings, N. Gehrels, C. Gronwall, K. L Page, Palmer D. M., Starling R. L. C, Ukwatta T. N., and the Swift team. GRB 130603B: Swift detection of a bright short burst. *GCN circular*, 2013.

C. Messenger and J. Read. Measuring a Cosmological Distance-Redshift Relationship Using Only Gravitational Wave Observations of Binary Neutron Star Coalescences. *Physical Review Letters*, 108(9):091101, March 2012. doi: 10.1103/PhysRevLett.108.091101.

B. D. Metzger and E. Berger. What is the Most Promising Electromagnetic Counterpart of a Neutron Star Binary Merger? ApJ, 746:48, February 2012. doi: 10.1088/0004-637X/746/1/48.

B. D. Metzger, G. Martínez-Pinedo, S. Darbha, E. Quataert, A. Arcones, D. Kasen, R. Thomas, P. Nugent, I. V. Panov, and N. T. Zinner. Electromagnetic counterparts of compact object mergers powered by the radioactive decay of r-process nuclei. MNRAS, 406:2650–2662, August 2010. doi: 10.1111/j.1365-2966.2010.16864.x.

B. S. Meyer. Decompression of initially cold neutron star matter - A mechanism for the r-process? ApJ, 343:254–276, August 1989. doi: 10.1086/167702.

H. Müller and B. D. Serot. Relativistic mean-field theory and the high-density nuclear equation of state. *Nuclear Physics A*, 606:508–537, February 1996. doi: 10.1016/0375-9474(96)00187-X.

T. Nakamura, K. Kashiyama, D. Nakauchi, Y. Suwa, T. Sakamoto, and N. Kawai. Soft X-ray Extended Emissions of Short Gamma-Ray Bursts as Electromagnetic Counterparts of Compact Binary Mergers; Possible Origin and Detectability. *ArXiv e-prints*, December 2013.

E. Nakar. Short-hard gamma-ray bursts. Phys. Rep., 442:166–236, April 2007. doi: 10.1016/j.physrep.2007.02.005.

E. Nakar and T. Piran. Detectable radio flares following gravitational waves from mergers of binary neutron stars. Nature, 478:82–84, October 2011. doi: 10.1038/nature10365.

R. Narayan, T. Piran, and A. Shemi. Neutron star and black hole binaries in the Galaxy. ApJ, 379:L17–L20, September 1991. doi: 10.1086/186143.

R. Oechslin, H.-T. Janka, and A. Marek. Relativistic neutron star merger simulations with non-zero temperature equations of state. I. Variation of binary parameters and equation of state. A&A, 467:395–409, May 2007. doi: 10.1051/0004-6361:20066682.

B. Paczynski. Common Envelope Binaries. In P. Eggleton, S. Mitton, and J. Whelan, editors, *Structure and Evolution of Close Binary Systems*, volume 73 of *IAU Symposium*, page 75, 1976.

B. Paczynski. Gamma-ray bursters at cosmological distances. ApJ, 308:L43–L46, September 1986. doi: 10.1086/184740.

Y. Pan, A. Buonanno, M. Boyle, L. T. Buchman, L. E. Kidder, H. P. Pfeiffer, and M. A. Scheel. Inspiral-merger-ringdown multipolar waveforms of nonspinning black-hole binaries using the effective-one-body formalism. Phys. Rev. D, 84(12):124052, December 2011. doi: 10.1103/PhysRevD.84.124052.

D. A. Perley, B. D. Metzger, J. Granot, N. R. Butler, T. Sakamoto, E. Ramirez-Ruiz, A. J. Levan, J. S. Bloom, A. A. Miller, A. Bunker, H.-W. Chen, A. V. Filippenko, N. Gehrels, K. Glazebrook, P. B. Hall, K. C. Hurley, D. Kocevski, W. Li, S. Lopez, J. Norris, A. L. Piro, D. Poznanski, J. X. Prochaska, E. Quataert, and N. Tanvir. GRB 080503: Implications of a Naked Short Gamma-Ray Burst Dominated by Extended Emission. ApJ, 696:1871–1885, May 2009. doi: 10.1088/0004-637X/696/2/1871.

E. S. Phinney. The rate of neutron star binary mergers in the universe - Minimal predictions for gravity wave detectors. ApJ, 380:L17–L21, October 1991. doi: 10.1086/186163.

T. Piran, E. Nakar, and S. Rosswog. The electromagnetic signals of compact binary mergers. MNRAS, 430:2121–2136, April 2013. doi: 10.1093/mnras/stt037.

E. Poisson and C. M. Will. Gravitational waves from inspiraling compact binaries: Parameter estimation using second-post-Newtonian waveforms. Phys. Rev. D, 52:848–855, July 1995. doi: 10.1103/PhysRevD.52.848.

S. F. Portegies Zwart and L. R. Yungelson. The possible companions of young radio pulsars. MNRAS, 309:26–30, October 1999.

M. Punturo, M. Abernathy, F. Acernese, B. Allen, N. Andersson, K. Arun, F. Barone, B. Barr, M. Barsuglia, M. Beker, N. Beveridge, S. Birindelli, S. Bose, L. Bosi, S. Braccini, C. Bradaschia, T. Bulik, E. Calloni, G. Cella, E. Chassande Mottin, S. Chelkowski, A. Chincarini, J. Clark, E. Coccia, C. Colacino, J. Colas, A. Cumming, L. Cunningham, E. Cuoco, S. Danilishin, K. Danzmann, G. De Luca, R. De Salvo, T. Dent, R. De Rosa, L. Di Fiore, A. Di Virgilio, M. Doets, V. Fafone, P. Falferi, R. Flaminio, J. Franc, F. Frasconi, A. Freise, P. Fulda, J. Gair, G. Gemme, A. Gennai, A. Giazotto, K. Glampedakis, M. Granata, H. Grote, G. Guidi, G. Hammond, M. Hannam, J. Harms, D. Heinert, M. Hendry, I. Heng, E. Hennes, S. Hild, J. Hough, S. Husa, S. Huttner, G. Jones, F. Khalili, K. Kokeyama, K. Kokkotas, B. Krishnan, M. Lorenzini, H. Lück, E. Majorana, I. Mandel, V. Mandic, I. Martin, C. Michel, Y. Minenkov, N. Morgado, S. Mosca, B. Mours, H. MüllerEbhardt, P. Murray, R. Nawrodt, J. Nelson, R. Oshaughnessy, C. D. Ott, C. Palomba, A. Paoli, G. Parguez, A. Pasqualetti, R. Passaquieti, D. Passuello, L. Pinard, R. Poggiani, P. Popolizio, M. Prato, P. Puppo, D. Rabeling, P. Rapagnani, J. Read, T. Regimbau, H. Rehbein, S. Reid, L. Rezzolla, F. Ricci, F. Richard, A. Rocchi, S. Rowan, A. Rüdiger, B. Sassolas, B. Sathyaprakash, R. Schnabel, C. Schwarz, P. Seidel, A. Sintes, K. Somiya, F. Speirits, K. Strain, S. Strigin, P. Sutton, S. Tarabrin, A. Thüring, J. van den Brand, C. van Leewen, M. van Veggel, C. van den Broeck, A. Vecchio, J. Veitch, F. Vetrano, A. Vicere, S. Vyatchanin, B. Willke, G. Woan, P. Wolfango, and K. Yamamoto. The Einstein Telescope: a third-generation gravitational wave observatory. *Classical and Quantum Gravity*, 27(19): 194002, October 2010. doi: 10.1088/0264-9381/27/19/194002.

D. Radice and L. Rezzolla. THC: a new high-order finite-difference high-resolution shock-capturing code for special-relativistic hydrodynamics. A&A, 547:A26, November 2012. doi: 10.1051/0004-6361/201219735.

J. S. Read, B. D. Lackey, B. J. Owen, and J. L. Friedman. Constraints on a phenomenologically parametrized neutron-star equation of state. Phys. Rev. D, 79(12):124032, June 2009. doi: 10.1103/PhysRevD.79.124032.

L. Rezzolla, B. Giacomazzo, L. Baiotti, J. Granot, C. Kouveliotou, and M. A. Aloy. The Missing Link: Merging Neutron Stars Naturally Produce Jet-like Structures and Can Power Short Gamma-ray Bursts. ApJ, 732:L6, May 2011. doi: 10.1088/2041-8205/732/1/L6.

S. Rosswog. The dynamic ejecta of compact object mergers and eccentric collisions. *Royal Society of London Philosophical Transactions Series A*, 371:20272, April 2013. doi: 10.1098/rsta.2012.0272.

S. Rosswog, M. Liebendörfer, F.-K. Thielemann, M. B. Davies, W. Benz, and T. Piran. Mass ejection in neutron star mergers. A&A, 341:499–526, January 1999.

S. Rosswog, M. B. Davies, F.-K. Thielemann, and T. Piran. Merging neutron stars: asymmetric systems. A&A, 360:171–184, August 2000.

S. Rosswog, T. Piran, and E. Nakar. The multimessenger picture of compact object encounters: binary mergers versus dynamical collisions. MNRAS, 430:2585–2604, April 2013. doi: 10.1093/mnras/sts708.

A. Rowlinson, K. Wiersema, A. J. Levan, N. R. Tanvir, P. T. O'Brien, E. Rol, J. Hjorth, C. C. Thöne, A. de Ugarte Postigo, J. P. U. Fynbo, P. Jakobsson, C. Pagani, and M. Stamatikos. Discovery of the afterglow and host galaxy of the low-redshift short GRB 080905A. MNRAS, 408:383–391, October 2010. doi: 10.1111/j.1365-2966.2010.17115.x.

M. Ruffert, H.-T. Janka, K. Takahashi, and G. Schaefer. Coalescing neutron stars - a step towards physical models. II. Neutrino emission, neutron tori, and gamma-ray bursts. A&A, 319:122–153, March 1997.

G. B. Rybicki and A. P. Lightman. *Radiative processes in astrophysics.* 1979.

R. Sari, T. Piran, and R. Narayan. Spectra and Light Curves of Gamma-Ray Burst Afterglows. ApJ, 497:L17, April 1998. doi: 10.1086/311269.

Y. Sekiguchi, K. Kiuchi, K. Kyutoku, and M. Shibata. Gravitational Waves and Neutrino Emission from the Merger of Binary Neutron Stars. *Physical Review Letters*, 107(5): 051102, July 2011a. doi: 10.1103/PhysRevLett.107.051102.

Y. Sekiguchi, K. Kiuchi, K. Kyutoku, and M. Shibata. Effects of Hyperons in Binary Neutron Star Mergers. *Physical Review Letters*, 107(21):211101, November 2011b. doi: 10.1103/PhysRevLett.107.211101.

M. Shibata. Fully general relativistic simulation of coalescing binary neutron stars: Preparatory tests. Phys. Rev. D, 60(10):104052, November 1999. doi: 10.1103/PhysRevD.60.104052.

M. Shibata. Axisymmetric general relativistic hydrodynamics: Long-term evolution of neutron stars and stellar collapse to neutron stars and black holes. Phys. Rev. D, 67 (2):024033, January 2003. doi: 10.1103/PhysRevD.67.024033.

M. Shibata. Constraining Nuclear Equations of State Using Gravitational Waves from Hypermassive Neutron Stars. *Physical Review Letters*, 94(20):201101, May 2005. doi: 10.1103/PhysRevLett.94.201101.

M. Shibata and J. A. Font. Robustness of a high-resolution central scheme for hydrodynamic simulations in full general relativity. Phys. Rev. D, 72(4):047501, August 2005. doi: 10.1103/PhysRevD.72.047501.

M. Shibata and T. Nakamura. Evolution of three-dimensional gravitational waves: Harmonic slicing case. Phys. Rev. D, 52:5428–5444, November 1995. doi: 10.1103/PhysRevD.52.5428.

M. Shibata and K. ō. Uryū. Simulation of merging binary neutron stars in full general relativity: Γ=2 case. Phys. Rev. D, 61(6):064001, March 2000. doi: 10.1103/PhysRevD.61.064001.

M. Shibata, K. Taniguchi, and K. Uryū. Merger of binary neutron stars with realistic equations of state in full general relativity. Phys. Rev. D, 71(8):084021, April 2005. doi: 10.1103/PhysRevD.71.084021.

J. Simmerer, C. Sneden, J. J. Cowan, J. Collier, V. M. Woolf, and J. E. Lawler. The Rise of the s-Process in the Galaxy. ApJ, 617:1091–1114, December 2004. doi: 10.1086/424504.

I. H. Stairs, S. E. Thorsett, J. H. Taylor, and A. Wolszczan. Studies of the Relativistic Binary Pulsar PSR B1534+12. I. Timing Analysis. ApJ, 581:501–508, December 2002. doi: 10.1086/344157.

G. Stratta, P. D'Avanzo, S. Piranomonte, S. Cutini, B. Preger, M. Perri, M. L. Conciatore, S. Covino, L. Stella, D. Guetta, F. E. Marshall, S. T. Holland, M. Stamatikos, C. Guidorzi, V. Mangano, L. A. Antonelli, D. Burrows, S. Campana, M. Capalbi, G. Chincarini, G. Cusumano, V. D'Elia, P. A. Evans, F. Fiore, D. Fugazza, P. Giommi, J. P. Osborne, V. La Parola, T. Mineo, A. Moretti, K. L. Page, P. Romano, and G. Tagliaferri. A study of the prompt and afterglow emission of the short GRB 061201. A&A, 474:827–835, November 2007. doi: 10.1051/0004-6361:20078006.

E. Symbalisty and D. N. Schramm. Neutron star collisions and the r-process. Astrophys. Lett., 22:143–145, 1982.

H. Takami, K. Kyutoku, and K. Ioka. High-Energy Radiation from Remnants of Neutron Star Binary Mergers. *ArXiv e-prints*, July 2013.

M. Tanaka and K. Hotokezaka. Radiative Transfer Simulations of Neutron Star Merger Ejecta. ApJ, 775:113, October 2013. doi: 10.1088/0004-637X/775/2/113.

M. Tanaka, K. Hotokezaka, K. Kyutoku, S. Wanajo, K. Kiuchi, Y. Sekiguchi, and M. Shibata. Radioactively Powered Emission from Black Hole-Neutron Star Mergers. *arXiv:1310.2774*, October 2013.

N. R. Tanvir, A. J. Levan, A. S. Fruchter, J. Hjorth, R. A. Hounsell, K. Wiersema, and R. L. Tunnicliffe. A 'kilonova' associated with the short-duration γ-ray burst GRB130603B. Nature, 500:547–549, August 2013. doi: 10.1038/nature12505.

J. H. Taylor, L. A. Fowler, and P. M. McCulloch. Measurements of general relativistic effects in the binary pulsar PSR 1913+16. Nature, 277:437–440, February 1979. doi: 10.1038/277437a0.

The LIGO Scientific Collaboration and the Virgo Collaboration, J. Aasi, J. Abadie, B. P. Abbott, R. Abbott, T. Abbott, M. R. Abernathy, T. Accadia, F. Acernese, and et al. First Searches for Optical Counterparts to Gravitational-wave Candidate Events. *ArXiv e-prints*, October 2013.

M. Thierfelder, S. Bernuzzi, and B. Brügmann. Numerical relativity simulations of binary neutron stars. Phys. Rev. D, 84(4):044012, August 2011. doi: 10.1103/PhysRevD.84.044012.

R. Tsutsui, D. Yonetoku, T. Nakamura, K. Takahashi, and Y. Morihara. Possible existence of the E_p-L_p and E_p-E_{iso} correlations for short gamma-ray bursts with a factor 5-100 dimmer than those for long gamma-ray bursts. MNRAS, 431:1398–1404, May 2013. doi: 10.1093/mnras/stt262.

J. S. Villasenor, D. Q. Lamb, G. R. Ricker, J.-L. Atteia, N. Kawai, N. Butler, Y. Nakagawa, J. G. Jernigan, M. Boer, G. B. Crew, T. Q. Donaghy, J. Doty, E. E. Fenimore, M. Galassi, C. Graziani, K. Hurley, A. Levine, F. Martel, M. Matsuoka, J.-F. Olive, G. Prigozhin, T. Sakamoto, Y. Shirasaki, M. Suzuki, T. Tamagawa, R. Vanderspek, S. E. Woosley, A. Yoshida, J. Braga, R. Manchanda, G. Pizzichini, K. Takagishi, and M. Yamauchi. Discovery of the short γ-ray burst GRB 050709. Nature, 437:855–858, October 2005. doi: 10.1038/nature04213.

J. Vines, É. É. Flanagan, and T. Hinderer. Post-1-Newtonian tidal effects in the gravitational waveform from binary inspirals. Phys. Rev. D, 83(8):084051, April 2011. doi: 10.1103/PhysRevD.83.084051.

R. M. Wald. *General relativity*. 1984.

S. Wanajo and H.-T. Janka. The r-process in the Neutrino-driven Wind from a Black-hole Torus. ApJ, 746:180, February 2012. doi: 10.1088/0004-637X/746/2/180.

J. M. Weisberg, D. J. Nice, and J. H. Taylor. Timing Measurements of the Relativistic Binary Pulsar PSR B1913+16. ApJ, 722:1030–1034, October 2010. doi: 10.1088/0004-637X/722/2/1030.

K. Yagi and N. Yunes. Love can be Tough to Measure. *ArXiv e-prints*, October 2013.

T. Yamamoto, M. Shibata, and K. Taniguchi. Simulating coalescing compact binaries by a new code (SACRA). Phys. Rev. D, 78(6):064054, September 2008. doi: 10.1103/PhysRevD.78.064054.

B. Zhang. Early X-Ray and Optical Afterglow of Gravitational Wave Bursts from Mergers of Binary Neutron Stars. ApJ, 763:L22, January 2013. doi: 10.1088/2041-8205/763/1/L22.